Dissertation

Structural and Mechanical Gradients in Nanostructured Thin Films

Jakub Zálešák

Montanuniversität Leoben

Department of Materials Physics

August 2017

Montanuniversität Leoben
Department of Materials Physics
Jahnstraße 12
8700 Leoben
Austria

Affidavit

I declare in lieu of oath, that I wrote this thesis and performed the associated research myself, using only literature cited in this volume.

Leoben, August 2017

Acknowledgments

This work would not have been possible without the great support of supervisors, co-workers, colleagues, friends and my family.

Christian Doppler Association provided financial support of this work in the framework of the Christian Doppler Laboratory for Application Oriented Coating Development and the companies Oerlikon Balzers Coating AG, Balzers (Liechtenstein) and PLANSEE Composite Materials, Lechbruck (Germany). Research funding was also provided by the European Union, within the large collaborative project ISTRESS, Grant Agreement No. 604646. A part of this work was supported by the FFG Project "CVDnanoCOAT" under the grant number 841137.

I would like to thank to my supervisors Jozef Keckes, Rostislav Daniel and Paul H. Mayerhofer for funding and supporting me on my way through the PhD studies. This support also extended to supporting me in attending several interesting conferences and especially TEM workshops.

Furthermore, I want to thank to all colleagues who contributed to my research directly or indirectly. Here I have to mention particularly ESI itself that became my second home and where I always felt like a member of a big family.

I particularly want to thank Daniel Kiener for introducing me to the *in situ* TEM experiments and for being friendly and helpful whenever I came into his office, also Christian Mitterer who was always friendly and enthusiastic, further Igor Matko for all the time that we spent together doing TEM work and drinking some beer afterwards, likwise "small Michael" for all the help with the *in situ* SEM experiments, similarly "big Michel" for being my first TEM apprentice and becoming a very good friend afterwards, same here the crew of "USS Dodge", David and Juraj, with whom I spent a great time on our California road trip, more Julian who was without any doubts the best office member, too Gabi Felber for preparation of a large number of samples.

Great thank is also due to all the secretaries: Viktoria, Regina, Angelica, Dani and Sabine who had to deal with my sclerosis and made sure that the essential administration was done.

I would like to address a very special thanks to David Holec who brought me into Leoben and keeps helping and supervising me not only on the field of science but also in daily life.

Last but not least, I want to thank my family and my beloved Pezi for all the love and support.

Abstract

Despite the fact that the $Ti_xAl_{1-x}N$-based thin films have been one of the most frequently studied protective thin film material in last the 25 years, the understanding of their complex structure-property relationship is far from being complete. In particular, the presence of nano-scale structural and functional gradients as well as their influence on overall functional properties, had been for a long time a topic only hardly accessible due to a non-sufficient resolution of analytical techniques. The obtained experimental data frequently represented just average values, and contributions of individual microstructural features and gradients were difficult to resolve. The advancement of position sensitive analytical methods achieved in the last decade, however, allowed to acquire data with sufficient lateral resolution, and to combine them with local mechanical properties obtained using traditional nanoindentation techniques as well as modern *in situ* methods.

The focus of this work is mainly on the application of advanced imaging and analytical methods of transmission electron microscopy, X-ray nano-beam diffraction, and in situ electron microscopy mechanical testing in physical vapor deposited $Ti_xAl_{1-x}N$ thin films as well as a development and studying of new self-organized low pressure chemical vapor deposited $Ti_xAl_{1-x}N$ thin films. The latter represent a new revolutionary material class with unique 3D self-assembled nanolamellar microstructure containing a meta-stable cubic AlN_y, which does not exist otherwise in a bulk form at ambient conditions. The understanding of this fascinating self-assembly process represents a milestone in thin film technology.

Three author contributions to the three studies of $Ti_xAl_{1-x}N$ thin films presented in this thesis are:

- A methodological approach for complex cross-sectional analysis and optimization of thin films was developed for a $2\,\mu$m thick compositionally-graded $Ti_xAl_{1-x}N$ thin film. Spatially resolved methods for chemical, phase and residual stress analyzes were combined with cross-sectional nanoindentation and *in situ* TEM cantilever beam bending. This work has proven the possibility to resolve the influence of simultaneously occurring gradients of crystalline phases, microstructure, chemical composition and strains on thin film cross-sections as well as local mechanical properties.

- Novel Al-rich $Ti_xAl_{1-x}N$ chemical vapor deposited coatings with self-organized microstructure were studied. An optimization process, derived from the previous study, was applied on a mixed cubic-hexagonal self-organized $Ti_{0.05}Al_{0.95}N$ coating in order to enhance its mechanical properties by a formation of a pure cubic phase. The resulting single-phase cubic $Ti_{0.2}Al_{0.8}N$ coating exhibits hardness of 36 GPa and reduced modulus of 522 GPa.

- In order to gain better understanding of the self-organization phenomenon in single-phase cubic LP-CVD $Ti_xAl_{1-x}N$ coatings, hetero-epitaxial films were grown on an Al_2O_3 (0001) substrate. The films, with an overall x fraction of $\sim$0.8, were composed of alternating non-stoichiometric cubic Al-rich and Ti-rich nanolamellae with thicknesses of $\sim$11 and $\sim$1.5 nm, respectively. X-ray diffraction, electron microscopy and electron energy loss spectroscopy indicate that the nanolamellae coherency is primarily a result of an N deficiency in Ti-rich nanolamellae and an N excess in Al-rich nanolamellae, which induce a decrease and an increase in nanolamellae lattice parameters, as compared with the lattice parameters of stoichiometric rock-salt c-TiN and c-AlN, respectively.

Kurzfassung

Obwohl $Ti_xAl_{1-x}N$-basierte Dünnschichten zu den am meisten untersuchten Schutzbeschichtungswerkstoffen der letzten 25 Jahre zählen, ist das Verständnis ihrer komplexen Struktur-Eigenschaftsbeziehungen noch lange nicht vollständig. Im Besonderen waren das Vorhandensein von nano-skalierten strukturellen und funktionalen Gradienten, wie auch deren Einfluss auf die funktionalen Eigenschaften der Gesamtschicht, aufgrund der unzureichenden Auflösung der vorhandenen Analysemethoden bisher nur schwer zugänglich. Die gemessenen Versuchsdaten stellten oft nur gemittelte Werte dar und die Beiträge einzelner Gefügemerkmale und Gradienten war schwer aufzulösen. Indes hat es innerhalb des letzten Jahrzehnts der Fortschritt bei ortsempfindlichen Analysetechniken ermöglicht, Daten mit ausreichender Ortsauflösung zu erlangen und diese mit lokalen mechanischen Eigenschaften zu kombinieren, die mittels traditioneller Nanoindentation und moderner *in situ* Methoden gemessen werden.

Der Schwerpunkt dieser Arbeit ist die Anwendung fortschrittlicher bildgebender und analytischer Verfahren der Transmissionselektronenmikroskopie, Nanostrahl-Röntgenbeugung und in situ elektronenmikroskopischer mechanischer Versuche an physikalisch aufgedampften $Ti_xAl_{1-x}N$ Dünnschichten, sowie die Entwicklung und Untersuchung von neuartigen selbstgeordneten bei Niederdruck chemisch aufgedampften $Ti_xAl_{1-x}N$ Dünnschichten. Letztere stellen eine neue, revolutionäre Werkstoffklasse dar, die ein einzigartiges 3D selbstgeordnetes Gefüge aufweist, welches metastabiles kubisches AlN_y beinhaltet, das sonst nicht in größeren Volumina bei Umgebungsbedingungen existiert. Das Verständnis dieses faszinierenden Selbstordnungsvorgangs stellt einen Meilenstein in der Dünnschichttechnologie dar.

Drei Autorenbeiträge zu den drei Studien an $Ti_xAl_{1-x}N$ Dünnschichten, die im Rahmen dieser Arbeit vorgestellt werden, sind:

- Ein methodischer Ansatz zur Analyse komplexer Querschnitte und Optimierung von Dünnschichten wurde anhand einer $2\,\mu$m dicken $Ti_xAl_{1-x}N$ Dünnschicht mit Zusammensetzungs-Tiefengradient entwickelt. Ortsaufgelöste Verfahren für die Untersuchung der chemischen Zusammensetzung, Phasenzusammensetzung, sowie von Eigenspannungen wurden mit Nanoindentation am Querschnitt und *in situ* TEM Biegebalkenversuchen kombiniert. Diese Arbeit erprobte die Möglichkeit zur Aufklärung des Einflusses von gleichzeitig auftretenden Gradienten der kristallinen Phasen, des Gefüges, der chemischen Zusammensetzung und von Dehnungen auf die Ausprägung von Dünnschicht-Quer-

schnitten, sowie auf lokale mechanische Eigenschaften.

- Neuartige Al-reiche chemisch aufgedampfte $Ti_xAl_{1-x}N$ Beschichtungen mit selbstgeordnetem Gefüge wurden untersucht. Ein optimiertes aus der vorhergehenden Studie abgeleitetes Verfahren wurde auf eine gemischt kubisch-hexagonale $Ti_{0.05}Al_{0.95}N$ Beschichtung angewandt, um ihre mechanischen Eigenschaften durch die Bildung einer rein kubischen Phase zu verbessern. Die daraus resultierende einphasig kubische $Ti_{0.2}Al_{0.8}N$ Beschichtung zeigt eine Härte von 36 GPa und einen reduzierten E-Modul von 522 GPa.
- Um ein besseres Verständnis des Selbstordnungsphänomens in einphasig kubischen LP-CVD $Ti_xAl_{1-x}N$ Beschichtungen zu erlangen, wurden hetero-epitaxe Schichten auf Al_2O_3 (0001) Substraten gewachsen. Die Schichten, mit mittlerer Zusammensetzung $x \sim 0.8$, waren aus abwechselnd nicht-stöchiometrischen kubischen Al-reichen und Ti-reichen Nanolamellen zusammengesetzt, mit Dicken von jeweils ∼11, bzw. ∼1.5 nm. Röntgenbeugung, Elektronenmikroskopie und Elektronenenergieverlustspektroskopie deuten darauf hin, dass die Kohärenz von Nanolamellen in erster Linie eine Folge des N-Mangels in Ti-reichen Nanolamellen und N-Überschusses in Al-reichen Nanolamellen ist, welche die jeweiligen Gitterparameter in den Nanolamellen im Vergleich zu stöchiometrischem NaCl-Typ c-TiN und c-AlN verkleinern, bzw. vergrößern.

Contents

H. Grain boundary design of thin films: Using tilted brittle interfaces for multiple crack deflection toughening **H–1**

1

Introduction

The constantly increasing demands for longer lifetimes and higher operating temperatures of industrial thin films used in metal working industry have triggered the rapid technological development in last decades. Despite the enormous progress, the original idea remains the same: a tool is coated with a thin film made of protective material in order to improve its lifetime and overall performance. To achieve this general goal, further specifications have to be however defined. For the field of cutting tools, the typical requirements are (i) high hardness, (ii) high fracture toughness, (iii) excellent thermal stability, (iv) high oxidation resistance, and (v) excellent adhesion. It turns out that the desired properties are often contradicting. For example, extremely hard materials are usually brittle. Higher working temperatures increase chemical reactivity and diffusion, therefore make oxidation easier, etc. Such opposing demands make the development of hard thin films to be challenging but also interesting topic for materials scientists.

Nowadays, a further development of advanced materials requires a detailed understanding of structural and functional relationships down to the atomistic scale. Modern experimental techniques can provide necessary insights, but the interpretation of the experimental data represents a difficult task. Especially in the case of unstable thin films prepared far from thermodynamic equilibrium, such as magnetron sputtered TiAlN and CrAlN, for which physical properties depend on many variables of the deposition process. An understanding of the interrelationships between the functional behaviour, physical properties and process parameters in a precise way presents not only a sampling problem, but is strongly dependent on the spatial resolution of the experimental techniques as well. Therefore, when considering costs for a single deposition run and a subsequent analysis, it is more efficient to vary one of the deposition parameters (such as the Ti/Al ratio) during the deposition process, and hence to obtain a thin film with a gradual evolution of composition, microstructure and functional properties. In combination with position-resolved analyses, a complex dependence of thin film properties on a deposition parameter can be obtained and subsequently used for the optimization. This concept is introduced in this thesis as a graded thin film concept, and was successfully applied to the TiAlN thin film systems synthesized using physical vapour deposition (PVD) and chemical vapour deposition (CVD).

Since the last 25 years, metastable face-centred cubic (fcc) $Ti_xAl_{1-x}N$ thin films have been one of the most common protective system [1] with numerous industrial applications due to their interesting high-temperature behaviour including spinodal decomposition into a cubic TiN (B1) and a metastable cubic AlN (B1) structures, the latter further transforming into a stable hexagonal AlN (B4) structure [2]. This process is accompanied by an extensive hardening effect [3], followed by a hardness drop and a film degradation above critical temperatures. Numerous experimental works have, however, demonstrated that the metastable cubic $Ti_xAl_{1-x}N$ can be synthesized using physical vapour deposition (PVD) only for $x<0.33$. A further decrease of the Ti-content leads to the formation of hexagonal $Ti_xAl_{1-x}N$ with much less favourable mechanical properties. Both effects, the spinodal decomposition and the solubility limit, pose key limitations on the application of $Ti_xAl_{1-x}N$ thin films. Recent progress in the CVD technique introduced a new type of thin films based on the fcc $Ti_xAl_{1-x}N$ and exhibiting a novel self-organized nanolamellar microstructure. This material system exhibits unique properties based on its 3D microstructure and an extraordinary high Al content compared with PVD $Ti_xAl_{1-x}N$ thin films. The unexpected self-organized microstructure as well as the thermal stability of this metastable material are subjects of this thesis.

Through this thesis, a large number of various experimental techniques were employed. Since protective thin films possess a typical thickness of a few microns, position sensitive methods with high spatial resolution were required to analyse graded films. X-ray nanodiffraction method has proven to be an efficient tool for obtaining information about crystal size and orientation, crystallographic texture, internal strains and phase composition with a point-to-point resolution down to 50 nm. This technique, however, does not allow assigning the obtained data directly to the nanoscopic features contained in the film microstructure. This limitation has been overcome by a combination of nanodiffraction technique and direct microscopic observations. The required spatial resolution can be achieved using scanning electron microscopy (SEM), and in particular transmission electron microscopy (TEM). These methods do not provide only a direct imaging, but are also capable of chemical analysis using associated methods. A combination of energy dispersive X-ray spectroscopy (EDX) and electron energy loss spectroscopy (EELS) covers a wide range of elements spanning from heavy (Al, Ti, Cr etc.) to light elements (C, N, O etc.). This suits well to common protective thin film systems based on transition-metal nitrides and carbides. The wide magnification range offered by SEM and TEM microscopes allows analysing individual microstructural features as well as obtaining 1-dimensional line-scans and 2-dimensional chemical concentration maps. A further extension of the graded thin film analysis is demonstrated by a combination of mechanical testing at a micron and a sub-micron level in situ in SEM and TEM using nano- and pico-indentors. In situ mechanical testing performed in SEM can be conducted on free standing cantilevers with a usual thickness equal to the thin film thickness, hence providing information about fracture stress σ, Young's modulus E, and fracture toughness K_c, of the thin film. On the contrary, a further miniaturization of this concept down to the sub-micron scale, as it is available in a TEM microscope, offers a possibility to test individual thin film regions along the cross-section.

The main purpose of the following introductory chapters is to provide an extension to the attached publications at the end of the thesis and introduce the TEM method. Moreover, additional results, which were not included in the papers, are introduced and discussed here. Hence, the introduction is structured into four main parts. Each individual part contains supplementary descriptions, results and a discussion in order to help creating a whole picture about the presented topics. The reader should therefore combine reading individual chapters with studying the corresponding first-authored papers.

1.1. Principles of Transmission Electron Microscopy

1.1.1. Basic Principles

Since its introduction in 1931, transmission electron microscopy (TEM) represents a versatile tool for scientists crosswise many disciplines because it allows to remove the fundamental resolution limitation of light microscopy. This problem was first described by Ernst Abbe in 1873 and in microscopy is known as "the Abbe's diffraction limit" or simply "the diffraction limit".

Abbe found out that light with a wavelength λ, travelling in a medium with a refractive index n and converging to a spot with angle θ, will make a spot with radius

$$d = \frac{\lambda}{2nsin\theta} \tag{1.1}$$

The finite size of the spot therefore limits the maximum achievable point-to-point resolution. In light microscopy, it is approximately 200 nm. In general, this principle

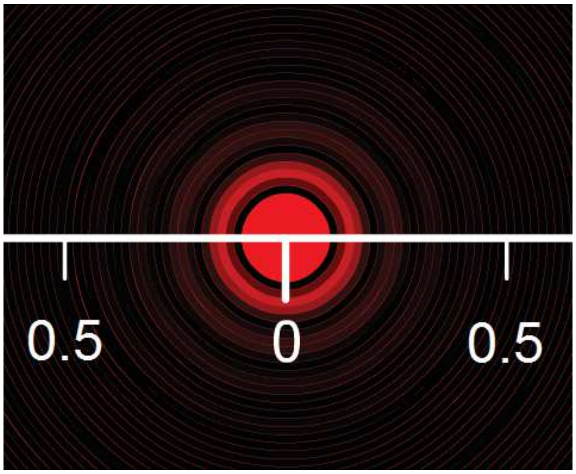

Figure 1.1.: An example of Airy discs simulated using coherent light $\lambda = 800\,\mathrm{nm}$ and circular aperture of $0.5\,\mathrm{mm}$ [4]. The scale is in degrees.

applies to any microscopy using as probes (quasi)particles with wave-like properties, because of their diffraction and interference.

A basic experiment demonstrating the duality of sub-atomic particles is a single-slit experiment using a point source of coherent light (laser), small slit and screen. When light in a form of parallel plane waves passes through the small circular aperture, an image of Airy discs appears on the screen (Fig. 1.1). This is due to photon diffraction on the slit and the wave interference.

This innocuous experiment has practical consequences in microscopy because each lens (even a human eye) has edges acting similarly as an aperture. Due to the Airy discs, even a perfect optical system cannot focus a point source of light back to a point. The resolution of an imaging process is therefore limited by the diffraction caused by the imagining system itself. The minimum resolvable distance is given by the Rayleigh criterion (Fig. 1.2) describing a situation when the first diffraction minimum of the image of the first point source coincides with the maximum of the second source [5].

The Abbe's equation offers principally two possibilities how to improve the resolution of an imaging system: either increase the size of lenses (large θ) or decrease the wavelength λ of the imagining (quasi-)particles.

Wavelength of small particles with a mass m, moving with a velocity v is described by the de Broglie equation as follows:

$$\lambda = \frac{h}{m \times v} \tag{1.2}$$

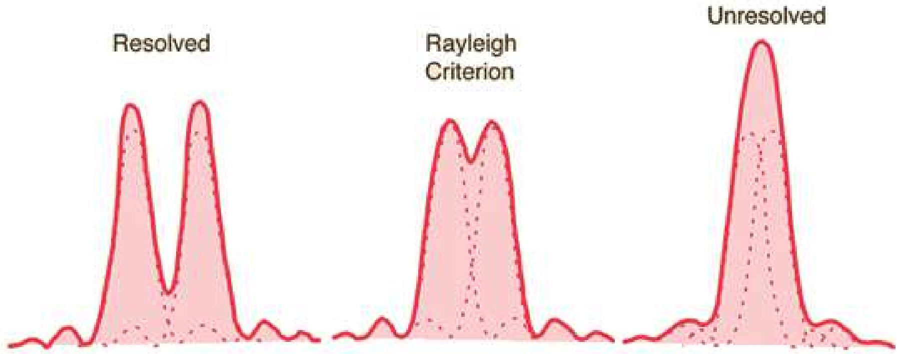

Figure 1.2.: Visualisation of the Rayleigh criterion as the closest position of two objects which can be resolved with an imaging system [6].

where h is the Planck's constant (6.6×10^{-27} m^2 kg s^{-1}). This basic quantum-mechanical relation can be applied also to electrons accelerated by a potential difference and considering relativistic effects, yielding:

$$\lambda = \frac{h}{\left(2m_0eU\left(\frac{1+eU}{2m_0c^2}\right)\right)} \tag{1.3}$$

where h is the Planck's constant, m_0 is the rest mass of an electron, e is an elementary charge, U is the accelerating voltage, and c is the speed of light in vacuum. Some typical accelerating voltages used in electron microscopy are listed in Table 1.1.

Table 1.1.: Wavelengths λ at accelerating voltages U and the fraction α of the speed of light.

E $[kV]$	λ $[m]$	$a = v/c$
5	1.7302×10^{-11}	0.14
30	6.9790×10^{-12}	0.33
120	3.3492×10^{-12}	0.59
200	2.5079×10^{-12}	0.70
300	1.9687×10^{-12}	0.78
1250	7.3572×10^{-13}	0.96

It follows that the usual wavelengths used in electron microscopy are in the order of picometers and for a standard TEM accelerating voltage (200 kV), the resulting speed of electrons is close to the speed of light. According to the Abbe's equation (Eq. 1.1), employing electrons as imagining particles allows to achieve resolution necessary for imagining of individual atoms.

1.1.2. Interaction of Electrons with Matter

The ability “to see” is based on an interaction of the used media (photons, electrons, neutrons, sound waves etc.) with the observed objects. Interactions depend on the kind of media chosen for imaging. Electrons interact with atoms via Coulomb forces. This results in significantly stronger ($\approx 10^4$ times more) interaction than in the case of electrically neutral X-rays. Electrons therefore “feel” both the electrons and nuclei, while X-rays interact only with electrons and neutrons only with nuclei. The practical consequence of this strong interaction is the possibility to observe extremely small features and to analyse various signals generated by them in TEM (Fig. 1.3). On the other hand, from the same reason, the TEM samples probed in a transmission geometry have to be very thin in order to allow electrons to pass through.

Signals Generated by Electrons

Most of the electrons passing through an electron transparent specimen will not interact. This electrons form a direct (transmitted) beam. The rest of the electrons, which actually interact with and hence probe the material, can be sorted into two main groups: elastically and inelastically scattered electrons.

Elastic scattering

Energy of elastically scattered electrons does not change upon scattering; however, the direction of their motion does. The probability of elastic scattering of an electron into a specific direction (ϑ) is described as atomic scattering factor for electrons $f_e(\vartheta)$, which can be written as follows [7]:

$$f_e\left(\vartheta\right) = \left(\frac{2m_e e^2}{4\pi h^2 \varepsilon_0}\right)\left(\frac{\lambda}{sin\theta}\right)^2 \left(Z - f_x\left(\vartheta\right)\right) \tag{1.4}$$

where $f_x(\vartheta)$ is calculated from the Schrödinger wave equation. The Eq. 1.4 implies that the scattering factor depends only on the scattering angle, charge and type of atom (Z). The heavier elements have in general larger scattering factors and scatter into larger angles. For small scattering angles, the amplitude of scattered electrons stays in phase with incoming electrons while scattering into large angles causes a phase shift.

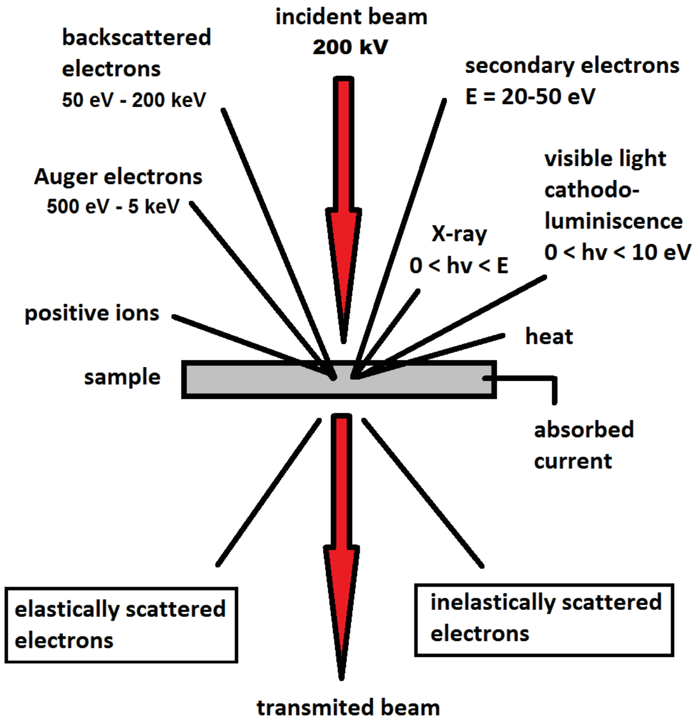

Figure 1.3.: Variety of signals produced when high-energy electrons (200 kV) hit a sample.

Inelastic scattering

Inelastic scattering includes a various forward and backward scattering events during which the energy of electrons is not preserved. In a standard 200 kV TEM following signals can be observed:

Secondary electrons (SE), backscattered electrons (BSE), Auger electrons (AE), Bremsstrahlung X-rays, characteristic X-rays, electron-hole pairs and cathodoluminescence, plasmons and phonons. Two main analytical methods in TEM are based on inelastic scattering. These are X-ray energy dispersive spectroscopy (EDS) and electron energy loss spectroscopy (EELS).

1.1.3. Electron Diffraction

Due to the strong interaction of electrons with matter, an electron diffraction (ED) can be on the one hand obtained from very small volumes but on the other hand requires thin samples for fulfilling kinematical conditions. Thick samples exhibit multiple scattering events and a dynamical diffraction theory has to be used for interpretation of the diffraction images.

If all conditions for kinematical diffraction are fulfilled (in particular thickness of the sample), the resulting diffraction can be treated in an analogical way to the X-ray diffraction. Electrons scatter at individual atoms and because these atoms are arranged on a periodically repeating lattice sites in crystals, the individual scattered electrons interfere with each other. The condition that the scattered waves are in phase (constructive interference) is called the Bragg's condition and is expressed using the Bragg's law:

$$2dsin\theta = n\lambda \tag{1.5}$$

where d is the interplanar spacing, θ is the scattering angle and n is an integer number. The scattering angle is usually small. For most of the materials observed with 200 kV electrons, it is within 2°. Scattered electron travel therefore very close to the optical axis. In comparison with laboratory X-ray diffractometers (large λ) are TEM microscopes tube-shaped rather than box-shaped like.

ED patterns reveal many kinds of useful information about observed materials. The symmetry of the ED pattern is related to the crystal symmetry, therefore the crystal orientation can be determined. The positions of diffraction spots are related to the magnitudes of the unit cell parameters and can be used for a strain mapping. Furthermore, the intensities of diffraction spots are related to the positions and Z number of atoms in the unit cell.

1.1.4. Observation Modes

Modern TEMs can operate in many different modes. This flexibility is based on a large number of electromagnetic lenses contained in an optical system of a TEM. This allows a huge variety of changes that can be applied nearly instantly. Two main imaging modes are a conventional TEM (CTEM) and a scanning TEM (STEM). The main difference lies in a formation of an incident electron beam and in a detection of the interaction of electrons with the sample. In the CTEM mode, the sample is illuminated with a broad nearly parallel beam. An image is magnified in a projector lenses and recorded on a charge-coupled device (CCD) eventually displayed on a florescence screen. In the STEM mode, a small probe is formed and quickly scanned across the sample. The step size and the physical spot size define the image resolution. For each step (pixel) a variety of signals can be recorded.

Regarding the actual settings of the electromagnetic lenses, the switch between the STEM and TEM modes is usually obtained by changing the current of the second (CL2) and the third condenser lens (CL3). In a TEM mode, CL1 focuses the image

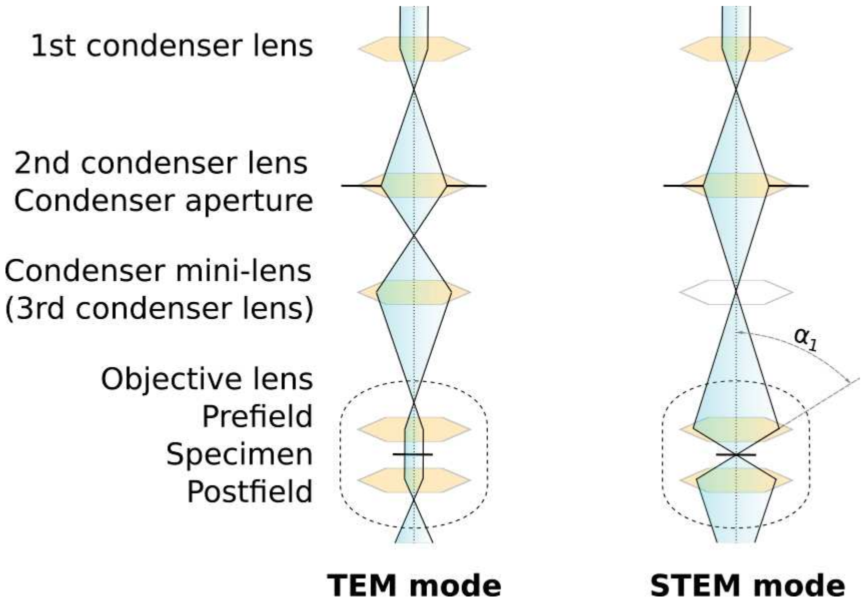

Figure 1.4.: Parallel TEM and convergent STEM probe formation in a common TEM.

of the source (C1 crossover), the CL2 strengthens to produce the focused image of the C1 crossover, and the CL3 focuses the C2 crossover to the front focal plane of the objective lens, as it is schematically shown in Fig. 1.4. The electron beam hitting the sample under this conditions is called „parallel beam“ although, strictly speaking, it is not completely parallel; nevertheless it is far from „very convergent“. In a STEM mode, the CL2 is weakened, CL3 is switched off and the objective pre-field lens focus strongly the beam to the sample. The angle α_1 represents the beam convergence angle. Such a probe is called „convergent“ although, in reality is α_1 actually very small.

It is important to mention that the simplified schematic settings in Fig. 1.4 represent one of many possible ways how to form the TEM and STEM probe. The actual optics settings can vary based on a microscope manufacturer and microscope type. In general, most of the microscopes have more lenses in the condenser and objective system than shown in Fig. 1.4 and the actual arrangement is much more complicated.

TEM mode

If we use TEM to observe a thin sample placed at an optimal position with respect to the objective lens (eucentric height), we will hardly see the sample itself. As mentioned above, although the electrons interact with the matter, most of them pass through without any interaction especially if the specimen is thin. Hence, it is necessary to filter out and process signal from those electrons that actually interact with the specimen. Let us consider only electrons that passed through the specimen. In general, electron waves can change both their amplitude and phase when travelling through the specimen, and both changes give rise to an image contrast. However, in the CTEM mode, it is the amplitude contrast that is mainly used for sample visualization. This includes a thickness-mass contrast and a diffraction contrast.

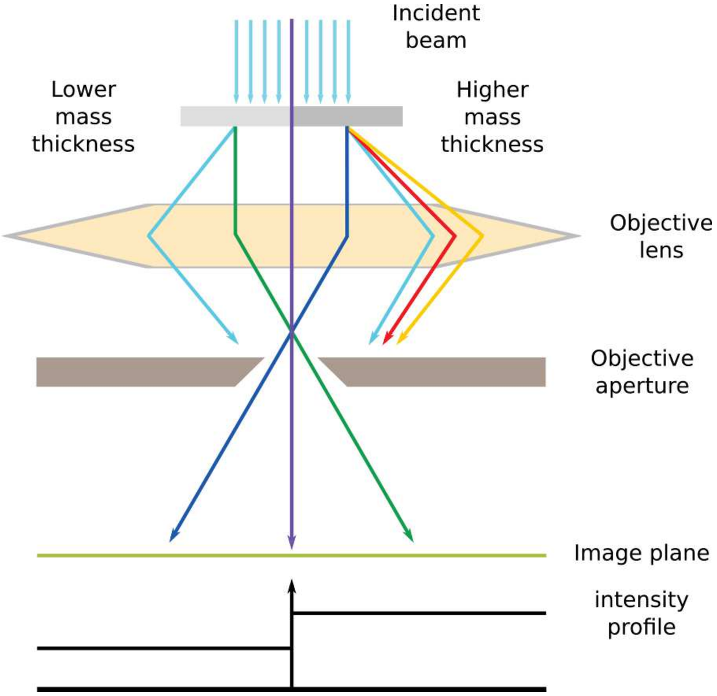

Figure 1.5.: Mechanism of mass-thickness contrast in a bright field (BF) image. Thinner or lower mass areas scatter electrons less than thicker or higher mass areas and therefore lighter or thinner areas and appear brighter. Adapted from [8].

Thickness-mass contrast is based on incoherent elastic scattering of electrons that strongly depends on the atomic number, Z, and the specimen thickness, t. Those are the sample variables of incoherent scattering. The TEM variables are the objective aperture size and the accelerating voltage. A basic situation is sketched in Fig. 1.5 where an objective aperture blocks the beams that were scattered into higher angles due to multiple scattering events in thicker sample parts or scattering from higher Z elements. The second part of the sample scatters less and the resulting horizontally flipped image shows higher intensity profile for the less scattering part of the sample.

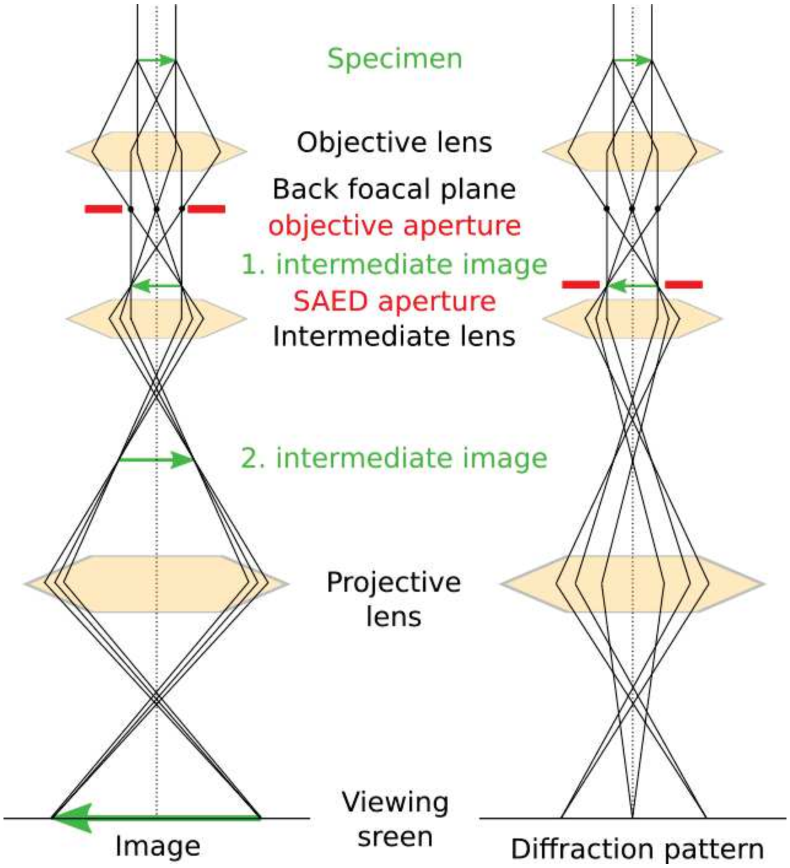

Figure 1.6.: Schematic representation of the TEM electron optic settings in an imagine mode (left) and a diffraction mode (right).

The diffraction contrast is created similarly to the previous case just the beams that are blocked or selected with an objective aperture are some diffracted beams or the primary beam. A TEM has a great advantage of having a possibility to switch easily from an image mode to a diffraction mode instantly. Upon such switch, the settings of the intermediate and the projector lenses are changed in order to image back focal plane (diffraction mode) or the first intermediate image plane (image mode) onto the viewing screen. This situation is schematically illustrated in Fig. 1.6

A removable multi-size aperture is traditionally placed in the back focal plane of an objective and limits the contribution of the diffracted beams to the image. This objective aperture is usually centred around the primary beam in order to block beams which were diffracted at high angles. In such case, a BF image is created. A

DF image can be formed if a small objective aperture selects one/or more diffracted beams and blocks the primary beam. The selection of contributing beam(s) is usually performed in the diffraction mode. There are, in general, two possibilities how to create the DF contrast. The objective aperture can be shifted from the central position to the position of the desired diffracted beam or the objective aperture stays at the position of the primary beam and the diffracted beam is shifted instead using a beam tilt coils. Traditionally, the beam shifting option has been more commonly used, because the beams travelling further away from the optical axis were more influenced by aberrations and astigmatism. This is not an issue any more in modern C_S-corrected microscopes.

1.2. Concept of Gradient Thin Films

In (laterally homogeneous) graded thin films, microstructure, composition, residual stresses and functional properties vary ordinarily only in the growth direction, along the film surface normal direction. Consequently, majority of the thin film analyses are performed on cross-sectional sample geometries. The concept of gradient thin films is based on the assumption that one or more parameters can be controlled during the deposition process, and this variation is recorded in the as-deposited thin film. Cross-sectional analysis therefore reveals the dependence of physical properties on the applied deposition parameter(s). This basic concept was successfully tested on a PVD magnetron sputtered Ti/Al-graded $Ti_xAl_{1-x}N$ thin film (Paper A) and further adapted for CVD Ti/Al-graded self-organized $Ti_xAl_{1-x}N$ thin films (Paper B). Further on, this concept was used to find an optimal composition with respect to the mechanical properties of self-organized CVD TiAlN thin film. The resulting thin film was thoroughly investigated in order to reveal and characterize the possible self-organization mechanism (Paper C).

1.2.1. PVD-Gradient $Ti_xAl_{1-x}N$ Thin Films (Paper A)

A magnetron sputtering process is affected by several parameters, such as substrate temperature, partial pressures of used gasses, power applied on targets, bias voltage etc. Unfortunately not all the parameters can be varied within a controlled manner during a continuous deposition process. For example, the parameters such as target temperature and partial pressures cannot be varied with a sufficient speed and accuracy, and therefore are usually set to constant values. On the contrary, powering of sputtering targets and changing the bias voltage can be easily controlled by com-

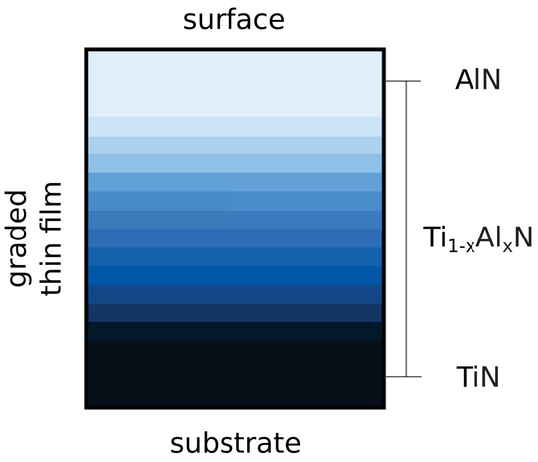

Figure 1.7.: A schematic of a graded $Ti_xAl_{1-x}N$ thin film consisting of a buffering TiN, $Ti_xAl_{1-x}N$ graded and terminating AlN region.

puter by changing the electric current. Independent generators are conventionally employed to generate power on targets during sputtering of multilayered and/or multicomponent systems. One of the best established three-component systems for industrial applications is $Ti_xAl_{1-x}N$ [1]. Due to the dependency of functional and structural properties of $Ti_xAl_{1-x}N$ on the Ti/Al ratio, this ternary system represents an ideal model system for testing and further development of the gradient concept as applied to PVD films.

A gradual change in the Ti/Al ratio across a $Ti_xAl_{1-x}N$ thin film thickness, resulting in a gradient of functional and structural properties, can be realized by a reactive co-sputtering from two targets, titanium and aluminium, at a constant pressure of Ar and N_2 gas mixture. The targets have to be powered from two independent generators providing a continuous power decrease on one of the targets and a continuous power increase on the other target. The concept of the resulting graded $Ti_xAl_{1-x}N$ thin film is schematically shown in Fig. 1.7, where the change in the chemical composition across the thin film thickness is achieved by several individual sub-layers across the thin film thickness. The actual change in the Ti/Al ratio can be carried out in a much smoother manner.

If we want to measure a dependence of functional and structural properties on cross-sectional position, the evolution of a thin film microstructure has to be taken into account. PVD magnetron-sputtered thin films may exhibit various microstructures, which are influenced by various deposition conditions, particularly by pressure,

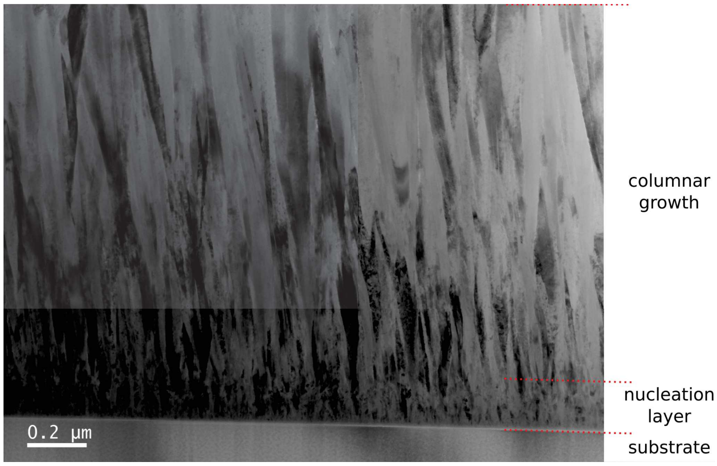

Figure 1.8.: Bright field (BF) STEM micrograph showing a nucleation layer and subsequent columnar-like growth of the graded $Ti_xAl_{1-x}N$ thin film.

temperature and energy of the sputtered particles. This dependency of microstructure on deposition conditions is visualized in structure zone diagrams [9, 10]. In our particular case we obtained a zone T microstructure which is composed of a thin nucleation layer at the substrate/thin film interface, gradually changing into a columnar microstructure. The nucleation layer exhibits usually mechanical properties significantly different from the rest of the film due to the small crystallites [11], large density of defects and high strains [12]. In Fig. 1.8, a bright field (BF) scanning transmission electron microscope (STEM) micrograph of a graded $Ti_xAl_{1-x}N$ thin film cross-section shows a nucleation layer with a thickness of up to 200 nm at the interface to Si(100). It is apparent that the nucleation layer is very small compared to the rest of the thin film. The first few hundreds nm of the thin film thickness were deposited under constant conditions (Fig. 1.7) resulting in the development of the microstructure with a fine-grained nucleation layer which turns into the columnar grains. The Ti-target power was kept constant at 300 W until TiN with a thickness of ∼500 nm was reached. Than the generators were set to provide a continuous increase of the power on the Al target from 0 to 300 W, and a coupled decrease of the power on the Ti-target from 300 to 0 W. This variation was realized at the thickness interval of ∼500-2000 nm. The deposition was terminated after reaching pure AlN for the maximum power on the Al-target (300 W). A cross-sectional dark field (DF) STEM image (Fig. 1.9a) shows the resulting microstructure. The deposition resulted in a fine grained region at the substrate/film interface (left) with thickness of ∼200 nm. The microstructure development resulted in gradual coarsening and development of the columnar microstructure, and was interrupted at the film thickness of ~1.4 µm by a clearly visible interface, where a new nucleation layer was formed. The microstructure developed again further into the columnar grain microstructure. A quantitative TEM-EDX line profile across the graded thin film microstructure is presented in Fig. 1.9b. The gradual change in the Ti/Al ratio recorded in the line-scan is in a perfect agreement with the settings of the deposition program. A verification is provided using a mathematical fit of the EDX data. Both datasets (Ti and Al) were fitted with a sigmoid function. This „S“-shaped curve can be expressed as follows

$$f = \frac{y_0 + a}{\left(1 + exp\left(\frac{-(x-x_0)}{b}\right)\right)^c} \tag{1.6}$$

where the a, b, c, y_0 and x_0 coefficients were determined by a curve fitting using SigmaPlot software. Both sets of experimental points expressing Ti and Al depth dependent gradients were fitted providing the fit parameters for the variables from Eq. 1.6 (Table 1.2). The results obtained by the fitting of the atomic concentrations of Ti and Al provided good match with an error of ~0.4 %.

Table 1.2.: Parameters of sigmoid functions fitted to Al and Ti EDX datasets.

Al dataset		Ti dataset	
a	101.8435	a	100.4118
b	0.1512	b	-0.1996
c	0.7147	c	1.9863
x_0	1.4112	x_0	1.5079
y_0	0.0256	y_0	-0.4929

The obtained analytical expressions for the atomic concentrations were further used to calculate Ti an Al atomic concentrations at arbitrary thin films depths. In combination with other methods of cross-sectional analysis, complex multi-dimensional data were thus obtained. For example, the position of the distinguishable interface in Fig. 1.9a was determined to be on average ~1442 nm away from the Si substrate. Using the Eq. 1.6 and the parameters of the Al dataset (Table 1.2), a composition of $Ti_{0.23}Al_{0.67}N$ is obtained. This result is an excellent agreement with Al-solubility limit in TiAlN cubic phase which was reported in the literature [13][3]. The interruption of the columnar growth of the gradient $Ti_xAl_{1-x}N$ thin film can be therefore attributed to the start of the growth of the hexagonal wurtzite phase. Due to the incoherency of the hexagonal/cubic phase interfaces and related misfit strains (Paper B), a new nucleation region of hexagonal sub-layer was formed. This conclusion was quantitatively confirmed using the X-ray nanodiffraction method (Paper A). A

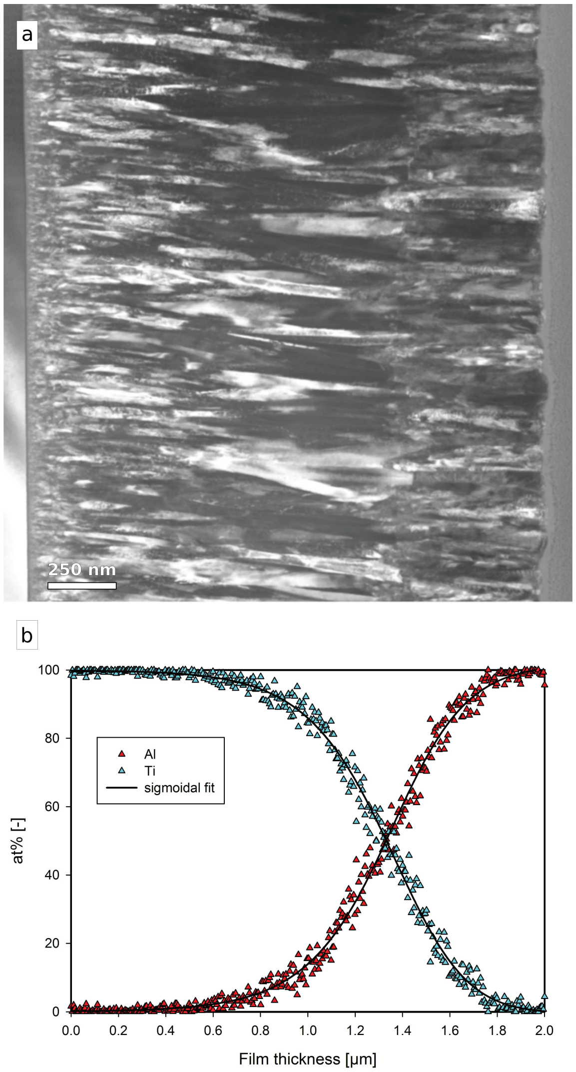

Figure 1.9.: (a) A cross-sectional DF STEM image of the PVD graded $Ti_xAl_{1-x}N$ thin film (b) atomic composition (Ti, Al) TEM-EDX line profile across the thin film thicknes graph showing a gradual change of the Ti/Al ratio.

qualitative evidence is provided in Fig. 1.10. The data were obtained using precession electron diffraction (PED) technique [14][15]. This method allows obtaining diffraction data from small volumes at a semi-kinematic condition in a TEM. The main benefit of this method, in comparison with the X-ray nanodiffraction method, is the possibility to directly assign diffraction data to an individual thin film microstructure, composition and the possibility to obtain diffraction from a very small volume which is beyond the resolution of X-ray nanodiffraction.

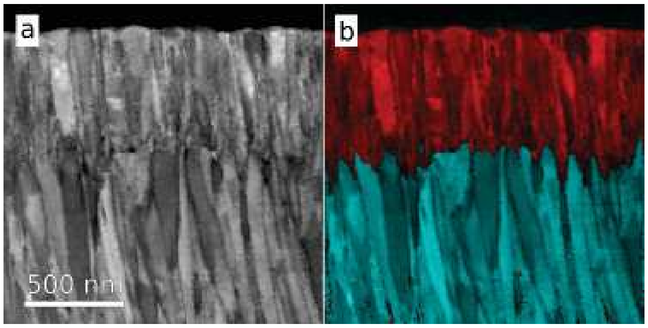

Figure 1.10.: (a) A cross-sectional virtual BF STEM image of the sub-layer in the PVD graded $Ti_xAl_{1-x}N$ thin film. (b) complementary phase composition map of a cubic phase (cyan) and hexagonal phase (red).

The micrograph in Fig. 1.10a shows the distinguishable interface in the graded thin film microstructure. The micrograph contrast was determined by a virtual aperture placed into the diffraction images in order to create a diffraction-like contrast for individual pixels of the scanned area. The contrast creation works in the following way. If the aperture is placed around the primary beam, a BF image is created. Similarly any diffracted beam can be selected by a virtual aperture. The contrast is based on the changes in the intensity of the selected primary/diffracted beam. In this case, the primary beam was selected which resulted in a visualization of the grain microstructure (Fig. 1.10a). Each pixel in the virtual BF image corresponds to a diffraction image. These data carry information about an orientation, a phase composition and a strain state. Next, a phase map was created based on fitting measured diffraction images to simulated diffraction images. For each crystallographic phase (hexagonal and cubic) a set of diffraction patterns covering a standard crystallographic projection with a resolution of one degree was simulated. A cross correlation fitting process allowed distinguishing both phases and compiling a colour-coded image (Fig. 1.10b). The cyan and red colours in the Fig. 1.10b represent fcc and hexagonal wurtzite phases in the samples, respectively. A relation of the distinct interface to the cubic-to-hexagonal transition is evident. The distribution of the hexagonal phase at the graded thin film cross-section suggests that the nucleation of the wurtzite phase is not homogeneous and is obviously influenced by the coarse-grained microstructure of the fcc region. The interface microstructure from Fig. 1.10b suggests that the hexagonal phase nucleates preferably at the triple junctions of grain boundaries. Smaller grains and intergranular space allows a formation of the hexagonal phase at earlier growth stage (smaller content of Al). These findings correlate well with the X-ray nanodiffraction analysis (Paper

A) where the hexagonal phase is detected in small amounts (low intensity) already at the thickness corresponding to the composition under the solubility limit. In the X-ray nanodiffraction experiment, a 40 µm thick cross-sectional sample (in the X-ray beam direction) was used. The diffraction signal was thus integrated over the whole sample thickness. Since the film microstructure is gradual at the interface between fcc-TiN and h-AlN, the X-ray diffraction peaks from the interface are diffuse and overlapping. On this example, benefits of combining the "local" PED method (thin sample) and "integral" X-ray nanodiffraction (thicker sample) are clearly demonstrated. PED technique provides very local information on the microstructural grain evolution, whereas X-ray nanodiffraction allows to obtain representative integrated data on the phase and strain occurrence. For a complex analysis a combination of both methods is profitable.

1.2.2. CVD-Gradient $Ti_xAl_{1-x}N$ Thin films (Paper B)

The concept of gradient thin films was further adapted for CVD deposited $Ti_xAl_{1-x}N$ thin films exhibiting a 3D self-organization. These materials were introduced by Keckes et al. [16] who reported on a spontaneous formation of altering cubic TiN and hexagonal AlN lamellae within randomly oriented grains of polycrystalline $Ti_{0.05}Al_{0.95}N$ thin films produced by a low pressure (LP)-CVD process. This can be considered as a breakthrough in thin film technology primarily because of the self-organization effect resulting in the formation of the complex 3D microstructure consisting of superlattices. In general, a formation of the nanolamellar microstructure can be realized by PVD processes as well, however, yielding only multilayers or superlattices with interfaces perpendicular to the growth direction. Such planar lamellar systems significantly enhance physical properties such as hardness, Young's modulus, fracture toughness, fracture stress etc. [17]. A formation of a 3D-lamellar structure within a thin film microstructure could therefore offer an additional improvement of these characteristics. In order to prove these assumptions, a set of gradient CVD thin films was deposited. The Ti/Al ratio was systematically varied across the film thickness in order to obtain the compositional and microstructural gradients. Subsequent mechanical tests of distinct self-organized microstructures revealed microstructure-mechanical property relationships.

To control the chemical composition in the CVD process and hence to synthetize gradual thin films, the flux of processing gasses into a reactor chamber, and their homogeneous distribution had to be tuned during the film growth. A homogeneous distribution is easier assured in a LP-CVD process where reactants have to approach substrates more closely due to a lower pressure as compared with an atmospheric pressure (AP)-CVD. On the one hand, resulting LP-CVD thin films show usually a better uniformity and homogeneity, and a smaller amount of defects. On the other hand, the controlling of processing gas fluxes using valves is much less precise than the corresponding variation of power on sputtering targets in PVD process. For this reason, the variation of the Al/Ti ratio in graded LP-CVD thin films is performed in a coarser step-like manner to form sub-layers.

The LP-CVD depositions of graded thin films were performed in a Bernex MT-CVD-300 medium temperature reactor at 800 °C and a total process pressure of 2.5 kPa using the process gases $AlCl_3$, $TiCl_4$, NH_3 and N_2, with H_2 as a carrier gas [18]. Varying pressure ratios of precursors $AlCl_3$ and $TiCl_4$ in the range of 0.6-2.75 were applied for the first deposition. A HAADF-STEM and a BF-STEM montage covering the cross-section of the whole resulting graded thin film are presented in Fig. 1.11a and 1.11b, respectively. The variation of precursor's pressure ratio across the thin film thickness resulted in varying microstructure. The first sub-layer (marked 1) exhibits a nano-composite microstructure. The BF-STEM image (Fig. 1.11b) suggests a large number of individual grains. The complementary HAADF-STEM image (Fig. 1.11a) shows a formation of nano-lamellar fragments of various geometrical shapes. Moreover the contrast variations point out differences in chemical composition for altering lamella and surrounding matrix. The second sub-layer (marked 2) exhibits completely different microstructure. Nano-composite arrangement is replaced by a columnar growth of large grains where the lamellar structure is not presented. The second sub-layer is therefore monolithic without pronounced composition-related changes. The third and fourth sub-layer (marked 3 and 4) show a continuing columnar grain growth with a distinct nano-lamellar microstructure within individual grains. This inner grain microstructure is well developed comparing to the second sub-layer. The last sub-layer (marked 5) exhibits gradual vanishing of the nano-lamellar microstructure and a growth of horizontally propagating thicker layers with altering chemical composition. In contrast to the third and fourth sub-layer (marked 3 and 4), altering layers in the fifth sub-layer (marked 5) are not filling individual grains. The layered microstructure propagates along the cross-section without changing direction at grain boundaries. The contrast in the HAADF image suggests significant changes in the chemical composition across the layered structures.

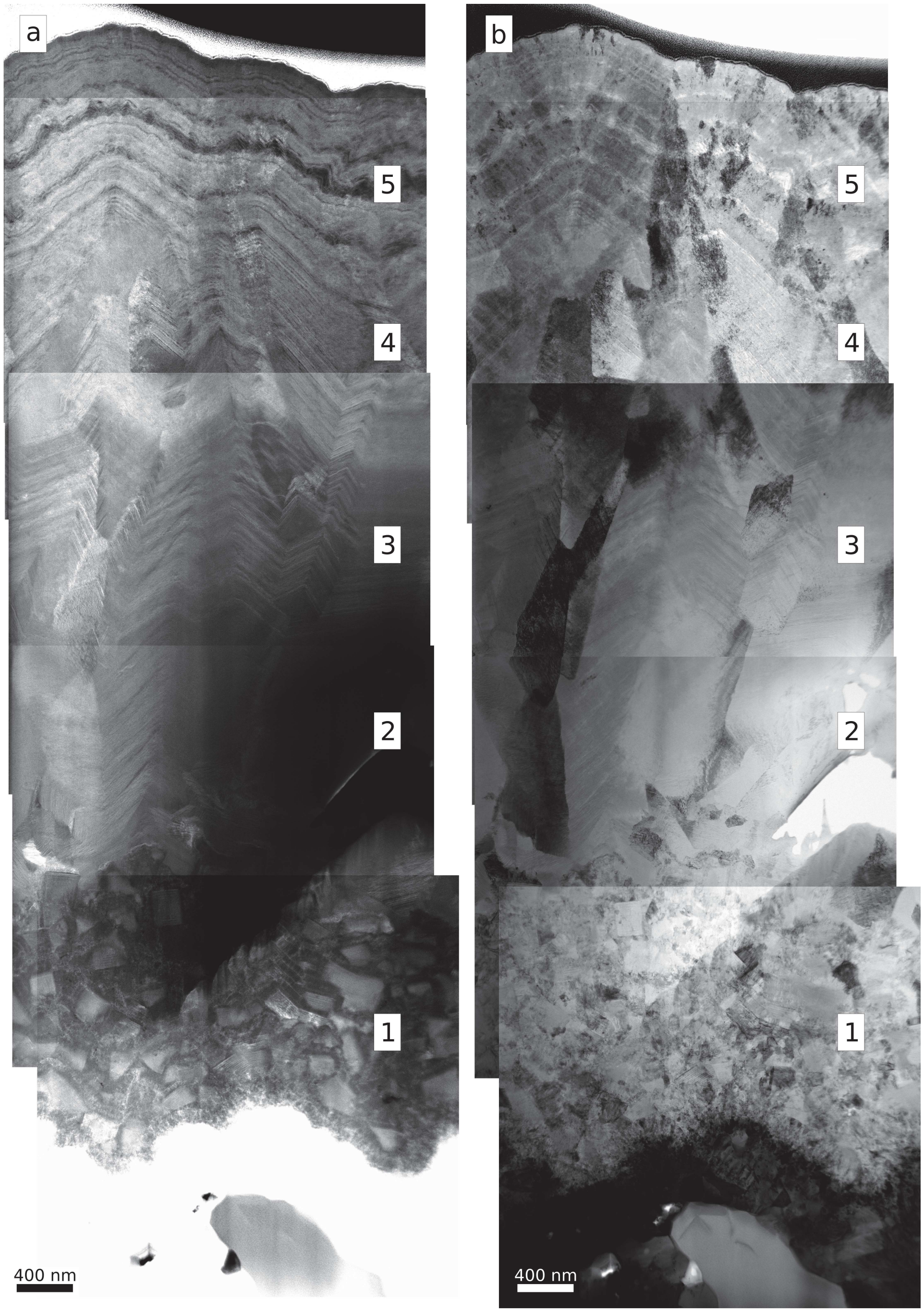

Figure 1.11.: (a) HAADF STEM and (b) BF STEM micrograph showing a complete cross-section of the LP-CVD graded layer A.

Microstructure of self-organized LP-CVD thin films

The gradient thin film contains individual self-organized structural features whose type, composition and internal nanostructure depend on the Al/Ti ratio. The microstructure obtained by this process can be devided into two variants: (i) a nano-composite variant containing both the cubic and the hexagonal phases, and (ii) a nano-lamellar variant composed purely of the cubic phase.

The nano-composite variant is presented in Fig. 1.11 in the first sub-layer (marked 1) of the graded thin film and in detail in Fig. 1.12. The HAADF STEM image (Fig. 1.12a) shows the variety of the nano-composite structural features. Multilayered fragments composed of layers with alternating chemical composition are randomly oriented in the plane of the TEM sample. The space between the individual fragments is filled with pure matrix or individual lamellae which have different periodicity as compared with the lamellar fragments. The multilayered fragments can be present in an incomplete (Fig. 1.12b) or a complete form (Fig. 1.12c). A common feature of the nano-composite variant is a presence of right angles within the multilayered fragments. Due to the 2D nature of the TEM sample and the size of the fragments, a complete 3D shape of the fragments cannot be easily deduced.

The phase-constitution of these multilayered fragments was briefly described by Keckes et al. [16] who reported that a combination of cubic lamellae (3 nm) and hexagonal (10 nm) lamellae was formed. Our further investigations revealed existence of two variants. The first variant is depicted in a HRTEM image (Fig. 1.13a) which shows a nano-lamellar fragment where cubic (approx. 2 nm thick) lamellae are alternating with hexagonal ones (approx. 10 nm thick). The hexagonal phase is depicted along the [0001] direction and the cubic phase along the [100] viewing direction. The orientation relationship was determined from HRTEM images as $[100]_{cubic} \| [0001]_{hexagonal}$; $(110)_{cubic} \| (11\bar{2}0)_{hexagonal}$, in agreement with the results from [16]. A HRTEM image (Fig. 1.13b) of the second variant shows that the whole nano-lamellar fragment is composed of the cubic phase which is oriented along the [110] viewing direction. The surrounding matrix is hexagonal and oriented along the $[1\bar{1}00]$ direction. The crystallographic orientation relationship was determined from HRTEM images as $[110]_{cubic} \| [1\bar{1}00]_{hexagonal}$; $(110)_{cubic} \| (0001)_{hexagonal}$. The size of the lamellae is approximately 10 nm and 1.5 nm for the thicker and for the thinner ones, respectively.

The nano-lamellar variant of the thin film microstructure is presented in Fig. 1.11 in the third and fourth sub-layer (marked 3 and 4) of the graded thin film. In this case, the lamellae fill up the grain interior completely, hence resulting in a fully

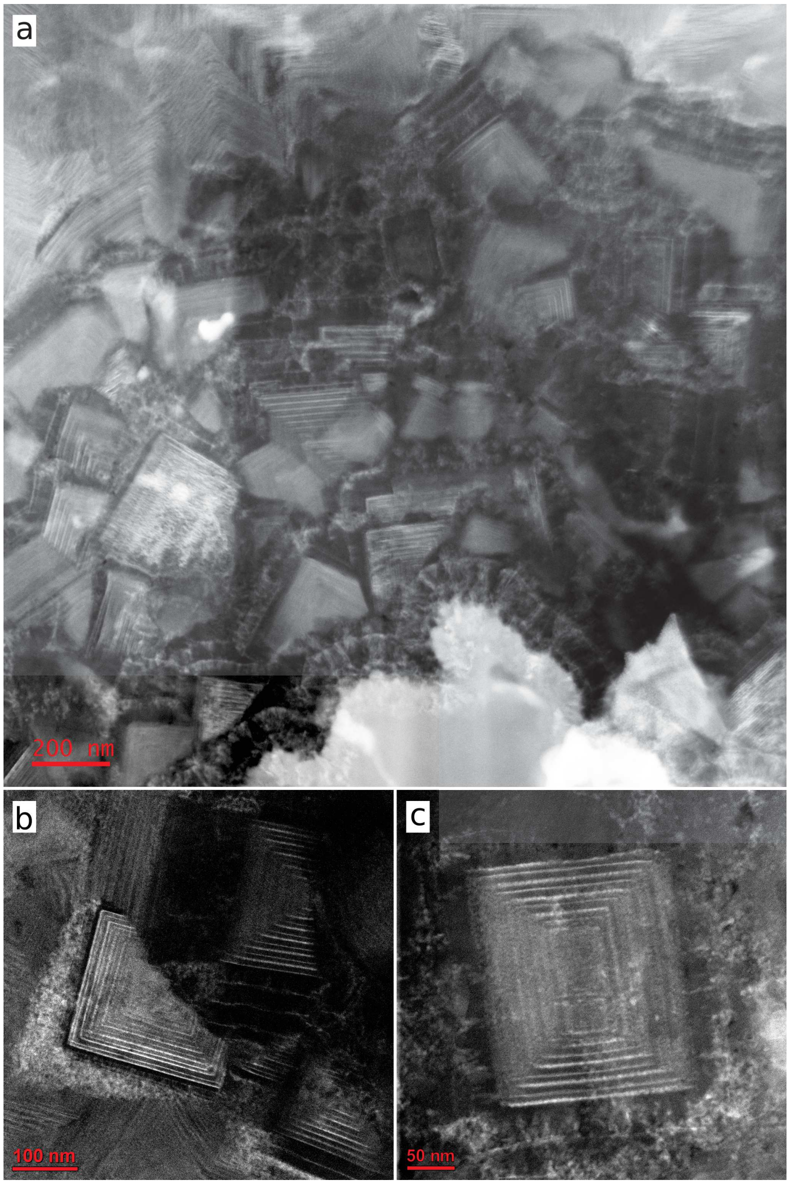

Figure 1.12.: HAADF STEM images of (a) a nano-composite microstructure (b) incomplete multilayered fragment (c) complete multilayered fragment.

cubic phase region. A complex development of this microstructural type within a monolithic self-organized thin film is presented in Fig. 1.14. Unlike the graded layer, this thin film was grown with a constant ratio of processing gasses. The microstructural development is depicted at three scales. An in-lens SEM cross-sectional micrograph (Fig. 1.14a) shows the overall orientation of the nano-lamellar

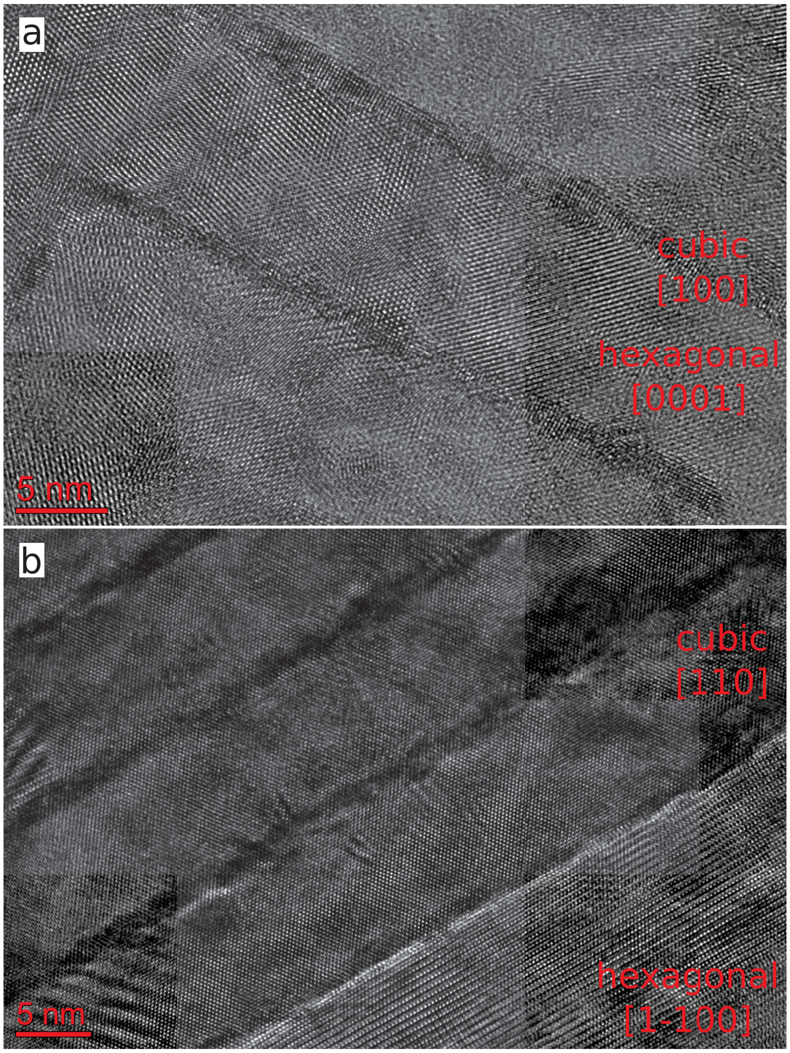

Figure 1.13.: Typical C_s-corrected HRTEM images of two nano-composite microstructural variants. (a) cubic/hexagonal lamellae recorded along[100] and [0001] direction respectively. (b) cubic/cubic lamellae recorded along [110] direction.

microstructure with respect to the columnar growth. Individual grains exhibit a zigzag growth where the orientation of the lamellae is switched in the grain interior. The abrupt change in the nano-lamellar orientation is also observed at the grain boundaries. This creates a typical jagged profile at the cross-section. A BF-STEM micrograph (Fig. 1.14b) provides an insight into a grain boundary region. The outstanding feature of the grain boundary is the connection of individual lamellae in one grain to their counterparts in the second grain. This can be understood as a

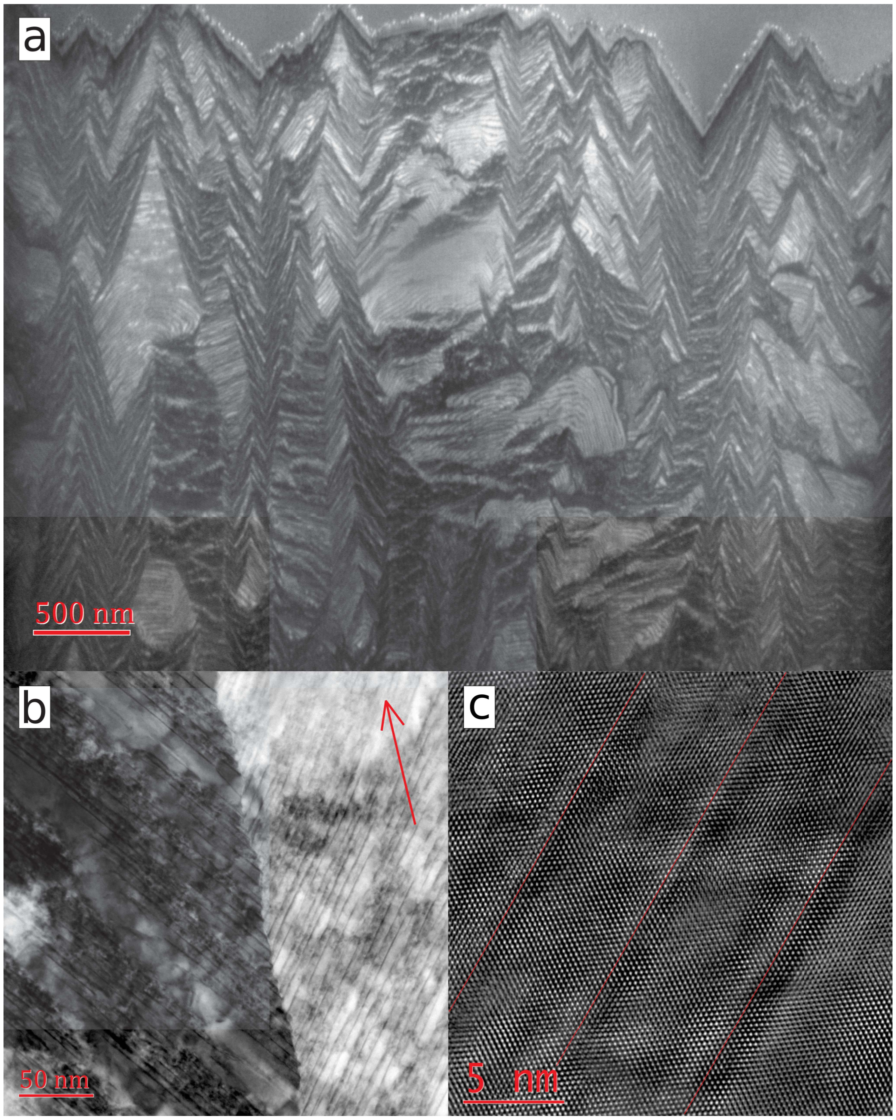

Figure 1.14.: TEM micrographs showing the nano-lamellar microstructure variant at three microstructural levels. (a) In-lens SEM picture of a coating cross-section depicting the orientation of the nano-lamellar microstructure with respect to the columnar growth. (b) detailed BF STEM picture depicting the organization of the nano-lamellar microstucture at the grain boundaries. The red arrow is indicates the growth direction. (c) a typical C_s-corrected HRTEM image of coherent cubic lamellae along[110](the image was was filtered in frequency space in order to remove the signal of amorphous phase). Red lines mark the position and orientation of thin lamellae.

product of the self-organized grain growth. The individual layers in the individual grains grow layer-by-layer in the direction of the growth marked with the red arrow. The high degree of the self-organization can be recorded at the atomic level as well. A typical C_s-corrected HRTEM image of the coherent cubic lamellae along the [110] direction is presented in Fig. 1.14c. The image was filtered in the frequency space in order to remove the signal of an amorphous phase. Red lines mark the position of the thin lamellae. The lemellae interfaces are highly coherent as it is apparent from non-interrupted crystal planes.

Chemical composition of self-organized LP-CVD thin films

The HAADF images pointed out the variations of chemical composition in both general variants of LP-CVD self-organized microstructure. This qualitative result is useful for interpreting local compositional changes (nano-lamellar structure) but for a more quantitative understanding of the atomic composition development in the graded thin films, EDX, EELS and EFTEM methods were employed. Due to the nano-lamellar character of the self-organized thin film, it is necessary to distinguish local and average atomic composition. The local changes are related to the alternating Ti-rich and Al-rich lamellae. Average variations can be revealed only if the atomic concentration is integrated in a volume with appropriate size with respect to the global gradient. In the case of the graded thin films, it is beneficial to perform SEM-EDX line-scans on the thin film cross-sections. In an SEM, a characteristic X-ray signal originates from a larger volume than is the actual spot size. This interaction volume is a function of the energy of electrons, the magnitude of the beam current, the angle of incidence of the beam, and the average atomic number (Z) of the observed material. The signal is thus integrated and provides, in principle, an average value. SEM-EDX line scans were recorded on an FIB cross-section of the graded thin film in order to reveal the global trends in the chemical composition. The in-lens SEM cross-sectional micrograph (Fig. 1.15a) shows the global microstructure of the graded thin film. Five individual sublayers (described in details in Fig. 1.11) can be distinguished based on the contrast. The blue arrow represents the direction of an EDX line-scan perpendicular to the sub-layers direction starting at the substrate/thin film interface. The dependence of atomic concentrations, normalized to $c_{(Al)} + c_{(Ti)} = 1$, on the cross-sectional position in the CVD thin film is given in Fig. 1.15b. The global trend in the atomic concentration (Ti and Al) across the thin film cross-section is clearly visible. Boundaries of individual sublayers can be detected by local minima (Al dataset) and maxima (Ti dataset). The composition ranges

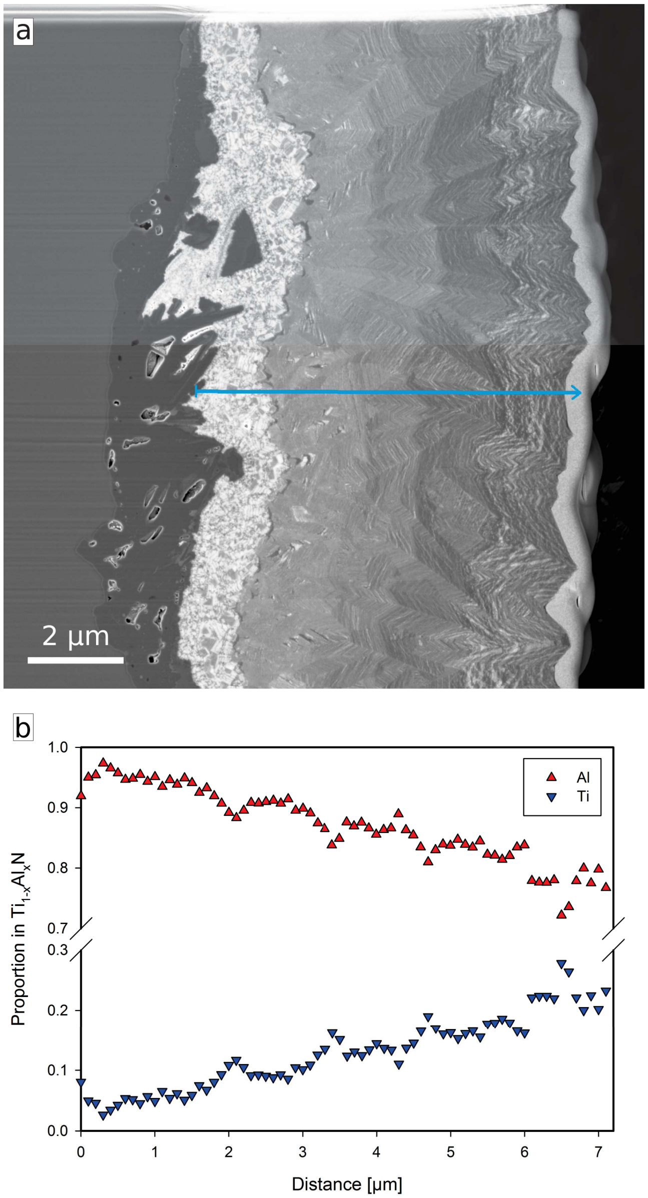

Figure 1.15.: (a) In-lens SEM cross-sectional micrograph of the graded CVD coating A. The blue arrow represents a direction of an EDX line-scan (b) dependence of atomic concentrations on the cross-sectional position in the CVD coating A. The atomic concentration of Ti and Al is expresend as their proportion in a stoichiometric $Ti_{1-x}Al_xN$.

for individual sub-layers (excluding the local extrema at sub-layer boundaries) are listed in Table 1.3.

Table 1.3.: Composition ranges for individual sub-layers and representative types of microstructure.

sublayer	composition range	microstructure
1	$Ti_{0.03}Al_{0.97}N$ – $Ti_{0.08}Al_{0.92}N$	nano-composite
2	$Ti_{0.11}Al_{0.91}N$ – $Ti_{0.11}Al_{0.89}N$	monolithic
3	$Ti_{0.13}Al_{0.87}N$ – $Ti_{0.14}Al_{0.86}N$	nano-lamellar
4	$Ti_{0.16}Al_{0.84}N$ – $Ti_{0.19}Al_{0.81}N$	nano-lamellar
5	$Ti_{0.22}Al_{0.78}N$ – $Ti_{0.23}Al_{0.77}N$	microstructure non-restricted compositional waves

The first sublayer exhibits the nano-composite microstructure as it was shown in Fig. 1.12 and Fig. 1.13. The composition range of the first sublayer represents compositional interval for an apperance of the nano-composite microstructure. These results are in line with the the earlier reported nano-composite $Ti_{0.05}Al_{0.95}N$ thin film [16]. The second sub-layer, defined a narrow compositional interval, composes of a monolithic $Ti_xAl_{1-x}N$ without any lamellar structure formed. This is consistent with the previously reported monolithic Al-rich cubic thin film [18]. The compositional interval $Ti_{0.13}Al_{0.87}N$ – $Ti_{0.19}Al_{0.81}N$ bounds the existence of the nano-lamellar microstructure (Fig. 1.14). Further decrease in the Al-content leads to a disintegration of local oriented nano-lamellar microstructure into a variant with global, microstructural non-restricted, compositional waves. This is related to the fifth sublayer in the Fig. 1.15, which is defined with the concentration range of $Ti_{0.22}Al_{0.78}N$ – $Ti_{0.23}Al_{0.77}N$.

1.3. 3D Self-organized Cubic $Ti_{0.2}Al_{0.8}N$ Thin Film (Paper C)

The final product of the microstructural and phase optimisation process (Paper B) is a cubic self-organized $Ti_{0.2}Al_{0.8}N$ thin film. This material was studied in depth in the Paper C where the main attention was paid to a detailed microstructural and chemical analysis of the self-organized nano-lamellar structure. In general, there are two fundamental questions. Firstly, it is not clear what is the driving force and the mechanism for the nano-lamellar microstructure formation. Secondly, why is the structure containing relatively very thick c-AlN_x-layers (thicker than the c-TiN layers) stable at ambient conditions and furthermore at high temperature conditions? Both questions represent keys to the understanding of this new self-organization phenomenon.

The first question is not trivial to answer. Currently, there are two main hypothesis. Paseuth *et. al* [19] proposed that the self-organized nano-lamellae formed by LP-CVD arise via a spinodal decomposition process of metastable c-$Al_xTi_{1-x}N$. In contrast, Todt *et. al* [20] suggested chemical oscillation reactions on the growing film surface as the formation mechanism. Although some indications supporting the latter scenario have been obtained, definite answering of this puzzle is beyond the scope of this study. Instead, the main focus has been laid here on the second topic, the explaining of the unprecedented stability of the metastable c-AlN_x-layers.

Transition metals nitrides show tendency to form various non-stoichiometric phases and defected structures. Consequently, point defects can significantly change the phase stability. This has been experimentally demonstrated e.g. for the Mo-N system, in which γ-MoN_x and ordered γ'-MoN_x metastable phases can be synthesized in addition to two thermodynamically stable phases, β-$MoN_{0.5}$ and δ_2-MoN [21]. An ordering effect was also reported experimentally in the Cr-N system where nitrogen vacancies were found to be ordered on the {111} atomic planes in the nitrogen deficient CrN_x layers [22]. Another experimental study revealed disordering of a hexagonal (hcp) Cr_2N structure by a systematic shift of nitrogen atoms away from their expected octahedral interstitial positions, consequently leading to a phase transformation from an hcp to an fcc structure by shearing Cr atoms in (100) planes [23].

There are also works investigating the impact of nitrogen non-stoichiometry on the properties of $(Ti_{1-x}Al_x)N_y$ alloys [24–27] which are of a direct relevance to the present study. Baben *et al.* [25] studied origin of nitrogen over- and under-stoichiometry in $Ti_{0.5}Al_{0.5}N_x$ alloy by means of *ab initio* calculations. Based on the lowest energy of formation criterion, they showed that the nitrogen understoichiometry is caused by nitrogen vacancies while the nitrogen overstoichiometry is due to metal vacancies. Furthermore, both types of point defects introduce shrinking of the lattice parameter in the investigated $Ti_{0.5}Al_{0.5}N_x$.

Our investigations (Paper C) revealed a significant systematic nitrogen deficiency in the Ti-rich nanolamellae and an N excess in the Al-rich nanolamellae. The inhomogeneous N distribution is shown in 1.16. The TEM image (1.16a) represents a typical self-organized nanolamellar structure with altering both cubic Ti-rich (thin) and Al-rich (thick) lamellae. The EFTEM nitrogen K edge map (1.16b) shows systematic decrease in the nitrogen content in the Ti-rich regions which is highlighted in the integrated intensity profile (1.16c). Together with EELS measurements presented in Paper C, this proves a significant nitrogen understoichiometry of the Ti-rich layers. Furthermore, the N deficiency in the thin Ti-rich nanolamellae is correlates

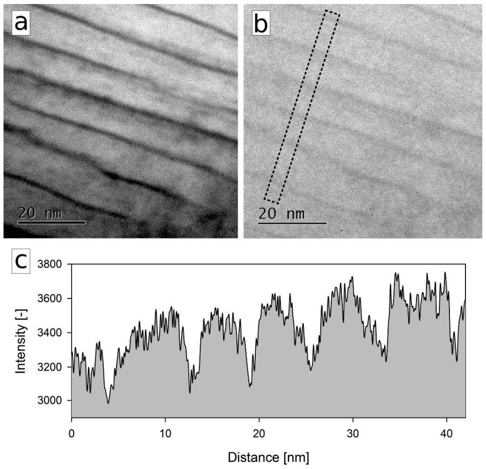

Figure 1.16.: (a) TEM image of the multilayer structure (b) EFTEM nitrogen K edge map obtained by „three windows“ method (bright areas are rich in nitrogen) (c) integrated intensity profile across the highlighted area in the nitrogen K edge map.

with the Ti content - the N content decreases with the increasing Ti content. This fits well with the results of Alling *et al.* [24], who studied the effect of nitrogen vacancies on the decomposition pattern in the cubic $(Ti_{1-x}Al_x)N_y$ alloy. They concluded that nitrogen vacancies prefer Ti neighbours in a $Ti_{0.5}Al_{0.5}N_y$.

The situation is different for c-AlN. In contrast to the transition metal nitrides, the group IIIA nitrides are most stable in a wurtzite structure exhibiting semiconducting rather than metallic character. These materials are therefore mainly used in optoelectronic applications, AlN being an exception with its equally important applications in protective thin films. Still, the majority of publications deals with the point defects in the wurtzite AlN [28] and/or study the impact of point defects in c-AlN with respect to the electric properties [29]. Nevertheless, there exist density functional theory (DFT) calculations predicting formation of both metal and nitrogen vacancies in c-AlN to be energetically unfavourable and causing increase in the cubic lattice parameter [30].

In order to investigate the influence of nitrogen deficiency/excess on the microstructure of the self-assembled nanolamellae, we subjected our samples to detailed C_s-corrected HRTEM investigations. State of the art aberration corrected microscopy can nowadays approach sub-angstrom resolution. In the case of our instrument (C_s-corrected JEOL JEM-2100F), the achievable resolution is around 1.3 $\AA$ or better. This resolution was sufficient to provide qualitative and semi-quantitative description of the position of metallic atoms in the fcc lattice. The nitrogen atoms

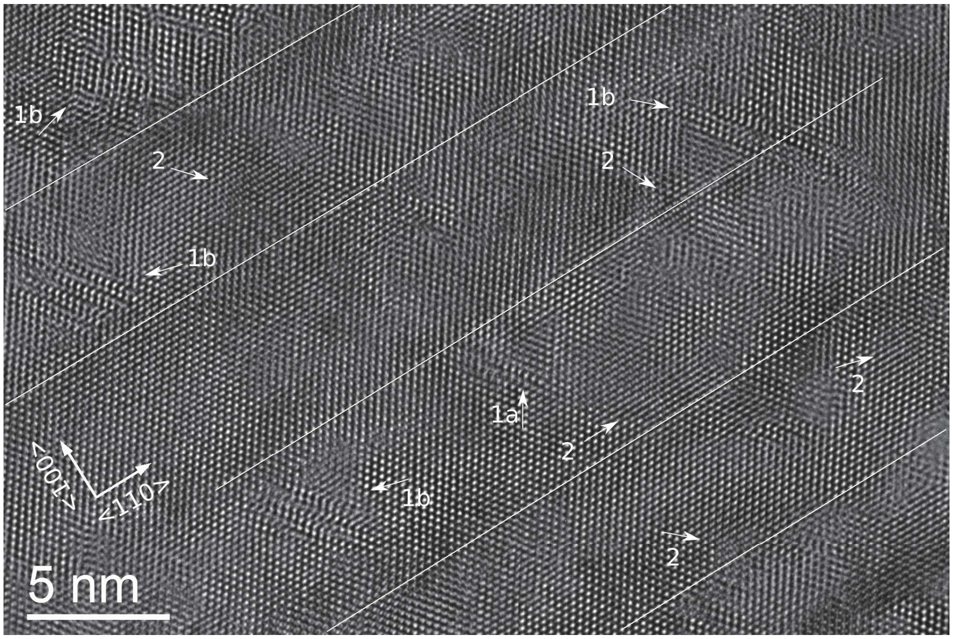

Figure 1.17.: Representative HRTEM lattice image of the FCC cubic phase acquired along [110]. The approximate positions of Ti-rich lamellae are marked with white lines. Altering lamellae are parallel to the {100} planes and perpendicular to the {110} planes and contain large amount of local lattice defects: Perfect dislocations combined with Shockley partial dislocations (marked 1a), stacking faults (marked 1b) and antisite boundaries (marked 2).

could not be resolved. A representative lattice image of the cubic phase acquired along the [110] zone is shown in 1.17. The white lines mark an approximate position of Ti-rich lamellae, which are parallel to the {100} crystallographic planes. The presence of several distinct types of lattice defects and imperfections is apparent and supported by a multiple image analysis. First of them (marked 1a) represents edge dislocations combined with Shockley partial dislocations at the {111} planes. Second type (marked 1b) denotes stacking faults arranged at {111} crystallographic planes and finally the third type stands for anti-phase boundaries (marked 2). The stacking faults (including Shockley partials) are typically found in the Al-rich layers and have various extent. The presence of edge and Shockley partial dislocations on {111} planes cause lattice deformation visible in a HRTEM micrograph as it can be seen in 1.18a. The burgers vector of partial dislocations typically lies in the {111} slip planes and has a magnitude of $a/\sqrt{6}$. Stacking faults tent to agglomerate leading to a formation of clusters with recognizable hexagonal stacking (ABAB..). A representative HRTEM image is shown in Fig. 1.18b. Six lattice planes exhibit

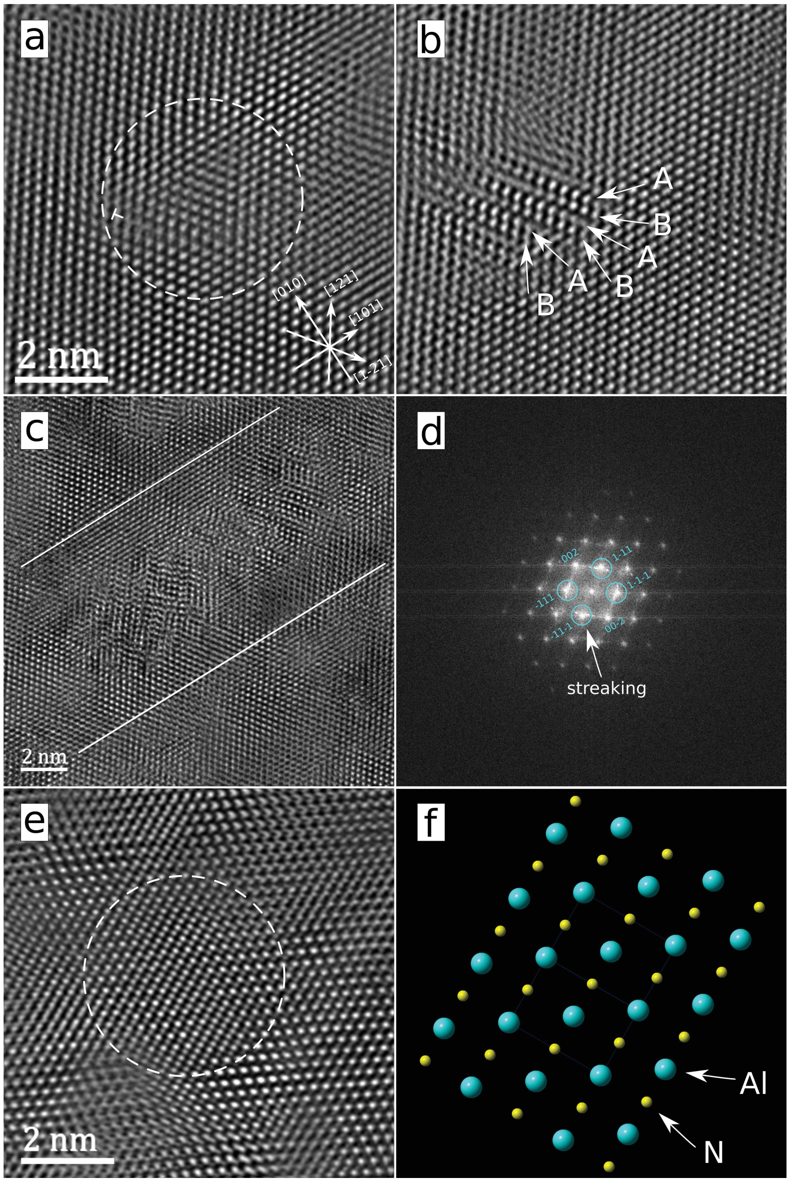

Figure 1.18.: (a) representative HRTEM micrograph of an Shockley partial dislocation combined with an edge dislocation. (b) The approximate positions of Ti-rich lamellae are marked with white lines (same scale bar like a). (c) agglomeration of stacking fault- based defect filling an Al-rich layer. Approximate positions of Ti-rich layers are denoted by white lines. (d) FFT image of the image (c) showing systematic satellite peaks around 111 peaks. (e) Individual antisite boundary where the N-sites are occupied with metal atoms. (f) FCC lattice simulation.

a zig-zag stacking characteristic for a hexagonal lattice. These agglomerations of stacking faults often locally fill the Al-rich lamellae as shown in Fig. 1.18c (white lines represent the approximate positions of the Ti-rich lamellae). The presence of the defect can be recognized in an FFT image (Fig. 1.18d) as well. Additional satellite peaks are systematically placed around the 111 peaks. Furthermore the positions of 111 peaks and 002 peaks are slightly displaced and indicates a lattice deformation. An individual anti-phase boundary is shown in Fig. 1.18e. Note that the N-atomic columns are invisible for our instrument. In the Fig. 1.18e, we can clearly distinguish regions with atomic columns visible at the N-positions (check with simulated lattice in Fig. 1.18f) as well as regions with perfect lattice. This is due to an occupation of these positions by metal atoms, leading to a volume region filled with anti-site defects with respect to a reference perfect lattice, so called anti-phase. These anti-phase boundaries were predominantly found in the Ti-rich lamellae.

Besides the isolated and agglomerated defects, also large-scale defects were observed. They occur either within the lamellar structure and cause a severe structure deformation or/and as regions completely transformed into a new phase ignoring the lamellar arrangement. The first situation is depicted in Fig. 1.19a. The approximate positions of Ti-rich lamellae are again marked with white lines. In addition to regions with a high concentration of stacking faults (marked 1-3), an extended defect (marked 4) occurred within the Al-rich layer and deformed the surrounding microstructure. A detailed filtered HRTEM image of the large defect lattice arrangement is depicted in Fig. 1.19. In this projection, we identified a rectangular basic structural unit that is marked in red. It seems to be rather structurally complicated and repeats across several lattice planes. Considering the size of this defect, we describe it as a new, yet unknown phase transformed from the parent structure. A Hanning filtered FFT (Fig. 1.19c) of the detailed image shows a corresponding symmetry to the basic structural unit in Fig. 1.19b. A comparison of this FFT image with simulated diffractograms of hexagonal B4 and B_k phases [31] covering the complete stereographic projection using 5161 individual diffractograms/phase did not yield a successful match. Another situation is documented in Fig 14a, where an interface between fcc and a region with agglomerated stacking faults is depicted. The embedded FFT images were taken from the fcc region (bottom) and ordered stacking faults region (top). The lamellar structure (not visible in the image) would be parallel to the <110> direction. Therefore, this large scale defect does not seem to be limited by the lamellar structure, in contrast to the previous case (Fig. 1.19a). A detailed filtered HRTEM image of the interface is shown in Fig. 1.20b. The fcc ABCABC

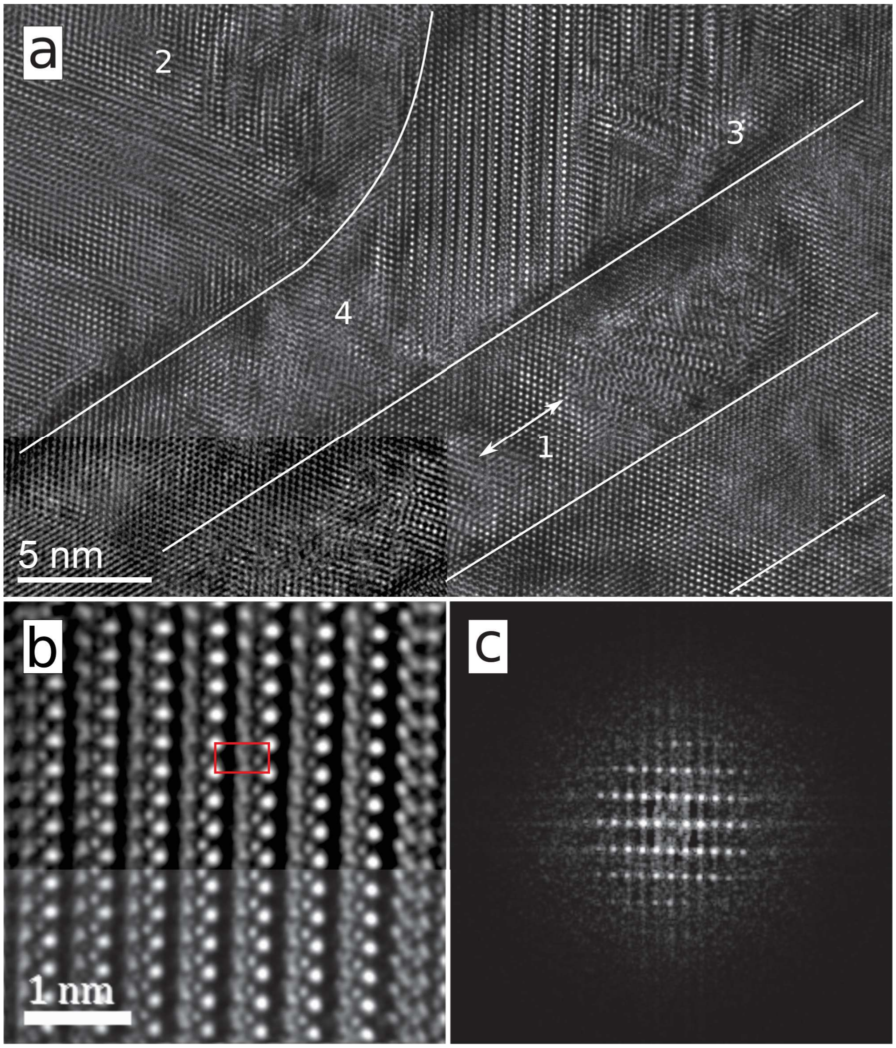

Figure 1.19.: (a) HRTEM lattice image of a large defect in the lamellar structure. The numbers 1-3 mark stacking faults near a large defect (marked 4). The approximate positions of Ti-rich lamellae are marked with white lines. (b) Detailed filtered HRTEM image of the large defect. The rectangle represents a repeating structural unit (c) Hanning filtered FFT of the image (b).

stacking sequence gradually brakes into partially displaced ABC stacking sequence. The orientation of individual planes with respect to the fcc lattice is recognizable from in the FFT image Fig. 1.20c from the image Fig. 1.20b. The cubic {111} planes are parallel to the stacking faults. The occurrence of the large defects is relatively rare, compared to the high density of individual and agglomerated defects.

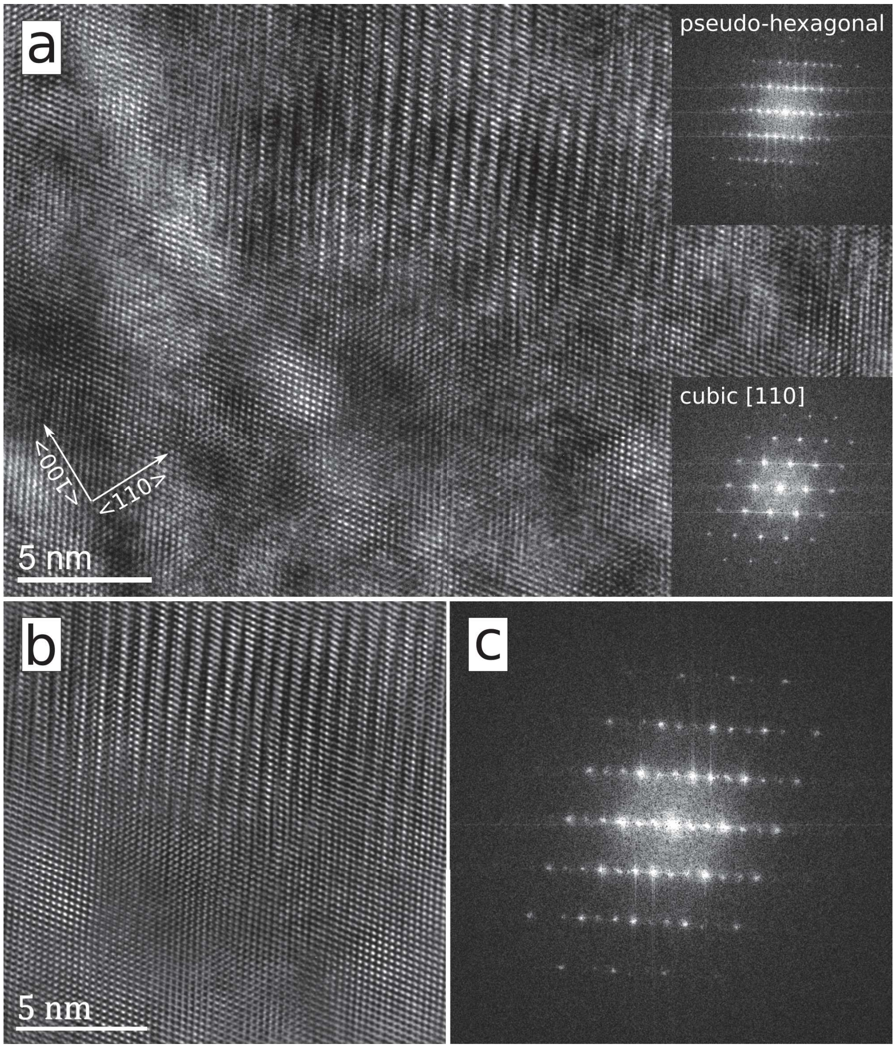

Figure 1.20.: (a) HRTEM micrograph of a phase boundary between FCC and partially ordered stacking faults on {111}. (b) Filtered detail of HRTEM micrograph (a). (c) FFT image of the micrograph (b).

Discussion on lattice defects in lamellar FCC phase

In the Paper C we have reported significant compositional fluctuations of various extend as well as a gradual changes of the lattice parameter across the lamellar microstructure in the fcc $Ti_{1-x}Al_xN_y$. Especially the observed systematic N-deficiency and N-excess imposed questions regarding the defects. In the previous section, we presented experimental observations of a large number of individual and agglomerated defect types as well as partially and completely transformed regions distributed in the nanolamellar structure. Especially in the case of Al-rich layers, agglomerations of stacking faults were found to occur systematically in our material. This is understandable in the context of our previous results (Paper C). Our DFT calculations showed that presence of point defect in the c-AlN phase is energetically highly unfavourable. On the other hand, the lattice constant of pure c-AlN ($\approx 4.05\,\AA$) is still not matching with the lattice constants of $\mathrm{Ti}_{1-x}\mathrm{Al}_x\mathrm{N}_y$ in the Ti-rich layers (composition oscillates). The remaining lattice misfit in combination with N-excess could therefore trigger the formation of stacking faults. The direct lattice constant measurements across the lamellar structure showed a gradual change of the lattice parameter across the Al-rich/Ti-rich layer interfaces. Nevertheless, this gradient does not extend further than several lattice planes into the relatively thick (7-10 nm) Al-rich layers. Most of the layer interior has therefore a lattice constant close to $4.05\,\AA$. The almost pure metastable c-AlN should therefore have a high tendency to transform into a stable B4 wurtzite phase. We have observed a systematic presence of stacking faults predominantly placed within the Al-rich layers interior. We therefore speculate that the presence of the stacking faults is related to the thermodynamic driving force for the transformation from the metastable cubic B1 structure to the stable wurtzite one. A textbook example of stacking faults actually concerns the fcc-hcp transformation. The ABC stacking sequence of fcc {111} lattice planes changes to ABAB stacking simply by removing the C planes. This is facilitated by a sequential shifting every third fcc {111} plane along the $[11\bar{2}]$ direction. The best fcc lattice orientation with respect to direct observations of stacking faults on {111} planes is along a [110] zone axis. This is exactly the zone axis that we obtain when we fabricate a cross-sectional FIB lamella out of our self-organized nanolamellar film with {111} planes parallel to the substrate surface. The agglomerated stacking faults that can be seen in the Al-rich layer interiors in Fig. 1.18c and Fig. 1.19a could be triggered by the lattice misfit and/or the nitrogen excess in the layers. Furthermore, the location of these agglomerations in the Al-rich layer interiors could locally help to decrease the strain caused by lattice misfit. These defects also show significant disorder that probably does not allow them to transform directly into any intermediate phase or directly to the wurtzite phase. On the other hand, the large defects in Fig. 1.19a, Fig. 1.20a and Fig. 1.20b are attended by stacking fault ordering. That could trigger, at certain extend and array of the defect, a transformation into the intermediate phase/phases. Our analysis showed that this phase is neither fcc nor B4, Bk. The rare occurrence of these large-scale defects indicates that such transitions are in the as-deposited state of the film not preferred.

Bibliography

[1] S. PalDey, and S. Deevi, *Mater. Sci. Eng., A* (2003) **342**, 58–79, DOI: 10.1016/S0921-5093(02)00259-9.

[2] R. Rachbauer, S. Massl, E. Stergar, D. Holec, D. Kiener, J. Keckes et al., *J Appl Phys* (2011) **110**, 11, DOI: 10.1063/1.3610451.

[3] P. Mayrhofer, A. Hörling, L. Karlsson, J. Sjölén, T. Larsson, C. Mitterer et al., *Appl Phys Lett* (2003) **83**, 2049–2051, DOI: 10.1063/1.1608464.

[4] U. of Leicester, *Airy disk simulation*, http://www.star.le.ac.uk/classroomspace/Airy%20Disc%20Diffraction.swf.

[5] J. Rayleigh, *Philosophical Magazine* (1879) **8**, 261–274, DOI: 10.1080/14786447908639684.

[6] R. Nave, *Hyper Physics*, Georgia State University, (2016) http://hyperphysics.phy-astr.gsu.edu.

[7] X. Zou, *Electron Crystallography: Electron Microscopy and Electron Diffraction*, Oxford University Press, 2011, (2011)

[8] C. B. C. D. B. Williams, *Transmission Electron Microscopy: A Textbook for Materials Science*, Springer Science & Business Media, 2nd edn., (2009)

[9] P. Barna, and M. Adamik, *Thin Solid Films* (1998) **317**, 27–33, DOI: 10.1016/S0040-6090(97)00503-8.

[10] A. Anders, *Thin Solid Films* (2010) **518**, 4087–4090, DOI: 10.1016/j.tsf.2009.10.145.

[11] E. Arzt, *Acta Mater.* (1998) **46**, 5611–5626, DOI: 10.1016/S1359-6454(98)00231-6.

[12] R. Daniel, A. Zeilinger, T. Schöberl, B. Sartory, C. Mitterer, and J. Keckes, *J Appl Phys* (2015) **117**, 235301, DOI: 10.1063/1.4922666.

[13] R. Zhang, and S. Veprek, *Mater. Sci. Eng., A* (2007) **448**, 111–119, DOI: 10.1016/j.msea.2006.10.012.

[14] P. Midgley, and A. Eggeman, *IUCrJ* (2015) **2**, 126–136, DOI: 10.1107/S2052252514022283.

[15] A. Eggeman, and P. A. Midgley, *Advances in Imaging and Electron Physics*, ed. P. W. Hawkes, Elsevier, (2012) vol. 170, pp. 1–63, DOI: 10.1016/B978-0-12-394396-5.00001-4.

[16] J. Keckes, R. Daniel, C. Mitterer, I. Matko, B. Sartory, A. Köpf et al., *Thin Solid Films* (2013) **545**, 29–32, DOI: 10.1016/j.tsf.2013.08.001.

[17] A. Zeilinger, R. Daniel, M. Stefenelli, B. Sartory, L. Chitu, M. Burghammer et al., *J Phys D Appl Phys* (2015) **48**, 295303, DOI: 10.1088/0022-3727/48/29/295303.

[18] J. Todt, R. Pitonak, A. Köpf, R. Weißenbacher, B. Sartory, M. Burghammer et al., *Surf. Coat. Technol.* (2014) **258**, 1119–1127, DOI: 10.1016/j.surfcoat.2014.07.022.

[19] A. Paseuth, K. Yamagata, A. Miura, M. Higuchi, and K. Tadanaga, *Journal of the American Ceramic Society* (2016) DOI: 10.1111/jace.14549.

[20] J. Todt, J. Zalesak, R. Daniel, R. Pitonak, A. Köpf, R. Weißenbacher et al., *Surface and Coatings Technology* (2016) **291**, 89–93, DOI: 10.1016/j.surfcoat.2016.02.027.

[21] F. F. Klimashin, N. Koutna, H. Euchner, D. Holec, and P. H. Mayrhofer, *Journal of Applied Physics* (2016) **120**, 185301, DOI: 10.1063/1.4966664.

[22] Z. Zhang, H. Li, R. Daniel, C. Mitterer, and G. Dehm, *Phys. Rev. B* (2013) **87**, 014104, DOI: 10.1103/PhysRevB.87.014104.

[23] P. Wan, Z. Zhang, D. Holec, R. Daniel, C. Mitterer, and H. Duan, *Acta Materialia* (2015) **98**, 119–127, DOI: 10.1016/j.actamat.2015.07.019.

[24] B. Alling, A. Karimi, L. Hultman, and I. A. Abrikosov, *Applied Physics Letters* (2008) **92**, 071903, DOI: 10.1063/1.2838747.

[25] M. to Baben, L. Raumann, D. Music, and J. M. Schneider, *Journal of Physics: Condensed Matter* (2012) **24**, 155401.

[26] I. Schramm, M. J. Joesaar, J. Jensen, F. Mucklich, and M. Oden, *Acta Materialia* (2016) **119**, 218–228, DOI: 10.1016/j.actamat.2016.08.024.

[27] H. Euchner, and P. Mayrhofer, *Surface and Coatings Technology* (2015) **275**, 214–218, DOI: 10.1016/j.surfcoat.2015.05.017.

[28] K. Laaksonen, M. G. Ganchenkova, and R. M. Nieminen, *Journal of Physics: Condensed Matter* (2009) **21**, 015803.

[29] C. Stampfl, and C. G. Van de Walle, *Phys. Rev. B* (2002) **65**, 155212, DOI: 10.1103/PhysRevB.65.155212.

[30] N. Koutna, MA thesis, Masaryk University, (2016)

[31] D. Holec, R. Rachbauer, D. Kiener, P. D. Cherns, P. M. F. J. Costa, C. McAleese et al., *Phys. Rev. B* (2011) **83**, 165122, DOI: `10.1103/PhysRevB.83.165122`.

2

List of Appended Publications

2.1. First Author Papers

Paper

J. Zalesak, M. Bartosik, R. Daniel, C. Mitterer, C. Krywka, D. Kiener, P.H. Mayrhofer and J. Keckes

Cross-sectional structure-property relationship in a graded nanocrystalline $Ti_{1\text{-}x}Al_xN$ thin film

Acta Materialia 102 (2016) 212-219

doi: 10.1016/j.actamat.2015.09.007

Paper

J. Zalesak, J. Todt, R. Pitonak, A. Köpf, R. Weißenbacher, B. Sartory, M. Burghammer, R. Daniel and J. Keckes

Combinatorial refinement of thin-film microstructure, properties and process conditions: Iterative nanoscale search for self-assembled TiAlN nanolamellae

Journal of Applied Crystallography 49 (6) 2217-2225

doi: 10.1107/S1600576716017258

Paper

J. Zalesak, D. Holec, I. Matko, M. Petrenec, B. Sartory, N. Koutná, R. Daniel, R. Pitonak and J. Keckes

Peculiarity of Self-Assembled Cubic Nanolamellae in the TiN/AlN System: Epitaxial Self-Stabilization by Element Deficiency/Excess

Acta Materialia 131 (2017) 391-399

doi: 10.1016/j.actamat.2017.04.009

2.2. Co-author Papers

Paper

H. Riedl, J. Zalesak, M. Arndt, P. Polcik, D. Holec and P. H. Mayrhofer

Ab initio studies on the adsorption and implantation of Al and Fe to nitride materials

Journal of Applied Physics 118, 125306 (2015)

doi: 10.1063/1.4931665

Paper

J. Todt, J. Zalesak, R. Daniel, R. Pitonak, A. Köpf, R. Weißenbacher, B. Sartory C. Mitterer, and J. Keckes

Al-rich cubic $Al_{0.8}Ti_{0.2}N$ coating with self-organized nano-lamellar microstructure: Thermal and mechanical properties

Surface & Coatings Technology 291 (2016) 89–93

doi: 10.1016/j.surfcoat.2016.02.027

Paper

M. Reisinger, J. Zalesak, R. Daniel, M. Tomberger, J.K. Weiss, A.D. Darbal, M. Petrenec, J. Zechner, I. Daumiller, W. Ecker, B. Sartory and J. Keckes

Cross-sectional stress distribution in $Al_xGa_{1-x}N$ heterostructure on Si(111) substrate characterized by ion beam layer removal method and precession electron diffraction

Materials and Design 106 (2016) 476–481

doi: 10.1063/1.4931665

Paper

R. Daniel, M. Meindlhumer, J. Zalesak, B. Sartory, A. Zeilinger, C. Mitterer and J. Keckes

Fracture toughness enhancement of brittle nanostructured materials by spatial heterogeneity: A micromechanical proof for CrN/Cr and TiN/SiO_x multilayers

Materials and Design 104 (2016) 227–234

doi: 10.1016/j.matdes.2016.05.029

Paper

R. Daniel, M. Meindlhumer, W. Baumegger, J. Zalesak, B. Sartory, M. Burghammer, C. Mitterer and J. Keckes

Grain boundary design of thin films: Using tilted brittle interfaces for multiple crack deflection toughening

Acta Materialia 1 (2017) 130-137

doi: 10.1016/j.actamat.2016.09.027

2.3. Contribution of the author to the papers

Table 2.1.: Contribution of the Author to the appended publications in percent.

Paper / Article	Conception and planning	Experiments	Analysis and interpretation	Manuscript preparation
A	80	90	90	70
B	50	50	50	50
C	80	80	80	70
D	20	25	25	20
E	25	25	25	20
F	25	25	25	20
G	20	20	20	20
H	20	20	20	20

A

Cross-sectional structure-property relationship in a graded nanocrystalline $Ti_{1-x}Al_xN$ thin film

J. Zalesak[a, b], M. Bartosik[c, d], R. Daniel[a], C. Mitterer[a], C. Krywka[e], D. Kiener[b], P. H. Mayrhofer[c], J. Keckes[b, f]

[a]Department of Physical Metallurgy and Materials Testing, Montanuniversität Leoben, Leoben, Austria
[b]Department of Materials Physics, Montanuniversität Leoben, Leoben, Austria
[c]Institute of Materials Science and Technology, TU Wien, Vienna, Austria
[d]Christian Doppler Laboratory for Application Oriented Coating Development at the Institute of Materials Science and Technology, TU Wien, Vienna, Austria
[e]Ruprecht Haensel Laboratory, University of Kiel and Helmholtz Zentrum Geesthacht, Germany
[f]Materials Center Leoben Forschung GmbH, Roseggerstraße 12, Leoben, Austria

Abstract

The influence of simultaneously occurring gradients of crystalline phases, microstructure, chemical composition and strains on overall as well as local mechanical properties of nanocrystalline thin films is challenging to understand. In this work, cross-sectional structure-property relationships in a graded nanocrystalline 2 µm thick $Ti_xAl_{1-x}N$ film were analyzed using in-situ bending tests on microcantilevers in transmission electron microscope, synchrotron X-ray nanodiffraction and nanoindentation. The results document that sub-micron depth variations of fracture stresses, hardness and elastic moduli depend on phases, crystallite sizes, crystallographic texture, Ti/Al ratio and residual strain. The local mechanical properties are primarily influenced by cross-sectional occurrence of binary and ternary phases and their intrinsic properties. Secondly, the hardness and fracture stress gradients depend on cross-sectional microstructure, especially on the local crystallite sizes and shapes as well as fiber textures. Two nucleation regions of cubic TiN and hexagonal $\mathrm{Ti}_x\mathrm{Al}_{1-x}\mathrm{N}$ phases with globular shaped crystal sizes in the nm range and relatively large in-plane residuals strains result in significantly higher hardness and fracture stresses in comparison with a coarse-grained region consisting of columnar cubic $\mathrm{Ti}_x\mathrm{Al}_{1-x}\mathrm{N}$ crystallites. The fracture behavior of cantilevers with $\sim 0.5\times0.5\,\mu m^2$cross-section depends also on the apparent grain size whereby the nucleation regions exhibit linear-elastic fracture in contrast to partly ductile response of the region with elongated nanocrystals. Finally, the experimental data indicate the possibility of mechanical optimization of nanocrystalline thin films through cross-sectional nanoscale design.

A.1. Introduction

Nanocrystalline thin films exhibit size effects of physical properties that originate from their small crystalline size [1] (typically below 100 nm) and high volume fraction of grain boundaries [2]. Another important feature of the nanocrystalline films is the presence of pronounced gradients [3], which are the result of (i) the gradual grain size, crystallographic texture and strain evolution during the self-organized film growth far from the thermodynamic equilibrium [4], (ii) the intentionally varying deposition conditions resulting in the nanoscale modulations of microstructure and strain [5], and (iii) the inhomogeneous thermal and/or mechanical loads induced during the film service [6]. Consequently, in order to understand the structure-property relationships in nanocrystalline thin films, it is necessary to correlate local composition, phases, microstructure and strain with local and overall physical properties.

Physical properties of thin films such as hardness, fracture toughness, electrical and thermal conductivity are usually examined on the film surface [7]. The experimental data obtained using such approaches do not provide the information on the role of distinct thin film regions, such as nucleation zones, individual sublayers and interfaces between them as well as graded regions on film functional behavior. This is also the reason why the optimization of functional properties of nanostructured, gradient and/or multi-phase films is in practice performed by a tedious variation of film composition, residual stress state and microstructure.

Recently, several characterization techniques have been developed, which can be used to assess thin film properties across the film thickness. Those were especially depth-resolved nanoindentation of the film cross-sections [8], [9] and [10] and micromechanical testing of miniaturized samples prepared selectively by the focused ion beam technique [11]. Another important step to analyze volume-representative microstructure and strain across thin films was the development of cross-sectional X-ray nanodiffraction, which can be routinely applied with a lateral resolution of 50 nm [12], [13] and [14]. Although the cross-sectional characterization of thin films is an emerging field, studies correlating local microstructure with mechanical properties are rare.

$Ti_xAl_{1-x}N$, used as hard protective thin film, represents one of the most investigated systems in the recent 25 years. The mechanical properties depend primarily on the Ti/Al ratio [15] and [16], microstructure and residual stress state [17]. The main interest in $Ti_xAl_{1-x}N$, besides its superior oxidation resistance and hardness compared to commonly used binary compounds such as TiN, originates especially from the age hardening effect [18]. This is related to the spinodal decomposition of the metastable face centered cubic (c) $Ti_xAl_{1-x}N$ phase and formation of c-TiN and c-AlN domains, whereby the latter transform subsequently into hexagonal (h) AlN [18]. However, also in the case of $Ti_xAl_{1-x}N$ films, it is currently not known, how the film cross-sectional gradients of microstructure and strain formed due to (i) the self-organized film growth and (ii) the variation of deposition conditions relate to the film cross-sectional structure-property relationships and further to the hardening effect.

The aim of this work is to analyze the structure-property relationships over the cross-section of a graded nanocrystalline 2 µm thick $Ti_xAl_{1-x}N$ film with a nanoscale variation of metallic components, microstructure and residual stresses. The motivation is to quantify the influence of the film structural and chemical gradients on the mechanical response.

A.2. Experimental methods

A.2.1. Thin film synthesis

Compositionally graded 2 µm thick $Ti_xAl_{1-x}N$ film was deposited on a Si(100) substrate by reactive magnetron sputtering in an AJA Orion 5 lab-scale deposition unit equipped with one 3-inch-diameter Al and one 2-inch-diameter Ti target. Prior to the deposition, the Si substrates were ultrasonically cleaned in ethanol and acetone for 5 min. The substrates were placed on the substrate holder in the deposition chamber and thermally cleaned at 500 °C for 20 min under vacuum conditions better than 10^{-6} mbar as well as Ar ion etched for 10 min at a pressure of 4×10^{-2} mbar. The deposition was carried out at a substrate temperature of 500 °C in an Ar and

N_2 gas atmosphere with a total pressure of 4×10^{-3} mbar and an Ar:N_2 flow ratio of 3:7 sccm/sccm. During the deposition, the substrates were continuously rotated and no bias voltage was applied (hence, the substrates had a floating potential). Starting with a monolithically grown TiN base layer, by constantly powering the Ti target with 300 W, the compositional gradient along the film growth direction was realized by setting the generators to provide continuous increase of the power for the Al target from 0 to 300 W and a decrease of the power for the Ti target from 300 to 0 W. As a top layer, AlN was monolithically grown by constantly powering the Al target with 300 W.

A.2.2. Cross-sectional characterization

The cross-sectional synchrotron X-ray nanodiffraction characterization was performed at the Nanofocus Endstation of MiNaXS (P03) beamline [19] at the PETRA III synchrotron radiation source in Hamburg, Germany, using a monochromatic synchrotron beam with an energy of 14.73 keV. The X-ray beam was focused by a pair of elliptical mirrors in crossed geometry, thereby providing a spatial resolution of $200 \times 200\,\text{nm}^2$. A film lamella with a thickness of 30 µm (in the beam direction) was prepared by mechanical grinding and polishing and analyzed in transmission wide angle diffraction geometry by moving the sample in the beam with a step size of 100 nm. The Debye–Scherrer rings were recorded using a 4k charge-coupled device (CCD) detector at a distance of 18.1 cm from the sample. The two-dimensional (2-D) diffraction data were treated using Fit2D software [20]. The data were used to compile depth-resolved phase plots for different orientations of the diffraction vectors. Moreover, the measured diameter and the ellipsoidal shape of the Debye–Scherrer rings were correlated with the in-plane X-ray elastic strain of the first order using the approach introduced in our previous works [12] and [21]. As discussed in Refs. [14] and [21], there exists a Debye–Scherrer ring azimuthal position δ_o for which the Bragg's angleθ_o and the corresponding lattice parameter d_o represents properties of stress free material in the equi-biaxially stressed film. The stress free azimuthal angle δ_o can be determined as follows

$$cos\delta_o cos\theta_o = \sqrt{\frac{1-\nu}{1+\nu}} \tag{A.1}$$

where ν represents the material Poisson's number. For simplicity it was supposed that ν across the graded film does not change significantly and the value of 0.3 from Ref. [16] was applied. It is supposed that using this simplified approach the in-plane

Table A.1.: Dimensions of the cantilevers were used to evaluate Young's moduli and fracture stresses of the thin film regions A, B, and C (Fig. A.1a) using Eq. (2) applying the slopes of the load–displacement curves from Fig. A.4.

Region	Cantilever width, length, thickness [µm]	Young's [GPa]	Fracture stress [GPa]
C	0.52, 3.00, 0.73	203.2	3.35
	0.56, 3.00, 0.72	182.1	3.12
B	0.36, 3.00, 0.55	262.1	4.49
	0.47, 3.00, 0.53	254.6	3.50
A	0.55, 3.00, 0.60	285.2	8.13
	0.55, 3.00, 0.55	296.7	8.84

strains calculated as $(d_{in-plane} - d_o)/d_o$ were quantified with an error smaller than 20 %. The advantage of this very simplified approach is the fact that the unknown values of Young's moduli are not applied. For scanning electron microscopy (SEM) characterization and focused ion beam (FIB) machining of sub-micron cantilevers as well as cross-section lamella for transmission electron microscopy (TEM) studies, a Tescan Lyra 3 workstation was used. The cross-section TEM lamella was fabricated [22] from the coated Si-substrate, mechanically polished to a thickness of about 30 nm, and subsequently glued on a TEM in-situ Cu-holder [23].

The cantilever fabrication was performed by FIB using an acceleration voltage of 30 kV and currents in the range from 20 nA to 50 pA. Special care was taken to avoid sample damage by Ga ions [24] by using low FIB cutting currents as well as Pt protective layers. Two cantilevers with length (l), width (b) and thickness (w) of about 3.0, 0.5 and 0.5 µm (cf. Table A.1 for exact dimensions), respectively, were fabricated from three film depth regions, namely from the nucleation Ti-rich region A (∼0.2–0.7 µm from the film/substrate interface), the film center (Ti–Al transition) region B (∼1.0–1.5 µm from the interface) and surface Al-rich region C (∼1.5−2.0 µm from the interface) as demonstrated schematically in Fig. A.1a. An exemplary pair of cantilevers is shown in an inclined view in Fig. A.2a. The TEM characterization as well as energy-dispersive X-ray spectroscopy (EDS) analysis in scanning TEM (STEM) mode were performed using a JEOL JEM-2100F TEM system operated at 200 keV with a 0.7 nm spot size (Fig. A.1a and b).

Bending tests of the cantilevers were performed using a Hysitron PI-95 TEM Picoindenter in JEOL microscope operated in a conventional (CTEM) mode (Fig. A.2) using a feedback enabled displacement-controlled deformation mode. A boron doped

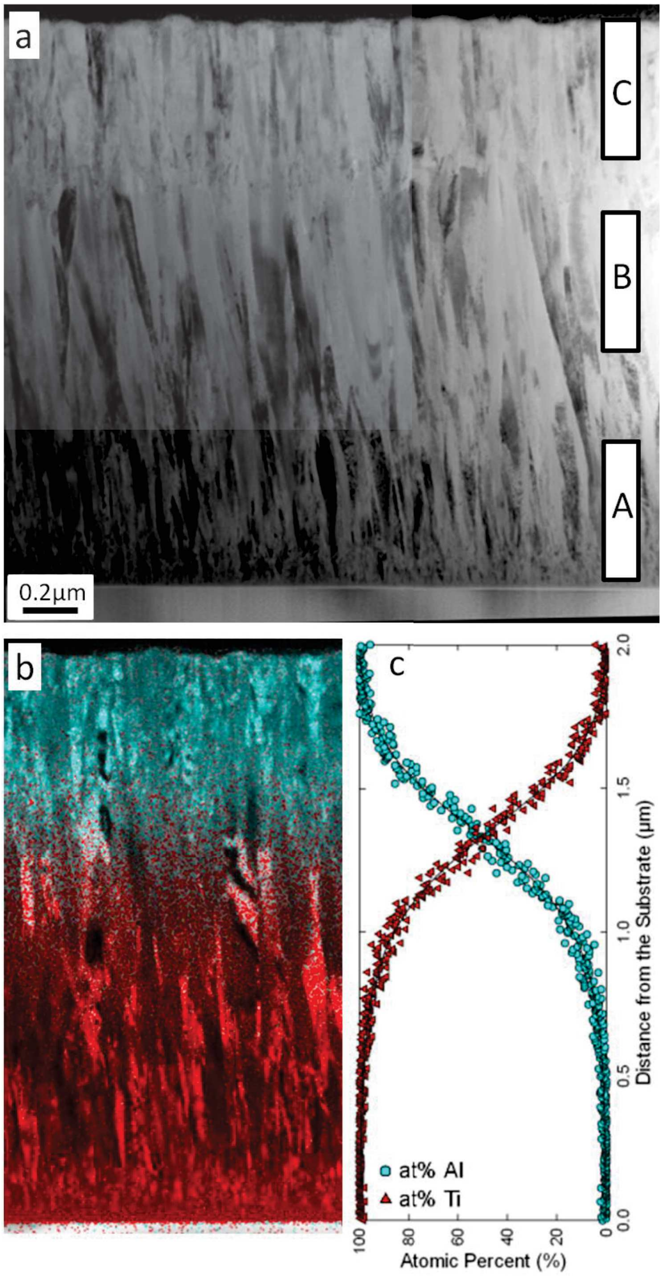

Figure A.1.: BF STEM micrograph (a) of the graded $Ti_{1-x}Al_xN$ film showing complex grain morphology across the film cross-section. EDS-STEM analysis (b, c) indicates the compositional gradients of Ti and Al across the film thickness. The bars in (a) schematically depict positions at which cantilevers with cross-sections of ∼0.5 × 0.5 µm^2 were machined using FIB.

cube-corner diamond indenter and a bending rate of 60 nm/s were used (Fig. A.2b). The reason to perform the bending tests in TEM was a possibility to test small cantilevers with better sensitivity of the TEM indenter compared to the setup using SEM as reported in our previous study [11].

After the bending tests, exact cross-sectional dimensions of the fracture surfaces were determined. From the load–displacement curves and the cantilever geometry, Young's moduli and fracture stresses were computed [11], [25] and [26]. The Young's modulus E was calculated from the recorded load-deflection curves as follows:

$$E = \frac{4F}{\delta b} \times \left(\frac{l}{w}\right)^3 \tag{A.2}$$

where δ represents the displacement at the applied load F, l is a distance from a beginning of cantilever beam to a loading point, b represents a cantilever width and w a cantilever thickness [11]. Cross-sectional characterization of hardness and reduced elastic modulus of a mechanically polished thin film cross-section was performed using an atomic force microscope (Veeco Dimension 3100), which was equipped with a sharp diamond cube-corner tip controlled by a Hysitron Triboscope transducer in a load–displacement mode. The film was considered as homogeneous at a given thickness and indented at various positions at the cross-section [9]. This approach allowed keeping a relatively large distance between individual indents. For the calibration, a mono-crystalline sapphire (0001) was used. For all the indents, a maximal load of 400 µN was applied.

A.3. Results and discussion

A.3.1. STEM imaging and EDS composition analysis

The cross-sectional morphology of the 2 µm thick $\mathrm{Ti}_{1-x}\mathrm{Al}_x\mathrm{N}$ film, shown in Fig. A.1a, exhibits a fine nanocrystalline region distributed up to ∼300 nm thickness from the film/substrate interface. Subsequently, a gradual coarsening of columnar grains can be observed. The columnar grain morphology with V-shaped grains is interrupted at a film thickness of 1.4 µm by a distinguishable interface at which a new nanocrystalline layer starts to nucleate. This sub-surface layer with a thickness of ∼0.6 µm shows another fine-grained nucleation region and subsequent development of columnar grains.

In Fig. A.1b and c, qualitative elemental mapping and quantitative STEM-EDS depth-resolved concentration profiles (using built-in sensitivity factors) for Ti and Al

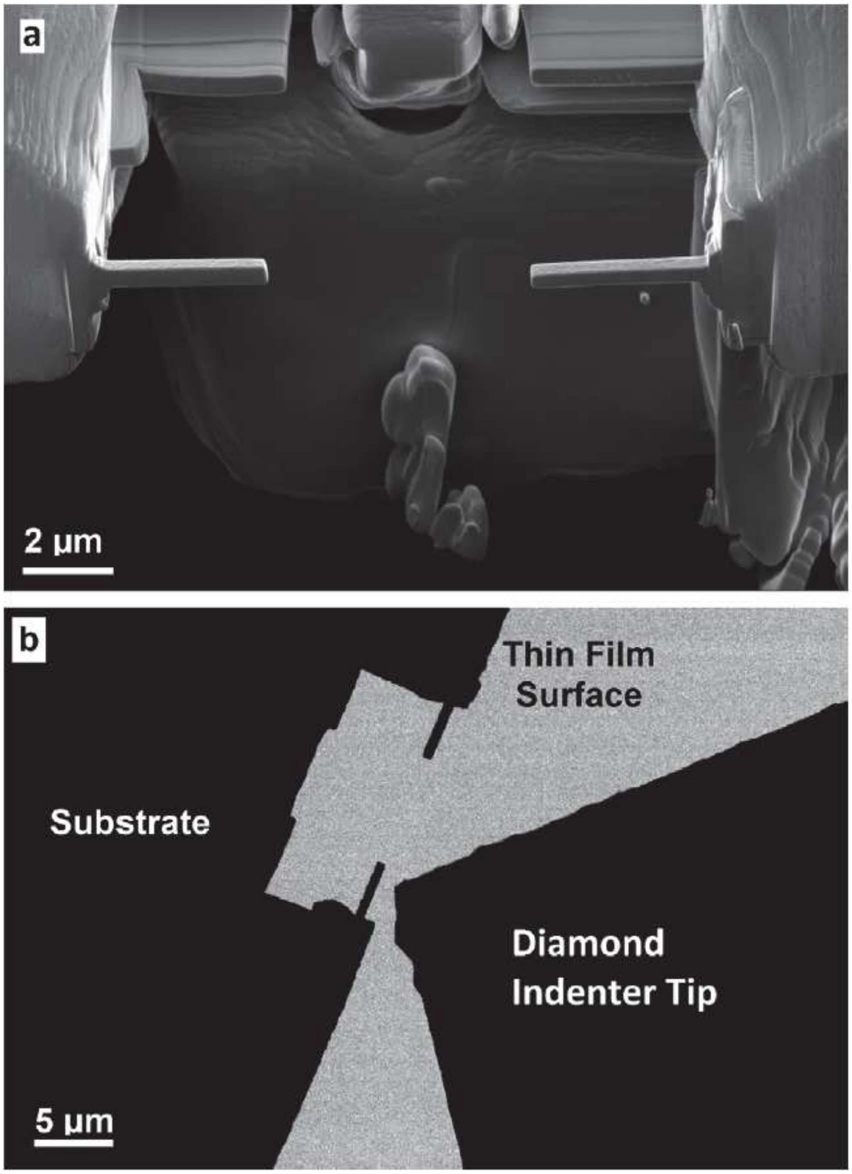

Figure A.2.: A pair of cantilevers used for bending tests (a) with cross-sections of $\sim$0.5 0.5 μm^2 and length of $\sim$3.5 μm each machined using FIB. Low magnification overview of the in-situ TEM experiment with two cantilevers and a cube-corner diamond indenter approaching one of them at a pre-selected position (b).

across the film thickness are presented. The nitrogen concentration across the film was found to be constant at 50 % and is therefore not shown here. Other elements such as oxygen or argon were not detected in a significant amount. The elemental analysis in Fig. A.1c indicates that the film consists of TiN- and AlN-based phases close to the film/substrate interface and in the sub-surface region, respectively. At the distance ∼0.5–1.8 µm from the film/substrate interface, the Al/Ti ratio changes gradually, in accordance with the variation of power applied to the targets and $Ti_{1-x}Al_xN$ phase is formed.

A.3.2. X-ray nanodiffraction analysis

The nanodiffraction data were used to compile depth-resolved phase plots for out-of-plane (Fig. A.3a) and in-plane (Fig. A.3b) orientations of the diffraction vectors. This was achieved by integrating the Debye–Scherrer rings in the azimuthal intervals of ∼(8,18) and ∼(80,100) deg of the angle ψ, whereby ψ represents the angle between the surface normal and the diffraction vectors, respectively [12]. Thus, the diffraction data presented in Fig. A.3a and b represents the diffraction on crystallographic planes oriented approximately at Bragg's angle θ with respect to the sample normal vector (out-of-plane orientation) and oriented perpendicular to the film-substrate interface (in-plane orientation), respectively. In the structural analysis, it was supposed that the film possesses a fiber texture and there is no epitaxial relationship with the substrate, as revealed by laboratory pole figure measurements not presented here.

An analysis of the diffraction angle 2θ positions of the reflections as well as of the full width of half maxima (FWHM) of the reflections in Fig. A.3 allows determining which crystalline phases were formed at which film depths and how the microstructure of the crystallites evolved during the growth. Developments and ratios of FWHMs of the individual reflections in Fig. A.3 allow analyzing the anisotropic film microstructure. Moreover, ratios of the diffraction intensities of the reflections across the film depth allow drawing conclusion about the crystallographic texture development.

At the substrate surface, cubic (c)-TiN was formed (Fig. A.3), in agreement with the data from Fig. A.1c. The FWHMs of c-TiN 111 and 200 reflections decrease as a function of the distance from the substrate surface in the range of $0-0.3$ µm. The larger FWHMs of the peaks collected close to the substrate surface document the formation of the film nucleation layer consisting of relatively small crystallites (visible in Fig. A.1a) and likely a high defect concentration [27]. The 2θ angle decrease of the c-TiN 110 and 200 reflections in Fig. A.3b can be qualitatively attributed to the pronounced compressive in-plane stress in the film interface regions [4]. The higher intensity of the c-TiN 200 reflection I_{200} compared to I_{111} in Fig. A.3a and

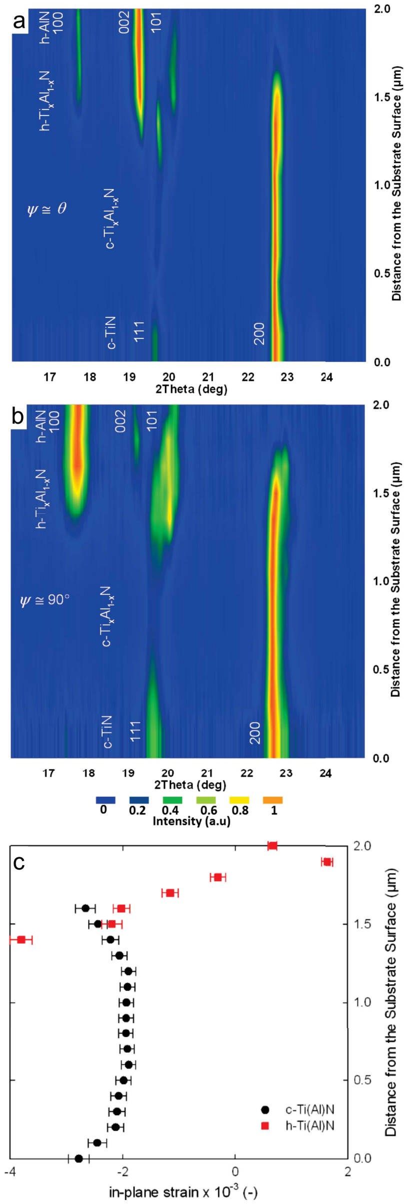

Figure A.3.: Phase-depth plots determined by X-ray nanodiffraction for approximately outof- plane (a) and in-plane (b) orientations of the diffraction vectors document the distribution of crystalline c-TiN, c-$Ti_{1-x}Al_xN$, h-$Ti_{1-x}Al_xN$ and h-AlN phases, as well as their microstructural development across the film thickness. The in-plane X-ray elastic strain (c) determined by the analysis of c-Ti(Al)N 111 and h-Ti(Al)N 100 reflections correlates with the film cross-sectional microstructural development.

b documents the (100) preferred orientation of c-TiN in this region. This type of fiber texture in transition metal nitride films is typically a result of strain energy minimization during film nucleation [28].

At a distance of ∼0.6 µm and farther from the substrate surface, the FWHM of the 111 and 200 reflections start to increase and the Bragg's angles increase also slightly. This effect can be attributed to the formation of the metastable solid solution of c-$Ti_{1-x}Al_xN$, as Al substitutes Ti in the c-TiN lattice, with an increased number of point defects and a smaller lattice parameter compared to c-TiN. The formation of the ternary c-$Ti_{1-x}Al_xN$ phase correlates also with the compositional gradient shown in Fig. A.1c, where the Al content starts to increase at the depth of ∼0.6 µm.

At a distance of ∼1.4 µm from the substrate surface, FWHMs and Bragg's angle of c-$Ti_{1-x}Al_xN$ 111 and 200 reflections increase significantly and, at even larger distances, a formation of hexagonal (h)-$Ti_{1-x}Al_xN$ is observed (Fig. A.3). A comparison of the composition (Fig. A.1c) and diffraction data (Fig. A.3) documents that c-$Ti_{1-x}Al_xN$ is present for $x <\sim 0.7$. For large Al concentrations, h-$Ti_{1-x}Al_xN$ developed, due to the lower formation energy and equilibrium formation enthalpy [29] and [30], which is in agreement with the results reported for monolithic magnetron sputtered $Ti_{1-x}Al_xN$ thin films [18].

FWHMs of h-$Ti_{1-x}Al_xN$ 100, 002 and 101 reflections in Fig. A.3b at the distance of ∼1.6 µm from the substrate surface are relatively large and then decrease towards the film surface. The increase in FWHM at the distance of ∼1.6 µm can be correlated with the formation of a nanocrystalline h-$Ti_{1-x}Al_xN$ nucleation layer (visible also in Fig. A.1a), consisted of small crystallites and exhibiting, probably, also a large amount of defects [3]. The formation of the new nucleation region within the nanocrystalline film was caused obviously by the transition from c-$Ti_{1-x}Al_xN$ to h-$Ti_{1-x}Al_xN$ and accompanied by the formation of probably incoherent interfaces between cubic (001)-oriented and hexagonal (001)-oriented crystallites. The h-$Ti_{1-x}Al_xN$ crystallites served as nucleation sites for the growth of new nanocrystalline hexagonal phase which developed at the distance of ∼1.6 µm and further from the interface.

The further film growth at the thicknesses above 1.6 µm is characterized by a slight increase in Bragg's angles of h-$Ti_xAl_{1-x}N$ 100 and 002 reflections. This can be interpreted by the increasing portion of smaller Al atoms accommodated into the lattice. At the film surface, only h-AlN peaks were detected in agreement with the EDS data (Fig. A.1c). The intensity ratios $I_{002} > I_{100}$ and $I_{002} < I_{100}$ of h-AlN reflections in Fig. A.3a and b, respectively, documents the (001) preferred orientation of h-AlN crystallites with the c-axis oriented approximately perpendicular to the film surface.

The larger FWHMs of practically all reflections in Fig. A.3b in comparison with FWHMs of the reflections from Fig. A.3a document a columnar film growth, i.e. smaller in-plane Scherrer's crystallite sizes and/or larger concentration of structural defects, as reported in our previous studies [27].

The in-plane strain presented in Fig. A.3c can be understood as a sum of intrinsic and thermal strain formed due the growth process and the cooling down after the deposition, respectively. Since the thermal strain can be considered approximately constant and positive, due to the larger coefficients of thermal expansion (CTE) of the film phases compared to the substrate CTE [31], strain gradient in Fig. A.3c can be interpreted mainly by the gradual microstructural development discussed above. A relatively high strain in c-TiN at the film/substrate interface correlates with the formation of the nucleation layer with small crystallites and a high density of grain boundaries. Energetic particle bombardment of the nucleation layer results in the generation of higher density of growth defects [32]. The displacement of atoms from their equilibrium positions, which is more pronounced at grain boundaries and on growing crystallite surfaces, results in an in-plane expansion of the growing film, which is however constrained by the substrate, giving origin to the relatively high in-plane compressive stress at the interface.

At the distance from ∼0.5 to 1.4 µm from the substrate surface, the compressive strain decreases and saturates at the value of -2×10^{-3}. This behavior can be interpreted by the gradual microstructure evolution, especially by a decrease of the grain boundary density. The presence of larges grains reduces the probability of the defect generation by the energetic particle bombardment and consequently also the radiation-induced in-plane compressive stress formation.

At the distance of ∼1.4 µm from the interface, the formation of the h-$Ti_{1-x}Al_xN$ nucleation layer results in a compressive strain increase. Similar as in the case of c-TiN nucleation layer, also in this case the presence of small crystallites and a high density of grain boundaries resulted in an increased radiation-induced damage, in-plane film expansion and formation of the in-plane compressive strain. The further compressive strain decrease and the switch to tensile stress can be explained by the gradual growth of the grains, which reduces the probability of the defect generation by the energetic particle bombardment. The actual formation of tensile stresses can be interpreted by the coalescence of h-$Ti_{1-x}Al_xN$ crystallites which induces an in-plane tensile loading of the crystallites interia [33].

A.3.3. Bending tests of cantilevers in TEM

Six cantilevers (with cross-sections of ∼0.5 × 0.5 µm^2 and length of ∼3.0 µm) were fabricated from three different thin film regions A, B, and C indicated by bars in Fig. A.1a. Load-displacement curves recorded during the bending tests in-situ in the TEM are presented in Fig. A.4. The results demonstrate distinct differences in the mechanical response of the cantilevers. The magnitudes of fracture stresses and elastic moduli are summarized in Table A.1. It should be noted that the slopes of the dependencies in Fig. A.4 can not be directly correlated with the elastic moduli of the cantilevers because of the varying cantilever dimensions presented in Table A.1.

Two cantilevers representing the region A (Fig. A.1 and Fig. A.4) exhibit a linear-elastic response and a maximum fracture stress from all three cantilever types. Differences in the slope of the two curves can be attributed to a variation of the cantilever dimensions and to a relative offset (up to about 50 nm) of their position at the film cross-section. The relatively high fracture stress of the cantilevers originates from the nanocrystalline nature of the nucleation layer which consists of small crystallites with sizes of a few tens nm and possesses a large portion of grain boundaries as well as point defects in crystallites interiors as indicated by TEM and X-ray nanodiffraction [34] (Fig. A.1 and Fig. A.3). The grains of the nucleation layer are (at least in-plane) misoriented to each other, and grain boundaries consist of disordered atoms, compared to the grain interiors. The high values of the fracture stresses can therefore be related to several factors such as reduction of crystallite sizes, microstructural homogenization, relative high (intrinsic) fracture stress of TiN nanocrystals and the crack propagation along grain boundaries forming triple junctions [35], [36] and [37]. It is supposed that the dominant failure mode of the nano-grained brittle material from the region A could be intergranular fracture [38], as we reported for brittle nanocrystalline CrN thin films [11] with similar microstructure.

Two cantilevers from the region B (Fig. A.1 and Fig. A.4) exhibit a relatively small fracture stress. The deformation curves show not purely linear-elastic response and suggests for plasticity-effects caused by cantilever in-plane compression and/or tension. These could be due to dislocation motions in the elongated grains, with a diameter of a few tens nanometers and length in the µm range (Fig. A.1a), or martensitic phase transformations of the metastable phases during the crack growth, preferably along the elongated grain boundaries.

The Al-rich cantilevers from region C, hence h-Al(Ti)N based, show a linear-elastic response, but the smallest fracture stress from all three cantilever types (Fig. A.2

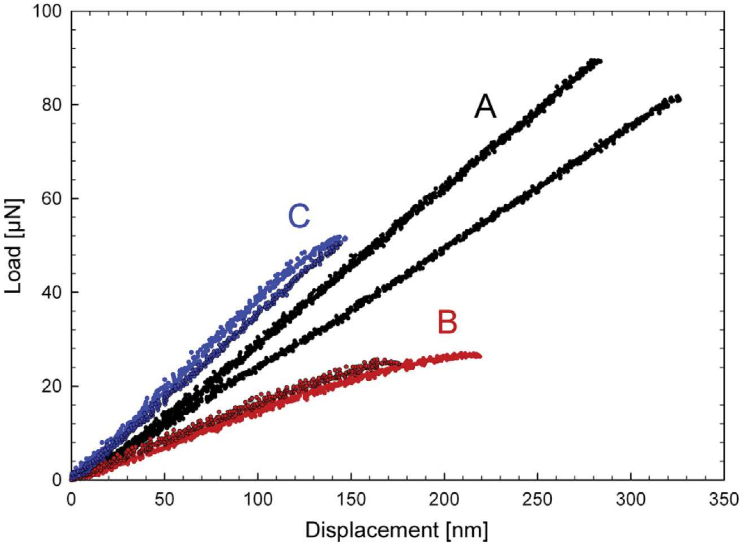

Figure A.4.: Load-displacement curves recorded during in-situ TEM bending experiments of cantilevers from the film regions A (black), B (red), and C (blue) (see Fig. 1a). (For interpretation of the references to colour in this figure legend, the reader is referred to the web version of this article.)

and Fig. A.4). The main reasons for this behavior could be a mechanical anisotropy of h-AlN crystal structure, (001) fiber texture and specific needle-like grain morphology. Consequently, elongated h-AlN crystallites are loaded preferably along [001] hexagonal axis and the fracture response is predefined by cohesive energies of (h00) and (hk0) faces as well as by activated shear bands of the needle-like crystallites. Based on typically lower cohesive energy along grain and phase boundaries of the nitride [11], we envision that crack growth in the cantilevers occurs probably along the grain boundaries and, due to the specific crystallographic orientations of the hexagonal grains, there is only negligible plastic deformation. An important parameter in the fracture response of the region C could be also the presence of the in-plane elastic strain (Fig. A.3a). It is not obvious how the tensile strain state changed in the film surface region after the cantilevers from region C were FIB machined by removing the substrate and the cantilever underneath regions, but a certain minor influence on the bending response cannot be excluded.

A comparison of the cantilever elastic moduli presented in Table A.1 documents that the A region is the stiffest one and the moduli decrease towards the surface with the increasing amount of Al in the film. This effect and the moduli magnitudes are discussed in Sec. 4.

A.3.4. Cross-sectional nanoindentation

Measured values of hardness (*H*) and reduced Young's modulus (*Er*) are plotted in Fig. A.5 as a function of the distance from the substrate surface. Since the surface and substrate near-regions of the film could not be analyzed due to difficult experimental conditions (too close to an embedding material/coating interface), the experimental data from the intervals (0, 0.4) and (1.8, 2) µm are unfortunately missing in Fig. A.5.

In the region of ∼0.4–0.8 µm from the substrate surface dominated by c-TiN and c-$Ti_{1-x}Al_xN$ (with only a small amount of Al), both $H = \sim 38$ GPa and $Er = \sim 290$ GPa remain approximately constant. This can be interpreted (i) by already saturated thin film microstructure with columnar grains (Fig. A.1 and Fig. A.3a, b), (ii) by an absence of a pronounced compositional gradient (Fig. A.2c) and (iii) by saturated in-plane strain (Fig. A.3c). In nanoceramic thin films, grain boundaries represent one of the most important strengthening microstructural feature, which hinder dislocation and crack propagation [39] and [40]. The grain boundaries represent obstacles for the dislocation and crack movement because significantly more energy is needed for a dislocation to change its slip system or to move into a differently oriented adjacent grain [41]. Since the grain boundary density across the region of ∼0.4–0.8 µm (Fig. A.5) does not change significantly, the hardness value remains also constant. Similar also a substitution of Ti atoms with Al atoms, up to about 10 at%, had obviously no significant influence on the hardness magnitude. Additionally, compressive in-plane strains in nanoceramics hinder crack growth between crystallites [11] and [42]. Additionally the constant in-plane strains (Fig. A.3c) had homogeneous influence on the hardness magnitude across the whole region of ∼0.4–0.8 µm.

In the region of ∼0.8–1.4 µm from the substrate surface, a monotonous decrease of *H* and *Er* is observed (Fig. A.5). This effect can be correlated with the accommodation of Al atoms into the crystal lattice [43] (Fig. A.1 and Fig. A.3) as well as with a pronounced grain coarsening visible in Fig. A.1a. The smaller concentration of grain boundaries and the presence of relatively large grains allow for easier dislocation motion (i.e. plastic deformation) in the imprint region because of a smaller concentration of crack obstacles.

In the relatively narrow region of ∼1.4–1.6 µm from the substrate, *H* and *Er* increase as a function of the increasing film thickness and then again decrease in the region from ∼1.6 to 1.8 µm (Fig. A.5) can be observed. The increase in hardness can be attributed to the presence of h-$Ti_{1-x}Al_xN$ nucleation layer (i) with relat-

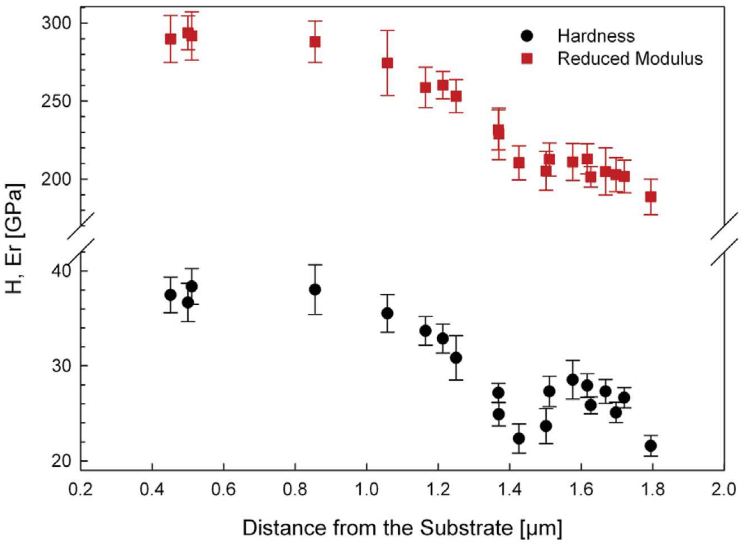

Figure A.5.: Hardness H and reduced Young's modulus E_r obtained from the nanoindentation experiments performed across the film cross-section.

ively small crystallites (Fig. A.1a), (ii) large compressive in-plane strain (Fig. A.3c) and (iii) large volume fraction of grain boundaries (Fig. A.1a) and expectedly large amount of defects in crystallite interiors (Fig. A.3a, b). As already discussed above, nanocrystalline microstructures with small crystallites, high density of grain boundaries, compressive strains and crystallographic defects in crystal interiors are very favorable for hardness response. The simultaneous occurrence of those microstructural features within the h-$Ti_{1-x}Al_xN$ nucleation layer (Fig. A.1) results in a very local synergic strengthening of the film due to the obvious energetically more expensive crack formation and growth under the indenter.

The further coarsening of the crystallites in the region above ~1.6 μm from the substrate (Fig. A.1a) results in a decrease of H due to the evolutionary development of the microstructure with larger grains which, as already discussed, influenced the crack nucleation and growth favorably.

A.4. Discussion on the complexity of the cross-sectional relationships

The reactive co-sputtering from Ti and Al targets with gradually varied power resulted in the formation of a 2 μm thick $Ti_{1-x}Al_xN$ film with pronounced compositional, microstructural and phase gradients, as revealed by TEM, EDS and XRD (Fig. A.1,

Fig. A.2 and Fig. A.3). Cross-sectional nanoindentation and bending tests on cantilevers machined from three different film depths demonstrated that also hardness, reduced Young's moduli, fracture stresses and Young's moduli significantly change across the film thickness (Fig. A.4 and Fig. A.5).

A comparison of the experimental data from the bending tests and the indentation analysis documents that the film compositional gradients (Fig. A.1), resulting in a complex distribution of crystalline phases (Fig. A.3), have a dominant influence on the cross-sectional dependence of the film mechanical properties. This conclusion can be made when comparing cross-sectional mechanical properties of the film from regions with similar microstructure but different composition. C–$Ti_{1-x}Al_xN$ phase occurring in the region of $\sim 0.4-0.8\,\mu m$ from the substrate surface (Fig. A.3) exhibited maximal hardness, fracture stresses and elastic moduli (cf. Table A.1 and Fig. A.4 and Fig. A.5). Although the region C possessed a similar microstructure as the region A, significantly smaller hardness values and moduli as well as fracture stresses were evaluated.

The variation of the film microstructure has a secondary effect on the local mechanical properties. The grain coarsening in c-$Ti_{1-x}Al_xN$ and h-$Ti_xAl_{1-x}N$ regions at the distances of $0.4-1.4$ and $1.7-2\,\mu m$ from the substrate surface, respectively, results in a decrease of hardness. In opposite, the formation of fine grained h-$Ti_xAl_{1-x}N$ nucleation regions is connected with the hardness increase caused by the presence of small grains in the examined region (Fig. A.2 and Fig. A.5). Also, the bending tests on the cantilevers from the region A demonstrated higher fracture stress (Table A.1) in comparison with the data obtained from the regions B and C. As already extensively discussed in Sec. 3.4, grain boundaries represent practically the most important microstructural strengthening component in nanoceramic films because they serve as obstacles for crack propagation [40].

To quantify the influence of in-plane residual strains presented in Fig. A.3c on the local mechanical properties is not trivial and has been discussed extensively in our previous study on epitaxial thin films [3], where the effect of grain boundaries was suppressed. In polycrystalline thin films, the strain variation is always very closely related to the film microstructure, especially to the grain size development. The hardness changes observed in Fig. A.5 could be thus interpreted not only by the microstructural evolution but also by the changes in the in-plane residual strain. Since, the bending experiments were performed on cantilevers without the presence of substrate-induced strain, the high values of fracture stresses of the cantilevers from region A (Table A.1) suggest that it is primary the film microstructure (grain size) which predefine fracture-stress as well as hardness behavior.

The X-ray nanodiffraction data (Fig. A.3a, b) allow to additionally assess the influence of the crystallographic texture on the mechanical behavior. Since in the region A, characterized by 100 fiber texture (Fig. A.3a, b), in-plane and out-of-plane directions are perpendicular to the (100) crystallographic planes of TiN crystallites, comparable values of the in-plane and out-of-plane moduli obtained from the bending tests and the nanoindentation, respectively, correlate well. Therefore, also the indentation data from Fig. A.5, which actually represent an average (not direction dependent) material elastic properties, can be considered as representative.

For c-TiN, however, the literature value of Young's modulus of 534 GPa along [100] direction from Ref. [44] is significantly higher than the experimentally found in-plane (Fig. A.5) and out-of-plane moduli (Table A.1, region A). The difference between the measured and literature values of the moduli could be interpreted by the polycrystalline nature of the film material with a high volume fraction of grain boundaries, which introduces a certain amount of porosity into the film.

Because of the h-AlN elastic anisotropy and the presence AlN 00.1 fiber texture, one would expect a difference in the in-plane (Fig. A.5) and out-of-plane (Table A.1) elastic response of the film in the C region. The reported literature values of AlN elastic moduli along [10.0] and [00.1] crystallographic directions are 297 and 325 GPa [45], respectively. The experimentally found values of Young's and reduced Young's moduli for h-AlN are however significantly smaller, in the range of $182-230$ GPa. Also here it is supposed that the significantly smaller magnitudes of the elastic moduli could be caused by the nanocrystalline nature of the region C with a high volume fraction of grain boundaries and a material porosity. Similar variation of elastic properties has been reported also for other nanocrystalline materials like W [46].

A.5. Conclusions

It was demonstrated that the understanding of the cross-sectional structure-property relationships of graded nanocrystalline thin films requires performing of complex position-resolved characterization of compositional, microstructural, phase and mechanical gradients across the film thickness with sub-micron resolution.

On the example of nanocrystalline graded Ti–Al–N thin film, it was demonstrated that the local mechanical properties are primarily influenced by the present crystalline phases and their intrinsic mechanical properties. Secondly, the local mechanical response is influenced by the film microstructure. The presence of nucleation layers with small crystallites and a high portion of grain boundaries as well as structural defects results in significant hardness enhancement. A gradual columnar grain growth results in a continuous hardness decrease. The influence of residual strain on the local mechanical response of the polycrystalline film is difficult to quantify absolutely, because its development is very strongly correlated with the local microstructure. The comparison of the results from the bending tests and cross-sectional hardness characterization suggests, however, that the role of microstructure is prevailing.

In summary, the results demonstrate an enormous importance of thin film microstructural, compositional and phase gradients, which, when correctly understood, can be used to effectively tune depth-resolved functional properties of nanocrystalline thin films.

Acknowledments

The authors acknowledge the financial support by the Christian Doppler Association in the framework of the Christian Doppler Laboratory for Application Oriented Coating Development and the companies Oerlikon Balzers Coating AG, Balzers (Liechtenstein) and PLANSEE Composite Materials, Lechbruck (Germany).

The nano-focus end-station was equipped through financial support by the German Federal Ministry of Education and Research (BMBF projects 05KS7FK3 and 05K10FK3) which is also greatly acknowledged. We thank the P03 team for provision of the beam to the nanofocus end station.

This work has received research funding from the European Union, within the large collaborative project ISTRESS, Grant Agreement No. 604646.

The authors are grateful to Mr. Bernhard Sartory from Materials Centre Leoben GmbH for fabricating TEM lamella.

Bibliography to paper A

[1] E. Arzt, *Acta Mater.* (1998) **46**, 5611–5626, DOI: `10.1016/S1359-6454(98)00231-6`.

[2] H. Gleiter, *Prog. Mater. Sci.* (1989) **33**, 223–315, DOI: `10.1016/0079-6425(89)90001-7`.

[3] R. Daniel, A. Zeilinger, T. Schöberl, B. Sartory, C. Mitterer, and J. Keckes, *J Appl Phys* (2015) **117**, 235301, DOI: `10.1063/1.4922666`.

[4] R. Daniel, K. Martinschitz, J. Keckes, and C. Mitterer, *Acta Mater.* (2010) **58**, 2621–2633, DOI: `10.1016/j.actamat.2009.12.048`.

[5] P. H. Mayrhofer, C. Mitterer, L. Hultman, and H. Clemens, *Prog. Mater Sci.* (2006) **51**, 1032–1114, DOI: `10.1016/j.pmatsci.2006.02.002`.

[6] M. Bartosik, R. Daniel, Z. Zhang, M. Deluca, W. Ecker, M. Stefenelli et al., *Surf. Coat. Technol.* (2012) **206**, 4502–4510, DOI: `10.1016/j.surfcoat.2012.02.035`.

[7] W. Oliver, and G. Pharr, *J Mater Res* (1992) **7**, 1564–1580, DOI: `10.1557/JMR.1992.1564`.

[8] S. Ulrich, C. Ziebert, M. Stueber, E. Nold, H. Holleck, M. Goeken et al., *Surf. Coat. Technol.* (2004) **188–189**, 331–337, DOI: `10.1016/j.surfcoat.2004.08.056`.

[9] C. Ziebert, C. Bauer, M. Stueber, S. Ulrich, and H. Holleck, *Thin Solid Films* (2005) **482**, 63–68, DOI: `10.1016/j.tsf.2004.11.117`.

[10] A. Zeilinger, R. Daniel, T. Schöberl, M. Stefenelli, B. Sartory, J. Keckes et al., *Thin Solid Films* (2015) **581**, 75–79, DOI: `10.1016/j.tsf.2014.10.106`.

[11] A. Riedl, R. Daniel, M. Stefenelli, T. Schöberl, O. Kolednik, C. Mitterer et al., *Scr. Mater.* (2012) **67**, 708–711, DOI: `10.1016/j.scriptamat.2012.06.034`.

[12] J. Keckes, M. Bartosik, R. Daniel, C. Mitterer, G. Maier, W. Ecker et al., *Scr. Mater.* (2012) **67**, 748–751, DOI: `10.1016/j.scriptamat.2012.07.034`.

[13] M. Stefenelli, R. Daniel, W. Ecker, D. Kiener, J. Todt, A. Zeilinger et al., *Acta Mater.* (2015) **85**, 24–31, DOI: `10.1016/j.actamat.2014.11.011`.

[14] M. Bartosik, R. Daniel, C. Mitterer, I. Matko, M. Burghammer, P. Mayrhofer et al., *Thin Solid Films* (2013) **542**, 1–4, DOI: `10.1016/j.tsf.2013.05.102`.

[15] S. PalDey, and S. Deevi, *Mater. Sci. Eng., A* (2003) **342**, 58–79, DOI: `10.1016/S0921-5093(02)00259-9`.

[16] C. Wüstefeld, D. Rafaja, V. Klemm, C. Michotte, and M. Kathrein, *Surface and Coatings Technology* (2010) **205**, 1345–1349, DOI: `10.1016/j.surfcoat.2010.07.057`.

[17] N. Schalk, C. Mitterer, J. Keckes, M. Penoy, and C. Michotte, *Surface and Coatings Technology* (2012) **209**, 190–196, DOI: `10.1016/j.surfcoat.2012.08.052`.

[18] P. Mayrhofer, A. Hörling, L. Karlsson, J. Sjölén, T. Larsson, C. Mitterer et al., *Appl Phys Lett* (2003) **83**, 2049–2051, DOI: `10.1063/1.1608464`.

[19] C. Krywka, H. Neubauer, M. Priebe, T. Salditt, J. Keckes, A. Buffet et al., *J Appl Crystallogr* (2012) **45**, 85–92, DOI: `10.1107/S0021889811049132`.

[20] A. P. Hammersley, S. O. Svensson, M. Hanfland, A. N. Fitch, and D. Hausermann, *High Pressure Res.* (1996) **14**, 235–248, DOI: `10.1080/08957959608201408`.

[21] M. Stefenelli, J. Todt, A. Riedl, W. Ecker, T. Müller, R. Daniel et al., *J Appl Crystallogr* (2013) **46**, 1378–1385, DOI: `10.1107/S0021889813019535`.

[22] R. M. Langford, and A. K. Petford-Long, *Journal of Vacuum Science & Technology A* (2001) **19**, 2186–2193, DOI: `10.1116/1.1378072`.

[23] M. Moser, D. Kiener, C. Scheu, and P. H. Mayrhofer, *Materials* (2010) **3**, 1573–1592, DOI: `10.3390/ma3031573`.

[24] D. Kiener, C. Motz, M. Rester, M. Jenko, and G. Dehm, *Materials Science and Engineering: A* (2007) **459**, 262–272, DOI: `10.1016/j.msea.2007.01.046`.

[25] C. Motz, D. Weygand, J. Senger, and P. Gumbsch, *Acta Materialia* (2008) **56**, 1942–1955, DOI: `10.1016/j.actamat.2007.12.053`.

[26] K. Matoy, H. Schönherr, T. Detzel, T. Schöberl, R. Pippan, C. Motz et al., *Thin Solid Films* (2009) **518**, 247–256, DOI: `10.1016/j.tsf.2009.07.143`.

[27] R. Daniel, J. Keckes, I. Matko, M. Burghammer, and C. Mitterer, *Acta Mater.* (2013) **61**, 6255–6266, DOI: `10.1016/j.actamat.2013.07.009`.

[28] I. Petrov, P. B. Barna, L. Hultman, and J. E. Greene, *Journal of Vacuum Science & Technology A* (2003) **21**, S117–S128, DOI: `10.1116/1.1601610`.

[29] I. A. Abrikosov, A. Knutsson, B. Alling, F. Tasnadi, H. Lind, L. Hultman et al., trans. by s, *Materials* (2011) **4**, 1599–1618, DOI: `10.3390/ma4091599`.

[30] D. Holec, R. Rachbauer, L. Chen, L. Wang, D. Luef, and P. H. Mayrhofer, *Surf. Coat. Technol.* (2011) **206**, 1698–1704, DOI: `10.1016/j.surfcoat.2011.09.019`.

[31] L. Karlsson, A. Hörling, M. Johansson, L. Hultman, and G. Ramanath, *Acta Materialia* (2002) **50**, 5103–5114, DOI: `10.1016/S1359-6454(02)00365-8`.

[32] I. Petrov, L. Hultman, U. Helmersson, J.-E. Sundgren, and J. Greene, *Thin Solid Films* (1989) **169**, 299–314, DOI: `10.1016/0040-6090(89)90713-X`.

[33] M. Adamik, P. Barna, and I. Tomov, *Thin Solid Films* (1998) **317**, 64–68, DOI: `10.1016/S0040-6090(97)00661-5`.

[34] P. Barna, and M. Adamik, *Thin Solid Films* (1998) **317**, 27–33, DOI: `10.1016/S0040-6090(97)00503-8`.

[35] S. Veprek, and A. S. Argon, *J. Vac. Sci. Technol., B* (2002) **20**, 650–664, DOI: `10.1116/1.1459722`.

[36] K. Kumar, H. V. Swygenhoven, and S. Suresh, *Acta Materialia* (2003) **51**, 5743–5774, DOI: `10.1016/j.actamat.2003.08.032`.

[37] E. Eiper, J. Keckes, K. J. Martinschitz, I. Zizak, M. Cabié, and G. Dehm, *Acta Mater.* (2007) **55**, 1941–1946, DOI: `10.1016/j.actamat.2006.10.052`.

[38] I. A. Ovid'ko, *Philos. Trans. R. Soc. London, Ser. A* (2015) **373**, 20140129, DOI: `10.1098/rsta.2014.0129`.

[39] I. Ovid'ko, and A. Sheinerman, *Acta Mater.* (2009) **57**, 2217–2228, DOI: `10.1016/j.actamat.2009.01.030`.

[40] I. Ovid'ko, and A. Sheinerman, *Scr. Mater.* (2009) **60**, 627–630, DOI: `10.1016/j.scriptamat.2008.12.028`.

[41] I. Ovid'ko, A. Sheinerman, and R. Valiev, *Scripta Materialia* (2014) **76**, 45–48, DOI: `10.1016/j.scriptamat.2013.12.012`.

[42] S. Massl, J. Keckes, and R. Pippan, *Acta Mater.* (2007) **55**, 4835–4844, DOI: `10.1016/j.actamat.2007.05.002`.

[43] D. Holec, F. Rovere, P. H. Mayrhofer, and P. B. Barna, *Scripta Materialia* (2010) **62**, 349–352, DOI: `10.1016/j.scriptamat.2009.10.040`.

[44] D. Holec, M. Friák, J. Neugebauer, and P. H. Mayrhofer, *Phys. Rev. B: Condens. Matter Mater. Phys.* (2012) **85**, 064101, DOI: `10.1103/PhysRevB.85.064101`.

[45] S. Saib, and N. Bouarissa, *Journal of Physics and Chemistry of Solids* (2006) **67**, 1888–1892, DOI: `10.1016/j.jpcs.2006.05.007`.

[46] H. Sun, Z. Song, D. Guo, F. Ma, and K. Xu, *Journal of Materials Science & Technology* (2010) **26**, 87–92, DOI: `10.1016/S1005-0302(10)60014-X`.

B

Combinatorial refinement of thin-film microstructure, properties and process conditions: iterative nanoscale search for self-assembled TiAlN nanolamellae

Jakub Zalesak[a,b,*], Juraj Todt[b,*], Reinhard Pitonak[c], Arno Köpf[c], Ronald Weißenbacher[c], Bernhard Sartory[d], Manfred Burghammer[e], Rostislav Daniel[a], Jozef Keckes[b]

[a]Department of Physical Metallurgy and Materials Testing, Montanuniversität Leoben, 8700 Leoben, Austria
[b]Department of Materials Physics, Montanuniversität Leoben, 8700 Leoben, Austria
[c]Böhlerit GmbH & Co. KG, 8605 Kapfenberg, Austria
[d]Materials Center Leoben GmbH, 8700 Leoben, Austria
[e]European Synchrotron Radiation Facility, 38043 Grenoble, France
[*]These authors contributed equally to this work

Abstract

Because of the tremendous variability of crystallite sizes and shapes in nanomaterials, it is challenging to assess the corresponding size-property relationships and to identify microstructures with particular physical properties or even optimized functions. This task is especially difficult for nanomaterials formed by self-organization, where the spontaneous evolution of microstructure and properties is coupled. In this work, two compositionally graded TiAlN films were (i) grown using chemical vapour deposition by applying a varying ratio of reacting gases and (ii) subsequently analysed using cross-sectional synchrotron X-ray nanodiffraction, electron microscopy and nanoindentation in order to evaluate the microstructure and hardness depth gradients. The results indicate the formation of self-organized hexagonal-cubic and

cubic-cubic nanolamellae with varying compositions and thicknesses in the range of 3-15 nm across the film thicknesses, depending on the actual composition of the reactive gas mixtures. On the basis of the occurrence of the nanolamellae and their correlation with the local film hardness, progressively narrower ranges of the composition and hardness were refined in three steps. The third film was produced using an $AlCl_3/TiCl_4$ precursor ratio of 1.9, resulting in the formation of an optimized lamellar microstructure with 1.3 nm thick cubic Ti(Al)N and 12 nm thick cubic Al(Ti)N nanolamellae which exhibits a maximal hardness of 36 GPa and an indentation modulus of 522 GPa. The presented approach of an iterative nanoscale search based on the application of cross-sectional synchrotron X-ray nanodiffraction and cross-sectional nanoindentation allows one to refine the relationship between (i) varying deposition conditions, (ii) gradients of microstructure and (iii) gradients of mechanical properties in nanostructured materials prepared as thin films. This is done in a combinatorial way in order to screen a wide range of deposition conditions, while identifying those that result in the formation of a particular microstructure with optimized functional attributes.

B.1. Introduction

In nanomaterials with crystallite sizes below 100 nm, the physical properties significantly differ from those of bulk materials. The properties of nanomaterials can be correlated with (i) the variation of lattice spacing and corresponding chemical bonding nature, especially at nanocrystal surfaces, and/or (ii) the large volume fraction of grain boundaries in polycrystalline materials [1, 2]. Owing to the tremendous variability of crystallite sizes and shapes in nanomaterials, it is not trivial to quantitatively evaluate the correlation between crystallite sizes and nanomaterial properties, the ‘size effect’ of physical properties.

Hard nanocrystalline thin films based, for example, on TiN, CrN and TiAlN (used in metal cutting applications) represent a typical example of a technological system in which small crystallites decisively contribute to enhanced functional properties such as high hardness, high wear resistance and toughness [3, 4]. In the case of thin films synthesized using physical and chemical vapour deposition (PVD and CVD), not only (i) specific phases but also (ii) the particular microstructure and (iii) the residual stress state play decisive roles in the functional behaviour of the film [5, 6]. Therefore the microstructural design is important, especially in the case of hard films where fracture toughness can be significantly enhanced by grain boundary engineering [6, 7].

In the case of PVD thin films prepared by magnetron sputtering, it is possible to control the microstructural development to a certain extent by varying the deposition parameters and conditions such as temperature, deposition rate, substrate bias and direction of incoming particles [7]. In particular, the application of intense ion bombardment can be used to synthesize materials of very complex microstructure far from thermodynamic equilibrium. However, in thin films whose microstructure is formed as a result of self-organization phenomena at or near thermodynamic equilibrium, like in the case of CVD thin films, it is not trivial (i) to identify deposition conditions resulting in the desired microstructure and subsequently (ii) to effectively tune functional properties [8].

In the context of characterizing very local structural properties of nanocrystalline thin films, the recently introduced technique of cross-sectional X-ray nanodiffraction has demonstrated the ability to assess volume-averaged crosssectional distributions of phases, microstructure and stresses in thin films [9, 10]. This new approach opened the way to correlate X-ray diffraction (XRD) data with the results from other techniques like crosssectional nanoindentation, to perform correlative nanoanalytics in order to determine structure-property relationships at the nanoscale. By achieving this milestone, it was for the first time possible to evaluate the role of distinct microstructural features in the mechanical response of thin films, as demonstrated in our previous study on a graded TiAlN thin film prepared by PVD [11].

The present work (i) introduces a new iterative combinatorial nanoscale approach which was used to (ii) characterize microstructured $\mathrm{Ti}_x\mathrm{Al}_{1-x}\mathrm{N}$ thin films prepared by CVD as a result of a self-organized growth from a gas phase. The specific film microstructure already introduced in our previous studies possesses a high volume fraction of self-assembled nanolamellae, which are formed as a result of oscillating chemical reactions during the growth [12, 13]. The aim of this work is to correlate the thickness and the composition of the nanolamellae, the local mechanical properties, and the deposition conditions in order to identify process conditions resulting in the formation of a nanolamellar film with a maximal hardness. For this purpose the combinatorial approach based on the combination of crosssectional synchrotron X-ray nanodiffraction and cross-sectional nanoindentation was developed and used to characterize compositionally graded $\mathrm{Ti}_x\mathrm{Al}_{1-x}\mathrm{N}$ films with varying nanolamellar periods.

B.2. Experiment

B.2.1. Thin Film Deposition

The $Ti_xAl_{1-x}N$ thin films characterized in this work were prepared in a Bernex MT-CVD-300 medium-temperature reactor using the process gases $AlCl_3$, $TiCl_4$, NH_3 and N_2 with H_2 as carrier gas [13]. For the deposition of the films on WC-Co (6 wt%) cemented carbide substrates, a deposition temperature of 1073 K and a total process pressure of 2.5 kPa were applied. For the deposition of graded films denoted as A and B, varying ratios of precursors $AlCl_3$ and $TiCl_4$ in the range of 0.6-2.75 were used, as shown in B.1. In order to evaluate the influence of (i) the substrate and (ii) the sequence of the applied $AlCl_3/TiCl_4$ ratios on the formation of the self-assembled thin films, films A and B were synthesized with decreasing and increasing $AlCl_3/TiCl_4$ ratios (B.1), respectively. For the deposition of the film denoted as C, a constant $AlCl_3/TiCl_4$ ratio of 1.9 was selected.

Film Label	Gas flow ratio range of $AlCl_3/TiCl_4$	Normaliyed Ti/Al atomic concentration ratio ranges	Film Thickness [µm]
A	$2.75 - 0.6$	$7:93 - 50:50$	8
B	$1.25 - 2.75$	$28:72 - 7:93$	9
C	1.9	$20:80$	3

Table B.1.: Basic process parameters used for synthesis of $Ti_xAl_{1-x}N$ films

B.2.2. Cross-Sectional X-ray Nanodiffraction

From all three thin films A, B and C, cross-sectional slices consisting of the substrate and the film with a slice thickness of 40 mm, a length of 4 mm and a height of 2 mm were prepared by mechanical polishing. The slices were analysed in transmission wide-angle diffraction geometry at the nanofocus extension of the ID13 beamline at the European Synchrotron Radiation Facility (ESRF) in Grenoble, France [14]. A monochromatic X-ray beam of energy $E = 13\,\mathrm{keV}$ was focused using a Fresnel zone plate, providing a beam with horizontal and vertical full widths at half-maximum (FWHMs) of 100 and 96 nm, respectively. The sample-detector distance was 9 cm. During the measurement, the thin-film slices were moved in the beam, applying a scanning step size (along the vertical z axis) of 100 nm, and Debye-Scherrer rings were collected for all cross-sectional thin-film z positions. The two-dimensional powder diffraction data were then treated using the software $FIT2D$ [15] in order to obtain intensity I versus Bragg angle Θ plots $I(\Theta)$. $I(\Theta)$ data obtained for various thin-film depths z were used to compile three-dimensional plots $I(\Theta, z)$.

Other details research describing cross-sectional X-ray nanodiffraction can be found in our previous reports [9, 16].

B.2.3. Cross-Sectional Nano-Indentation

Cross-sectional characterization of the mechanical properties of mechanically polished $\mathrm{Ti}_x\mathrm{Al}_{1-x}\mathrm{N}$ thin-film cross sections was performed using an atomic force microscope (Veeco Dimension 3100), which was equipped with a sharp diamond cube-corner tip controlled by a Hysitron Triboscope transducer in load-displacement mode. For the indenter calibration, monocrystalline sapphire (0001) was used. For all indents, a maximal load of 400 mN was applied [11]. The films were indented at various cross-sectional positions, and the measured load-displacement curves were used to evaluate the hardness $H(z)$ and indentation modulus $E(z)$ at various film depths z according to the Oliver & Pharr [17] method.

B.2.4. Cross-Sectional Transmission Electron Microscopy

The cross-sectional morphologies of the films were investigated using a Zeiss AURIGA scanning electron microscope equipped with an energy-dispersive X-ray spectroscopy (EDX) unit in order to evaluate concentration profiles (using built-in sensitivity factors) for Ti and Al across the films' thicknesses.

In order to obtain complementary information on the microstructural properties of the films, transmission electron microscopy (TEM) was employed. For this purpose, crosssectional TEM lamellae of samples A and C were machined using a focused ion beam milling workstation (Orsay Physics Cobra Z-05) attached to a Zeiss Auriga 60 Crossbeam field emission gun scanning electron microscope. The crosssectional TEM lamellae were glued onto a Cu TEM holder and subsequently polished to a thickness of about 30 nm. The TEM characterization was performed using an image-side-corrected JEOL JEM-2100F TEM system operated at 200 keV in both scanning transmission electron microscopy (STEM) and TEM mode. For the STEM imaging, a 0.7 nm spot size and a high-angle annular dark-field detector were used in order to visualize the Z contrast. The main aim of the TEM analysis was to resolve the nanoscale morphology and microstructure of the self-organized nanolamellae formed in the films.

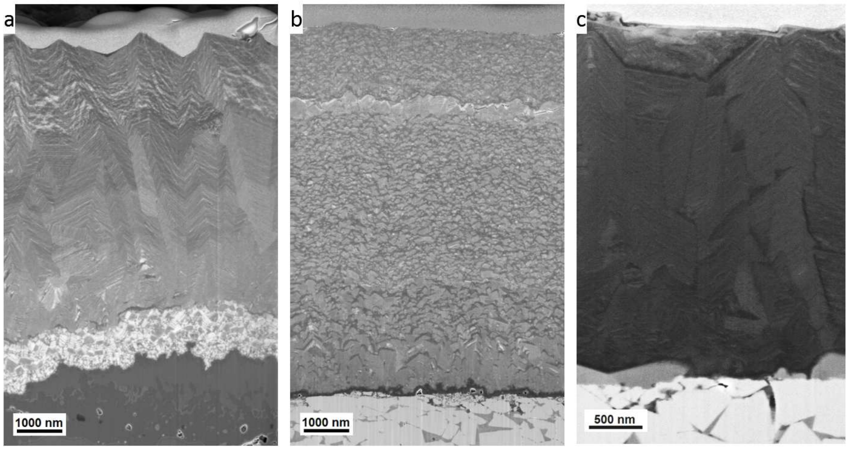

Figure B.1.: SEM micrographs showing cross sections of the analysed thin films A (*a*), B (*b*) and C (*c*) on WC-Co substrates. In films A and B, the variation of the deposition conditions during the film growth resulted in the formation of graded microstructure.

B.3. Results

B.3.1. Thin Film A

As already indicated in Sec. B.2.1, film A was prepared by using varying deposition conditions, namely the precursor ratio $AlCl_3/TiCl_4$ was changed in steps of about 0.1 during the deposition process (*cf.* Table B.1). In the region near the film-substrate interface, with a thickness of about $1.5\,\mu$m, film A possessed the composite grain microstructure (with small dark grains of various shapes and sizes embedded in a light matrix) visible in the scanning electron microscopy (SEM) image in Fig. B.1a. At distances greater than $1.5\,\mu$m from the interface, a columnar grain microstructure with a chevron-like morphology developed. SEM-EDX analysis indicated that the Ti/Al atomic concentration ratio in film A increased linearly towards the surface, in accordance with the variation of gas flow ratio, as presented in B.1.

The X-ray nanodiffraction phase plot $I(\theta, z)$ in Fig. B.2(*a*) indicates cross-sectional changes in the phase occurrence and the diffractions peak morphology in film A. At a distance of $\sim 0 - 2.3\,\mu$m from the film-substrate interface, diffraction peaks of hexagonal (h) and cubic (c) phases, h-100, h-002, h-101, h-102 and c-111, c-200 can be identified. At a distance of $2.3 - 8\,\mu$m from the interface, the hexagonal peaks diminish and only cubic phase peaks were recorded (*cf.* Fig. B.2*a*). Additionally, the FWHMs of the cubic peaks and the lattice parameter of the cubic phase significantly increased towards the surface. For instance, the FWHMs of the c-200 reflections

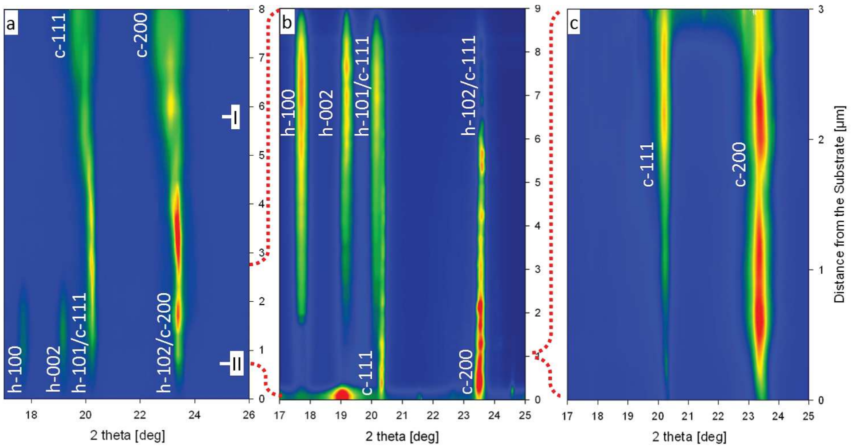

Figure B.2.: Phase plots $I(2\Theta, z)$ obtained using cross-sectional X-ray nanodiffraction from samples A (a), B (b) and C (c). Labels indicate the presence of hexagonal (h) and cubic (c) phases with the corresponding diffraction peaks. The transitions from hexagonal to cubic and from cubic to hexagonal phases occur at distances of 2.3 and 1 μm from the interface in (a) and (b), respectively. In the monolithic film C, only cubic peaks were observed. Positions I and II in (a) indicate regions for which the cross-sectional TEM micrographs in Figs. 3(a) and 3(b) and Figs. 4(a) and 4(b) were recorded, respectively. The dotted lines schematically indicate the iteratively narrowing phase, microstructure and process windows.

and the evaluated lattice parameters changed from 0.179 to 1.19 and from 0.4177 to 0.424 nm between the distances of 2.3 and 8 μm from the interface, respectively.

The cross-sectional positions denoted as I and II in Fig. B.2(a) indicate the approximate positions of the thin-film regions for which the cross-sectional TEM micrographs in Fig. B.3(a) and 3(b), respectively, were recorded. The bright-field TEM images in Fig. B.3, as well as additional TEM studies, documented that across the whole thin film thickness the film possesses a nanolamellar internal grain microstructure with a lamellae thickness of $\sim 3 - 15$ nm, visible as bright and dark lines in Fig. B.3.

The high-resolution (HR) TEM micrographs in Fig. B.4(a) and (b) were also collected, respectively, from the approximate cross-sectional positions denoted as I and II in Fig. B.2(a). The HR-TEM data as well as EDX analyses (not presented here) showed that the alternating bright and dark lamellae from Fig. B.3 actually consisted of AlN and TiN phases with a small fraction of Ti and Al atoms, respectively, at the interstitial positions, and therefore these will be further denoted as Al(Ti)N and Ti(Al)N lamellae. In all three films, the overall nitrogen concentration was approximately stoichiometric. Electron energy loss spectroscopy (not presented here), however, showed an oscillation of nitrogen concentration across the lamellae.

The HR-TEM analysis of the film (B.4(*b*) from position II (cf. B.2(*a*) indicated (i) that in this region film A consisted of cubic and hexagonal nanolamellae, giving rise to the hexagonal and cubic peaks in B.2(*a*), and (ii) that the interfaces between hexagonal Al(Ti)N and cubic Ti(Al)N lamellae were incoherent. HR-TEM data collected from film position I (cf. B.2(*a*) indicated that hexagonal lamellae were no longer present in the film, which is in agreement with the XRD data from B.2(*a*). This region of film A consisted of predominantly coherent c-Al(Ti)N and c-Ti(Al)N lamellae, shown in detail in B.4(*a*). The phase plot in B.2(*a*) and the TEM micrographs in B.4 suggest that, as a result of the increase in the relative amount of $TiCl_4$ precursor in the deposition chamber, only alternating c-Al(Ti)N

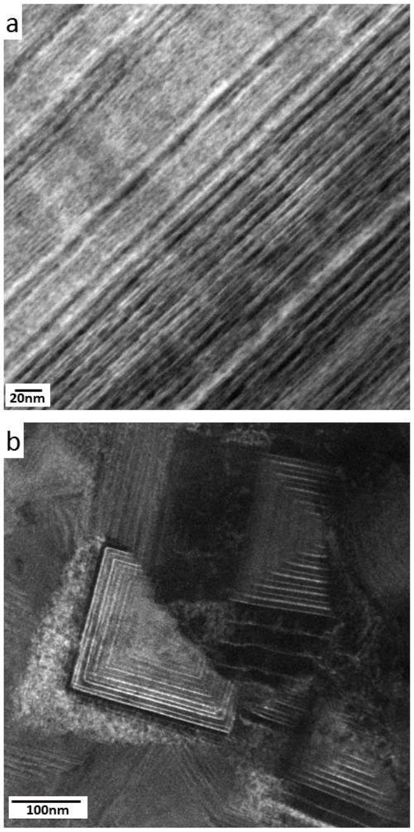

Figure B.3.: Bright-field TEM micrographs (*a*) and (*b*) were collected from film A at the cross-sectional positions denoted as I and II in B.2(*a*). The bright and dark lines represent Al(Ti)N and Ti(Al)N nanolamellae, respectively, whose thicknesses change across the film cross section in the range of 3-15 nm.

and c-Ti(Al)N lamellae were formed in the film at distances greater than 2.3 μm from the interface.

In order to correlate the microstructural information from Figs. B.1-B.4 with the local mechanical properties, cross-sectional nanoindentation experiments were performed on the film A. In Fig. B.5*a*, depth dependencies of indentation hardness $H(z)$ and indentation modulus $E(z)$ are presented. The results show that the maximum hardness of $\sim 35\,\text{GPa}$, as well as the maximum indentation modulus of $\sim 522\,\text{GPa}$, correspond to the A film region located at a distance ranging from about 2.3 µm to 4.5 µm from the substrate surface, where the hexagonal Al(Ti)N phase continuously changed to the cubic Al(Ti)N phase (*cf.* Fig. B.2*a*). Further film growth, dominated by the cubic Al(Ti)N phase, resulted in a slight decrease in hardness and

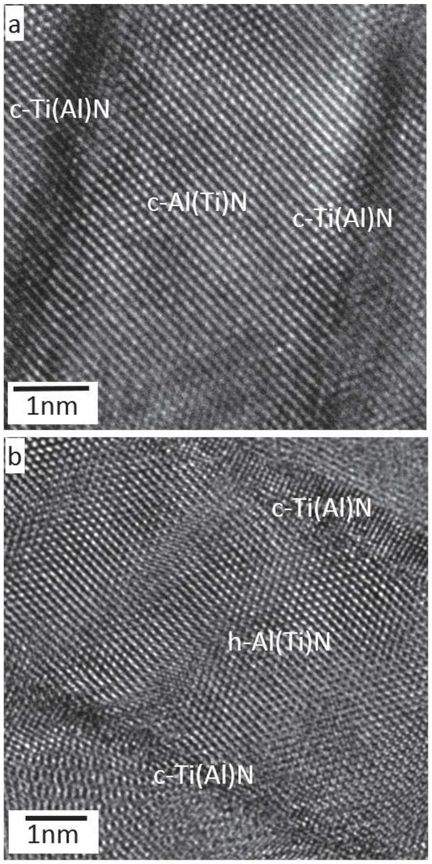

Figure B.4.: HR-TEM micrographs showing alternating (*a*) coherent c-Al(Ti)N and c-Ti(Al)N nanolamellae and (*b*) incoherent h-Al(Ti)N and c-Ti(Al)N nanolamellae in the film A at positions I and II (*cf.* Fig. B.2a).

indentation modulus. This observation obviously indicates that the cubic phase is beneficial for the mechanical properties of the film, as already reported by others [18, 19]. The formation of the film microstructure with the maximum hardness is therefore related to the extinction of the h-Al(Ti)N phase, while the Al content of the layer remains comparatively high at a distance of 2.3-4.5 µm from the interface (cf. B.2*a* and B.5*a*).

Since the main aims of this study were (i) to clarify the microstructure-property relationship and (ii) to identify deposition parameters resulting in the highest hardness, a new graded sample denoted as B was produced using a much narrower window of $AlCl_3/TiCl_4$ precursor ratio (cf. B.1). Thus a higher resolution for the precise identification of optimal microstructure, hardness and, ultimately, deposition process parameters was obtained.

B.3.2. Thin Film B

As documented in B.1, the precursor ratio in film B was increased during the deposition (contrary to film A) and therefore the variation of microstructure, phases and mechanical properties is expected to be inverted. The cross-sectional phase plot $I(2\theta, z)$ from sample B presented in Fig. B.2(b) indicates that, at a distance of $\sim 0 - 1$ µm from the substrate, only cubic diffraction peaks only cubic diffraction peaks [originating from c-Al(Ti)N and c-Ti(Al)N lamellae] were detected. The

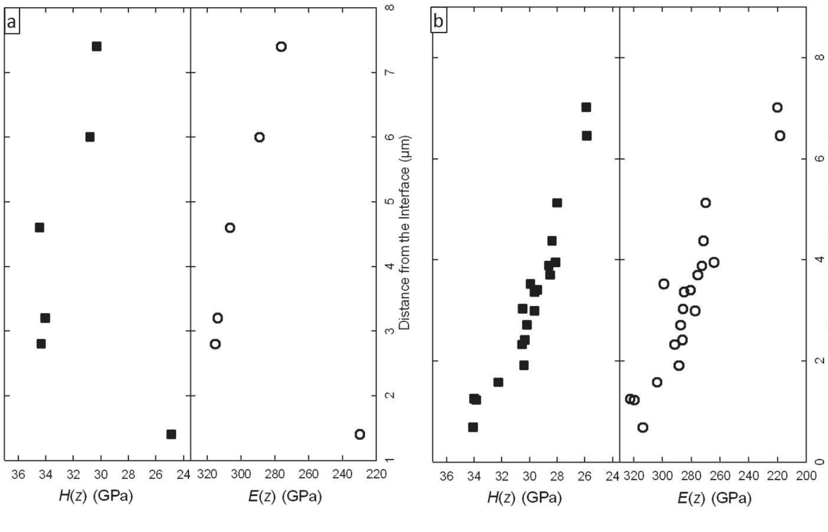

Figure B.5.: Cross-sectional dependencies of indentation hardness $H(z)$ and indentation modulus $E(z)$ in sample A (a) and B (b) possessing maxima at $z \cong 2.3$ and $z \cong 1.0$ µm, respectively.

formation of h-Al(Ti)N lamellae was observed at a distance of 1 µm and farther from the film-substrate interface. The corresponding depth dependencies of the indentation hardness $H(z)$ and elastic modulus $E(z)$ of the cross-sectional nanoindentation experiment performed on film B are shown in B.5(b). The maximum hardness and indentation modulus were observed at a distance of 1 µm from the interface, which corresponds to the cubic-hexagonal Al(Ti)N transition shown in the XRD data in B.2(b). In the film region dominated by the hexagonal phases, both hardness and elastic modulus decrease with increasing volume fraction of the hexagonal lamellae. SEM-EDX analysis indicated that the Ti/Al atomic concentration ratio in film B decreased linearly towards the surface, in accordance with the variation of gas flow ratio, as presented in B.1.

A comparison of (i) XRD data $I(2\Theta, z)$ from B.2(b), (ii) the crosssectional distributions of hardness $H(z)$ and indentation modulus $E(z)$ from B.4(b), and (iii) the recorded deposition process parameters allowed us to identify an $AlCl_3/TiCl_4$ precursor ratio of 1.9 as the most favourable process gas composition for the formation of (i) cubic Al(Ti)N nanolamellae with a maximum thickness of 12 nm and (ii) subsequently an AlTiN thin film with maximum hardness and elastic modulus. Finally, after the second iteration step, it was possible to synthesize a monolithic thin film with optimized mechanical properties (Sec. B.3.3).

B.3.3. Thin Film C

Sample C was synthesized using a constant $AlCl_3/TiCl_4$ precursor ratio of ~ 1.9, identified from the analysis of the graded sample B (Sec. B.3.2). For this reason, the sample possessed constant composition across the whole thickness, as documented by the cross-sectional phase plot $I(2\theta, z)$ in Fig. B.2(c). The intensity variation of the diffraction peaks in Fig. B.2(c) was caused by the crystallographic texture gradients associated with specific film-forming mechanisms during film growth. The observed c-111 and c-200 peaks in Fig. B.2(c) indicate a purely cubic thin film nature. SEM-EDX analysis indicated that the atomic concentration ratio of Ti/Al was 20:80 [20]. The HR-TEM micrograph of the film C in Fig. B.6 documents that the film consisted of alternating cubic Al(Ti)N and cubic Ti(Al)N nanolamellae with a thicknesses of ~ 12 and ~ 1.25 nm, respectively, in which interfaces between the lamellae were coherent, similar to the interfaces of the cubic region II of the film A (Fig. B.4b). Hardness and indentation modulus characterization of the film surface provided values of 36.6 and 522 GPa, respectively. It might be expected that film C would exhibit a certain cross-sectional variation of mechanical properties and

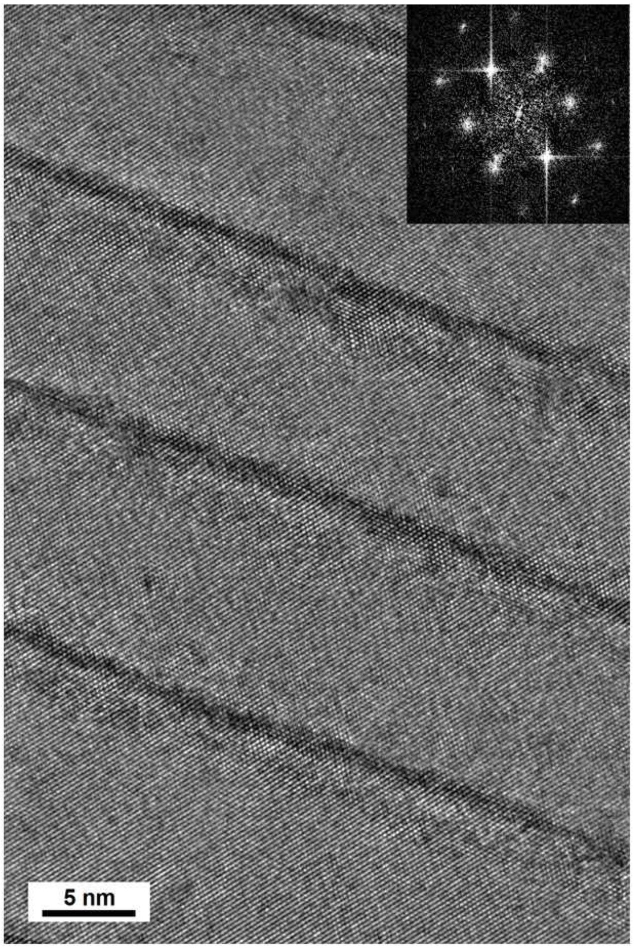

Figure B.6.: An HR-TEM micrograph showing alternating coherent c-Al(Ti)N and c-Ti(Al)N nanolamellae in the film C. An inset with a fast Fourier transformation indicates the presence of the only cubic phase within the probed volume.

internal grain microstructure, which can be attributed to the evolution of the CVD growth kinetics during the otherwise constant process conditions. The evaluation of this effect is, however, not in the focus of this combinatorial work.

B.4. Discussion

By the application of cross-sectional X-ray nanodiffraction, cross-sectional nanoindentation and TEM, it was possible to iteratively refine deposition conditions, resulting in the formation of an optimized TiAlN film with a specific nanolamellar microstructure composed of coherently arranged c-Ti(Al)N and c-Al(Ti)N nanolamellae with thicknesses of 1.25 and 12 nm, respectively. In particular, the presence of the c-Al(Ti)N phase was identified as very beneficial for the film's mechanical properties.

The phase plots in Figs. 2(*a*) and 2(*b*) document that an increase in the relative amount of $TiCl_4$ precursor in the deposition chamber gives rise to the formation of alternating cubic Al(Ti)N and Ti(Al)N lamellae in the films. Note that the AlN phase can exist under ambient conditions only in the hexagonal modification since the cubic polytype is metastable [18]. A first-order phase transition from hexagonal to cubic structure is observed for AlN at high pressure [21]. It is thus evident from the XRD diffraction data (B.2*a*) and from TEM investigations (B.4*a*) that cubic Ti(Al)N sublayers stabilized the Al(Ti)N lamellae and promoted the growth of a cubic (very probably metastable) Al(Ti)N phase in the films. This effect can be considered as epitaxial stabilization. The effect has already been reported in superlattice structures of CrN-AlN [22, 23], TiN-AlN [24, 25] and other [26–28] thin films deposited using molecular beam epitaxy and magnetron sputtering. In those cases, cubic AlN sublayers with a thickness in the nanometre rage were strain stabilized by surrounding cubic CrN or TiN sublayers. In the present case, however, the formation of cubic Al(Ti)N sub-lamellae occurs spontaneously, probably as a result of oscillating chemical reactions at the surface of the thin film during its growth [29]. The formation of the cubic Al(Ti)N phase is therefore a result of the specific deposition process giving rise to the formation of the distinct nanolamellar microstructure. This argument is supported also by the fact that the interfaces between the c-Al(Ti)N and c-Ti(Al)N nanolamellae are coherent (cf. B.4*a*). The presence of ternary c-Al(Ti)N and c-Ti(Al)N phases can also serve as an explanation for the formation of relatively thick cubic Al(Ti)N nanolamellae. This is because the relatively small concentration of Ti or Al atoms alloyed into AlN and TiN, respectively, will increase and reduce the Al(Ti)N and Ti(Al)N lattice parameters, respectively, which subsequently reduces the lattice strain needed for the stabilization of the cubic Al(Ti)N phase. Thus the cubic Al(Ti)N lamellae may have significantly greater thickness than pure c-AlN layers in CrN/AlN mutlilayers [23–25].

The crystallographic orientation relationship at the interfaces between incoherent cubic-hexagonal and coherent cubic-cubic lamellae from B.4 can be expressed as c-Ti(Al)- N(110)‖h-Al(Ti)N(10.0) and c-Ti(Al)N(100)‖c-Al(Ti)N(100), respectively. The reported literature values of c-AlN, h-AlN and c-TiN lattice parameters are 0.406, 0.437 and 0.424 nm, respectively [30, 31]. Consequently, an epitaxial growth of TiN on h-AlN and c-AlN (and vica versa, as observed in B.4) results in a lattice mismatch of 4.2 and 3.1 %. Such high mismatches lead usually to high interfacial energy and the formation of misfit dislocations. Therefore, in the case of incoherent c-Ti(Al)N/h-Al(Ti)N interfaces (cf. B.4*b*), a relatively large density of dislocations was observed (cf. B.4*b*), contrary to a very small number of defects at the coherent c-Ti(Al)N/ h-Al(Ti)N interfaces (cf. B.4*a*). The latter can be interpreted as the result of a smaller lattice mismatch between c-TiN and c-AlN and the presence Al and Ti atoms in the substitutional positions in the respective phases.

The correlation of the highest hardness with the greatest thickness of the cubic Al(Ti)N lamellae of 12 nm can be explained by the volume increase of 26 % during the cubic to hexagonal phase transformation [23]. It can be expected that during an indentation experiment, the cracks propagating in the brittle material under the indenter tip modify the local strain state and generate new free surfaces at the crack tip, allowing for a localized cubic to hexagonal phase transformation. Subsequently, the volume increase may result (i) in the formation of compressive strains at the crack tip, as well as (ii) in the absorption of the crack energy and (iii) in the crack deceleration, deflection or even termination. Whenever a free volume is generated at the crack tip, accompanied by a phase transformation, the effect of the volume increase should be larger in the vicinity of relatively thick cubic Al(Ti)N nanolamellae than in very thin cubic Al(Ti)N lamellae neighbouring comparatively thick cubic Ti(Al)N nanolamellae.

Another, maybe simpler, explanation might be that the nanolamellar composite can benefit most from the improved mechanical properties of cubic Al(Ti)N over its hexagonal counterpart, when the volume fraction of the cubic phase dominates. This, however, does not necessarily mean that the mechanical properties of cubic Al(Ti)N are better than those of cubic Ti(Al)N. Since with an increasing thickness of the cubic Al(Ti)N lamellae also lamellar compositions and thereby stabilizing lattice strains are altered, it is not unlikely that the maximal volume fraction of cubic Al(Ti)N leads to the most favourable residual stress state, resulting in the maximum hardness [32].

The advantage of the presented new methodological approach is the possibility to screen relatively large thin-film cross sections for novel microstructures as well as phases and to identify promising regions using fast X-ray nanodiffraction. The nanodiffraction scans in B.2 took less than 1 min each. This opens the possibility for high-throughput combinatorial structure-property refinement in nanomaterials. Although the TEM analysis was very beneficial for the understanding of the particular nanolamellar microstructure (Figs. 3 and 4), the actual correlation of the cross-sectional phase evolution (Figs. 2a and 2b) and physical properties (B.5) was achieved by the comparison of the XRD and nanoindentation data. The high-temperature behavior of the novel nanostructure was discussed in our previous report [20].

In the future, it can be expected that the search for novel nanomaterials using cross-sectional synchrotron X-ray nanodiffraction will be performed by analysing thick cross sections of graded thin films, which were deposited by employing the consecutive variation of much more than only one deposition parameter. In this way, (i) combinatorial and high-throughput screening of whole nanomaterial 'libraries' will be performed and (ii) deposition conditions resulting in the formation of novel materials will be identified.

Conclusions

A set of nanoscale experiments were used to search for the optimum phase composition, microstructure and mechanical properties of nanolamellar TiAlN thin films prepared under specifically selected process conditions. Using an iterative refinement of the structural and functional properties of cross sections of subsequently deposited thin films with progressively narrower structure-function-process windows, it was possible to identify (i) the film composition and microstructure resulting in optimized functional properties of the films and (ii) the corresponding process conditions.

The results demonstrate that, in self-organized TiAlN thin films, Al(Ti)N nanolamellae can spontaneously form in hexagonal and cubic modifications, while Ti(Al)N nanolamellae are always cubic. It has been observed that the film with the maximum hardness can be obtained when the cubic Al(Ti)N lamellae have a maximum thickness of 12 nm, while the thickness of Ti(Al)N is 1.3 nm. This microstructure has resulted in a hardness of 36 GPa.

Acknowledments

The authors greatly appreciate the support from the Austrian funding agency FFG within the project 841137; from the Austrian Federal Government (in particular from Bundesministerium für Verkehr, Innovation und Technologie and Bundesministerium für Wirtschaft, Familie und Jugend) represented by Österreichische Forschungsförderungsgesellschaft mbH; and from the Styrian and the Tyrolean Provincial Government, represented by Steirische Wirtschaftsförderungsgesellschaft mbH and Standortagentur Tirol, within the framework of the COMET Funding Programme. A part of the work has received research funding from the European Union, within the large collaborative project ISTRESS, grant agreement No. 604646. The nanodiffraction experiments were performed on the ID13 beamline at the ESRF, Grenoble, France. We are grateful to Dr Manfred Burghammer at ESRF for providing assistance in using beamline ID13.

Bibliography to paper B

[1] E. Arzt, *Acta Mater.* (1998) **46**, 5611–5626, DOI: 10.1016/S1359-6454(98)00231-6.

[2] H. Gleiter, *Prog. Mater. Sci.* (1989) **33**, 223–315, DOI: 10.1016/0079-6425(89)90001-7.

[3] S. Veprek, and A. S. Argon, *J. Vac. Sci. Technol., B* (2002) **20**, 650–664, DOI: 10.1116/1.1459722.

[4] S. Zhang, D. Sun, Y. Fu, and H. Du, *Surface and Coatings Technology* (2003) **167**, 113–119, DOI: 10.1016/S0257-8972(02)00903-9.

[5] S. Veprek, S. Mukherjee, P. Karvankova, H.-D. Männling, J. L. He, K. Moto et al., *J. Vac. Sci. Technol., A* (2003) **21**, 532–544, DOI: 10.1116/1.1558586.

[6] S. Zhang, H. L. Wang, S.-E. Ong, D. Sun, and X. L. Bui, *Plasma Processes and Polymers* (2007) **4**, 219–228, DOI: 10.1002/ppap.200600179.

[7] P. H. Mayrhofer, C. Mitterer, L. Hultman, and H. Clemens, *Prog. Mater Sci.* (2006) **51**, 1032–1114, DOI: 10.1016/j.pmatsci.2006.02.002.

[8] K. Choy, *Prog. Mater Sci.* (2003) **48**, 57–170, DOI: 10.1016/S0079-6425(01)00009-3.

[9] J. Keckes, M. Bartosik, R. Daniel, C. Mitterer, G. Maier, W. Ecker et al., *Scr. Mater.* (2012) **67**, 748–751, DOI: 10.1016/j.scriptamat.2012.07.034.

[10] M. Stefenelli, J. Todt, A. Riedl, W. Ecker, T. Müller, R. Daniel et al., *J Appl Crystallogr* (2013) **46**, 1378–1385, DOI: 10.1107/S0021889813019535.

[11] J. Zalesak, M. Bartosik, R. Daniel, C. Mitterer, C. Krywka, D. Kiener et al., *Acta Mater.* (2016) **102**, 212–219, DOI: 10.1016/j.actamat.2015.09.007.

[12] J. Keckes, R. Daniel, C. Mitterer, I. Matko, B. Sartory, A. Köpf et al., *Thin Solid Films* (2013) **545**, 29–32, DOI: 10.1016/j.tsf.2013.08.001.

[13] J. Todt, R. Pitonak, A. Köpf, R. Weißenbacher, B. Sartory, M. Burghammer et al., *Surf. Coat. Technol.* (2014) **258**, 1119–1127, DOI: 10.1016/j.surfcoat.2014.07.022.

[14] C. Riekel, M. Burghammer, and R. Davies, *IOP Conf Ser Mater Sci Eng* (2010) **14**, 012013, DOI: 10.1088/1757-899X/14/1/012013.

[15] A. P. Hammersley, *Journal of Applied Crystallography* (2016) **49**, 646–652, DOI: 10.1107/S1600576716000455.

[16] M. Bartosik, R. Daniel, C. Mitterer, I. Matko, M. Burghammer, P. Mayrhofer et al., *Thin Solid Films* (2013) **542**, 1–4, DOI: 10.1016/j.tsf.2013.05.102.

[17] W. Oliver, and G. Pharr, *J Mater Res* (1992) **7**, 1564–1580, DOI: 10.1557/JMR.1992.1564.

[18] P. Mayrhofer, A. Hörling, L. Karlsson, J. Sjölén, T. Larsson, C. Mitterer et al., *Appl Phys Lett* (2003) **83**, 2049–2051, DOI: 10.1063/1.1608464.

[19] S. PalDey, and S. Deevi, *Mater. Sci. Eng., A* (2003) **342**, 58–79, DOI: 10.1016/S0921-5093(02)00259-9.

[20] J. Todt, J. Zalesak, R. Daniel, R. Pitonak, A. Köpf, R. Weißenbacher et al., *Surface and Coatings Technology* (2016) **291**, 89–93, DOI: 10.1016/j.surfcoat.2016.02.027.

[21] M. Ueno, A. Onodera, O. Shimomura, and K. Takemura, *Phys. Rev. B* (1992) **45**, 10123–10126, DOI: 10.1103/PhysRevB.45.10123.

[22] J. Lin, J. Moore, B. Mishra, M. Pinkas, and W. Sproul, *Surf. Coat. Technol.* (2009) **204**, 936–940, DOI: 10.1016/j.surfcoat.2009.04.013.

[23] M. Schlögl, C. Kirchlechner, J. Paulitsch, J. Keckes, and P. Mayrhofer, *Scr. Mater.* (2013) **68**, 917–920, DOI: 10.1016/j.scriptamat.2013.01.039.

[24] M. Setoyama, A. Nakayama, M. Tanaka, N. Kitagawa, and T. Nomura, *Surface and Coatings Technology* (1996) **86–87, Part 1**, 225–230, DOI: 10.1016/S0257-8972(96)03033-2.

[25] A. Madan, I. W. Kim, S. C. Cheng, P. Yashar, V. P. Dravid, and S. A. Barnett, *Phys Rev Lett* (1997) **78**, 1743–1746, DOI: 10.1103/PhysRevLett.78.1743.

[26] M. Lattemann, S. Ulrich, H. Holleck, M. Stüber, and H. Leiste, *Diamond and Related Materials* (2002) **11**, 1248–1253, DOI: 10.1016/S0925-9635(01)00622-7.

[27] H. Söderberg, and M. O. T. L. L. H. J. M. Molina-Aldareguia, *Appl. Phys. Lett.* (2006) **88**.

[28] M. Stueber, H. Holleck, H. Leiste, K. Seemann, S. Ulrich, and C. Ziebert, *Journal of Alloys and Compounds* (2009) **483**, 321–333, DOI: 10.1016/j.jallcom.2008.08.133.

[29] K. Bartsch, A. Leonhardt, and E. Wolf, *Surf. Coat. Technol.* (1992) **54**, 193–197, DOI: 10.1016/S0257-8972(09)90049-4.

[30] W. Kohn, and L. J. Sham, *Phys. Rev.* (1965) **140**, A1133–A1138, DOI: `10.1103/PhysRev.140.A1133`.

[31] N. E. Christensen, and I. Gorczyca, *Phys. Rev. B* (1994) **50**, 4397–4415, DOI: `10.1103/PhysRevB.50.4397`.

[32] *Thin Films and Coatings: Toughening and Toughness Characterization*, ed. S. Zhang, CRC Press, (2015)

C

Peculiarity of Self-Assembled Cubic Nanolamellae in the TiN/AlN System: Epitaxial Self-Stabilization by Element Deficiency/Excess

J. Zalesak[1,2] , D. Holec[1], I. Matko[3], M. Petrenec[4], B. Sartory[5], N. Koutná[6,7], R. Daniel[1], R. Pitonak[8], J. Keckes[2],

[a]Department of Physical Metallurgy and Materials Testing, Montanuniversität Leoben, Leoben, Austria
[b]Department of Materials Physics, Montanuniversität Leoben, Leoben, Austria
[c]Institute of Physics, Slovak Academy of Sciences, Bratislava, Slovakia
[d]Tescan Brno s.r.o., Brno, Czech Republic
[e]Materials Center Leoben Forschung GmbH, Leoben, Austria
[f]Faculty of Science, Masaryk University, Brno, Czech Republic
[f]Institute of Materials Science and Technology, TU Wien, Vienna, Austria
[f]Boehlerit GmbH & Co KG, Kapfenberg, Austria

Abstract

Synthesis of self-assembled thin films with multi-layered microstructures and outstanding functional properties represents a challenging task. In this work, detailed microstructural and chemical analyses of a self-assembled ∼3.8 µm thick cubic (c) $(Al_xTi_{1-x})_yN_{1-y}$ film grown by low pressure chemical vapour deposition on a $Al_2O_3(0001)$ substrate is discussed. The film with an overall x fraction of ∼0.8 consists of alternating non-stoichiometric cubic Al-rich and Ti-rich nanolamellae with thicknesses of ∼11 and ∼1.5 nm. X-ray diffraction, electron microscopy and electron energy loss spectroscopy indicate that the nanolamellae coherency is primarily a result of an N deficiency in Ti-rich nanolamellae and an N excess in Al-rich nanolamellae, which induce a decrease and an increase in nanolamellae lattice parameters, compared to the lattice parameters of stoichiometric rock-salt c-TiN and c-AlN, respectively. Therefore the self-assembly allows a formation of c-$(\mathrm{Al}_x\mathrm{Ti}_{1-x})_y\mathrm{N}_{1-y}$ nanolamellae with Al atomic fraction x of 0.9-1.0, which are stabilized by neighbouring Ti-rich nanolamellae as a result of cube-on-cube epitaxy. The effect of the lattice parameter self-adjustment in the coherent nanolamellae by element deficiency and excess is verified by ab initio calculations. The compositional and morphological matches of the nanolamellae interfaces at the grain boundaries, the terraced growth with tetrahedral surface morphology and unzipped facets as well as the uniform nanolamellae thickness across the film depth indicate that the nanolamellae are formed as a result of kinetically-controlled oscillating reactions during the film growth. The understanding of this fascinating self-assembled nanolamellar microstructure containing a meta-stable c-AlN_y, which does not exist in a bulk form at ambient conditions, represents a milestone in thin film technology.

C.1. Introduction

In an effort to develop microstructured thin films and coatings with attractive mechanical properties, the main scientific focus of last years has concentrated on the refinement of composition, microstructure and residual stresses, on the exploitation of size effects of various physical properties and on the optimization of complex deposition routes [1–3]. A relatively little attention has, however, been devoted to develop unique microstructures and to achieve a new functionality by (i) utilizing synthesis methods based on self-assembly and/or (ii) incorporating crystalline polytypes with attractive physical properties, which normally do not exist at ambient conditions, like in the present case of non-stoichiometric cubic (c) AlN.

Metastable c-$(\mathrm{Al}_x\mathrm{Ti}_{1-x})_y\mathrm{N}_{1-y}$ thin films with rock-salt structure have attracted a significant attention in the last years due to their interesting high-temperature behaviour including spinodal decomposition [4] into c-TiN (B1) and metastable c-AlN (B1) structures, which further transform into stable hexagonal (h) AlN (B4) structure [5, 6]. This behaviour is even more interesting as it is accompanied by extensive hardening effect and subsequent hardness drop and film degradation above critical temperatures [6]. Numerous experimental works have however demonstrated that c-$(\mathrm{Al}_x\mathrm{Ti}_{1-x})_y\mathrm{N}_{1-y}$ polytype can be synthetized using physical vapour deposition (PVD) only for $x \lesssim 0.67$ and h-$(\mathrm{Al}_x\mathrm{Ti}_{1-x})_y\mathrm{N}_{1-y}$ structure with much less favourable mechanical properties is formed for higher Al contents during the deposition [5, 7]. The spinodal decomposition and the solubility limit were analysed in numerous theoretical works and have practical consequences for material functional properties [8–11].

On the other hand, in the case of $(\mathrm{Al}_x\mathrm{Ti}_{1-x})_y\mathrm{N}_{1-y}$ thin films prepared by chemical vapour deposition (CVD), monolithic cubic films with $x \cong 0.9$ were surprisingly reported [12]. Additionally, CVD $(\mathrm{Al}_x\mathrm{Ti}_{1-x})_y\mathrm{N}_{1-y}$ thin films consisting of alternating self-assembled c-TiN/h-AlN (for x=0.95) and c-TiN/c-AlN (for x=0.73, 0.8, 0.82) nanolamellae were observed. It was found that the self-assembled c-TiN and c-AlN nanolamellae with thicknesses in the range of 2-15 nm are highly non-stoichiometric and were therefore denoted as c-Ti(Al)N and c-Al(Ti)N [13–17]. The formation of CVD (i) c-$(\mathrm{Al}_x\mathrm{Ti}_{1-x})_y\mathrm{N}_{1-y}$ monolithic thin films with high Al amount of $x>0.67$ and (ii) nanolamellar c-Ti(Al)N/c-Al(Ti)N films is however not consistent with the numerical predictions as well as experimental observations for PVD films [5].

Though PVD routes provides many possibilities to synthetize thin films with nanoscale multi-layered modulations, CVD processes usually result in the formation of monolithic thin films. In the case of $(\mathrm{Al}_x\mathrm{Ti}_{1-x})_y\mathrm{N}_{1-y}$ CVD process, although there is no controlled alternation of processing gases, the self-assembled c-Ti(Al)N/c-Al(Ti)N nanolamellae possess very regular multi-layered microstructure and, despite of the high Al-content, they are cubic [13, 17]. However, (i) the microstructure and compositional gradients of the c-Ti(Al)N/c-Al(Ti)N nanolamellae as well as (ii) the mechanisms responsible for their formation have not been satisfactorily described yet. For the later, it was discussed that (i) oscillating chemical reactions could be responsible for the formation of nanolamellar microstructure during low pressure chemical vapour deposition (LPCVD) process [13] or (ii) spinodal decomposition takes place during the film growth [13, 16].

It is important to note, that AlN is expected to form under ambient conditions in the hexagonal B4 modification [18]. Up to now, a formation of cubic AlN rock-salt (B1) or zinc-blende (B3) structures was reported (i) during a first-order wurtzite-to-rocksalt phase transition at 22.9 GPa [19], (ii) in c-TiN/c-AlN and c-CrN/c-AlN superlatice structures prepared by magnetron sputtering and molecular beam epitaxy with c-AlN sublayer thickness $\lesssim$3 nm [20–22], (iii) during solid state reactions at annealed epitaxial Al/c-TiN interfaces with the c-AlN sublayer thickness of ~12-20 nm [23, 24] and (iv) during the growth on foreign substrates as a result of epitaxial stabilization [25]. In the early Petrov's and Hultman's studies on epitaxial Al/c-TiN interfaces [23, 24], however, the presence of zinc-blende structures was evaluated on the basis of the sublayer lattice parameters, which is expected to be ~0.438 compared to ~0.406 nm of the rock-salt structure [19, 21].

In this work, (i) very detailed microstructural and compositional analyses of the peculiar self-assembled coherent non-stoichiometric c-Ti(Al)N/c-Al(Ti)N nanolamellar microstructure prepared by the LPCVD process are carried out. Additionally, (ii) first-principles calculations analysing the influence of various element excess and deficiency in $(\mathrm{Al}_x\mathrm{Ti}_{1-x})_y\mathrm{N}_{1-y}$ system on the formation of "forbidden" crystalline polytypes are performed. Finally, the results (iii) allow drawing conclusions about possible mechanisms governing the nanolamellae formation and (iv) demonstrate the possibility to synthetize thick mutilayered hard films by the fast self-assembly process.

C.2. Methods

C.2.1. Experiment

An epitaxial c-$(\mathrm{Al}_x\mathrm{Ti}_{1-x})_y\mathrm{N}_{1-y}$ film with a thickness of ~3.7 µm was grown using LPCVD process on a monocrystalline $\mathrm{Al_2O_3}$(0001) substrate in a Bernex MT-CVD-300 medium temperature reactor at 800 °C and at a pressure of 2.5 kPa. The deposition rate in the presence of $\mathrm{AlCl_3}$, $\mathrm{TiCl_4}$ and $\mathrm{NH_3}$ as process gases and $\mathrm{N_2}$ and $\mathrm{H_2}$ as carrier gasses was ~10 µm/hour. In order to grow the thin film with exclusively cubic structure, the ratio of the $\mathrm{AlCl_3}/\mathrm{TiCl_4}$ precursors was set to 1.9.

For scanning electron microscopy (SEM) characterization and focused ion beam (FIB) machining, Zeiss AURIGA CrossBeam and Tescan GAIA3 workstations were used. Zeiss system was equipped with an energy dispersive X-ray spectrometer (EDX), which allowed to evaluate Ti and Al concentrations by using specific built-in sensitivity factors.

A cross-sectional TEM lamella with a thickness of ~50 nm for structural characterization was fabricated using Zeiss system applying an acceleration voltage of 30 kV and currents in the range from 20 nA to 50 pA. Another TEM lamella for electron energy loss spectroscopy (EELS) and energy dispersive X-ray spectroscopy (EDX) analyses with a thickness in the range of 10-100 nm was prepared by Tescan system using varying voltage and current conditions.

X-ray diffraction phase and texture analysis was performed using Rigaku SmartLab 5-circle diffractometer equipped with Cu-Kα radiation, a primary parabolic multilayer mirror and a secondary graphite monochromator. Cross-sectional transmission electron microscopy (TEM) was performed using a C_s-corrected JEOL JEM-2100F system operated at 200 kV. The qualitative and semi-quantitative compositional analysis by EELS and EDX was performed in a scanning TEM (STEM) mode using a probe-corrected FEI Titan Themis platform operated at 200 kV and equipped with a Gatan Enfinium ER spectrometer as well as FEI Super-X EDX four quadrant detectors. The collected EDX signal was treated using Bruker Esprit software applying built-in standards. The EELS spectra were recorded at dispersion of 1 eV/channel in order to use all 2000 eV spectrometer range for a simultaneous recording of signals for all elements, namely N (K) edge (401 eV), Ti (L_3, L_2) edges (456, 462 eV) and Al (K) edge (1560 eV). The entrance aperture was set to 5 mm. The convergence and collection semi-angles during acquisition were 25.0 and 19.4 mrad, respectively.

C.2.2. Calculations

First principles calculations within the framework of density functional theory were performed using Vienna Ab initio Simulation Package [26, 27] together with projector augmented method enabled pseudopotentials [28] and generalised gradient approximation [29] for the exchange-correlation potential. Simulation supercells consisted of 2x2x2 conventional cubic 8-atomic cells representing the B1 structure (double-face centred cubic lattice) and contained 32 N and 32 metal sites. Vacancies on either sublattice were distributed according to the quasi-random structure method [30] as previously employed for similar calculations in TaN and MoN systems [31]. The plane-wave cut-off energy set to 700 eV and Monkhorst-Pack k-mesh sampling of at least 13500 k-points per atom guarantee the total energy accuracy in the 1 meV/at range. All cells were fully relaxed with respect to atom positions, cell shape and volume. The cubic lattice parameter was estimated from the resulting supercell volume V as

$$a = \sqrt[3]{\frac{V}{8}} \tag{C.1}$$

.

C.3. Results

C.3.1. Microstructure

XRD scan collected from the film in symmetric XRD geometry shows cubic 111, 200 and 222 c-$(Al_xTi_{1-x})_yN_{1-y}$ reflections, from which the 200 reflection is very weak (Fig. 1a). The scan demonstrates that the film is composed of cubic structure, which grows on the substrate with a strong 111 texture. The 2θ values of the reflections lie (i) very close the tabulated values of the c-AlN reflections and (ii) between the c-AlN and c-TiN reflections. The peak profiles are asymmetric; possess a form of exponentially modified peak function, which can be attributed to (i) a variation of the lattice parameters and/or (ii) a certain kind of structural defects. The asymmetric film 222 reflection in Fig. 1a was fitted using exponentially-modified Gauss profile and the evaluated lattice spacing indicated a value of 4.0421 Å, which corresponds to the position of the intensity maximum of the 222 reflection and is very close to ∼4.06 Å of rock-salt AlN [18].

Complementary XRD pole figure analysis was used to determine the orientation-relationship between the film and the $Al_2O_3(0001)$ substrate (Fig. 1b). The cubic thin film grows evidently with (111) plane parallel to the substrate surface. Moreover, 111 and 200 pole figures with six-fold symmetry indicate a presence of two grain orientation variants, differing by 60 °, as schematically indicated in the crystal model of Fig. 1b showing two cubic crystals with always three {100} facets on (0001) face. A comparison of the substrate and film pole figures (Fig. 1b) allows to derive an orientation relationship of $Al_2O_3(0001)[01\bar{1}0] \parallel (Al_xTi_{1-x})_yN_{1-y}(111)[01\bar{1}]$ between the cubic film and the trigonal substrate.

SEM micrographs collected in an orthogonal view from the film surface show tetrahedral pyramidal structures representing surfaces of individual grains (cf. the text below) with two variants differing by 60 ° with respect to the film surface normal (Fig. 2), in agreement with the pole figures from Fig. 1b. Some tetrahedral facets exhibit distinct steps indicating that the facets might be formed by a step-wise lateral overgrowth from the gas phase. The estimated thickness of the facet steps (obtained from the SEM micrographs) is in the range of ∼10-30 nm. Since (i) the terrace structures progress towards the pyramid edges and (ii) the facets are in most cases unzipped at the edges, the nucleation of new layers appears to take place in the valleys of the tetrahedral structures and the lateral overgrowth proceeds towards the edges.

A cross-sectional thin film inner grain microstructure depicted in STEM bright field micrographs indicates a columnar grain growth (Fig. 3a) and a regular grain interior arrangement (Fig. 3b). All grains within the film exhibited lamellar microstructure. The central grain in Fig. 3b consists of alternating thin dark and thick bright sublayers, which correspond to the presence of heavy (Ti) and light (Al) elements and will be further denoted as nanolamellae. In Fig. S1 of Supplemental Data, bright field and HAADF micrographs indicate the internal nanolamellar microstructure of the grains from Fig. 3b in full resolution. The interfaces between the nanolamellae are parallel to {100} crystallographic planes and are altered along <100> crystallographic directions [as demonstrated by high-resolution TEM (HR-TEM)

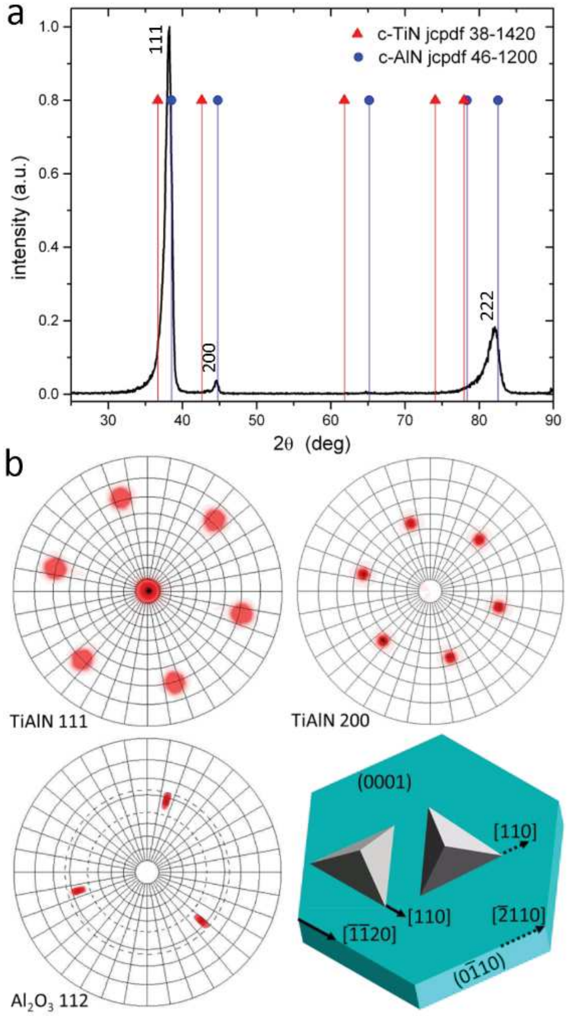

Figure C.1.: (a) XRD pattern from a ∼3.8 µm thick c-$(Al_xTi_{1-x})_yN_{1-y}$film on Al_2O_3(0001) substrate showing the cubic film structure, asymmetric hhh reflections and a presence of a strong 111 texture. The vertical lines indicate the peak positions of selected phases according to the database of Joint Committee on Powder Diffraction Standards (JCPDS) (b). Pole figures from the film and the substrate document a biaxial texture of the film with six-fold symmetry, which originates from two (111) cubic crystal orientation variations, as indicated by the model with always three {100} facets of two cubic crystals on (0001) face.

data below]. Within one grain, the nanolamellae interfaces exhibit systematically an orientation change by 90 ° (around <010> directions) resulting in a formation of very characteristic and, in each grain present, zig-zag morphologies. The tet-

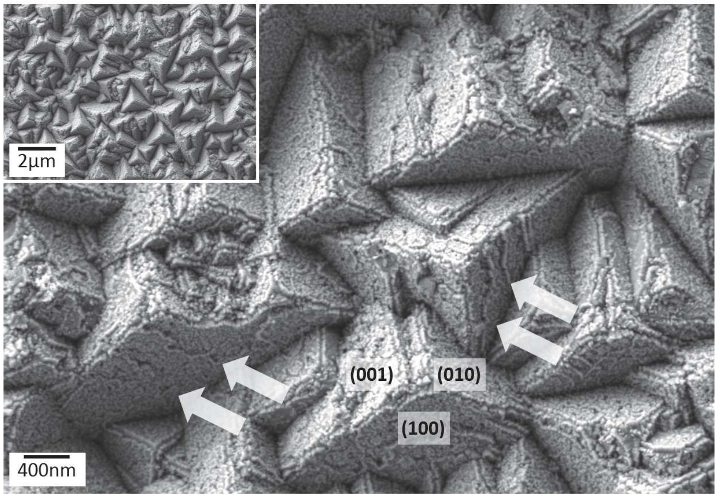

Figure C.2.: SEM micrographs of the c-$(Al_xTi_{1-x})_yN_{1-y}$ film surface show tetrahedral morphology, {100} facets with terraced growth indicated by arrows and unzipped edges of the pyramidal structures.

rahedral surface facets in Fig. 2 indicate obviously {100} faces being parallel to the {100} crystallographic planes in Fig. 3b. HR-TEM micrographs in Fig. S2 of Supplemental Data documents that the zig-zag morphology is not a result of crystallographic twinning because the grain regions on both sides of the mirror plane (passing through the zig-zag structure) possess approximately equal crystallographic orientation.

Remarkably, neither the film nor its individual columnar grains (Fig. 3) show any depth gradient of nanolamellae thicknesses and elemental composition, the latter being reflected by the contrast in the TEM micrograph. On the other hand, a certain variability of neighbouring nanolamellae thicknesses was observed especially at the grain boundaries, as shown in Fig. 4a. It is important however to note that the thicknesses and the sequences of the nanolamellae in neighbouring grains correlate (Fig. 4a). Despite the abrupt changes of the crystallographic orientation at the grain boundaries, as indicated by selected area electron diffraction (SAD) patterns in Fig. 4b, (Ti- and Al-rich) nanolamellae from different grains systematically meet at the grain boundaries and possess approximately the same thickness (Fig. 4a,b). The compositional and geometrical match of the nanolamellae at the grain boundaries supports the above suggestion that the nucleation of the new surface facet layers starts in the valleys of the tetrahedral structures (Fig. 2), which coincide with the boundaries of the columnar grains (Fig. 3b). This is probably because of (i) a higher temperature being present in the valleys and/or (ii) a spatial confinement

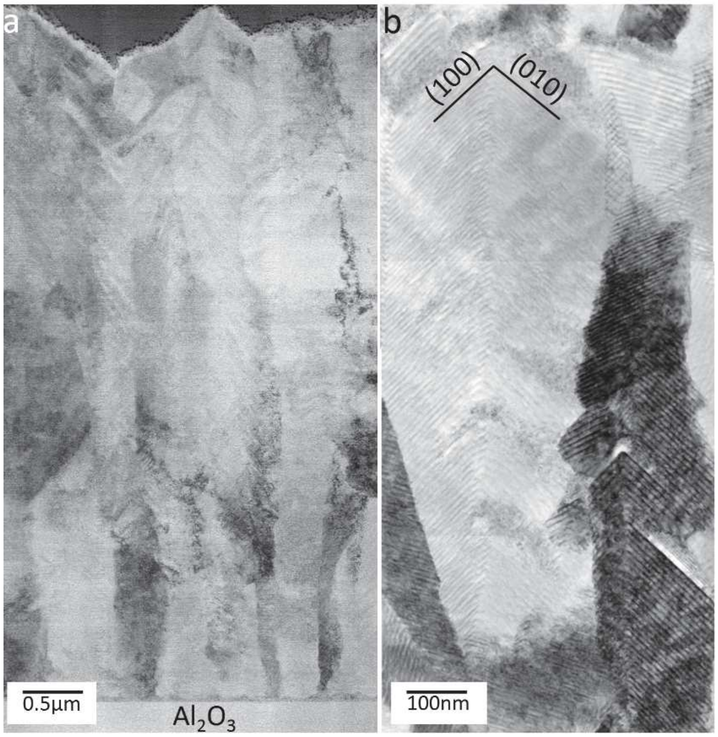

Figure C.3.: STEM micrographs document (a) a columnar film microstructure and (b) regular nanolamellar internal grain microstructure. The nanolamellae interfaces are parallel to the {100} planes. In Fig. S1 of Supplemental Data, the micrograph in (b) is presented in full resolution.

of the reactants during the film growth. Altogether, the above observations might suggest that the nanolamellae are formed during a self-organized growth from the gas phase as a result of sequential lateral overgrowth of the tetrahedral facets (Fig. 2).

In Fig. 5a, a Cs-corrected HR-TEM micrograph acquired along [110] zone indicates a presence of coherent thin (Ti-rich) and thick (Al-rich) nanolamellae with thicknesses of ∼1.5 and ∼11 nm, respectively. The coherency between the nanolamellae could be a result of a sequential epitaxial overgrowth of the facet surfaces indicated by the terrace morphologies in Fig. 2. A fast Fourier transformation (FFT) in Fig. 5b, based on the HRTEM micrograph (including thin and thick nanolamellae from Fig. 5a), documents a presence of cubic lattice whereby 111, 200 and 220 reflections show an anisotropic streaking. The stripes could be attributed to the presence of ordered lattice defects. A similar reflection streaking and a formation of additional reflections were observed in CrN_x defective layers of $CrN/CrN_x/Cr$

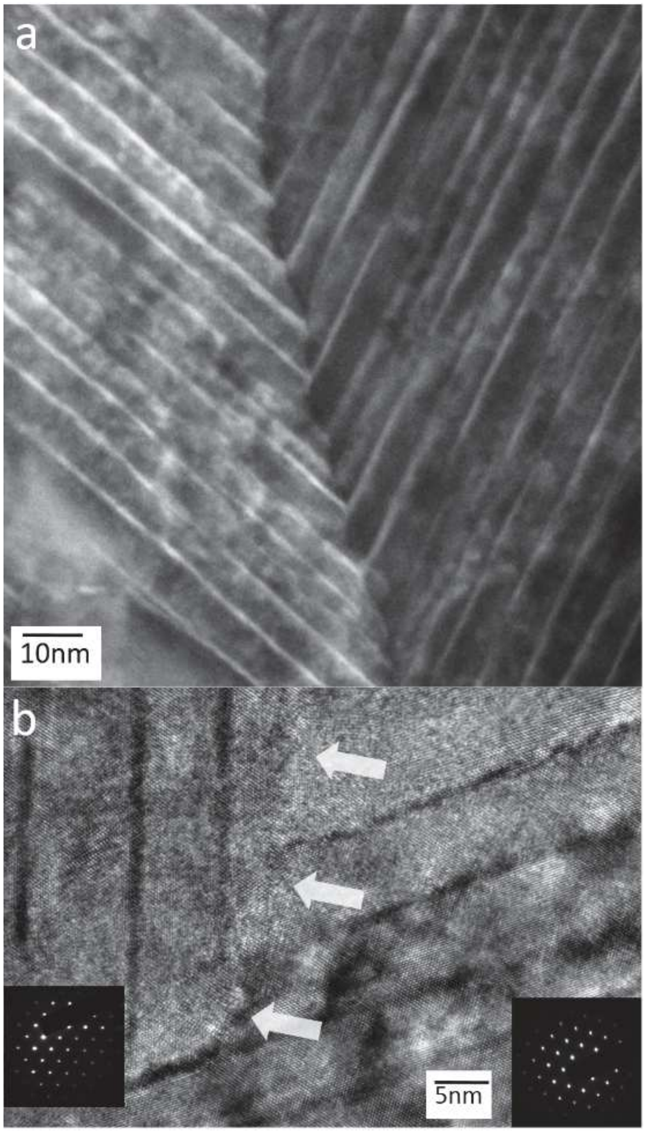

Figure C.4.: STEM micrographs collected from a grain boundary region indicating a compositional and morphological match between the nanolamellae of the neighbouring grains (a). Arrows in the HR-TEM image (b) show a grain boundary between two grains of different orientation, as indicated by SAD patterns.

system and was attributed to the presence of N vacancies in the lattice [32]. In the present case, it can be expected that the self-organized growth of the coherent nanolamellae results in the formation of locally ordered atomistic defects, such as interstitials and vacancies, which are responsible for the anisotropic streaking in the

FFT image (Fig. 5b).

Cs-corrected HR-TEM micrographs were used to determine lattice parameters of Ti-rich and Al-rich nanolamellae. For this reason, lattice spacings of both nanolamella types in HR-TEM data were evaluated by averaging lattice spacing of ∼20 atomic columns along <110> direction. Lattice parameter measurements was performed at five positions within one HR-TEM micrograph and the data were averaged. In Fig. 5c, a lattice parameter distribution across the nanolamellae indicates that the parameter shows a plateau in Al-rich region with a value of ∼4.075 nm and maximal values of ∼4.14 nm in Ti-rich regions, resulting in a lattice mismatch of ∼1.5 %.

HR-TEM analysis also indicated an epitaxial relationship between the film and the sapphire substrate. The film lattice was however relaxed after a few c-$(\mathrm{Al}_x\mathrm{Ti}_{1-x})_y\mathrm{N}_{1-y}$ monolayers were grown resulting in a formation of misfit dislocations. Since the formation of nanolamellae was observed also on polycrystalline substrates, it is not expected that the sapphire plays an important role in the nanolamellae formation. The pole figures from Fig. 1b, however, unambiguously document that the in-plane orientation of the c-$(\mathrm{Al}_x\mathrm{Ti}_{1-x})_y\mathrm{N}_{1-y}$ crystallites is influenced by the substrate.

C.3.2. Chemical analysis

The SEM-EDX analysis yielded an overall Al/Ti concentration ratio of the film of ∼0.8:0.2. However, as the Z-contrast of TEM micrographs in Figs. 3,4 revealed, concentration gradients across the nanolamellar microstructure are to be expected. Therefore, STEM EDX and -EELS analyses with high spatial resolution and chemical sensitivity were performed.

An EDX line scan was carried out in the direction perpendicular to the nanolamellae interfaces in a TEM lamella region with a thickness of ∼100 nm, which was slightly misaligned from [110] zone. The relatively thick TEM lamella is expected to provide better signal to noise ratio and the collected data thus represent volume-averaged quantities. The very oscillatory EDX profile with an absence of abrupt compositional transitions (Fig. 6), which could be expected on the basis of TEM micrographs from Figs. 3-5, can be interpreted by concentration gradients across the investigated 100 nm thick TEM lamella, which result in a EDX signal averaging and the profile smoothening. The averaged EDX line scan in Fig. 6 revealed that (i) the Al-to-Ti fraction periodically changes across the nanolamellae from ∼0.5:0.5 to ∼0.9:0.1, (ii) neighbouring nanolamellae exhibit always an unequal Al/Ti ratio and (iii) there exists a long-range modulation of the concentrations with

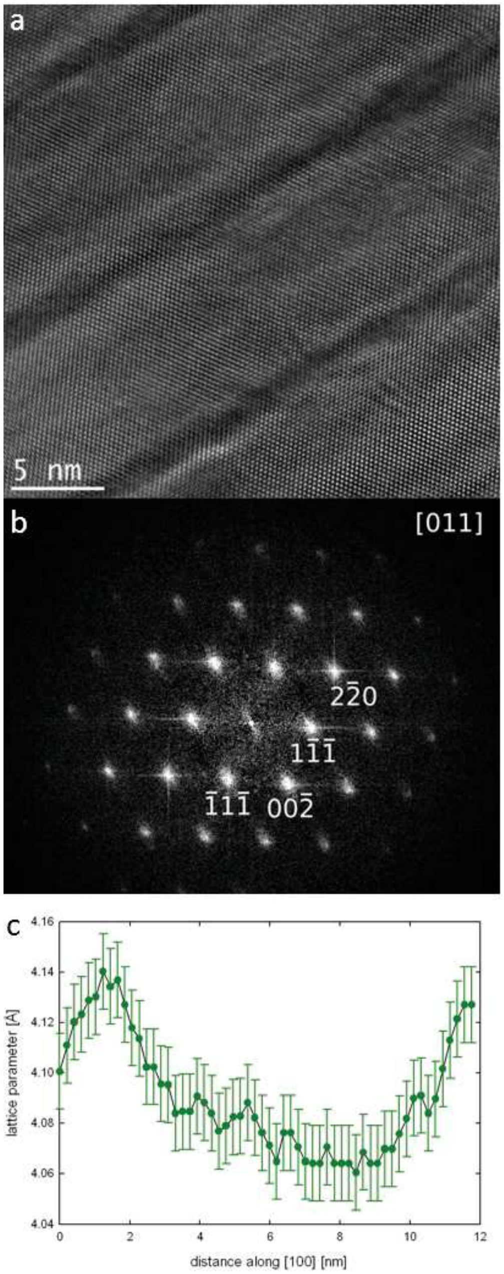

Figure C.5.: (a) HR-TEM image shows coherent Al- and Ti-rich nanolamellae of ∼11 and ∼1.5 nm, re (a). (b) FFT obtained from the whole micrograph indicates a cubic lattice and an anisotropic streaking of selected reflections. Lattice parameter development (c) across the nanolamellae (along a [100] direction) indicates a continuously varying lattice parameter.

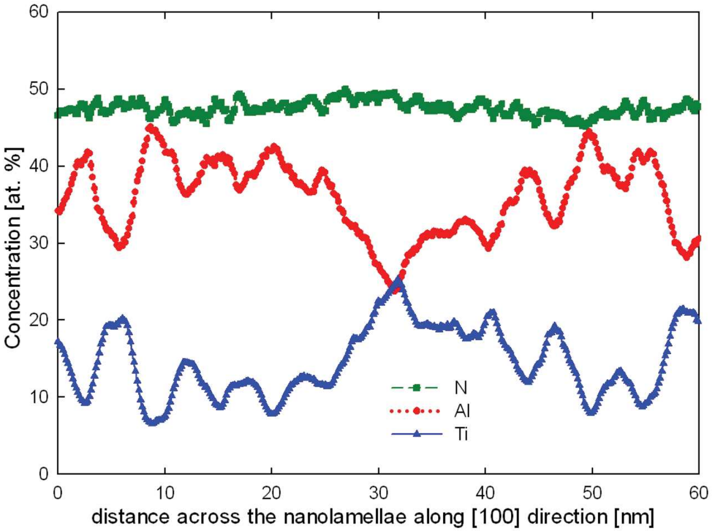

Figure C.6.: An EDX concentration profile collected from c-(AlxTi1-x)yN1-y film across the nanolamellae interfaces show average Al, Ti and N in a TEM lamella with a thickness of ~100 nm. The smooth profile is caused by the EDX signal being averaged across thick TEM probes possessing concentration gradients.

a period of ∼60 nm, which was concluded on the basis of a sample statistical analysis. The observation of the long-range compositional modulation, being observed very systematically across the whole thin film thickness, is likely to be a result of a self-organization phenomena present during the nanolamellae formation. The N-profile (Fig. 6) across the nanolamellae exhibited random concentration fluctuations y of 0.45-0.5. However, it should be noted that the EDX Kα peak of N (0.392 keV) is very close to the Lα peak of Ti (0.452 keV) and, because of the detector energy resolution of ∼150 eV, both peaks are merged in the EDX spectrum. Since a deconvolution procedure has to be implemented in order to resolve the N signal, the accuracy of the EDX N-analysis is significantly limited.

In order to get rid of the deficiency of the EDX analysis, a quantitative EELS line scan across the 15-20 nm thin region of the TEM lamella was recorded in the direction perpendicular to the nanolamellae interfaces in a single grain. Unlike the EDX data, the EELS line-scan in Fig. 7 documents abrupt changes in the evolution of Al, Ti and N concentrations across the thick Al-rich and thin Ti-rich nanolamellae in the c-$(\mathrm{Al}_x\mathrm{Ti}_{1-x})_y\mathrm{N}_{1-y}$ film. In the Al-rich nanolamellae, the metallic fraction x of Ti is below ∼0.1 and, in the Ti-rich thin sub-nanolamellae, the Al fraction is x∼0.54-1.0. Similarly to the EDX data from Fig. 6, also the EELS data indicate long-range composition oscillations, whereby the Al and Ti concentrations changed

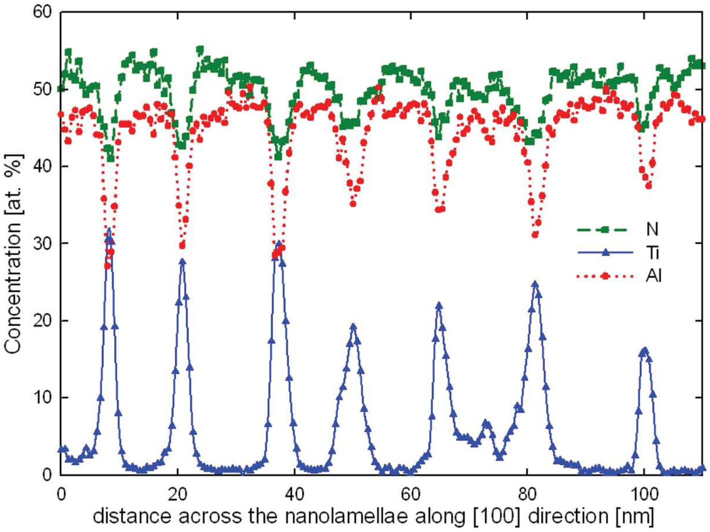

Figure C.7.: An EELS concentration profile collected from c-$(Al_xTi_{1-x})_yN_{1-y}$ film across the nanolamellae interfaces showing Al, Ti and N concentrations in a TEM lamella with a thickness of only ~15-20 nm. There is an N excess in thick (Al-rich) nanolamellae and an N deficiency in thin (Ti-rich) nanolamellae evident.

even between the neighbouring nanolamellae. Additionally and very remarkably, the N content changes periodically across the nanolamellae and there is (i) an N excess in thick Al-rich nanolamellae and (ii) an N deficiency in thin Ti-rich nanolamellae. The N deficiency in the thin Ti-rich nanolamellae is, however, inversely proportional to the Al content - the N content increases, with an increasing Al. These findings indicate that the Al, Ti and N concentrations change significantly within individual nanolamellae and there is an obvious correlation between the concentrations of the individual elements.

The evolution of the Al, Ti and N concentrations in the EELS line-scan from Fig. 7 differs however from those in the EDX line-scan (Fig. 6). The difference can be explained by the different thicknesses of the TEM lamellae used for the EELS and EDFX analysis. HAADF signal collected from various thin film regions exhibited (i) periodic long-range brightness fluctuations across several nanolamellae and (ii) even local brightness fluctuations within the individual nanolamellae, which can be interpreted by a variation of concentrations of heavy (Ti) and light (Al) atoms. Therefore, the signal from the relatively thick TEM lamella region of 100 nm in thickness selected for the EDX analysis represented only an average compositional information. On the other hand, EELS data from the 15-20 nm thin TEM lamella region showed very local concentration fluctuations, especially with respect to the N concentration.

C.4. Discussin

C.4.1. Lattice Coherency and Compositional Fluctuations

The complementary SEM, XRD and TEM analyses in Sec. 3 uncovered that (i) the nanolamellar c-$(Al_xTi_{1-x})_yN_{1-y}$ film grows with (111) planes parallel to the substrate surface and (ii) the surface morphology consists of two sets of mutually 60 ° misorientated tetrahedral pyramids with {100} facets being parallel to the {100} nanolamellae interfaces. The cross sectional microstructure revealed a set of nanolamellae with alternating chemistry and thicknesses, which are film depth-independent and continuous over neighbouring grains. XRD, HR-TEM, FFT and EELS analyses indicated a presence of (i) similar lattice parameters within thin (Ti-rich) and thick (Al-rich) nanolamellae (Fig. 5), (ii) lattice defects resulting in the anisotropic broadening of the XRD and FFT reflections (Figs. 1,6) and (iii) concentration oscillations with N excess and deficiency in Al- and Ti-rich nanolamellae (Fig. 7), respectively.

The presence of the relatively small lattice mismatch of ∼1.5 %, which is gradually accommodated across the nanolamelae along the <100> directions, as the continuous lattice parameter development across the compositionally distinct layers in Fig. 5c indicates, is a remarkable result. Usually, a strain of ∼4.3 % corresponding to the difference in the lattice parameters of c-TiN (a=4.24nm) and c-AlN (a=4.06nm) can be expected at the interface between both phases in the case of cube-on-cube epitaxy [21]. Significant coherency strains were reported also for other superlattice systems [20, 21, 33]. Nevertheless, the EELS analysis showing an N deficiency and an excess in Ti- and Al-rich nanolamellae (Fig. 7), respectively, provides a hint that the formation of coherent nanolamellae with the low coherency strains might be related to the film non-stoichiometry.

For this reason, ab initio predicted compositionally dependent lattice constants of c-$(Al_xTi_{1-x})_yN_{1-y}$ crystal structures containing metal as well as N vacancies and interstitials were evaluated (Fig. 8) [34]. As expected, interstitial defects like N in c-AlN_y and c-TiN_y, Ti in c-Ti_zN and Al in c-Al_zN increase the lattice parameter (Fig. 8). On the other hand, N vacancies in TiN_y and Ti vacancies in Ti_zN decrease the lattice parameter; an effect more significant for the metal vacancies. Surprisingly and remarkably, however, the Al vacancies in c-Al_zN are predicted to keep the lattice

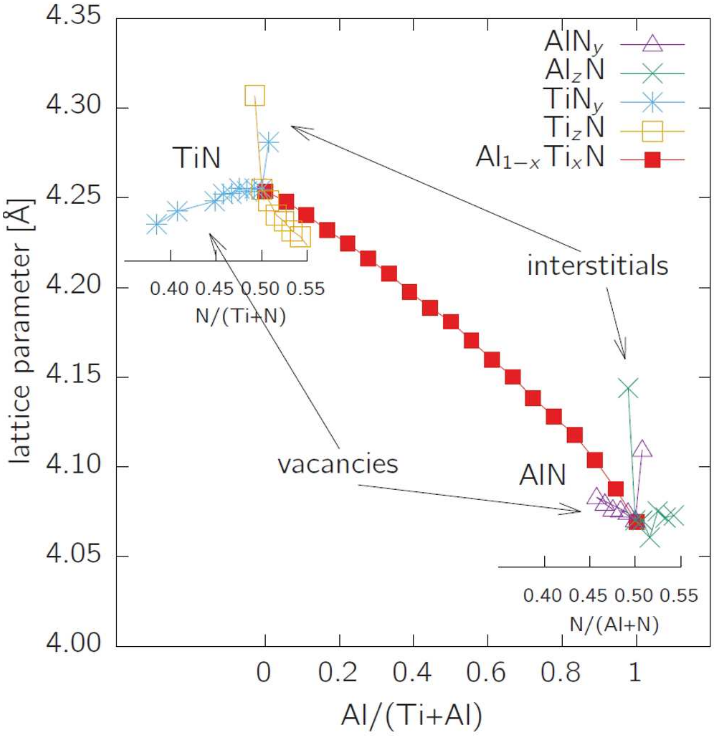

Figure C.8.: Ab-initio calculated lattice parameters for various c-$(Al_xTi_{1-x})_yN_{1-y}$ structures containing metal and N vacancies as well as interstitials. Interstitial defects like N in c-AlN$_y$ and c-TiN$_y$, Ti in c-Ti$_z$N and Al in c-Al$_z$N evidently increase the lattice parameter. On the other hand, N vacancies in TiN$_y$ and Ti vacancies in Ti$_z$N decrease the lattice parameter. Remarkably, N vacancies in c-AlN$_y$ increase the lattice parameter with respect to the stoichiometric c-AlN.

parameter almost constant or slightly increase it with respect to the stoichiometric c-AlN. Consequently, in the case of non-stoichiometric N-rich c-AlN nanolamellae (Fig. 7), no matter what type of defects is responsible for the off-stoichiometry, the lattice parameter is larger than that of stoichiometric c-AlN (Fig. 8).

Since the EELS spectra revealed the N deficiency in Ti-rich sub-lamellae and the N excess in Al-rich sub-lamellae (Fig. 7), the self-assembled nanolamellae non-stoichiometry caused a decrease and an increase in the lattice parameters of thin Ti-rich and thick Al-rich nanolamellae compared to the lattice parameters of stoichiometric c-TiN and c-AlN, respectively.

Consequently, the ab initio data from Fig. 8 document that the observed N modulations across the nanolamellae with various Al/Ti ratios presented in Fig. 7 effectively minimise the lattice mismatch between Al- and Ti-rich nanolamellae. In other words, the coherency strains and strain energy are expected to be effectively reduced by the film compositional modulations which are expected to contribute primarily to the stabilization of the nanolamellar microstructure.

The effect of point defects, especially the N deficiency in c-$(\mathrm{Al}_x\mathrm{Ti}_{1-x})_y\mathrm{N}_{1-y}$ structures, has been extensively studied with regard to the spinodal decomposition in PVD films by others [9, 10, 31]. Though the theoretical studies suggested that the vacancies on metal and/or non-metal sites only slightly affect the cubic to hexagonal transition region in c-$(\mathrm{Al}_x\mathrm{Ti}_{1-x})_y\mathrm{N}_{1-y}$ system [9], the recent experimental findings from PVD thin films [10] have indicated that the N deficiency clearly reduces the driving force for a transformation of c-$(\mathrm{Al}_x\mathrm{Ti}_{1-x})_y\mathrm{N}_{1-y}$ into hexagonal polytype. This result well correlates with the present observations, which show that the c-$(\mathrm{Al}_x\mathrm{Ti}_{1-x})_y\mathrm{N}_{1-y}$ non-stoichiometry plays a crucial role in the stabilization of the cubic structure of Al-rich sub-nanolamellae.

Up to now, an intentional epitaxial stabilization of c-AlN sublayers has been reported for CrN/AlN and TiN/AlN systems produced by magnetron sputtering and molecular beam epitaxy [20, 21, 33]. It has been found that the stabilization is possible only for c-AlN with critical thicknesses in the range of 2-3 nm. Above this threshold, AlN was found to exist only in the hexagonal state. The present observations clearly document that even thicker c-AlN_y layers (with Al/Ti ratio of $\sim$1:0) are stable at ambient conditions as a result of (i) cube-on-cube epitaxy of non-stoichiometric c-TiN/c-AlN as well as (ii) N deficiency and excess in neighbouring Ti- and Al-rich sub-nanolamellae, respectively.

C.4.2. Note on Possible Self-Assembly Mechanisms

A remaining and still puzzling question is what is the driving force for the self-assembly of the coherent nanolamellae in the CVD reactor (Figs. 3-5). Already in the first work on the self-assembled h-AlN/c-TiN system, it was suggested that the nanolamellae formation can be a result of (i) a phase separation at the deposition temperature via surface diffusion or (ii) kinetically-controlled oscillating reactions at the film surface [13]. Recently, Praseuth et al. [35] argued that the nanolamellae are products of spinodal decomposition, which occur during film growth. Although a driving force for such process certainly exists in the c-$(\mathrm{Al}_x\mathrm{Ti}_{1-x})_y\mathrm{N}_{1-y}$ system, in accordance with the equilibrium thermodynamics and had been numerously reported in the literature for the monolithic c-$(\mathrm{Al}_x\mathrm{Ti}_{1-x})_y\mathrm{N}_{1-y}$ films in the past [6], the evidences accumulated in this paper suggest that it is unlikely the case of the structures discussed here. For example, if the nanolamellae were products of spinodal decomposition due to a high thermal load during the deposition process, they would have likely possessed different thicknesses as a result of different exposures to the high temperature (because film regions closer to the film/substrate interface are in principal exposed to the high temperature over longer time allowing thicker nanolamellae to develop). This is not the case as demonstrated by the cross-sectional micrograph in Fig. 3b. Similarly, if the nanolamellae would have been formed by the spinodal process, proceeding independently in each grain, the development of nanolamellae interfaces perfectly geometrically and compositionally matching at the grain boundaries would have been highly unlikely (Fig. 4a).

Therefore, the formation of the compositional variations in the form of nanolamellae is most likely a consequence of (non-equilibrium) kinetically controlled oscillatory reactions at the film surface during the CVD growth as suggested by Bartsch et al. [36]. Moreover, it is believed that the microstructure of the nanolamellae is controlled by a sequential epitaxial overgrowth of {100} facets (Fig. 2) by individual Al- and Ti-rich sub-layers. Since the system tends to minimize the free energy, the CVD process results in the self-adjustment of the nanolamellae composition and lattice parameters in order to minimize the crystallographic mismatch and form the coherent microstructure.

In conclusion, we suggest that the resulting microstructure of the alternating Al-rich and Ti-rich nanolamellae is a frozen-in record of a complex oscillatory reactions taking place during the CVD process rather than a product of a spinodal decomposition taking place during the film synthesis.

C.5. Conclusions

The XRD, electron microscopy, EDX and EELS techniques were used to characterize the morphology, microstructure and chemistry of the self-assembled alternating cubic Al- and Ti-rich nanolamellae. We demonstrate that the nanolamellae coherency is a result of the N deficiency in Ti-rich sub-lamellae and the N excess in Al-rich sub-lamellae, which are responsible for the small crystallographic mismatch between the cubic nanolamellae, respectively. The self-assembly allows a local formation of c-AlN_y nanolamellae with a thickness of $\sim$11 nm and with Al/(Al+Ti) content of 0.9-1, which are stabilized by cube-on-cube epitaxy by neighbouring Ti-rich nanolamellae. The film morphology, compositional and morphological nanolamellae coherency at the grain boundaries and a homogenous nanolamellae thickness across the film depth suggest that the nanolamellae are formed during film growth very likely as a result of kinetically-controlled oscillating reactions.

The microstructures reported here are absolutely fascinating because of the self-assembly processes, i.e. spontaneous formation of the well-defined superlattice structure without external control. Based on the detailed microstructural and compositional characterisation of the self-assembled structures, the development of alternating Al-rich and Ti-rich nanolamellae within the c-$(\mathrm{Al}_x\mathrm{Ti}_{1-x})_y\mathrm{N}_{1-y}$ film is suggested to be self-controlled by complex oscillatory reactions proceeding during the CVD process rather than to be a product of a spinodal decomposition taking place during the film synthesis. The insights and hypotheses provided in this communication shall serve as a motivation for follow-up research on a detail description and understanding of the oscillatory reactions in such microstructure as well as on a synthesis of similar nanolamellar materials.

Acknowledments

The analytical part of this work has received research funding from the European Union, within the collaborative project ISTRESS, Grant Agreement No. 604646. The computational results presented have been achieved in part using the Vienna Scientific Cluster (VSC). Access to computing and storage facilities owned by parties and projects contributing to the National Grid Infrastructure MetaCentrum, provided under the programme "Projects of Large Research, Development, and Innovations Infrastructures" (CESNET LM2015042), is also greatly appreciated. A part of this work was supported by the FFG Project No. 841137 “CVDnanoCOAT”.

Bibliography to paper C

[1] P. H. Mayrhofer, C. Mitterer, L. Hultman, and H. Clemens, *Prog. Mater Sci.* (2006) **51**, 1032–1114, DOI: 10.1016/j.pmatsci.2006.02.002.

[2] E. Arzt, *Acta Mater.* (1998) **46**, 5611–5626, DOI: 10.1016/S1359-6454(98)00231-6.

[3] I. Petrov, P. B. Barna, L. Hultman, and J. E. Greene, *Journal of Vacuum Science & Technology A* (2003) **21**, S117–S128, DOI: 10.1116/1.1601610.

[4] J. W. Cahn, *Acta Metallurgica* (1962) **10**, 179–183, DOI: 10.1016/0001-6160(62)90114-1.

[5] S. PalDey, and S. Deevi, *Mater. Sci. Eng., A* (2003) **342**, 58–79, DOI: 10.1016/S0921-5093(02)00259-9.

[6] P. Mayrhofer, A. Hörling, L. Karlsson, J. Sjölén, T. Larsson, C. Mitterer et al., *Appl Phys Lett* (2003) **83**, 2049–2051, DOI: 10.1063/1.1608464.

[7] R. Rachbauer, S. Massl, E. Stergar, D. Holec, D. Kiener, J. Keckes et al., *J Appl Phys* (2011) **110**, 11, DOI: 10.1063/1.3610451.

[8] D. Seol, S. Hu, Y. Li, J. Shen, K. Oh, and L. Chen, *Acta Materialia* (2003) **51**, 5173–5185, DOI: 10.1016/S1359-6454(03)00378-1.

[9] H. Euchner, and P. Mayrhofer, *Surface and Coatings Technology* (2015) **275**, 214–218, DOI: 10.1016/j.surfcoat.2015.05.017.

[10] I. Schramm, M. J. Joesaar, J. Jensen, F. Mucklich, and M. Oden, *Acta Materialia* (2016) **119**, 218–228, DOI: 10.1016/j.actamat.2016.08.024.

[11] D. Holec, F. Rovere, P. H. Mayrhofer, and P. B. Barna, *Scripta Materialia* (2010) **62**, 349–352, DOI: 10.1016/j.scriptamat.2009.10.040.

[12] I. Endler, M. Hähn, M. Herrmann, H. Holzschuh, R. Pitonak, S. Ruppi et al., *Surf. Coat. Technol.* (2010) **205**, 1307–1312, DOI: 10.1016/j.surfcoat.2010.09.002.

[13] J. Keckes, R. Daniel, C. Mitterer, I. Matko, B. Sartory, A. Köpf et al., *Thin Solid Films* (2013) **545**, 29–32, DOI: 10.1016/j.tsf.2013.08.001.

[14] J. Todt, R. Pitonak, A. Köpf, R. Weißenbacher, B. Sartory, M. Burghammer et al., *Surf. Coat. Technol.* (2014) **258**, 1119–1127, DOI: 10.1016/j.surfcoat.2014.07.022.

[15] J. Todt, J. Zalesak, R. Daniel, R. Pitonak, A. Köpf, R. Weißenbacher et al., *Surface and Coatings Technology* (2016) **291**, 89–93, DOI: 10.1016/j.surfcoat.2016.02.027.

[16] A. Paseuth, K. Yamagata, A. Miura, M. Higuchi, and K. Tadanaga, *Journal of the American Ceramic Society* (2016) DOI: 10.1111/jace.14549.

[17] J. Zalesak, J. Todt, R. Pitonak, A. Kopf, R. Weißenbacher, B. Sartory et al., *Journal of Applied Crystallography* (2016) **49**, 2217–2225, DOI: 10.1107/S1600576716017258.

[18] N. E. Christensen, and I. Gorczyca, *Phys. Rev. B* (1994) **50**, 4397–4415, DOI: 10.1103/PhysRevB.50.4397.

[19] M. Ueno, A. Onodera, O. Shimomura, and K. Takemura, *Phys. Rev. B* (1992) **45**, 10123–10126, DOI: 10.1103/PhysRevB.45.10123.

[20] M. Setoyama, A. Nakayama, M. Tanaka, N. Kitagawa, and T. Nomura, *Surface and Coatings Technology* (1996) **86–87, Part 1**, 225–230, DOI: 10.1016/S0257-8972(96)03033-2.

[21] A. Madan, I. W. Kim, S. C. Cheng, P. Yashar, V. P. Dravid, and S. A. Barnett, *Phys Rev Lett* (1997) **78**, 1743–1746, DOI: 10.1103/PhysRevLett.78.1743.

[22] M. Schlögl, J. Paulitsch, J. Keckes, and P. Mayrhofer, *Thin Solid Films* (2013) **531**, 113–118, DOI: 10.1016/j.tsf.2012.12.057.

[23] I. Petrov, E. Mojab, R. C. Powell, J. E. Greene, L. Hultman, and J.-E. Sundgren, *Appl. Phys. Lett.* (1992) **60**, 2491, DOI: 10.1063/1.106943.

[24] L. Hultman, S. Benhenda, G. Radnoczi, J.-E. Sundgren, J. Greene, and I. Petrov, *Thin Solid Films* (1992) **215**, 152–161, DOI: 10.1016/0040-6090(92)90430-J.

[25] W.-T. Lin, L.-C. Meng, G.-J. Chen, and H.-S. Liu, *Applied Physics Letters* (1995) **66**, 2066–2068, DOI: 10.1063/1.113904.

[26] G. Kresse, and J. Furthmüller, *Phys. Rev. B* (1996) **54**, 11169–11186, DOI: 10.1103/PhysRevB.54.11169.

[27] G. Kresse, and J. Furthmüller, *Computational Materials Science* (1996) **6**, 15–50, DOI: 10.1016/0927-0256(96)00008-0.

[28] G. Kresse, and D. Joubert, *Phys. Rev. B* (1999) **59**, 1758–1775, DOI: 10.1103/PhysRevB.59.1758.

[29] J. P. Perdew, K. Burke, and M. Ernzerhof, *Phys. Rev. Lett.* (1996) **77**, 3865–3868, DOI: `10.1103/PhysRevLett.77.3865`.

[30] S.-H. Wei, L. G. Ferreira, J. E. Bernard, and A. Zunger, *Phys. Rev. B* (1990) **42**, 9622–9649, DOI: `10.1103/PhysRevB.42.9622`.

[31] F. F. Klimashin, N. Koutna, H. Euchner, D. Holec, and P. H. Mayrhofer, *Journal of Applied Physics* (2016) **120**, 185301, DOI: `10.1063/1.4966664`.

[32] Z. Zhang, H. Li, R. Daniel, C. Mitterer, and G. Dehm, *Phys. Rev. B* (2013) **87**, 014104, DOI: `10.1103/PhysRevB.87.014104`.

[33] M. Schlögl, C. Kirchlechner, J. Paulitsch, J. Keckes, and P. Mayrhofer, *Scr. Mater.* (2013) **68**, 917–920, DOI: `10.1016/j.scriptamat.2013.01.039`.

[34] D. Holec, R. Rachbauer, L. Chen, L. Wang, D. Luef, and P. H. Mayrhofer, *Surf. Coat. Technol.* (2011) **206**, 1698–1704, DOI: `10.1016/j.surfcoat.2011.09.019`.

[35] N. Ranganathan, K. Prasad, N. Balasubramanian, and K. L. Pey, *J. Micromech. Microeng.* (2008) **18**, 075018, DOI: `10.1088/0960-1317/18/7/075018`.

[36] K. Bartsch, A. Leonhardt, and E. Wolf, *Surf. Coat. Technol.* (1992) **54**, 193–197, DOI: `10.1016/S0257-8972(09)90049-4`.

D

Ab initio studies on the adsorption and implantation of Al and Fe to nitride materials

H. Riedel[1], Jakub Zalesak[2,3], M. Arndt[4], P. Polcik[5], D. Holec[1,3], P.H. Mayrhofer[1,6]

[1]Christian Doppler Laboratory for Application Oriented Coating Development at the Institute of Materials Science and Technology, TU Wien, A-1040 Wien, Austria
[2]Erich Schmid Institute for Materials Science, Austria Academy of Science, A-8700 Leoben, Austria
[3]Department of Physical Metallurgy and Materials Testing, Montanuniversität Leoben, A-8700 Leoben, Austria
[4]Oerlikon Balzers, Oerlikon Surface Solutions AG, LI-9496 Balzers, Liechtenstein
[5]Plansee Composite Materials GmbH, D-86983 Lechbruck am See, Germany

[6]Institute of Materials Science and Technology, TU Wien, A-1040 Vienna, Austria

Abstract

The formation of transfer material products on coated cutting and forming tools is a major failure mechanism leading to various sorts of wear. To describe the atomistic processes behind the formation of transfer materials, we use *ab initio* to study the adsorption energy as well as the implantation barrier of Al and Fe atoms for (001)-oriented surfaces of TiN, $\mathrm{Ti}_{0.50}$ $\mathrm{Al}_{0.50}\mathrm{N}$, $\mathrm{Ti}_{0.90}\mathrm{Si}_{0.10}\mathrm{N}$, CrN, and $\mathrm{Cr}_{0.90}\mathrm{Si}_{0.10}\mathrm{N}$. The interactions between additional atoms and nitride-surfaces are described for pure adhesion, considering no additional stresses, and for the implantation barrier. The latter, we simplified to the stress required to implant Al and Fe into sub-surface regions of the nitride material. The adsorption energies exhibit pronounced extrema at high-symmetry positions and are generally highest at nitrogen sites. Here, the

binary nitrides are comparable to their ternary counterparts and the average adhesive energy is higher (more negative) on CrN than TiN based systems. Contrary, the implantation barrier for Al and Fe atoms is higher for the ternary systems $Ti_{0.50}$ Al $_{0.50}$N, $Ti_{0.90}Si_{0.10}N$, and $Cr_{0.90}Si_{0.10}N$ than for their binary counterparts TiN and CrN. Based on our results, we can conclude that TiN based systems outperform CrN based systems with respect to pure adhesion, while the Si-containing ternaries exhibit higher implantation barriers for Al and Fe atoms. The data obtained are important to understand the atomistic interaction of metal atoms with nitride-based materials, which is valid not just for machining operations but also for any combination such as interfaces between coatings and substrates or multilayer and phase arrangements themselves.

D.1. Introduction

The performance of various tools during advanced machining operations is often directly connected with the applied hard protective coatings, like TiN- or CrN-based materials (e.g., TiN, Ti-Al-N, Ti-Si-N, CrN, and Cr-Si-N), prepared by chemical vapor or physical vapor deposition. Such coating materials provide higher hardnesses, higher thermal stability, and improved wear and oxidation resistance with respect to the native tool materials to be protected [1–6]. However, also such hard protective coatings are subject to various sorts of wear, which are a complex combination of abrasion, oxidation, diffusion, and adhesion mechanisms [7, 8]. Especially, transfer materials, which are increasingly formed at high temperatures and forces during machining operations [7, 9], often lead to the formation of various wear processes such as flank and crater wear. There are different studies to increase tool lifetime by improving the applied coatings with respect to such wear mechanisms. Such studies often deal with alloying concepts [10], superlattice effects of protective coatings [11], or even micro stripe textured surfaces of tools and coating materials [12]. Magneli phases (e.g., V_2O_5), possessing easy shear-able glide planes, are also applied to improve the tribological performance [13, 14], as thereby also fewer transfer materials can form.

There is a wide range of applications suffering from adhesion problems starting with simple cutting operations over metal forming processes up to injection molding processes [15–17]. For the formation of an adhesive wear product on a certain material, the chemical structure between and within the two solids is crucial [18]. Kendall [19] discussed the relationships between the scale ranges of adhesion (from atomistic to microscopic to engineering scale) and pointed out that the work of adhesion is an important parameter for adhesive processes, apart from thicknesses or elastic moduli of the involved materials and applied forces. The work of adhesion is derived from the Young-Dupré relation, which itself depends on the surface energies, and thus on the atomic structures. Consequently, adhesion and/or adsorption mechanisms originate from the atomic- or nano-scale [20–24]. In addition, the adhesion and interface energies are not only important for wear related failure mechanisms but also for film growth and phase formation as well as grain refinement mechanisms. For example, Al shows no adhesion on TiB_2 phases [25] and also leads to grain refinement within Al-Ti-B alloys [26]. Here, we use the power of *ab initio* calculations to study the adsorption energy and implantation barrier of Al and Fe atoms to different nitride materials: TiN, $Ti_{1-x}Al_xN$, $Ti_{1-x}Si_xN$, CrN, and $Cr_{1-x}Si_xN$. We concentrate on Al and Fe ad atoms because they are the majority elements found in our experimental investigations of adhesive transfer (buildup formation), and these elements are the basis and major content of important materials to be machined or formed. The selection of the mentioned face centered cubic (fcc) nitride materials is based on a broad screening concerning the lowest adsorption energies (obtained at any position or surface orientation) of Al ad atoms on various materials such as SiC (diamond-structure), Si (diamond-structure), MoN (hexagonal closed packed, hcp), Ti (hcp), W (body centered cubic, bcc), Mo (bcc), and the fcc nitride materials mentioned above [27]. These fcc nitrides exhibit significantly lower adsorption energies than the other materials, which is in agreement with earlier studies on Al adhesion to TiN surfaces [28, 29].

D.2. Methods

D.2.1. Calculation details

Density Functional Theory (DFT) calculations employing the Vienna Ab-initio Simulation Package (VASP) [30, 31] were performed to investigate the adsorption energy and implantation barrier of Al and Fe atoms to different coating materials. The projector augmented plane-wave (PAW) method [32] was used to describe the ion-electron interactions as well as the general gradient approximation (GGA), as parameterized by Perdew-Burke-Ernzerhof (PBE) [33], to treat the exchange and correlation effects [34]. To guarantee for a total energy accuracy of meV per atom, we used a plane wave cut-off of 450 eV and a $6\times6\times1$ k-point mesh according to the Monkhorst-Pack scheme [35] for the $2\times2\times3$ supercell (next paragraph) and corresponding meshes for other supercell sizes.

In order to model the different coating materials—TiN, $Ti_{0.50}Al_{0.50}N$, $Ti_{0.90}Si_{0.10}N$, CrN, and $Cr_{0.90}Si_{0.10}N$—we used a supercell approach based on the cubic rock-salt B1 structure [36]. The optimization yielded the following relaxed lattice constants: $a_{c\text{–}TiN} = 4.242\,Å$, $a_{c\text{–}TiAlN} = 4.160\,Å$, $a_{c\text{–}TiSiN} = 4.225\,Å$, $a_{c\text{–}CrN} = 4.135\,Å$, and $a_{c\text{–}CrSiN} = 4.154\,Å$. Al and Si were distributed along the metal sublattice within TiN and CrN using Special Quasi-random Structures (SQS) [37]. For $Ti_{0.90}Si_{0.10}N$ and $Cr_{0.90}Si_{0.10}N$, supercells were chosen containing Si in the surface-near regions. The SQS approach was also used to distribute the magnetic spins of Cr for a paramagnetic description [38]. Fe ad atoms were considered as spin-polarized. Cell size variation, from 1×1×3 supercells (24 atoms) up to 3×3×3 supercells (216 atoms), was used to study the convergence of the interaction between Al or Fe single ad atoms and the (001) nitride surfaces. All structures (slab thickness $3\cdot a_c$, e.g., 12.73 $Å$ for TiN) were combined with ≈12 $Å$ vacuum in the [001] direction to fulfill the periodic boundary conditions [39]. The maximum considered distance between the (001) surface and an ad atom was ≈2.0 $Å$. In all calculations, the atoms were allowed to relax only in the [001] direction, e.g., perpendicular to the (001) surface.

The calculated (001) surface energies of the different supercells in the relaxed state were calculated as ≈76, 78, 67, 59, and 73 $\mathrm{meV}/Å^2$ for TiN, $Ti_{0.50}Al_{0.50}N$, $Ti_{0.90}Si_{0.10}N$, CrN, and $Cr_{0.90}Si_{0.10}N$, respectively, which is in good agreement with other literature reports [23, 34, 40, 41] and proofs the correct setup of our supercells. The adsorption energy, E_{ads}, was calculated after

$$E_{ads} = E_{total} - E_{slab} - E_{ad} \tag{D.1}$$

Here, E_{total} is the total energy of the supercell with vacuum and an Al or Fe ad atom, E_{slab} describes the system without an Al or Fe ad atom, and E_{ad} is the total energy of an isolated Al or Fe atom in vacuum. The adsorption energy indicates the tendency of an ad atom to stick onto a surface as used in Ref. [34], and it is also a comparable quantity to the work of separation, used in other literature reports [19, 23, 42, 43]. Through the term “adsorption energy,” we want to highlight that this is the energy gained (when negative) by sticking an ad atom to the surface. Hence, E_{ads} should be positive, or as close to zero as possible, for avoiding or minimizing adhesion, or should be as negative as possible for maximum adhesion.

D.2.2. Experimental setup

$Cr_{1-x}Si_xN$ coatings (with an additional CrN bond layer) were deposited onto steel pins (diameter $10\times10\,\mathrm{mm}^3$) using an AJA Orion 5 laboratory scale magnetron sputtering system, equipped with a 3-in. $Cr_{0.95}Si_{0.05}$ and a 2-in. Cr target (99.99 % purity, PLANSEE Composite Materials GmbH), respectively. The steel pins and the targets were pre-cleaned using RF-etching (10 min) and sputter-cleaning (5 min) in an Ar plasma at a total pressure of 6 Pa, respectively. The basepressure was always below 1×10^{-4} Pa. The sputter process was performed in a mixed Ar/N_2 (6/4 flow rate ratio) glow discharge at a total pressure of 1 Pa and a target power density of $6\,W/cm^2$. A temperature of 500 °C and a continuous rotation of 60 rpm were applied to the substrate holder. To improve the adhesion of the $Cr_{0.95}Si_{0.05}N$ coating on the steel pin, we deposited a CrN bond layer using the same deposition parameters.

High temperature wear tests (HT-SRV) were performed using a linear oscillating testing machine (Optimol Instruments). A normal load of 10 N was applied to the coated pin, which was reciprocating against an AlSi coated Ultra High Strength Steel (UHSS) sheet for 50 min. The pin and the sheet were kept at a constant temperature of 900 °C. Subsequently, the formed wear products were investigated using a standard *in situ* lift-out method as applied for Transmission Electron Microscope (TEM) sample preparation, utilizing a TESCAN LYRA3 FEG microscope. The preparation was done in two steps. In the first step, the Focused Ion Beam (FIB) was operated at 30 keV, and in the second step, the accelerating voltage was lowered to 5 keV for the final lamella polishing. The TEM analysis was carried out using a JEOL JEM-2100F equipped with an Oxford INCA Energy TEM 200 Energy Dispersive X-ray spectroscopy (EDS) system. TEM images were recorded in STEM mode with a pixel dwell time of 50 ms. Qualitative EDS maps were obtained with a frame rate of 0.33 frames per minute.

D.3. Results and discussion

D.3.1. Experimental findings

Fig. D.1 presents a summary of the results for the performed HT-SRV tests on a $Cr_{0.95}Si_{0.05}N$ coating, which was tested against an AlSi coated UHSS sheet for 50 min. During this test, adhesive wear products were formed onto the coated steel pin, see Figs. D.1(a) and D.1(b) showing top and side view scanning electron micrographs, respectively, taken during FIB preparation. A clear separation between the formed build up, the $Cr_{0.95}Si_{0.05}N$ coating, and bulk material can be recognized in Fig. D.1(b). On the top of the build up, we deposited a platinum layer to protect the underlying materials during FIB preparation, see Fig. D.1(b). Detailed chemical investigations, obtained by EDS in scanning TEM mode, suggest that the formed build up mainly consists of Al and Fe with lower amounts of Si and O (see Fig. D.1(c)).

The build up exhibits a porous structure, which indicates a progressive formation during the test and an adhesiondominated wear behavior. The formation of plastic zones and micro welds lead to a metal transfer in the form of multiple wear fragments. The detected Fe originates from enhanced diffusion processes within the

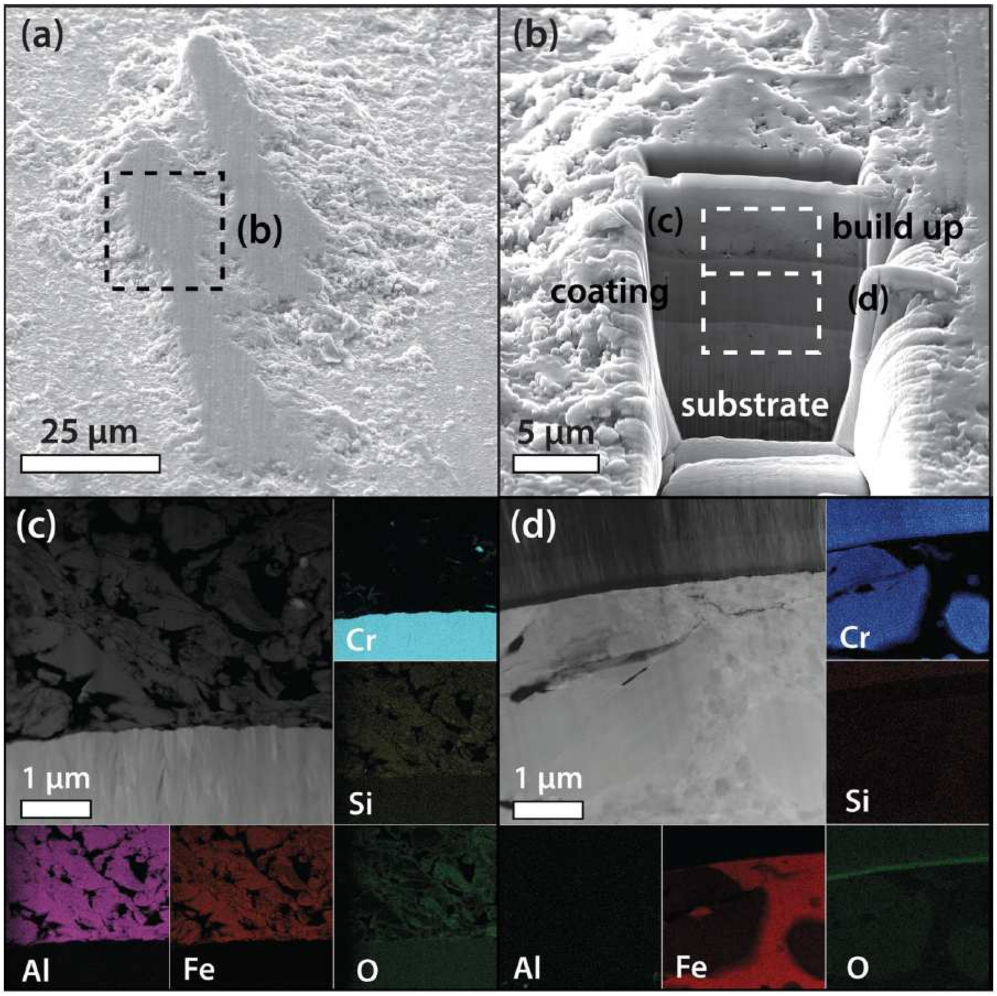

Figure D.1.: SEM top view of an adhesive wear product (a), which is formed during HT-SRV tests. Corresponding side view during FIB preparation of a TEM lamella for detailed chemical analysis (b). Elemental maps (using STEM) of the interface region between wear product and $Cr_{0.95}Si_{0.05}N$ (c), and between $Cr_{0.95}Si_{0.05}N$ and bulk material (d).

UHSS sheet, as Fe tends to form Al-Fe phases. However, diffusion seems to play a minor role during the formation process of the wear products because no promoted diffusion pathways can be seen at the interfaces between build up and coating as well as between coating and steel pin, Figs. Figure D.1 on page D–6(c) and Figure D.1 on page D–6(d). The interface between $Cr_{0.95}Si_{0.05}N$ and steel pin (substrate material) clearly shows the Cr-rich bond layer, no Si, no Al, and Fe only within the steel pin. The very thin O-rich layer, see the oxygen map in Fig. Figure D.1 on page D–6(d), stems from the native oxide of the steel pin, which was not fully removed during the etching process prior to the deposition. The results prove that especially Al and Fe play a significant role for the adhesion processes in machining and forming operations. Consequently, we selected these two elements to study their adsorption and implantation behavior to the model coating systems TiN, $Ti_{1-x}Al_xN$, $Ti_{1-x}Si_xN$, CrN, and $Cr_{1-x}Si_xN$, which are preferably used for such applications. Additionally, Fe and Al are also important elements within substrates and thin film growth itself, respectively. Hence, adsorption and implantation mechanisms between these metals and the mentioned nitrides are important parameters for vast research and application fields wherever such metals grow on nitrides (during the growth of multilayers or nanocomposites themselves) or vice versa (during interface formation to the substrates).

D.3.2. Adsorption behavior

To obtain an optimum between computational power and accuracy, we performed convergence tests for TiN (which we treat as a reference system) with Al ad atoms. As depicted in Fig. D.2, the coverage (Θ) and hence the supercell size (in-plane dimension) is varied between $\Theta = 0.25$, 0.063, and 0.028 $\mathring{A}^{-2}$, respectively. The adsorption energy initially decreases with decreasing coverage, which can be related to an increased distance between the ad atoms through the periodic boundary conditions for increased cell size. This trend is in excellent agreement with earlier studies [44]. The dependence of Eads on the slab height was studied by varying the slab height between 3 and 12 times of the lattice constant ac of the 1×1 and 2×2 squared super cells.

The results clearly show that this dependency is within the error of calculations for 2×2 squared supercells, see the overlap of the values obtained for 2×2(×3) and 2×2(×13) supercells (half-filled black diamond and red circle). Based on our convergence tests (Fig. D.2), we selected a 2×2×3 supercell as a representative size for all further calculations of the ad atom/slab interaction, exhibiting excellent accuracy

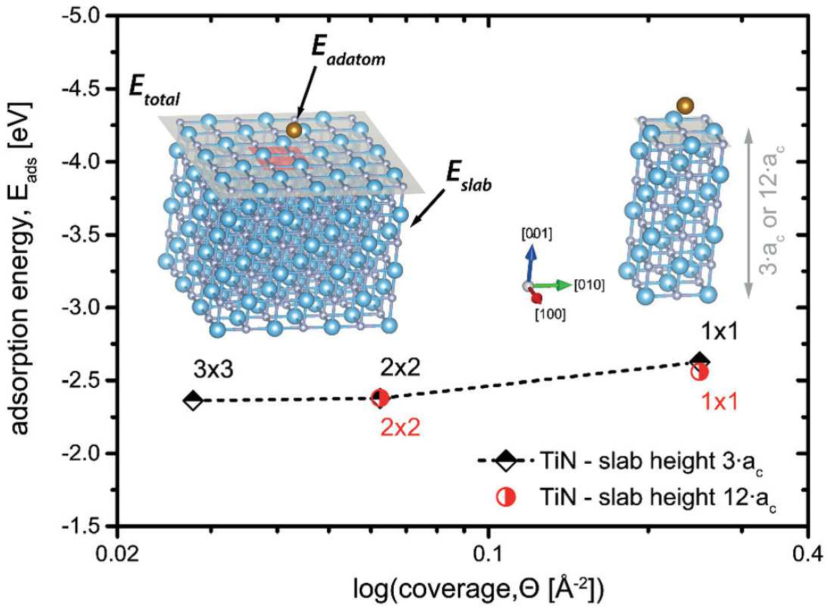

Figure D.2.: Influence of the supercell size (in-plane and height) on the adsorption energy of Al ad atoms on TiN (001) surfaces. The coverage was varied between $0.25\,\mathring{A}^{-2}$ (1×1) and $0.028\,\mathring{A}^{-2}$ (3×3) and the slab height varied between 3 and $12{\cdot}a_c$ (black diamonds and red circles), respectively. The TiN structures are visualized using VESTA [45].

with a reasonable computational time at the sophisticated Vienna Scientific Cluster.

Three different high-symmetry positions exist on TiN (001) surfaces: N site, hollow site (cubic interstice), and Ti site (Fig. 3(a)). The corresponding adsorption energies are abbreviated with E_{ads}^{N}, E_{ads}^{hollow}, and E_{ads}^{Ti}, respectively. The adsorption energies for Al ad atoms (half filled diamonds) range from $E_{ads}^{N} = -2.377\,\text{eV}$ to $E_{ads}^{hollow} = -1.909\,\text{eV}$ and $E_{ads}^{Ti} = -1.078\,\text{eV}$. A similar trend is obtained for Fe ad atoms, with slightly more negative values for all these three positions, see the open diamonds in Fig. 3(a). To obtain a closer insight to the adsorption energy variations across the (001) surfaces, we calculated the adsorption energies for 81 positions across a square of about $9\,\mathring{A}^2$. The thereby obtained adsorption energy landscapes (see Figs. D.3(b) and D.3(c)), AEL, for Al or Fe on TiN (001) surfaces are topologically very similar. For Al and Fe, the preferred adsorption site (the most negative adsorption energy) is above N atoms, followed by the hollow site, and is least attractive above Ti atoms. The higher adsorption energy of Al ad atoms to N than to Ti, Fig. D.3(b), is in good agreement with earlier literature reports [24,

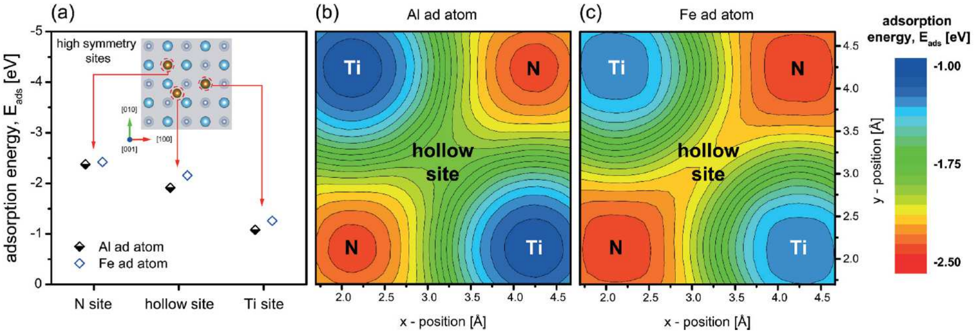

Figure D.3.: Adsorption energy (E_{ads}) of Al (half full black diamonds) and Fe ad atoms (blue open diamonds) on high-symmetry positions (nitrogen-, hollow-, and metal-site) on TiN (001) surfaces (a). Al (b) and Fe (c) ad atom adsorption energy landscapes for representative of TiN (001) surface. Contours correspond to 0.075 eV steps. The snapshot of the crystal structure was visualized using VESTA [45].

34]. The adsorption behavior of Al and Fe ad atoms to different coating systems can be quantified, for example, by an overall adsorption strength defined as adsorption energy integrated over the considered surface area A (sampled by the vector $\vec{r}$), divided by A

$$E_{ads}^{int} = \frac{\int_A E\left(\vec{r}\right) d\vec{r}}{A} \tag{D.2}$$

To calculate E_{ads}^{int}, the whole AEL is needed. Figures D.3(b) and D.3(c) show that the adsorption energies exhibit pronounced extrema directly at the Ti, N, and hollow sites. Therefore, we calculated the median E_{ads}, of these extrema, where we need to consider that there are two full Ti and N positions but four full hollow site positions per TiN (001) surface unit corresponding to the (001) facet of the cubic B1 conventional cell. Consequently, E_{ads} is calculated as

$$E_{ads} = \frac{2 \cdot E_{ads}^{N} + \bar{2} \cdot E_{ads}^{Ti} + 4 \cdot E_{ads}^{hollow}}{8} \tag{D.3}$$

Using these equations, Eqs. (D.2) and (D.3), we obtained adsorption energies of $E_{ads}^{int} = -1.77\,\text{eV}$ and $E_{ads} = -1.81\,\text{eV}$ for Al ad atoms and $E_{ads}^{int} = -1.90\,\text{eV}$ and $E_{ads} = -2.06\,\text{eV}$ for Fe ad atoms on TiN (001) surfaces. These data clearly show that the median of the adsorption energy E_{ads}, Eq. (D.3), is in decent agreement with the integrated adsorption energy E_{ads}^{int}, Eq. (D.2). Thus, E_{ads} can be used to efficiently (less computational intensive) evaluate the adsorption behavior for various materials, such as shown in Fig. D.4 for Al (half filled diamonds) and Fe ad atoms (open diamonds) on (001) surfaces of TiN, $Ti_{0.50}Al_{0.50}N$, $Ti_{0.90}Si_{0.10}N$, CrN, and $Cr_{0.90}Si_{0.10}N$, respectively. Here, we need to mention that due to the implementation of SQS structures, the distribution of the alloying elements (Al and Si) is random. Hence, the number of highsymmetry positions per surface unit can have irregularities depending on the overall chemical composition.

The data suggest that the adsorption of Al ad atoms is weaker on $Cr_{0.90}Si_{0.1}0N$ than on CrN surface and on $Ti_{0.50}Al_{0.50}N$ than on TiN surface. The lowest (the least negative) adsorption energies of Al ad atoms are obtained on the $Ti_{0.50}Al_{0.50}N$ surface, whereas Fe ad atoms exhibit the lowest adsorption energies on the $Ti_{0.90}Si_{0.10}N$ surface (directly followed by $Ti_{0.50}Al_{0.50}N$). The results for fcc $Ti_{0.50}Al_{0.50}N$ are very similar to those of fcc AlN exhibiting almost identical median adsorption energy E_{ads} for Al. However, fcc AlN provides the lowest adsorption energy for Al among all systems studied directly at the metal site (i.e., in this case, the Al site) [27]. Furthermore, our calculations clearly yield that the N sites are the preferred adsorption sites with the most negative adsorption energies for Al ad atoms for all systems studied. The most negative adsorption energy for Fe ad atoms is obtained at N sites on TiN, $Ti_{0.50}Al_{0.50}N$, and $Ti_{0.90}Si_{0.10}N$ surfaces but at the hollow sites on CrN and $Cr_{0.90}Si_{0.10}N$ surfaces. The weakest adsorption of Al and of Fe ad atoms is always obtained at the metal sites of the systems studied.

Assuming that the surface diffusion preferably happens along energy valleys [24, 34] in the AEL (hence along the areas of most negative adsorption energies, see Figs. D.3(b) and D.3(c)), the surface diffusion of Al and Fe ad atoms will predominantly proceed along the nitrogen to hollow site directions on the (001) nitride surfaces studied (hence along the $\langle 110\rangle$ directions). If we consider the adsorption energy topography along this diffusion track as the barrier against diffusion, TiN would yield the highest barrier for Al ad atoms (adsorption energy difference $\delta = 0.47\,\text{eV}$) and CrN yields the highest barrier for Fe ad atoms ($\delta = 0.90\,\text{eV}$). Alloying silicon to these binaries significantly reduces their adsorption energy differences δ along the $\langle 110\rangle$ directions for Al and Fe ad atoms. However, alloying aluminum to TiN only reduces the adsorption energy differences δ along the $\langle 110\rangle$ directions for Al but increases it for Fe ad atoms. These data are especially important to understand the processes during film growth.

D.3.3. Implantation behavior

Within many techniques (e.g., film formation during sputter deposition but also machining and forming applications), the implantation barrier for individual atoms

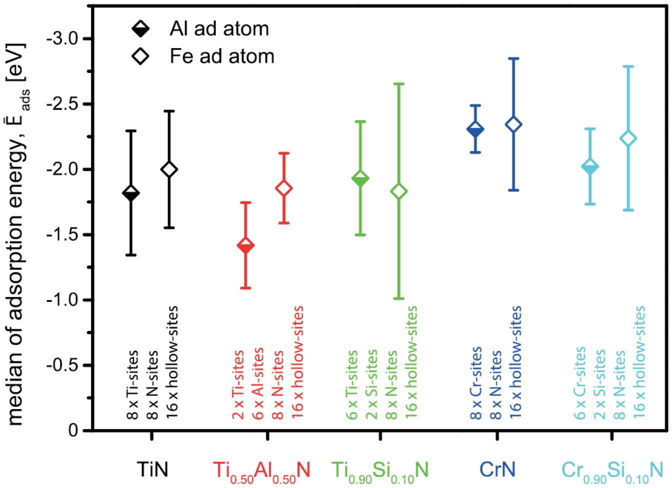

Figure D.4.: Median adsorption energies for Al and Fe ad atoms across the highsymmetry positions of TiN, $Ti_{0.50}Al_{0.50}$ N, $Ti_{0.90}Si_{0.10}N$, CrN, and $Cr_{0.90}Si_{0.10}N$ (001) surfaces. The labels below the data points give the total number and identification of the individual high-symmetry positions across the (001) surface of the supercell used. The error bars give the variation in adsorption energies across these high-symmetry positions.

into a surface region is of utmost importance. Therefore, in addition to the adsorption energy, we also calculated the repulsion/attraction potential and force for Al and Fe atoms to the individual material surface. We envision that the heavy loads during any machining and forming operation not just lead to adsorption but also implantation. Definitely, such processes are important for sputter deposition where mainly neutral atoms arrive at a growing film and are adsorbed, diffuse there, and are implanted or repelled. Here, we do not consider the in-diffusion as a result of increased temperature, but which energetic barrier ($U*$) the Al and Fe atoms need to pass to be attracted to or even implanted into the individual material surfaces. Furthermore important is also, at which distances ($d*$, between the Al or Fe atoms and the considered material surfaces) are these attraction or implantation barriers (for simplicity, we will refer to this distance as “critical distance” in analogy to the “critical nuclei size” for overcoming the nucleation barrier). This is schematically represented in Fig. D.5.

If an ad atom is further than above the critical distance $d*$, it is energetically favorable to increase its distance to the free surface, Fig. D.5(a), and the atom is repelled. If the ad atom is placed nearer than the critical distance $d*$, it is energetically favorable to decrease this distance, Fig. D.5(b), and the atom is attracted to or

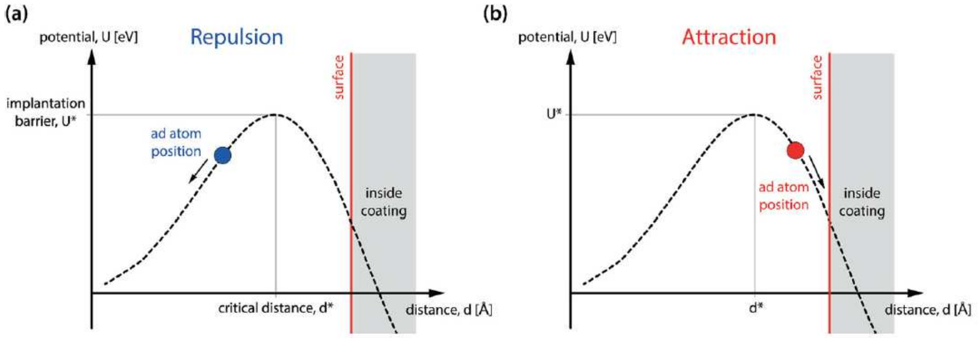

Figure D.5.: Schematic representation of the potential to distance curve of our implantation test for the repulsive (a) and the attractive (b) case.

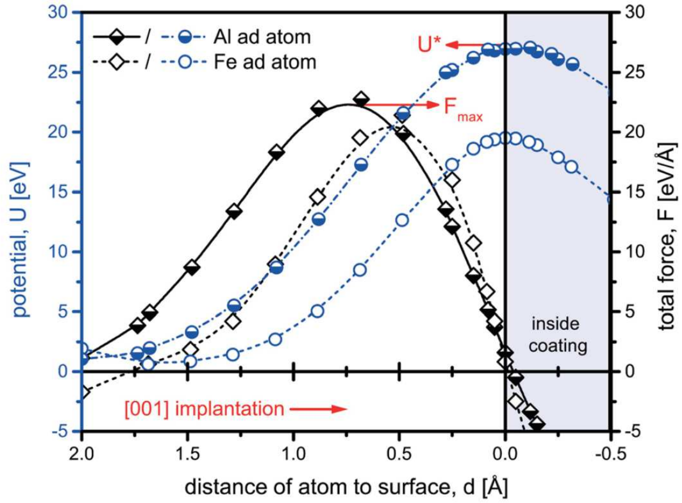

Figure D.6.: Potential (circles) and total force (diamonds) for Al (half filled symbols) and Fe (open symbols) atoms as a function of the distance to the hollow site of a TiN (001) surface.

even implanted into the bulk material. Through the implantation of the additional atom, the structure can be disturbed. During the calculations of the implantation behavior, the atomic positions were fixed and a series of calculations with various ad-atom-to-surface distances was carried out. The potentials U for the Al and Fe atoms exhibit a maximum (energetic barrier, $U*$) slightly underneath the TiN (001) surface at a distance of -0.06 and $-0.05\,Å$, see Fig. D.6. This maximum (i.e., the implantation barrier) is significantly higher for Al than for Fe atoms. The calculations also give the corresponding total forces (as the first derivative of the potential)

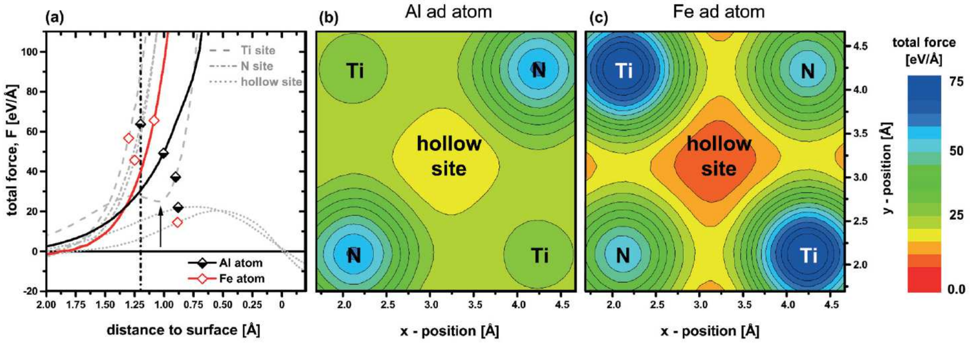

Figure D.7.: Total force, as a function of atom-to-surface distance for Al (half filled diamonds) and Fe (open diamonds) above high symmetry sites (Ti site: dashed lines; N site: dot dashed lines; hollow site: doted lines; weighted mean value of these sites: solid lines) of a TiN (001) surface (a). The discontinuity within the total force evolution of Al atoms above the N sites is marked with an arrow. Total force landscapes at a constant ad atom-to-surface distance of 1.2 $\AA$ for Al (b) and Fe (c). This distance is indicated in (a) by a dashed dotted vertical line. The contours within the force landscape correspond to 5 eV/$\AA$ steps.

with the maxima at the inflection points of the potential (the force zero-crossing is at the maximum of the potential). Consequently, the maximum force, F_{max}, which has to be overcome to implant atoms into TiN (001) surfaces at the hollow sites, is higher for Al than for Fe. One explanation for this behavior (based on the hard sphere model) is that the atomic radius of Al, $r_{Al} = 140\,\text{pm}$, is larger as that of Fe, $r_{Fe} = 125\,\text{pm}$.

Figure D.7(a), representing the total forces for Al and Fe atoms as a function of the distance to the (001) TiN surface at the three high-symmetry positions (Ti, N, and hollow sites), indicates that implantation is only possible through the hollow sites. The forces on the Al and Fe atoms at N- and Ti-sites rapidly increase (nearly exponentially) for atom-to-surface distances smaller than 1.75 $\AA$. Aluminum atoms exhibit a pronounced interruption of this increase in repulsive forces at a distance of ≈1.0 $\AA$ above the Ti-sites, see the region, which is marked with an arrow in Fig. D.7(a). As this is not the case for Fe atoms, the increase of the average-forces (calculated like the median for the adsorption energy, hence, double weighing the hollow sites, as there are twice as much possibilities as for Ti or N sites) is significantly lower for Al than for Fe atoms, see Fig. D.7(a). The already indicated behavior (see Fig. D.7(a)) of smaller forces at hollow sites than at N or Ti sites is clearly represented by the force landscape for Al an Fe atoms above (distance d = 1.2 $\AA$) the (001) TiN surface, see Figs. D.7(b) and D.7(c), respectively.

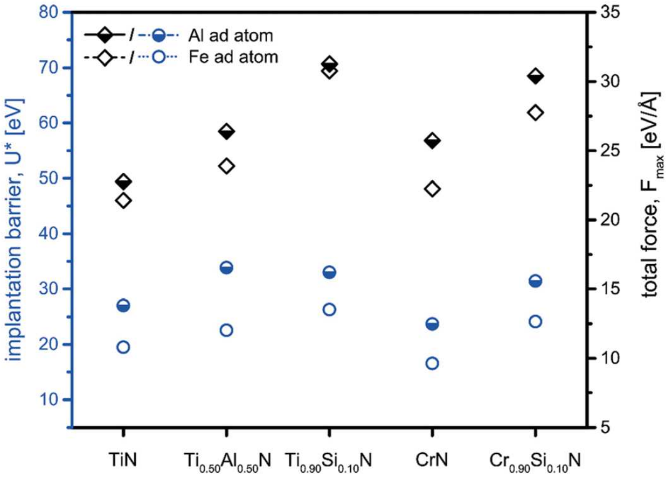

Figure D.8.: Implantation barrier (blue circles) and total force (black diamonds) for Al (half filled symbols) and Fe (open symbols) atoms at TiN, $Ti_{0.50}Al_{0.50}N$, $Ti_{0.90}Si_{0.10}N$, CrN, and $Cr_{0.90}Si_{0.10}N$ (001) surfaces.

These data clearly suggest that also for the implantation behavior (as well as for the adhesion behavior) of Al and Fe atoms, the efficient (computational power) calculation of the interaction with high symmetry positions (ion site positions and hollow sites) is extremely representative and allows screening and comparing several material combinations. For example, Fig. D.8 shows the implantation barrier, $U*$, and the maximum repulsive force, F_{max}, for Al (half-filled symbols) or Fe (open symbols) atoms at the hollow sites of (001) surfaces of TiN, $Ti_{0.50}Al_{0.50}N$, $Ti_{0.90}Si_{0.10}N$, CrN, and $Cr_{0.90}Si_{0.10}N$. The maximum implantation barrier significantly increases when alloying Al or Si to the respective binary coatings TiN and CrN, respectively, and $U*$ is higher for Al than for Fe atoms. The implantation barrier is in the range between 15 and 35 eV, see the blue circles in Fig. D.8. A comparable energy range is reported for the implantation of B or N atoms in carbon nanotubes requiring 50 eV for a direct substitution [46]. In addition, the magnetic moment of Fe ad-atoms significantly decreases when approaching the nitride surfaces and is nearly zero for $\pm 0.5\,\mathring{A}$ distance from the nitride surfaces. Therefore, the magnetic moment of Fe has only a negligible effect on the implantation behavior. However, $U*$ is slightly lower for the implantation of Al into $Ti_{0.90}Si_{0.10}N$ than into $Ti_{0.50}Al_{0.50}N$ (at their (001) surface hollow sites). A corresponding trend is also obtained for the maximum repulsive forces, whereas $Ti_{0.90}Si_{0.10}N$ exhibits the highest maximum force for Al and Fe atoms. According to the higher Al implantation barrier, also the distance of Fmax for Al is higher than for Fe atoms for all systems studied. Nevertheless, our data clearly suggest that the implantation of Al is more difficult than the implantation of Fe.

The most essential information from this part of the study is the temperature range, in which the cubic solid solution phases of the Al-rich and Ti-rich lamellae were found to be stable, namely up to 900 °C, with an additional partial stability up to 1000 °C.

D.4. Conclusions

High temperature wear tests of $Cr_{0.95}Si_{0.05}N$ coated steel pins against AlSi coated ultra high strength steel sheets clearly show adhesion-dominated wear processes. Therefore and because the interaction between metals and nitrides is crucial for sputter deposition processes, we employed first principle calculations to study the atomistic processes of Al and Fe atoms on different nitride based coating materials. Based on atomistic pre-studies, showing that face centered cubic nitride materials exhibit lower adsorption energies to Al than diamond-structured SiC and Si, bcc-W, bcc-Mo, or hcp-MoN, we used fcc TiN, $Ti_{0.50}Al_{0.50}N$, $Ti_{0.90}Si_{0.10}N$, CrN, and $Cr_{0.90}Si_{0.10}N$ for in-depth studies of adsorption and implantation behavior.

Adsorption energy landscapes of Al and Fe atoms on (001) TiN surfaces highlight pronounced extrema at the highsymmetry positions, Ti-, N-, and hollow-sites. Our results highlight that because of this, the median of the adsorption energies at these positions excellently represents the integrated adsorption energy over the (001) surface. This allows to computationally efficient calculation of the adsorption energies of elements on various material surfaces. For example, Al and Fe ad atoms exhibit the highest adsorption energies on CrN surfaces and the lowest on $Ti_{0.50}Al_{0.50}N$ and $Ti_{0.90}Si_{0.10}N$ surfaces, respectively. However, the adsorption energy for Fe is only slightly lower on $Ti_{0.90}Si_{0.10}N$ than on $Ti_{0.50}Al_{0.50}N$ surfaces. Generally, the adsorption energy for Al and Fe is higher on CrN-based than on TiN-based systems, and the values are comparable for the binaries and their ternary counterparts.

This is in contrast to the results obtained for the implantation behavior of Al and Fe into TiN, $Ti_{0.50}Al_{0.50}N$, $Ti_{0.90}Si_{0.10}N$, CrN, and $Cr_{0.90}Si_{0.10}N$, which clearly yield higher necessary forces and implantation barriers for the ternary nitrides than their binary counterparts. Face centered cubic structured $Ti_{0.90}Si_{0.10}N$ and $Cr_{0.90}Si_{0.10}N$ provide the highest barriers and total forces for the implantation of Al or Fe into their (001) surfaces.

Based on our adsorption and implantation of ab initio studies, we can conclude that for adsorption dominated mechanisms, TiN-based materials yield lower adsorption energies than their CrN-based counterparts. Here, the ternaries and corresponding binaries yield comparable adsorption energies for Al and Fe ad atoms. Contrary, for implantation dominated mechanisms, the ternary nitrides provide higher implantation barriers than their binary counterparts and the CrN-based and TiN-based systems are comparable. These data are important whenever it comes to the interaction between metals and nitrides, as for example, during film growth processes and the formation of multilayer or multiphased structures.

Acknowledgements

The financial support by the Austrian Federal Ministry of Economy, Family and Youth and the National Foundation for Research, Technology and Development is gratefully acknowledged. We also thank for the financial support of Plansee Composite Materials GmbH and Oerlikon Balzers, Oerlikon Surface Solutions AG. The computational results presented have been achieved using the Vienna Scientific Cluster (VSC).

Bibliography to paper D

[1] W. Münz, *Journal of Vacuum Science & Technology A* (1986) **4**, 2717–2725, DOI: 10.1116/1.573713.

[2] P. H. Mayrhofer, C. Mitterer, J. G. Wen, I. Petrov, and J. E. Greene, *Journal of Applied Physics* (2006) **100**, DOI: 10.1063/1.2222406.

[3] J. Gu, G. Barber, S. Tung, and R.-J. Gu, *Wear* (1999) **22-229, Part 1**, 273–284, DOI: 10.1016/S0043-1648(99)00074-5.

[4] R. Rachbauer, S. Massl, E. Stergar, D. Holec, D. Kiener, J. Keckes et al., *J Appl Phys* (2011) **110**, 11, DOI: 10.1063/1.3610451.

[5] J. Hardell, and B. Prakash, *International Journal of Refractory Metals and Hard Materials* (2010) **28**, 106–114, DOI: 10.1016/j.ijrmhm.2009.07.009.

[6] P. H. Mayrhofer, *Comprehensive Materials Processing*, (2014) pp. 355–388.

[7] J. Endrino, G. Fox-Rabinovich, and C. Gey, *Surface and Coatings Technology* (2006) **200**, 6840–6845, DOI: 10.1016/j.surfcoat.2005.10.030.

[8] V. P. Astakhov, *Tools (Geometry and Material) and Tool Wear*, Springer London, (2008) ch. Tools (Geometry and Material) and Tool Wear, pp. 29–57, DOI: 10.1007/978-1-84800-213-5_2.

[9] M. Wieland, *Tribology in Industry* (2012) **34**, 11–17.

[10] M. Arndt, and T. Kacsich, *Surface and Coatings Technology* (2003) **163–164**, 674–680, DOI: http://dx.doi.org/.

[11] S. PalDey, and S. Deevi, *Mater. Sci. Eng., A* (2003) **342**, 58–79, DOI: 10.1016/S0921-5093(02)00259-9.

[12] T. Sugihara, and T. Enomoto, *Precision Engineering* (2013) **37**, 888–896, DOI: 10.1016/j.precisioneng.2013.05.007.

[13] K. Kutschej, P. Mayrhofer, M. Kathrein, P. Polcik, and C. Mitterer, *Surface and Coatings Technology* (2004) **188-189**, 358–363, DOI: 10.1016/j.surfcoat.2004.08.022.

[14] R. Franz, J. Neidhardt, R. Kaindl, B. Sartory, R. Tessadri, M. Lechthaler et al., *Surface and Coatings Technology* (2009) **203**, 1101–1105, DOI: 10.1016/j.surfcoat.2008.10.003.

[15] M. R. de Figueiredo, *International Polymer Processing* (2013) **28**, 415–420, DOI: 10.3139/217.2767.

[16] M. Vilaseca, J. Pujante, G. Ramírez, and D. Casellas, *Wear* (2013) **308**, 148–154, DOI: `10.1016/j.wear.2013.07.003`.

[17] M. Fleming, and M. Hashmi, *Journal of Materials Processing Technology* (1992) **32**, 481–88, DOI: `10.1016/0924-0136(92)90204-6`.

[18] A. Banerjea, *Fundamentals of Adhesion*, ed. L.-.-.-H. Lee, Springer US, (1991) pp. 325–348, DOI: `10.1007/978-1-4899-2073-7_11`.

[19] K. Kendall, *Science* (1994) **263**, 1720–1725, DOI: `10.1126/science.263.5154.1720`.

[20] L. Hector, *Integration of Material, Process and Product Design: A Conference Dedicated to the 70th Birthday of Owen Richmond* (1999) ed. S. Springs, 39–46.

[21] D. G. Sangiovanni, D. Edström, L. Hultman, V. Chirita, I. Petrov, and J. E. Greene, *Phys. Rev. B* (2012) **86**, 155443, DOI: `10.1103/PhysRevB.86.155443`.

[22] A. Arya, and E. A. Carter, *The Journal of Chemical Physics* (2003) **118**, 8982–8996, DOI: `10.1063/1.1565323`.

[23] D. Gall, S. Kodambaka, M. A. Wall, I. Petrov, and J. E. Greene, *Journal of Applied Physics* (2003) **93**, 9086–9094, DOI: `10.1063/1.1567797`.

[24] B. Alling, P. Steneteg, C. Tholander, F. Tasnádi, I. Petrov, J. E. Greene et al., *Phys. Rev. B* (2012) **85**, 245422, DOI: `10.1103/PhysRevB.85.245422`.

[25] M. Berger, and S. Hogmark, *Surface and Coatings Technology* (2002) **149**, 14–20, DOI: `10.1016/S0257-8972(01)01361-5`.

[26] Y. Han, Y. Dai, D. Shu, J. Wang, and B. Sun, *Applied Physics Letters* (2006) **89**, DOI: `10.1063/1.2358951`.

[27] H. Riedl, Ph.D. Thesis, TU Wien, (2015)

[28] D. J. Siegel, L. G. Hector, and J. B. Adams, *Phys. Rev. B* (2003) **67**, 092105, DOI: `10.1103/PhysRevB.67.092105`.

[29] L. Liu, S. Wang, and H. Ye, *Acta Materialia* (2004) **52**, 3681–3688, DOI: `10.1016/j.actamat.2004.04.022`.

[30] G. Kresse, and J. Furthmüller, *Phys. Rev. B* (1996) **54**, 11169–11186, DOI: `10.1103/PhysRevB.54.11169`.

[31] G. Kresse, and J. Furthmüller, *Computational Materials Science* (1996) **6**, 15–50, DOI: `10.1016/0927-0256(96)00008-0`.

[32] G. Kresse, and D. Joubert, *Phys. Rev. B* (1999) **59**, 1758–1775, DOI: 10.1103/PhysRevB.59.1758.

[33] J. P. Perdew, K. Burke, and M. Ernzerhof, *Phys. Rev. Lett.* (1996) **77**, 3865–3868, DOI: 10.1103/PhysRevLett.77.3865.

[34] C. Tholander, B. Alling, F. Tasnádi, J. Greene, and L. Hultman, *Surface Science* (2014) **630**, 28–40, DOI: 10.1016/j.susc.2014.06.010.

[35] H. J. Monkhorst, and J. D. Pack, *Phys. Rev. B* (1976) **13**, 5188–5192, DOI: 10.1103/PhysRevB.13.5188.

[36] D. Holec, R. Rachbauer, L. Chen, L. Wang, D. Luef, and P. H. Mayrhofer, *Surf. Coat. Technol.* (2011) **206**, 1698–1704, DOI: 10.1016/j.surfcoat.2011.09.019.

[37] S.-H. Wei, L. G. Ferreira, J. E. Bernard, and A. Zunger, *Phys. Rev. B* (1990) **42**, 9622–9649, DOI: 10.1103/PhysRevB.42.9622.

[38] L. Zhou, D. Holec, and P. H. Mayrhofer, *Journal of Applied Physics* (2013) **113**, DOI: 10.1063/1.4789378.

[39] Z. Lin, and P. D. Bristowe, *Phys. Rev. B* (2007) **75**, 205423, DOI: 10.1103/PhysRevB.75.205423.

[40] D. Holec, J. Paulitsch, and P. H. Mayrhofer, *ArXiv e-prints* (2012)

[41] D. Holec, and P. H. Mayrhofer, *Scripta Materialia* (2012) **67**, 760–762, DOI: 10.1016/j.scriptamat.2012.07.027.

[42] D. J. Siegel, L. G. Hector, and J. B. Adams, *MRS Proceedings* (2011) **654**, DOI: 10.1557/PROC-654-AA4.2.1.

[43] D. Music, D. Lange, L. Raumann, M. to Baben, F. von Fragstein, and J. M. Schneider, *Surface Science* (2012) **606**, 986–989, DOI: 10.1016/j.susc.2012.02.022.

[44] H. Ibach, *Surface Science* (2004) **556**, 71–77, DOI: 10.1016/j.susc.2004.03.038.

[45] K. Momma, and F. Izumi, *Journal of Applied Crystallography* (2011) **44**, 1272–1276, DOI: 10.1107/S0021889811038970.

[46] J. Kotakoski, A. V. Krasheninnikov, Y. Ma, A. S. Foster, K. Nordlund, and R. M. Nieminen, *Phys. Rev. B* (2005) **71**, 205408, DOI: 10.1103/PhysRevB.71.205408.

E

Al-rich cubic $Al_{0.8}Ti_{0.2}N$ coating with self-organized nano-lamellar microstructure: Thermal and mechanical properties

Juraj Todt[a,b], **Jakub Zalesak**[a,c], **Rostistlav Daniel**[c], **Reinhard Pitonak**[d],
Arno Köpf[d], **Ronald Weißenbacher**[d], **Bernhard Sartory**[e], **Christian Mitterer**[c], **Jozef Keckes**[a,b]

[a]Department of Materials Physics, Montanuniversität Leoben, Leoben, Austria
[b]Erich Schmid Institute for Materials Science, Austrian Academy of Sciences, Leoben, Austria
[c]Department of Physical Metallurgy and Materials Testing, Montanuniversität Leoben, Leoben, Austria
[d]Böhlerit GmbH & Co. KG, Kapfenberg, Austria
[e]Materials Center Leoben GmbH, Leoben, Austria

Abstract

The synthesis of Al-rich cubic AlTiN coatings represents a challenging task. Recent advances achieved using chemical vapour deposition (CVD) demonstrated the possibilities to produce (i) cubic monophase coatings with Al ratio up to $x = 90\,\%$ and (ii) self-organized nano-lamellar $Al_xTi_{1-x}N$ coatings consisting of alternating wurtzite and cubic lamellae. In this work, a further development of the self-organized nano-lamellar CVD coating type is presented, namely the synthesis and physical properties of a purely cubic $Al_{0.8}Ti_{0.2}N$ coating. The effect of the reduced Al content was investigated with respect to the coating's nano-lamellar microstructure, oxidation resistance, phase stability and nanoindentation hardness. Although the newly developed $Al_{0.8}Ti_{0.2}N$ coating exhibited a slightly decreased oxidation resistance in comparison with the prior wurtzite-cubic nano-lamellar $Al_{0.95}Ti_{0.05}N$ coating, the phase stability remained the same, while simultaneously a hardness increase of more than 30 % was observed. This hardness of 36 GPa was stable up to 1050 °C, exhibiting a maximum value of 38 GPa around 950 °C. Furthermore, investigations by transmission electron microscopy revealed a modified arrangement of coherent nano-lamellae within columnar grains, forming an irregularly faceted layered coating morphology. In summary, the novel coating material grown with the rate of 5 µm per hour not only possesses a unique microstructure but attracts also by remarkable physical properties.

E.1. Introduction

AlTiN hard coatings prepared predominantly by a variety of physical vapour deposition (PVD) techniques have become an industrial standard for applications on cutting tools for dry and high speed metal machining. Owing to their improved oxidation resistance and high temperature hardness, they provide a superior tool lifetime compared to earlier TiN coatings [1–3]. In the past 25 years, the development of these coatings has experienced an enormous progress and numerous studies have been devoted especially to physical vapour deposition (PVD) processes. It was observed that in PVD as-deposited $Al_xTi_{1-x}N$ coatings, a wurtzite (w) AlN phase emerges at high Al contents of x above 67, % [4–7], which is detrimental to the mechanical coating properties, since this phase is comparatively soft [8]. However, high Al content is desirable for an improved oxidation resistance, since Al_2O_3 formed during oxidation is a more effective oxygen diffusion barrier than various Ti-containing oxides, which are typically rather porous and permit continued oxidation of underlying coating material [9]. At higher temperature above about 850 °C [10], it was found that cubic (fcc) Al-rich $Al_xTi_{1-x}N$ phase decomposes into metastable coherent fcc-$Ti_{1-x}Al_xN$ and fcc-AlN domains responsible for AlTiN age hardening [10], which then further transform into stable w-AlN [5, 10]. This thermally activated process was observed in PVD coatings with a purely cubic structure in the as-deposited state, where the decomposition process was studied intensively using transmission electron microscopy (TEM), calorimetric methods, atom probe tomography and diffraction techniques as well as modelling using the ab-initio approach [10–15].

Contrary to these findings, however, it was recently demonstrated, that using a low pressure chemical vapour deposition (LPCVD) technique, cubic $Al_xTi_{1-x}N$ and $Al_xTi_{1-x}CN$ coatings with a relatively high Al content of $x = 90\,\%$ can be synthesized under certain specific process conditions [16, 17]. Additionally the authors demonstrated in their previous work, that $Al_xTi_{1-x}N$ coatings with $x \cong 0.95$

consisting of a self-organized microstructure of soft Al-rich wurtzite and hard Ti-rich cubic nano-lamellae can be synthesized. Although the amount of Al is high, a relatively high hardness of about 27 GPa was found and attributed to the unique nano-lamellar microstructure. [18, 19].

As a continuation of the authors' work on LPCVD-based $Al_xTi_{1-x}N$ coatings, this contribution aims to present results from the characterization of a novel nano-lamellar $Al_{0.8}Ti_{0.2}N$ coating, which consists of a lamellar microstructure with alternating cubic phases. To date, there have been oral presentations at scientific conferences by Stiens *et al.* and Halvarsson *et al.* and there is a recently published patent [20] dealing with the synthesis and microstructure of similar Al-rich $Al_xTi_{1-x}N$ coatings with a cubic structure in as-deposited state.

The main aims of the present work are (i) primarily to analyse functional properties of the $Al_{0.8}Ti_{0.2}N$ coating, such as oxidation resistance, hardness after annealing at high temperatures in vacuum and phase stability and (ii) to describe the microstructure of the novel nano-lamellar $Al_{0.8}Ti_{0.2}N$ coating, since it is different from the coating reported in the patent and the aforementioned oral presentations.

E.2. Experimental details

The investigated coating was prepared in a Bernex MT-CVD-300 medium temperature reactor using the process gases $AlCl_3$, $TiCl_4$, NH_3 and N_2, with H_2 as a carrier gas. First a nanocrystalline TiN bonding layer with a thickness in the order of 100 nm was grown, before the 3 µm thick $Al_{0.8}Ti_{0.2}N$ layer with cubic–cubic nano-lamellar microstructure was deposited at 800 °C under a pressure of 2.5 kPa. Substrates were plain square cutting inserts made from WC–Co (6 wt. %) cemented carbide. The reference samples $Al_{0.95}Ti_{0.05}N$ with wurtzite–cubic alternating nano-lamellae were deposited with the same equipment onto substrates of the same kind, according to [18, 19]. In order to exclude any influence of Co diffusion from the substrate into the coating during high temperature tests, also other substrates were coated during the same deposition. These included wafers of polycrystalline and single crystalline (0001) Al2O3, as well as MgO (100), ferritic steel foil and austenitic steel plates. The microstructure of the coating was characterized by a JEOL JEM-2100F TEM equipped with a C_S corrector, using high resolution TEM imaging (HRTEM) and scanning TEM imaging (STEM). The coating's elemental composition was verified by energy dispersive X-ray spectroscopy (EDX) inside the TEM using an Oxford INCA Energy TEM 200 EDX system. Samples for the TEM were prepared by a Zeiss AURIGA CrossBeam focused ion beam (FIB) workstation equipped with a Cobra-Orsay-Physics FIB column, using a low current in order to minimize ion beam damage to the sample.

Oxidation tests were performed for 1 h in ambient air at constant temperatures in the range of $700 - 1000$ °C in steps of 50 °C. Samples were heated with 20 K/min and kept in the furnace for cooling. Vacuum annealing was performed in a HTM-Reetz cold wall vacuum furnace with tungsten net heating elements using a heating rate of 20 K/s, 30 min holding time and a cooling rate of 20 K/s, as far as possible. Hardness measurements were made on the vacuum-annealed samples with a CSIRO UMIS II indenter equipped with a Berkovich tip on lightly polished samples using a set of 25 indents each, with loads ranging from 15 to 25 mN. The evaluation was made according to the Oliver & Pharr method [21].

A Rigaku SmartLab 5-circle diffractometer with thin film attachment, equipped with Cu–Kα radiation, a primary parabolic multilayer mirror and a secondary graphite monochromator was used for XRD phase analysis. In order to suppress the substrate diffraction signal, the measurements were performed in grazing incidence geometry with 2.5 ° incidence angle, so that the X-ray penetration depth was about 0.7 µm.

E.3. Results and discussion

E.3.1. Microstructural characterization

In Fig. E.1a a HRTEM cross-sectional micrograph of the as-deposited $Al_{0.8}Ti_{0.2}N$ coating is presented, where the respective thicknesses of approximately 12 nm for the Al-rich lamellae and 2 nm for the Ti-rich lamellae are visible. The inset in Fig. E.1a shows a fast Fourier transform (FFT) of the micrograph, illustrating that both phases exhibit fcc structure. Further evidence for the same type of crystal structure in both kinds of lamellae is given by continuous lattice fringes that are also visible in Fig. E.1a, which further indicates that lamellae are coherent.

Since the focus of this study is primarily on the functional properties of the coating, only tentative investigations of the lamella composition were performed in TEM using EDX. The results indicated that the Al content in Al-rich lamellae within the as-deposited CVD-$Al_{0.8}Ti_{0.2}N$ is above $x = 0.67$, but still far from pure AlN and correspondingly there are traces of Al in Ti-rich lamellae. The detailed study of atomistic lamella compositions would require the elaboration of a very detailed chemical analysis, which is beyond the scope of this work.

The observed cubic crystal structure of the 12 nm thick Al-rich lamella raises a

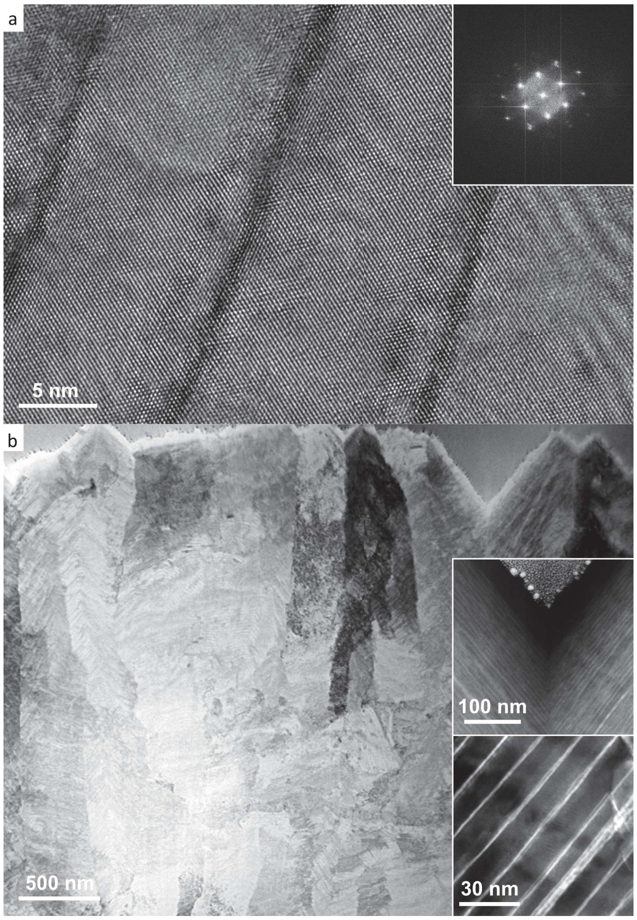

Figure E.1.: (a) HRTEM image of individual Al-rich (bright) and Ti-rich (dark) regions within an $Al_{0.8}Ti_{0.2}N$ coating, showing lamella thicknesses of 12 nm and 2 nm, respectively. Furthermore, continuous lattice fringes show that the nano-lamellae are coherent and a FFT (inset) of the shown micrograph demonstrates the cubic (fcc) crystal structure of both kinds of lamellae. (b) Cross-sectional bright field STEM image of an $Al_{0.8}Ti_{0.2}N$ coating showing the overall coating microstructure with columnar grains and zig-zagging lamellae. Single bright and dark grains are due to different grain orientations and changing diffracting conditions. The two insets show details of the surface region, as well as a high magnification view from a single grain interior, imaged using high angle annular dark field (HAADF) STEM. The high regularity of nano-lamellae is visible and a terminating Al-rich layer can be seen, which forms due to process control constraints.

question regarding the polytype stability. Since the coherent lamellae microstructure was observed (Fig. E.1a), the presence of an epitaxial relationship between fcc-Ti-rich and fcc-Al-rich lamellae is obvious. The stabilization of fcc-Al-rich phase by the fcc-Ti-rich phase, as a single cause for the fcc-Al-rich lamellae presence, is however not probable, because (i) Al-rich lamellae are significantly thicker than Ti-rich ones and (ii) it contradicts also the findings of Madan *et al.* [22] who stated a maximum thickness of 2 nm for pure AlN stabilized by pure TiN, considering the lattice mismatch between fcc AlN and TiN phases of 4.8 % [22]. Since the EDX analysis indicated that both TiN and AlN cubic lamellae contain also traces of Al and Ti atoms, respectively, it can be expected that the actual lattice mismatch between the two solid solutions Ti(Al)N and Al(Ti)N would be much smaller, thus permitting the locally epitaxial growth of thicker cubic Al-rich lamellae stabilized by comparatively thin Ti-rich lamellae [23, 24].

Another cause for the formation of cubic Al-rich lamellae could be found in film growth kinetics. One indication that this might be true is that the employed LPCVD process features an exceptional film growth rate in the order of 5 µm/h, leading to film growth conditions that are not necessarily near the thermodynamic equilibrium, even though the process temperature is relatively high.

Nano-lamellar microstructure was reported also in a recent publication by Ghafoor *et al.* [25], where a $Zr_xAl_{1-x}N$ thin film was grown onto MgO (001) under high mobility conditions. The $Zr_xAl_{1-x}N$ film had a self-organized nano-labyrinthine microstructure of interwoven single-crystalline cubic Zr-rich and hexagonal Al-rich phases, morphologically similar to the present nano-lamellar microstructure. It has to be pointed out, however, that this type of high temperature laminar growth is different to the present case for the following reasons. (i) In Ghafoor's work there is an epitaxial relationship between the single-crystalline substrate and the thin film, which is to some extent responsible for the formation of the lamellar structure, whereas here the WC–Co substrate is polycrystalline and no epitaxial growth is induced by the substrate. (ii) In the case of the $Zr_xAl_{1-x}N$ coating there is also the hexagonal phase present in the as-deposited state, which is explained by phase segregation of an immiscible system, occurring already during deposition. In the case of present $Al_{0.8}Ti_{0.2}N$ phase, however, it cannot be assumed that the phases present in the as-deposited state are already in a stable segregated state, as they clearly undergo further segregation and decomposition during annealing (*cf.* Section E.3.3, Fig. E.3).

As can be seen in Fig. E.1b, the CVD-$Al_{0.8}Ti_{0.2}N$ coating exhibits columnar grain morphology and nano-lamellae permeate the entire volume of every grain. This is contrary to the reference $Al_{0.95}Ti0_{.05}N$ coating, where small equiaxed lamellar grains were embedded in a cubic solid solution matrix [18, 19]. Lamellae extend over long distances and a characteristic zig-zag-like morphology within the individual grains is visible in cross-sectional view of Fig. E.1b. Moreover, the lamellae exhibit a relatively high regularity, even at the surface. The topmost layer is thicker and Al-rich, which is due to constraints from the deposition process control hardware. Moreover, it was observed during first preliminary machining tests (not presented here) that this layered type of microstructural architecture might be beneficial for the overall wear behaviour of the coating, as a slow and steady wear by layers could be seen, which seems to coincide with the global arrangement of nano-lamellae.

E.3.2. Oxidation resistance

Optical images of the oxidized $Al_{0.8}Ti_{0.2}N$ samples are presented in Fig. E.2. After the heat treatment at 800 °C, the coating samples showed first surface discoloration, while no delamination was observed until 900 °C. From then on, both the coating and the cemented carbide substrate showed significant oxide growth and within the next 100 °C the sample was destroyed completely. In comparison to the wurtzite–cubic nano-lamellar $Al_{0.95}Ti_{0.05}N$ reference sample, the onset of oxidation is about $150-200$ °C earlier, while the progression of oxidation over temperature is less rapid. This somewhat lowered oxidation resistance can be attributed to the reduced availability of Al for the formation of a protective Al_2O_3 natural oxide scale, which is related to the reduced Al content that was necessary in order to obtain cubic–cubic nano-lamellae. Hence the natural oxide overlayer still grows, but is very likely less dense and has a smaller thickness at the same temperature, thus being slightly less effective as an oxidation barrier. In many tooling applications of hard coatings, however, temperatures do not reach the high levels that $Al_{0.95}Ti_{0.05}N$ can withstand, or tools

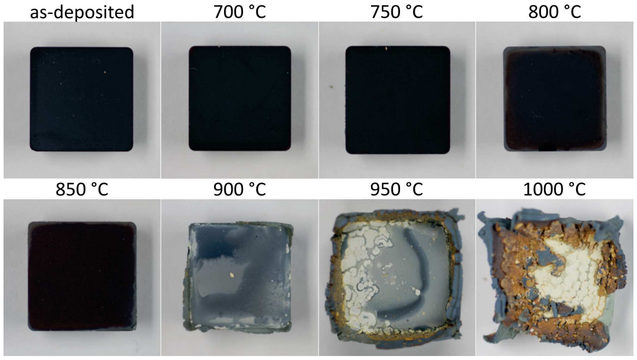

Figure E.2.: Optical images of $Al_{0.8}Ti_{0.2}N$ coating samples oxidized for 1 h at different temperatures in ambient air. Discoloration starts at 800 °C and significant oxide formation can be seen from 900 °C onwards. Above 1000 °C the samples are destroyed completely.

have a lifetime significantly shorter than the 1 h that was used in the oxidation test conditions of this work. Thus only a low detrimental impact of the lowered oxidation resistance is to be expected, when considering cubic $Al_{0.8}Ti_{0.2}N$ for cutting and tooling applications.

Typical PVD-$Al_xTi_{1-x}N$ coatings with a high Al concentration (usually up to $x \cong 0.7$) show broadly similar oxidation behaviour, depending on their phase composition, amount of growth defects (such as droplets in coatings grown by cathodic arc evaporation) and their general microstructure, as all of those parameters decisively influence oxygen mobility [4, 26–28].

E.3.3. Phase stability

After the $Al_{0.8}Ti0_{.2}N$ samples were annealed in vacuum at 500, 700 and $800 - 1100$ °C (in 50 °C steps), their phase composition was analysed by XRD. By comparing XRD scans of samples deposited onto various substrates it was possible to rule out an influence of Co diffusion on the phase stability. Fig. E.3 indicates that in the as-deposited state and at low temperatures, (i) the coating only consists of fcc phases and (ii) all diffraction peaks appear very broad with a low-angle asymmetry. The main contribution to the peaks' intensity originates from the Al-rich lamellae, since (i) their higher volume fraction also means a stronger diffraction signal and (ii) because the lattice parameter of fcc-AlN is smaller than that of TiN (Fig. E.3). Consequently, the low-angle asymmetric broadening (Fig. E.3) represents the diffraction signal from Ti-rich nanolamellae. Since the measurement was made with a fixed shallow incidence angle to avoid diffraction from the substrate, no straightforward information about preferred growth orientation can be obtained from relative peak intensities.

In the temperature range of $800 - 900$ °C (Fig. E.3), 111 and 220 diffraction peaks at 2θ angles of ~ 38 and $\sim 64\,°$ originating from the Al-rich phase shift increasingly to lower diffraction angles. Unfortunately it is not easy to quantify these shifts, due to overlapping peaks and the subsequently difficult peak position fitting, especially for the low-intensity peaks. Since the diffraction vector for these two peaks is oriented at approximately ~ 18 and $\sim 31\,°$ with respect to the substrate surface, the peak shifts can be interpreted (i) by an increase of tensile stresses in the coating due to the higher thermal stress contribution after the annealing to a temperature higher than deposition temperature and/or (ii) by a formation of nanoscopic defects which induce an increase in lattice parameter. The latter could be caused by a diffusion of Ti and Al atoms between or within lamellae and/or formation of dislocations at phase interfaces. To elucidate the origin of the peak shift, a further TEM analysis

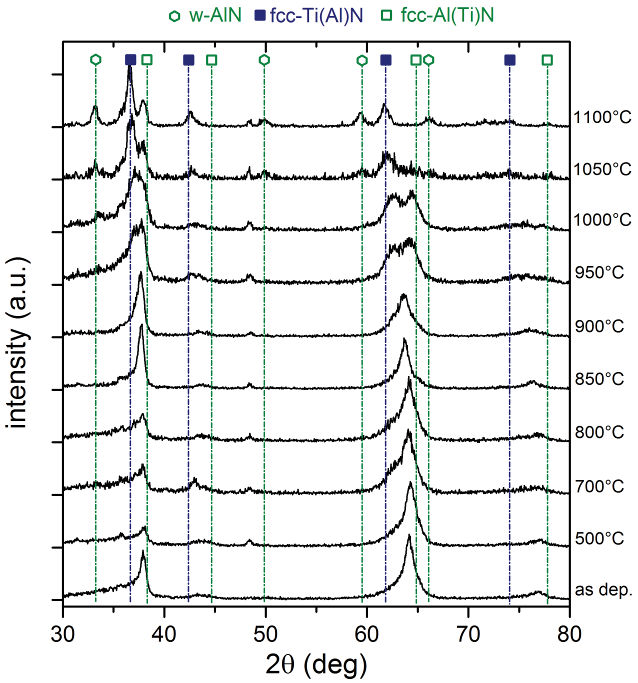

Figure E.3.: XRD scans of vacuum-annealed $Al_{0.8}Ti_{0.2}N$ coating samples, showing overlapping fcc peaks corresponding to Al-rich and Ti-rich lamellae of the nanocomposite microstructure. Up to 900 °C double peaks approach each other, and above that temperature, they separate again. This separation implies phase decomposition and is in agreement with the appearance of w-AlN from 1000 °C onwards. For enhanced clarity, the 00.2 w-AlN peak is not marked, since it overlaps with the 111 TiN peak, as well as some further w-AlN peaks that also remain unmarked, as their intensities are very low.

of annealed samples would be necessary, but that is beyond the scope of this work.

In the temperature range of 900 – 1000 °C (Fig. E.3), the 111 and 220 peak shifts are reversed (compared to the 800 – 900 °C range) and above 1000 °C the Al-rich phase peak intensities drop rapidly, while the peaks from the Ti-rich phase continue to shift noticeably in the opposite direction. From 950 °C onwards, also the hexagonal Al-rich phase emerges. These cubic phase peaks shifts towards the peak positions of the pure phases between 900 °C and 1000 °C indicate phase segregation, as it would be found during the first stage of high Al content $Al_xTi_{1-x}N$ spinodal decomposition [10, 11, 26]. Another point that fits well with the progression of spinodal decomposition is that the formation of the hexagonal Al-rich phase is slightly delayed with respect to the onset of peak separation at 900 °C. As can be recognized for the 220 cubic peaks at 900 °C, the peak positions of the Al-rich and

Ti-rich phase are very close and therefore the system should not be understood as already phase segregated and thus it is not unreasonable to assume that spinodal decomposition takes place above this temperature. With regards to the starting temperature of spinodal decomposition, it is likely that is modified by the presence of coherency strains.

The most essential information from this part of the study is the temperature range, in which the cubic solid solution phases of the Al-rich and Ti-rich lamellae were found to be stable, namely up to 900 °C, with an additional partial stability up to 1000 °C.

E.3.4. Hardness evolution

In comparison to the reference $Al_{0.95}Ti_{0.05}N$ coating with wurtzite and cubic nano-lamellae [18, 19], the cubic–cubic coating exhibits a significantly higher hardness in the as-deposited state, with a relative increase of more than 30 %, to about 36 GPa (Fig. E.4). This hardness enhancement remains in the range of $30 - 35$ % and reaches a maximum of 38 GPa at 950 °C. After the treatment at even higher temperatures the hardness started to decrease again, as recovery and recrystallization become dominant and as the hexagonal phase emerges (*cf.* Fig. E.3) [26]. Finally, at 1100 °C the measured value of 32 GPa is still significantly higher than for both reference coatings (*cf.* Fig. E.4). The higher hardness level, as compared to $Al_{0.95}Ti_{0.05}N$ [18, 19], can be related to the change of wurtzite Al-rich lamellae to a cubic crystal structure, since wurtzite Al(Ti)N is much softer in comparison [8].

On the other hand, in comparison to a reference PVD coating of composition $Al_{0.62}Ti_{0.38}N$ [26], another important contribution to the overall hardness stems from the nano-lamellar microstructure. This is similar to superlattice coatings, where high coherence strains between dense single layers (*cf.* Fig. E.1a) give rise to superior mechanical properties that cannot be explained by simple rule of mixture [24]. $Al_{0.95}Ti_{0.05}N$ however, also benefits from a nano-composite contribution to hardness, albeit probably not from a superlattice effect, since in that case w-Al(Ti)N lamellae are not necessarily coherent with fcc-Ti(Al)N lamellae [19].

E.4. Conclusions

An $Al_{0.8}Ti_{0.2}N$ coating containing a self-organized nano-lamellar microstructure was synthesized using a chemical vapour deposition technique. The individual lamellae consist of an either Al-rich or Ti-rich nitride solid solution and all lamellae have a cubic crystal structure in the as-deposited state. Lamellae are coherent and have a thickness of 12 nm and 2 nm, respectively.

Vacuum annealing tests revealed that up to 950 °C the coating is entirely composed of cubic phases while the shifts of cubic XRD peaks between 900 °C and 1000 °C indicate further phase segregation. Concurrently, although somewhat delayed, hexagonal phase peaks appear while the peaks from the Al-rich cubic phase disappear. This behaviour is consistent with that of a spinodally decomposing Al-rich $Al_xTi_{1-x}N$ coating. Additional shifts of cubic peaks were observed between 800 °C and 900 °C, but their origin is not apparent at this stage.

Nanoindentation measurements evidenced a high hardness of 36 GPa in the as-deposited state, which remains largely stable until the peak hardness of 38 GPa is reached at 950 °C, before the coating starts to soften. At 1100 °C hardness still remained at 32 GPa. Compared to an earlier self-organized nano-lamellar $Al_{0.95}Ti_{0.05}N$ coating, this means a hardness enhancement ranging between $30 - 35\,\%$.

Oxidation tests showed that the coating is stable in ambient air up to temperatures below 900 °C, while the ensuing oxide formation proceeds slowly in comparison to $Al_{0.95}Ti_{0.05}N$, which was partially stable up to 1100 °C, but already completely oxidized at 1150 °C [19].

In summary, the investigated coating promises a significant performance increase

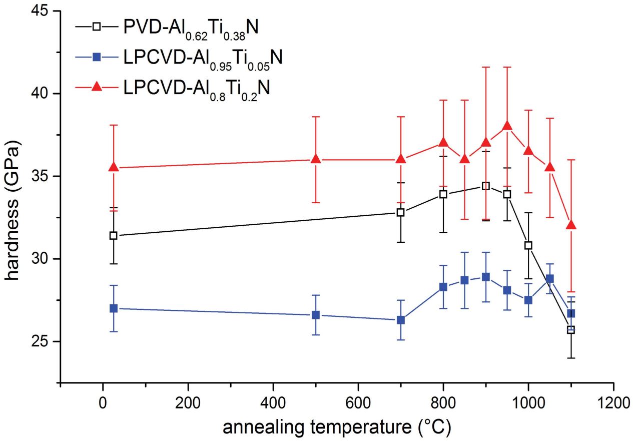

Figure E.4.: Nanohardness of an $Al_{0.8}Ti_{0.2}N$ coating as a function of annealing temperature, compiled for comparison with earlier self-organized nano-lamellar $Al_{0.95}Ti_{0.05}N$ and typical age-hardening Al-rich $Al_{0.62}Ti_{0.38}N$, deposited by magnetically unbalanced magnetron sputtering [26]. An increase in excess of 30 % over $Al_{0.95}Ti_{0.05}N$ can be seen at room temperature, while at high temperatures hardness stays largely stable. The investigated coating outperforms both reference coatings significantly at all investigated temperatures.

in application as a wear resistant coating for cutting tools under high loads and in dry conditions, and at temperatures up to about 900 °C.

Acknowledgements

Financial support from the Austrian Federal Government is gratefully acknowledged, in particular from the Österreichische Forschungsförderungsgesellschaft mbH under the CVDnanoCoat grant (No. 841137) and from the Styrian and Tyrolean Provincial Government within the COMET funding programme (grant No. 837900). The hardness characterization was performed by Dr. Rostislav Daniel and is highly appreciated.

Bibliography to paper E

[1] M. Stüber, L. Hultman, and A. Matthews, *Surf. Coat. Technol.* (2014) **257**, 1–2, DOI: 10.1016/j.surfcoat.2014.08.060.

[2] L. Hultman, *Vacuum* (2000) **57**, 1–30, DOI: 10.1016/S0042-207X(00)00143-3.

[3] S. PalDey, and S. Deevi, *Mater. Sci. Eng., A* (2003) **342**, 58–79, DOI: 10.1016/S0921-5093(02)00259-9.

[4] Y. Tanaka, T. M. Gür, M. Kelly, S. B. Hagstrom, T. Ikeda, K. Wakihira et al., *J. Vac. Sci. Technol., A* (1992) **10**, 1749–1756, DOI: 10.1116/1.577742.

[5] R. Rachbauer, E. Stergar, S. Massl, M. Moser, and P. Mayrhofer, *Scr. Mater.* (2009) **61**, 725–728, DOI: 10.1016/j.scriptamat.2009.06.015.

[6] R. Zhang, and S. Veprek, *Mater. Sci. Eng., A* (2007) **448**, 111–119, DOI: 10.1016/j.msea.2006.10.012.

[7] A. Kimura, H. Hasegawa, K. Yamada, and T. Suzuki, *Surf. Coat. Technol.* (1999) **120–121**, 438–441, DOI: 10.1016/S0257-8972(99)00491-0.

[8] A. Guillaumot, F. Lapostolle, C. Dublanche-Tixier, J. C. Oliveira, A. Billard, and C. Langlade, *Vacuum* (2010) **85**, 120–125, DOI: 10.1016/j.vacuum.2010.04.012.

[9] D. McIntyre, J. E. Greene, G. Hakansson, J.-E. Sundgren, and W.-D. Munz, *J Appl Phys* (1990) **67**, 1542–1553, DOI: 10.1063/1.345664.

[10] P. Mayrhofer, A. Hörling, L. Karlsson, J. Sjölén, T. Larsson, C. Mitterer et al., *Appl Phys Lett* (2003) **83**, 2049–2051, DOI: 10.1063/1.1608464.

[11] R. Rachbauer, S. Massl, E. Stergar, D. Holec, D. Kiener, J. Keckes et al., *J Appl Phys* (2011) **110**, 11, DOI: 10.1063/1.3610451.

[12] I. A. Abrikosov, A. Knutsson, B. Alling, F. Tasnadi, H. Lind, L. Hultman et al., trans. by s, *Materials* (2011) **4**, 1599–1618, DOI: 10.3390/ma4091599.

[13] L. Johnson, M. Thuvander, K. Stiller, M. Odén, and L. Hultman, *Thin Solid Films* (2012) **520**, 4362–4368, DOI: 10.1016/j.tsf.2012.02.085.

[14] A. Riedl, R. Daniel, J. Todt, M. Stefenelli, D. Holec, B. Sartory et al., *Surf. Coat. Technol.* (2014) **257**, 108–113, DOI: 10.1016/j.surfcoat.2014.03.045.

[15] M. Bartosik, R. Daniel, Z. Zhang, M. Deluca, W. Ecker, M. Stefenelli et al., *Surf. Coat. Technol.* (2012) **206**, 4502–4510, DOI: `10.1016/j.surfcoat.2012.02.035`.

[16] I. Endler, M. Hähn, M. Herrmann, R. Pitonak, S. Ruppi, M. Schneider et al., *Surf. Coat. Technol.* (2008) **203**, 530–533, DOI: `10.1016/j.surfcoat.2008.04.098`.

[17] I. Endler, M. Hähn, M. Herrmann, H. Holzschuh, R. Pitonak, S. Ruppi et al., *Surf. Coat. Technol.* (2010) **205**, 1307–1312, DOI: `10.1016/j.surfcoat.2010.09.002`.

[18] J. Keckes, R. Daniel, C. Mitterer, I. Matko, B. Sartory, A. Köpf et al., *Thin Solid Films* (2013) **545**, 29–32, DOI: `10.1016/j.tsf.2013.08.001`.

[19] J. Todt, R. Pitonak, A. Köpf, R. Weißenbacher, B. Sartory, M. Burghammer et al., *Surf. Coat. Technol.* (2014) **258**, 1119–1127, DOI: `10.1016/j.surfcoat.2014.07.022`.

[20] D. Stiens, T. Manns, and S. Ruppi, DE102014103220, (2015)

[21] W. Oliver, and G. Pharr, *J Mater Res* (1992) **7**, 1564–1580, DOI: `10.1557/JMR.1992.1564`.

[22] A. Madan, I. W. Kim, S. C. Cheng, P. Yashar, V. P. Dravid, and S. A. Barnett, *Phys Rev Lett* (1997) **78**, 1743–1746, DOI: `10.1103/PhysRevLett.78.1743`.

[23] R. Bruinsma, and A. Zangwill, *J. Physique I* (1986) **47**, 2055–2073, DOI: `10.1051/jphys:0198600470120205500`.

[24] A. Cavaleiro, and J. T. M. De Hosson, *Nanostructured Coatings*, Springer New York, (2006) DOI: `10.1007/978-0-387-48756-4`.

[25] N. Ghafoor, L. J. S. Johnson, D. O. Klenov, J. Demeulemeester, P. Desjardins, I. Petrov et al., *APL Materials* (2013) **1**, 022105, DOI: `10.1063/1.4818170`.

[26] L. Chen, J. Paulitsch, Y. Du, and P. H. Mayrhofer, *Surf. Coat. Technol.* (2012) **206**, 2954–2960, DOI: `10.1016/j.surfcoat.2011.12.028`.

[27] A. Hörling, L. Hultman, M. Odén, J. Sjölén, and L. Karlsson, *J. Vac. Sci. Technol., A* (2002) **20**, 1815, DOI: `10.1116/1.1503784`.

[28] M. Lembke, D. Lewis, and W.-D. Muenz, *Surf. Coat. Technol.* (2000) **125**, 263–268, DOI: `10.1016/S0257-8972(99)00571-X`.

F

Cross-sectional stress distribution in Al$_x$Ga$_{1-x}$N heterostructure on Si(111) substrate characterized by ion beam layer removal method and precession electron diffraction

M. Reisinger[1], J. Zalesak[2], R. Daniel[2], M. Tomberger[3], J.K. Weiss[4], A.D. Darbal[4], M. Petrenec[5], J. Zechner[6], I. Daumiller[3], W. Ecker[7], B. Sartory[7], J. Keckes[1]

[1]Department of Materials Physics, Montanuniversität Leoben, Leoben, Austria
[2]Department of Physical Metallurgy and Materials Testing, Montanuniversität Leoben, Leoben, Austria
[3]Infineon Technologies Austria AG, Villach, Austria
[4]AppFive LLC, Tempe, AZ, USA
[5]TESCAN Brno s.r.o., Libušina tř. 1, Brno, Czech Republic
[6]KAI Kompetenzzentrum Automobil - u. Industrieelektronik GmbH, Villach, Austria
[7]Materials Center Leoben Forschung GmbH, Roseggerstraße 12, Leoben, Austria

Abstract

A residual stress depth gradient is characterized in a 1.8 μm thick AlN/Al$_{0.25}$Ga$_{0.75}$N/-GaN/Al$_{0.22}$Ga$_{0.78}$N heteroepitaxial structure grown using metallic-organic chemical vapour deposition on Si(111) substrate. The cross-sectional stress profile is evaluated with a step of 100 nm using ion beam layer removal (ILR) method based (i) on a sequential focused ion beam milling of a microcantilever, (ii) on an evaluation of a cantilever bending after every milling step and (iii) on a stress profile recalculation using finite element simulation. The profile shows tensile stress of

~1.5 GPa in AlN nucleation layer, stress changing from compressive to tensile in $Al_{0.25}Ga_{0.75}N$ and GaN sublayers and relatively small stresses below 100 MPa in the top $Al_{0.22}Ga_{0.72}N$ sublayer. The stress profile is qualitatively correlated with the results from precession electron diffraction which indicates approximately the same stress behavior. The cross-sectional stress magnitude and variation are interpreted by the mismatches of lattice constants and coefficients of thermal expansion as well as by growth mode changes during $Al_{0.25}Ga_{0.75}N$ and GaN sublayer formation. The approach demonstrates the possibility to resolve nanoscale variation of residual stresses in heteroepitaxial structures using ILR method.

F.1. Introduction

GaN and related semiconductors possess extensive technological potential because of their remarkable optical and electrical properties utilized especially in high-power electronic and optical devices [1]. Due to the availability of relatively lowcosts and large size Si substrates, there has been a significant effort to grow GaN thin films on Si by metallic-organic chemical vapour deposition (MOCVD) [2, 3]. There is however (i) a large lattice mismatch of ~17 % and (ii) a large mismatch of coefficients of thermal expansion (CTEs) of ~–56 % between Si and GaN [4, 5]. For this reason, several production quality issues like (i) insufficient GaN crystal quality, (ii) wafer bow, (iii) film brittleness and cracking and (iv) inhomogeneous film properties across the wafer had to be minimized [2, 6, 7]. Most of those issues can be directly or indirectly related to stresses formed in the film during the MOCVD growth and during cooling down after the process [8, 9]. Therefore, the characterization, the understanding and the optimization of the stress state represent fundamental topics in the development of high crystal quality GaN films on heteroepitaxial substrates.

In order to manage stresses in GaN thin films, an AlN nucleation layer and $Al_xGa_{1-x}N$ transition layers have been applied primarily (i) to minimize the wafer-bow and (ii) to produce crack-free $Al_xGa_{1-x}N$ films on Si [10, 11]. By changing the thickness, the morphology and the stoichiometry of the layers, it has been possible to tune the stress state in GaN effectively. Especially the growth of an AlN nucleation layer on Si(111) substrates represented a significant achievement in the stress management and in the improvement of GaN crystal quality [11, 12].

In majority of the cases, stress characterization in GaN films has been performed using X-ray diffraction (XRD), Raman spectroscopy and wafer-bow measurements [7, 11, 13]. Usually volume-averaged stresses were determined for individual sublayers or even for the complete heterostructures by analyzing (i) complete heterostructures or (ii) individual sub-layers in stepwise deposited heterostructures.

In order to effectively control stresses in $Al_xGa_{1-x}N$ heterostructures, there is a need to avoid especially tensile and compressive stress concentrations within the structures, which are favourable for crack initiation and subsequent propagation [14, 15]. In order to identify heterostructure regions with such critical stress states, a detailed cross-sectional stress characterization over the as-deposited structures at sub-micron scale is necessary.

The aim of this contribution is to characterize a residual stress profile in a representative $Al_xGa_{1-x}N$ heterostructure on Si(111) using focused ion beam (FIB) based ion beam layer removal (ILR) method. This relatively new experimental technique, first proposed in 2007, has been already applied to polycrystalline, single crystalline as well as amorphous thin films [16–20]. Also methodological aspects and related errors have been discussed extensively. The stress characterization is performed by analyzing the curvature of FIB machined micro-cantilevers which consist of the thin film and a certain portion of a substrate. The film is incrementally thinned by FIB and the stress state in the remaining film region is subsequently determined from the actual cantilever deflection. Since the deflection of the cantilever is recorded after each FIB milling step, the calculation of the internal stress profile across the film thickness with the spatial resolution of themilling steps is straightforward. The approach can be complimented with a finite-element (FE) simulation, considering anisotropic film and substrate elastic properties [19]. One very important prerequisite to use the ILR method is the negligible plastic deformation within film and substrate during the whole FIB milling process. In this work, the ILR method is used for the first time to quantify stress gradients in an epitaxial heterostructures consisting of a sequence of single crystalline sublayers. Complementary precession electron diffraction [21–24] is used to verify the results from ILR method qualitatively.

F.2. Experiment

The $AlN/Al_{0.25}Ga_{0.75}N/GaN/Al_{0.22}Ga_{0.78}N$ heterostructure with a thickness of 1.8 µm was grown on a 6 in. Si wafer with (111) orientation using an Aixtron G5 planetary MOCVD reactor. Trimethylaluminum (TMA), trimethylgallium (TMG) and ammonia (NH_3) were used as precursors for aluminium, gallium and nitrogen, respectively. The carrier gas was hydrogen (H_2). Fig. F.1 shows the heterostructure cross-sectional morphology with thicknesses and compositions of the individual sublayers.

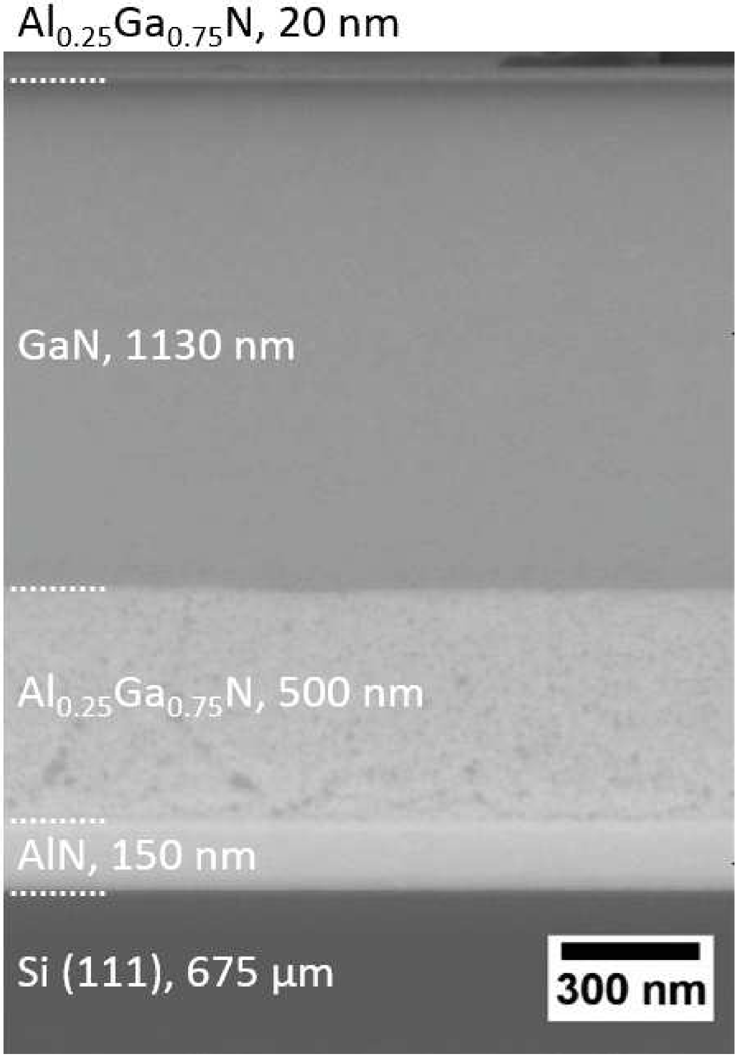

Figure F.1.: A scanning electron microscopy micrograph from the heterostructure on Si(111) substrate with thicknesses of the individual sublayers.

A Rigaku SmartLab 5 circle diffractometer equipped with a CuKα radiation, a parabolic multilayer mirror and a Ge(400) 2-bounce monochromator in the primary beam was used for an XRD analysis. A symmetric diffraction scan was used to obtain basic structural data from the heterostructure.

A plate with an area of $1 \times 1\,\mathrm{cm}^2$ was cut out from the wafer using a diamond wire saw. Subsequently, one edge of the plate was polished with an ion-polisher Hitachi E-3500 to remove the deformation layer produced by the saw cutting process. In this

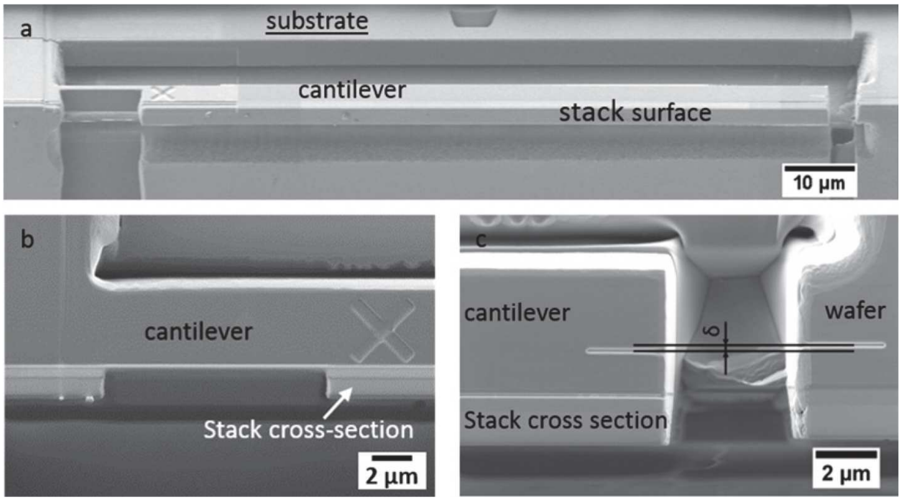

Figure F.2.: A scanning electron micrograph of a FIB machined microcantilever (a). A detailed view of the microcantilever with the region, which was incrementally milled in steps of 100 nm using FIB (b). The mutual positions of tw omarkers milled into the microcantilever and into the wafer (c) were used to quantify the microcantilever deflection δ caused by the stress state in the remaining heterostructure region (b).

step, low energy Ar ions were used to remove the material which was not covered by a mask. In the vicinity of the pre-treated edge, a microcantilever with the dimensions of $110.9 \times 5.9 \times 3.4\ \mu\mathrm{m}^3$ (Fig. F.2a) was fabricated using a Zeiss Auriga workstation, which combines a gallium operated focussed ion beam (FIB) and a high resolution scanning electron microscope (SEM).

After the microcantilever was fabricated, it possessed a curvature caused by the presence of the residual stress state in the heterostructure. This curvature was quantified by the measurement of a deflection δ between the microcantilever and the remaining wafer (Fig. F.2c). As a next step, heterostructure sections in the cantilever region from Fig. F.2b were removed incrementally in steps of 100 nm using FIB. The gradual FIB milling was performed with a relatively low ion current of 50 pA and high voltage of 30 kV. After everymilling step, the remaining thickness of the structure (Fig. F.2b) and the deflection (Fig. F.2c) were measured by SEM with accuracy better than ∼14 nm. As supplementary material, Videos 1 and 2 are provided which were collected during the cantilever machining and show the stepwise material removal and the changes in the cantilever deflection δ.

In order to determine the residual stress distribution $\sigma(z)$ from the measured microcantilever deflections as a function of the heterostructure depth z, a three di-

Table F.1.: Single crystal elastic constants in GPa used in the FE model [28–30].

Elastic constant	GaN	AlN	Si
C_{11}	390	410	165
C_{12}	145	149	64
C_{13}	106	99	
C_{33}	398	389	
C_{44}	105	125	80

mensional finite element model (FEM) using a commercial software package Abaqus was developed and used in a least square optimization procedure. In order to minimize the influence of the boundary conditions at the root of the cantilever, the geometrical model was not only reduced to the microcantilever itself but included also a block of the base structure of three times the width, about two times the height and about one third the length of the microcantilever. The boundary conditions fixed the displacement perpendicular to the limit faces of this block to zero. The cross-sectional heteroepitaxial structure morphology from Fig. F.1 was considered. The elastic properties of the individual sublayers and Si from Table F.1 were used. The elastic behaviour of $Al_{0.25}Ga_{0.75}N$, $Al_{0.22}Ga_{0.78}N$ and GaN was set to be identical, which is, with respect to the small difference in the elastic constants of GaN and AlN, a reasonable assumption. The finite elementmesh consisted of 84,180 s order hexagonal brick elements with reduced integration (C3D8R). For performance reasons, the chosen maximum aspect ratio of 15 was rather high, but mesh sensitivity studies showed no negative effect onto the results. The residual stress distribution across the structure was determined using an iterative optimization until calculated deflections matched the experimental data. In the present case, a gradient-based Levenberg-Marquardt algorithm [25, 26] was used. The residual stress re-calculation procedure is described in detail in Refs. [19, 27].

Based on the error analysis discussed in previous studies, residual stress magnitudes across the heteroepitaxial structure were determined using ILR method with an error smaller than ∼15 %.

In order to qualitatively verify the cross-sectional stress distributions in the heteroepitaxial structure determined using ILR, position-resolved precession electron diffraction (PED) patterns were acquired from a cross section of the layer stack. PED has been developed recently as a means to very precisely measure small amounts of elastic strain, and when combined with a field emission gun transmission electron microscope (TEM), the spatial resolution can approach 1 nm [21, 22]. For this purpose, two cross-sectional TEM lamellae with a thickness of ∼100 nm were fabricated using a Tescan GAIA3 FIB workstation from the heterostructure. In order to protect the layer structure from ion damage, a platinum line was deposited on the surface before the FIB milling. The lamellae were prepared using standard preparation steps with a last cleaning step of low energy (5 kV) to reduce the ion beam damage. In one lamella denoted further as L1, the heterostructure was free standing, disconnected from the substrate, in order to remove the stress induced by the Si substrate. In the second lamella denoted further as L2, the heterostructure was firmly connected to the substrate and therefore it was supposed that the uniaxial stress component induced by the substrate along the lamella interface, the stress of the first order, was still preserved. PED patterns were acquired using a Zeiss Libra 200 FE TEM operating at 200 kV and equipped with a NanoMEGAS DigiStar precession device controlled by Topspin Strain Measurement software. For this investigation the TEM was set to STEM mode with a camera length of 180 mm and the precession angle was set to 1.02 °. The condenser lens setting with a condenser aperture of 5 µm enabled a quasi-parallel nanobeam with a convergent angle of 1 mrad and a probe size of 1.5 nm. For the strain mapping the lamella L2 was scanned over a predefined area and the diffraction patterns were recorded by using an external ultrafast CCD camera mounted in front of the TEM screen. The spatial resolution was limited by the step size which was set to 2 nm for the series scans. The unstrained reference patterns were acquired from the relaxed surface region of the lamella L2. For a comparison, unstrained patterns were collected also form the (unstrained) lamella L1 providing very similar results as the calibration patterns obtained from the lamella L2.

The PED patterns were analyzed with the Topspin Strain Measurement software to determine the variation in the lattice parameter at each depth in the heterostructure [21]. The data were used to evaluate the variation in the ratio between lattice parameters c and a of the hexagonal sublayers within the heterostructure. The experimentally obtained ratio depth profile $c(z)/a(z)$ was then compared with tabulated values c_o/a_o of unstressed lattice parameters of the respective materials from the literature.

F.3. Results

In Fig. F.3, XRD pattern obtained from the heteroepitaxial structure is presented. Besides the substrate 111 reflection, there are 0002 reflections from $\mathrm{Al}_x\mathrm{Ga}_{1-x}\mathrm{N}$ sub-

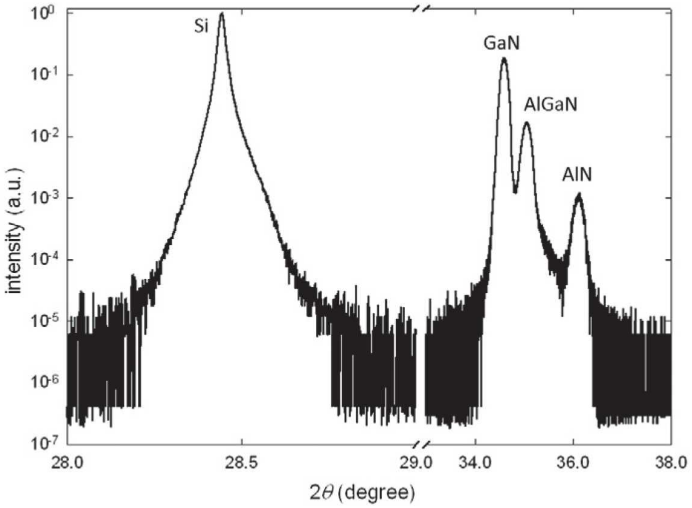

Figure F.3.: XRD pattern collected from the heteroepitaxial structure with 111 peak of Si and 0002 peaks of GaN, $Al_{0.25}Ga_{0.75}N$ and AlN detected at 2Θ positions of 28.443, 35.057, 35.599 and 36.1185 with FWHMs of 0.025, 0.159, 0.219 and 0.214, respectively.

layers visible. The diffraction data document the growth of the hexagonal sublayers with (0001) crystallographic planes approximately parallel to the substrate (111) plane. Unfortunately, a diffraction signal from the top 20 nm thick $Al_{0.22}Ga_{0.78}N$ sublayer (Fig. F.1) is in Fig. F.3 not visible. In Fig. F.4, cantilever deflections δ after the individual milling steps are presented as a function of the remaining heterostructure thickness (Fig. F.2b). The complex δ dependence can be at this stage qualitatively interpreted by a presence of a non-linear residual stress distribution within the film. The two deflection maxima in $Al_{0.25}Ga_{0.75}N$ and GaN at ∼250 and ∼800 nm in Fig. F.4 document the presence of pronounced stress changes as a function of film depth $\delta\sigma(z)/\delta z$ in these sublayers.

The deflection data from Fig. F.4 were used to calculate the residual stress distribution within the structure using the FEM algorithm. In Fig. F.5 , the evaluated cross-sectional stress distribution in the heterostructure is presented. The stress profile $\sigma(z)$ documents a relatively high tensile stress of ∼1.5 GPa in the interface AlN sublayer which changes to high compressive stress state of ∼1 GPa in $Al_{0.25}Ga_{0.75}N$. Interestingly, residual stresses change from compressive to tensile in both $Al_{0.25}Ga_{0.75}N$ and GaN sublayers. At the heterostructure surface the stress practically vanishes. A comparison of the data from Figs. F.4 and F.5 documents that the two pronounced peaks in $\delta(z)$ in Fig. F.4 correspond to abrupt stress changes

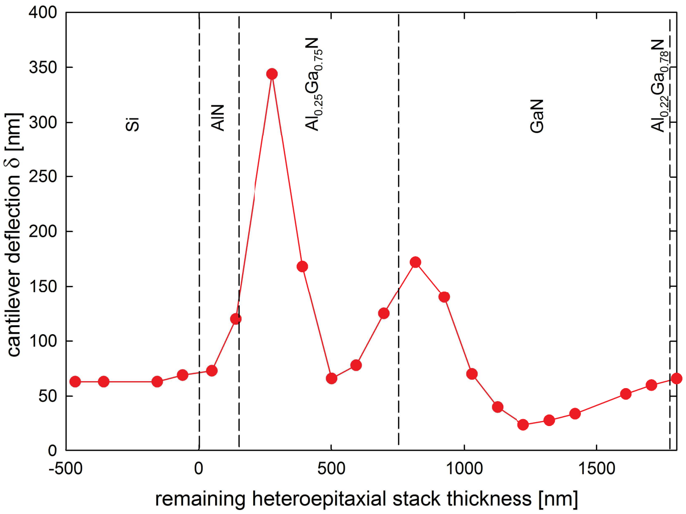

Figure F.4.: The measured deflection δ of the free standing microcantilever determined during the incremental FIB milling experiments (Fig. F.2) as a function of the remaining heterostructure thickness indicates a nonlinear variation of the stress state. The nonzero cantilever deflection at $\sim\delta(0)$ corresponds to the stress free state in the film.

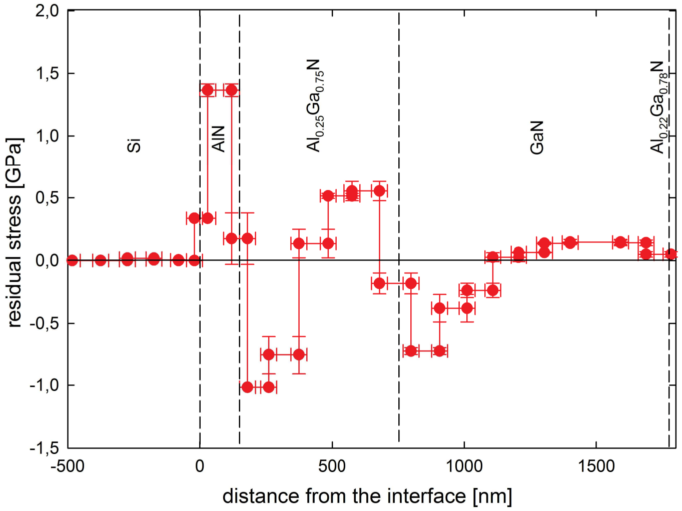

Figure F.5.: Cross-sectional stress distribution of residual stresses in $Al_xGa_{1-x}N$ heterostructure on Si(111) evaluated using FEM documents a presence of relatively high tensile and compressive stress concentrations. The stepwise form of the stress profile originates from the applied FIB milling depth steps of ∼100 nm (Fig. F.2b).

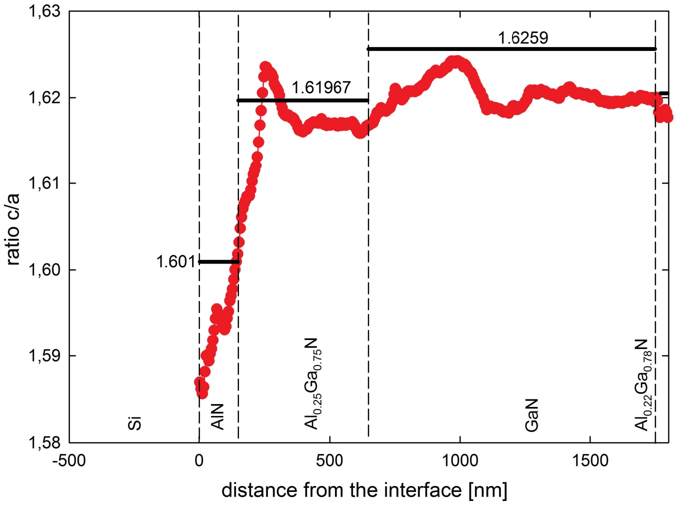

Figure F.6.: Cross-sectional dependence of the lattice parameter ratio $c(z)/a(z)$ determined using PED. Bold vertical lines represents magnitudes of unstressed lattice parameter ratios co/ao of the individual sublayer materials [31]. Experimental points lying above and below those lines are expected to represent heterostructure regions under compression and tension, respectively.

at interfaces between AlN/$Al_{0.25}Ga_{0.75}N$ and $Al_{0.25}Ga_{0.75}N$/GaN. Also the valley between the two peaks in Fig. F.4 corresponds to the compressive-to-tensile stress transition within $Al_{0.25}Ga_{0.75}N$ sublayer.

As already mentioned, position-resolved precession electron diffraction was used to evaluate $c(z)/a(z)$ as a function of the heterostructure depth. The data presented in Fig. F.6 are compared with the literature values of GaN and AlN unstressed lattice parameter ratios c_o/a_o [31]. For $Al_xGa_{1-x}N$ sublayers, the ratios were calculated using Vegard's law. In the case of uniaxial stressed TEM lamella, tensile and compressive stresses would induce elastic crystal lattice deformation with $c(z)/a(z)$ ratios smaller and larger than the values of co/ao.

In Fig. F.7 , a cross-sectional TEM micrograph of the heterostructure is shown. The micrograph shows a relatively high concentration of structural defects in the interface AlN sublayer as well as in the $Al_{0.25}Ga_{0.75}N$ and GaN sublayers next to AlN and $Al_{0.25}Ga_{0.75}N$ sublayers, respectively. The gradients of the defect density across the $Al_{0.25}Ga_{0.75}N$ and GaN sublayers indicate a continuous improvement of their crystallographic quality and were used to interpret the stress data from Fig. F.5.

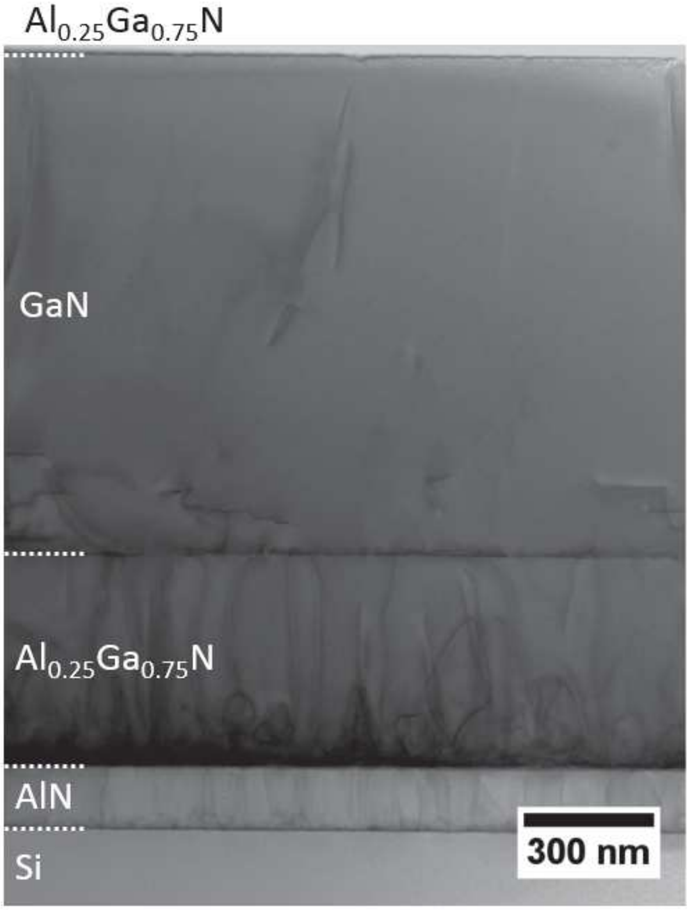

Figure F.7.: Cross-sectional TEM lamella from the heterostructure indicates a relatively high density of structural defects in the AlN sublayer as well as gradients of the defect density in the $Al_{0.25}Ga_{0.75}N$ and GaN sublayers.

F.4. Discusion

Residual stress profile from Fig. F.5 obtained using the ILR method was qualitatively confirmed by the PED experiment. High tensile stress within the AlN sublayer shown in Fig. F.5, which decreases towards the AlN/$Al_{0.25}Ga_{0.75}N$ interface, is in reasonable agreement with the $c(z)/a(z)$ values from Fig. F.6. Also the stress dependence in the $Al_{0.25}Ga_{0.75}N$ sublayer with a compressive-to-tensile stress transition (Fig. F.5) correlates relatively well with the $c(z)/a(z)$ behaviour from Fig. F.6, where also a stress reversal was observed. The ILR results for the GaN sublayer from Fig. F.5 indicates a presence of compressive stress, which decreases towards the surface, becomes tensile and then practically vanishes. This behaviour was unfortunately not fully confirmed by the $c(z)/a(z)$ dependence in Fig. F.6,where the stress state remained always tensile within GaN. This discrepancy could be interpreted e.g. by the used incorrect c_o/a_o ratio in Fig. F.6 and/or by a very probable partial stress relaxation in the surface region of the TEM lamella. In general, however, the results from Fig. F.6 confirm, at least qualitatively, the stress-depth dependence obtained using the ILR method.

XRD data from Fig. F.3 were used to evaluate the out-of-plane lattice spacing c of 0.49697 and 0.51152 nm for AlN and GaN sublayers, respectively. The experimental values appear smaller than the literature values of the AlN and GaN lattice parameters c of 0.4982 and 0.5186 nm from Ref. [32]. Therefore the XRD results from Fig. F.3 indicates the presence of tensile stresses in the nitride sublayers, in agreement with the PED data from Fig. F.6. Similarly, also the tensile stresses evaluated using the ILR method in the AlN sublayer (Fig. F.5) are qualitatively in agreement with the XRD results from Fig. F.3. The oscillatory stress profile with the near zero sum of the stresses in the GaN sublayer (Fig. F.5), however, disagrees with the XRD data (Fig. F.3). Possible explanations could be an uncertainty in the stress magnitude of the GaN sublayer surface region determined using the ILR method (Fig. F.5) and/or a stronger contribution of the tensely-stressed GaN sublayer near-surface region (cf. Fig. F.5) to the XRD signal in Fig. F.3.

The data from Fig. F.6 indicate a very complex stress profile within the heteroepitaxial structure. The AlN interface layer (Fig. F.1) is standardly used to improve the crystalline quality and to reduce tensile stresses in subsequent $Al_xGa_{1-x}N$ sublayers [11, 12, 33]. The high tensile stress up to 1.5 GPa observed in this sublayer can be interpreted as being caused by a large lattice and CTEs mismatches between AlN and Si [3, 4]. The layer can obviously accommodate very large tensile stresses. This ability can be interpreted by the presence of nanometer-sized crystalline domains within AlN sublayer (Fig. F.7). According to Blasing et al. [11], the AlN layer deteriorates the coherence between subsequent layers and the underlying substrate, which subsequently results in lower stresses and better crystallographic quality of subsequent sublayers. The presence of relative high compressive stresses in $Al_{0.25}Ga_{0.75}N$ and GaN sublayers at the interfaces to AlN and $Al_{0.25}Ga_{0.75}N$ can be interpreted by the smaller lattice constants of AlN and $Al_{0.25}Ga_{0.75}N$ with respect to the subsequent sublayers, respectively. The stress transition from compressive to tensile within the $Al_{0.25}Ga_{0.75}N$ and GaN sublayers can be explained by changes in the growthmodes fromthe nucleation, three-dimensional growth and subsequent lateral overgrowth to coalescence [34–36]. This is in agreement with the changes in the defect density gradients across the $Al_{0.25}Ga_{0.75}N$ and GaN sublayers visible in Fig. F.7. Finally, in the top $Al_{0.22}GaN_{0.78}N$ sublayer, the tensile stress is relatively low (Fig. F.5), resulting in nearly equilibrium physical properties without the stress influence.

The stress profile from Fig. F.6 can also be discussed from the point of view mechanical stability of the structure. The tensile stress concentrations are obviously very unfavourable for the fracture toughness of the heterostructure. The cracks can be initiated especially at the interface between the AlN sublayer and Si substrate and propagate along the interface to release the tensile stress. Though the tensile stress magnitudes in the $Al_{0.25}Ga_{0.75}N$ and GaN sublayers are significantly smaller than the tensile stress state in AlN, the actual tensile strength of the $Al_{0.25}Ga_{0.75}N$ and GaN ceramic sublayers is expected to be significantly smaller than that of AlN with nanometer-sized crystalline domains (Fig. F.7). Therefore also tensile stresses in $Al_{0.25}Ga_{0.75}N$ and GaN sublayers can represent a serious reliability issue.

F.5. Conclusions

The ILR method was used to determine the cross-sectional residual stress profile across the $AlN/Al_{0.25}Ga_{0.75}N/GaN/Al_{0.22}Ga_{0.72}N$ heterostructure on Si(111). A FEM was used to quantify the actual stress depth profile by using the microcantilever deflection data obtained during sequential FIB heterostructure milling. The results indicate very complex stress dependence with a large tensile stress of 1.5 GPa in the AlN sublayer, compressive-to-tensile stress transition within the $Al_{0.25}Ga_{0.75}N$ and GaN sublayers and relative low tensile stress below 100 MPa in the top $Al_{0.22}Ga_{0.72}N$ sublayer. The stresses were correlated with the lattice and CTE mismatches as well as with the variation of the sublayer growth modes. Complementary, precession TEM was used to determine the cross-sectional variation of the lattice parameters $c(z)/a(z)$, which qualitatively confirms the stress-depth variation determined by the ILR method. Supplementary data to this article can be found online at `http://dx.doi.org/10.1016/j.matdes.2016.06.001`.

Acknowledments

This work was jointly funded by the Austrian Research Promotion Agency (FFG Grant No. 854247) and the Carinthian Economic Promotion Fund (KWF Grant No. KWF-1521/28101/40388). The stress characterization of the heterostructure has received research funding from the European Union, within the large collaborative project ISTRESS, Grant Agreement No. 604646. Financial support by the Austrian

Federal Government (in particular from the Bundesministerium für Verkehr, Innovation und Technologie and Bundes-ministerium für Wissenschaft, Forschung und Wirtschaft) represented by Österreichische Forschungs-förderungsgesellschaft mbH and the Styrian and the Tyrolean Provincial Government, represented by Steirische Wirtschaftsförderungsgesellschaft mbH and Standortagentur Tirol, within the framework of the COMET Funding Programme is gratefully acknowledged.

Bibliography to paper F

[1] W. A. Hadi, M. S. Shur, and S. K. O'Leary, *Journal of Materials Science: Materials in Electronics* (2014) **25**, 4675–4713, DOI: 10.1007/s10854-014-2226-2.

[2] B. Leung, J. Han, and Q. Sun, *physica status solidi* (2014) **11**, 437–441, DOI: 10.1002/pssc.201300690.

[3] A. Dadgar, J. Bläsing, A. Diez, A. Alam, M. Heuken, and A. Krost, *Japanese Journal of Applied Physics* (2000) **39**, L1183, DOI: 10.1143/JJAP.39.L1183.

[4] J. del Alamo, and J. Joh, *Microelectronics Reliability* (2009) **49**, 1200–1206, DOI: 10.1016/j.microrel.2009.07.003.

[5] F. Scholz, *Semiconductor Science and Technology* (2012) **27**, 024002, DOI: 10.1088/0268-1242/27/2/024002.

[6] D. G. Zhao, S. J. Xu, M. H. Xie, S. Y. Tong, and H. Yang, *Applied Physics Letters* (2003) **83**, 677–679, DOI: 10.1063/1.1592306.

[7] B. Zhang, and Y. Liu, *Chinese Science Bulletin* (2014) **59**, 1251–1275, DOI: 10.1007/s11434-014-0169-x.

[8] E. Feltin, B. Beaumont, M. Laügt, P. de Mierry, P. Vennegues, H. Lahreche et al., *Applied Physics Letters* (2001) **79**, 3230–3232, DOI: 10.1063/1.1415043.

[9] A. Dadgar, M. Poschenrieder, J. Bläsing, K. Fehse, A. Diez, and A. Krost, *Applied Physics Letters* (2002) **80**, 3670–3672, DOI: 10.1063/1.1479455.

[10] A. Watanabe, T. Takeuchi, K. Hirosawa, H. Amano, K. Hiramatsu, and I. Akasaki, *Journal of Crystal Growth* (1993) **128**, 391–396, DOI: 10.1016/0022-0248(93)90354-Y.

[11] J. Bläsing, A. Reiher, A. Dadgar, A. Diez, and A. Krost, *Applied Physics Letters* (2002) **81**, 2722–2724, DOI: 10.1063/1.1512331.

[12] A. Krost, A. Dadgar, J. Blasing, A. Diez, T. Hempel, S. Petzold et al., *Applied Physics Letters* (2004) **85**, 3441–3443, DOI: 10.1063/1.1808237.

[13] S. Tripathy, S. J. Chua, P. Chen, and Z. L. Miao, *Journal of Applied Physics* (2002) **92**, 3503–3510, DOI: 10.1063/1.1502921.

[14] M. Wei, X. Wang, X. Pan, H. Xiao, C. Wang, C. Yang et al., *Journal of Materials Science: Materials in Electronics* (2011) **22**, 1028–1032, DOI: 10.1007/s10854-010-0254-0.

[15] G. Meneghesso, G. Verzellesi, F. Danesin, F. Rampazzo, F. Zanon, A. Tazzoli et al., *IEEE Transactions on Device and Materials Reliability* (2008) **8**, 332–343, DOI: `10.1109/TDMR.2008.923743`.

[16] S. Massl, J. Keckes, and R. Pippan, *Acta Mater.* (2007) **55**, 4835–4844, DOI: `10.1016/j.actamat.2007.05.002`.

[17] S. Massl, J. Keckes, and R. Pippan, *Scripta Materialia* (2008) **59**, 503–506, DOI: `10.1016/j.scriptamat.2008.04.037`.

[18] S. Massl, H. Kostenbauer, J. Keckes, and R. Pippan, *Thin Solid Films* (2008) **516**, 8655–8662, DOI: `10.1016/j.tsf.2008.06.091`.

[19] R. Schöngrundner, R. Treml, T. Antretter, D. Kozic, W. Ecker, D. Kiener et al., *Thin Solid Films* (2014) **564**, 321–330.

[20] R. Treml, D. Kozic, J. Zechner, X. Maeder, B. Sartory, H.-P. Gänser et al., *Acta Materialia* (2016) **103**, 616–623, DOI: `10.1016/j.actamat.2015.10.044`.

[21] A. Darbal, R. Narayan, C. Vartuli, G. Lian, R. Graham, F. Shaapur et al., *Microscopy and Microanalysis* (2013) **19**, 702–703, DOI: `10.1017/S1431927613005503`.

[22] A. D. Darbal, R. D. Narayan, C. Vartuli, T. Aoki, J. Mardinly, S. Nicolopoulos et al., *Microscopy and Microanalysis* (2014) **20**, 1066–1067, DOI: `10.1017/S1431927614007053`.

[23] J. Weiss, A. Darbal, R. Narayan, S. Kim, and S. Nicolopoulos, (2016)

[24] D. Cooper, N. Bernier, and J.-L. Rouviere, *Nano Letters* (2015) **15**, 5289–5294, DOI: `10.1021/acs.nanolett.5b01614`.

[25] K. Levenberg, *Quart. Appl. Math.* (1944) **2**, 164–168.

[26] D. W. Marquardt, *Journal of the Society for Industrial and Applied Mathematics* (1963) **11**, 431–441, DOI: `10.1137/0111030`.

[27] L. Margulies, G. Winther, and H. F. Poulsen, *Science* (2001) **291**, 2392–2394, DOI: `10.1126/science.1057956`.

[28] A. Polian, M. Grimsditch, and I. Grzegory, *Journal of Applied Physics* (1996) **79**, 3343–3344, DOI: `10.1063/1.361236`.

[29] J. J. Wortman, and R. A. Evans, *Journal of Applied Physics* (1965) **36**, 153–156, DOI: `10.1063/1.1713863`.

[30] A. F. Wright, *Journal of Applied Physics* (1997) **82**, 2833–2839, DOI: `10.1063/1.366114`.

[31] Y. Fu, *Integrated Power Devices and TCAD Simulation*, CRC Press 2014, (2014)

[32] *GaN and ZnO-based Materials and Devices*, ed. S. Pearton, Springer Berlin Heidelberg, (2012) vol. 156, DOI: 10.1007/978-3-642-23521-4.

[33] S. Raghavan, and J. M. Redwing, *Journal of Applied Physics* (2005) **98**, DOI: 10.1063/1.1978991.

[34] H. Amano, I. Akasaki, K. Hiramatsu, N. Koide, and N. Sawaki, *Thin Solid Films* (1988) **163**, 415–420, DOI: 10.1016/0040-6090(88)90458-0.

[35] S. Figge, T. Böttcher, S. Einfeldt, and D. Hommel, *Journal of Crystal Growth* (2000) **221**, 262–266, DOI: 10.1016/S0022-0248(00)00696-5.

[36] T. Szymanski, M. Wosko, B. Paszkiewicz, R. Paszkiewicz, and M. Drzik, *Journal of Vacuum Science & Technology A* (2015) **33**, DOI: 10.1116/1.4921581.

G

Fracture toughness enhancement of brittle nanostructured materials by spatial heterogeneity: A micromechanical proof for CrN/Cr and TiN/SiO$_x$ multilayers

Rostislav Daniel[1], Michael Meindlhumer[2], Jakub Zalesak[3], Bernhard Sartory[4], Angelica Zeilinger[4], Christian Mitterer[3], Jozef Keckes[2]

[1]Christian Doppler Laboratory for Advanced synthesis of novel multifunctional coatings at the Department of Physical Metallurgy and Materials Testing, Montanuniversität Leoben, Leoben, Austria
[2]Department of Materials Physics, Montanuniversität Leoben and Erich Schmid Institute for Materials Science, Austrian Academy of Sciences, Leoben, Austria
[3]Department of Physical Metallurgy and Materials Testing, Montanuniversität Leoben, Leoben, Austria
[4]Materials Center Leoben Forschung GmbH, Leoben, Austria

Abstract

The search for simultaneously strong and tough materials requires the development of novel design strategies and synthesis routes. In this work, it is demonstrated that a nanoscale variation in material mechanical property distributions can serve as a universal concept for improvement of fracture behavior of nanostructured brittle thin films. Mechanical tests performed on microcantilever beam specimens of multilayered TiN/SiO$_x$ thin films show that the fracture toughness of this hierarchical, microstructurally and mechanically heterogeneous material can be enhanced up to 60 % with respect to either of its single-layered constituents, which is attributed to a large difference in their elastic modulus. Similarly, micro-bending tests of multilayered CrN/Cr thin films reveal an increase in fracture toughness of 40 % with

respect to CrN and Cr single layers. In this case, the enhancement of fracture toughness is attributed to the difference in strength of both constituents. These results indicate that the fracture toughness enhancement in brittle nanostructured films is conditioned by simultaneously occurring microstructural heterogeneity and a difference in the intrinsic mechanical properties of the material constituents, which ensure an effective increase of energy dissipation through the alternation of the crack path and crack deflection at the interfaces.

G.1. Introduction

The development of stronger and harder materials for severe applications has been considered as an important topic in materials research in last decades. However, the strength is not the only property required; materials have to be also sufficiently damage-tolerant. Brittle materials thus cannot be used in many applications due to low toughness despite other perspective properties such as high strength, thermal stability or resistance against oxidation and corrosion. The selection of suitable materials for a given application is thus commonly compromised by a search for rather less strong but tough materials to avoid unacceptable catastrophic failure during operation. For this reason, extraordinary strong yet brittle materials are often avoided in engineering applications due to lack of plasticity, which may cause that a crack, once initiated, immediately propagates through the entire sample in an unstable fashion already at small strains. An improvement of material ductility and toughness is thus of a vital importance to maintain the subcritical extension of the crack and so to avoid an uncontrolled fracture. Although strength and toughness are commonly exclusive and common approaches in increasing fracture toughness are typically accompanied by a decrease in strength of the material, examples in nature indicate that strong materials may exist with very high fracture toughness even if composed of brittle constituents. A key for super-strong super-tough damage-tolerant materials is the structural and compositional heterogeneity together with spatial variations in properties as observed in biological [1] and [2] and synthetic materials [3]. In these cases, inelastic deformation of individual constituents of the composite material during loading results in an extraordinary damage tolerance. If the local stress is repeatedly dissipated (or at least alleviated) at hierarchical interfaces between individuby spatial heterogeneity: A micromechanical proof for CrN/Cr and TiN/SiO$_x$ al microstructural constituents during crack growth, the critical fracture stress can reach unexpectedly high values [4]. Also other extrinsic toughening mechanisms associated with plasticity such as phase transformation in some metals [5], steels [6] or oxides [7], crack bridging by ductile phases in composite materials [8], have the same effect. Although very diverse in nature, all these mechanisms effectively resist crack growth, once initiated upon loading. They, however, do not affect the crack initiation itself and other strategies are thus needed to further increase the damage-resistivity of the material. The refinement of the microstructure, control of bulk and shear modulus as well as the compressive stress state are very effective in suppressing crack initiation [9].

The concept of heterogeneous, hierarchically structured materials over large scales observed in nature, is, however, usually hardly applicable in synthetic materials. This is due to the requirement of complex hierarchical structures where materials extremely differing in their microstructure, physical properties and chemical composition are expected to be combined. Some successful attempts have been made by reinforcement of brittle ceramic materials with acrylic glass [10], carbon nanotubes [11] and [12] or graphene [13]; however, preparation of these special composite materials is technologically challenging. Attention is thus paid to more simple structures that exhibit enhanced fracture toughness while preserving high strength. Suitable materials include nanocomposite or lamellar structures where, in particular, extrinsic toughening mechanisms such as coherency strain or inelastic deformation through phase transformation dominate in suppressing crack propagation [1], [7] and [14].

The intention of this work was to study possible toughening mechanisms in nanostructured brittle materials, to identify the role of spatial heterogeneity of the material structure and properties in enhancement of the fracture toughness and damage-resistance, to prove theoretical predictions of effective crack deflection in composite structures and to manifest their practical relevance in synthetic materials. We demonstrate that fracture toughness of hard nanostructured brittle materials may be effectively enhanced if they are designed in a multilayered fashion of constituents differing in elastic modulus or strength. Finally, general strategies of preserving strength of these materials and simultaneous enhancement of fracture toughness are discussed.

G.2. Experimental details

In this study, two different sets of samples combining hard and soft constituents were investigated. In the first set, hard brittle nanocrystalline TiN was combined with compliant amorphous SiO_x in various architectures prepared by magnetically unbalanced reactive pulsed direct current magnetron sputtering. While TiN was sputter deposited from a Ti target in an Ar + N_2 plasma discharge at a total pressure

$p_{\mathrm{TOT}} = p_{\mathrm{Ar}} + p_{\mathrm{N_2}} = 0.4 + 0.6\,\mathrm{Pa}$ and a target current density I_d of $37\,\mathrm{mA/cm^2}$, SiO_x (x = 2.2) was deposited from a Si target in an Ar + O_2 reactive gas mixture at a total pressure $p_{TOT} = p_{Ar} + p_{O_2} = 0.5 + 0.5\,\mathrm{Pa}$ and $I_d = 12\,\mathrm{mA/cm^2}$. The substrate temperature and the bias voltage were kept constant at 200 °C and −100 V, respectively. The second set of samples combined hard brittle CrN with soft metallic Cr. These samples were sputter deposited from a Cr target at a substrate temperature of 350 °C and target current density of $I_d = 59\,\mathrm{mA/cm^2}$ in a reactive gas mixture ($p_{Ar} + p_{N_2} = 0.75 + 0.25\,\mathrm{Pa}$) and a non-reactive Ar discharge ($\mathrm{p_{TOT}} = \mathrm{p}_{Ar} = 1\,\mathrm{Pa}$), respectively. The density and microstructure of the films were controlled by the substrate bias voltage varying between −40 and −80 V. All films were grown onto pre-cleaned and plasma-etched Si(100) substrates.

Morphology of the films in cross-section and of fracture planes after micromechanical testing was studied by scanning electron microscopy (SEM, Auriga Crossbeam, Zeiss). The surface of the fracture planes was additionally investigated in detail by atomic force microscopy (AFM, BRR, DME) operated in tapping mode.

Advanced structure and phase analyses were carried out by cross-sectional X-ray nanodiffraction experiments performed in transmission geometry at the nanofocus extension of ID13 beamline of the European Synchrotron Radiation Facility (ESRF) in Grenoble, France. The high brilliance X-ray source and dedicated X-ray focusing optics combined with a nano-positioning sample stage allowed for a spatially resolved microstructure characterization using a beam of 100 nm in diameter and a photon energy of 14.7 keV. The Debye-Scherrer rings collected at a 2D detector after exposure of samples prepared as slices with a width of about 100 µm [15] were subsequently processed by the Fit2D software package [16].

Hardness and indentation modulus of the films were determined by nanoindentation (UMIS, Fischer-Cripps Laboratories) using a Berkovich diamond tip calibrated for its shape by a fused silica reference sample. The load-displacement curves of at least 20 measurements at each sample were analysed according to the Oliver&Pharr method [17]. The maximum load was varied between 0.5 and 20 mN to assess the surface mechanical properties as well as the macroscopic mechanical response of the composite material.

Complementary measurements of the mechanical properties were conducted by in-situ micromechanical testing of microcantilever beam specimens inside a SEM (LEO 982, Crossbeam 1540XB, Zeiss) equipped with a nanoindenter (PicoIndenter 85, Hysitron). The microcantilevers were fabricated by a focus ion beam (FIB, Auriga Crossbeam, Zeiss) workstation with a length l, width b and height w, where the latter corresponds to the film thickness (Fig. G.1).

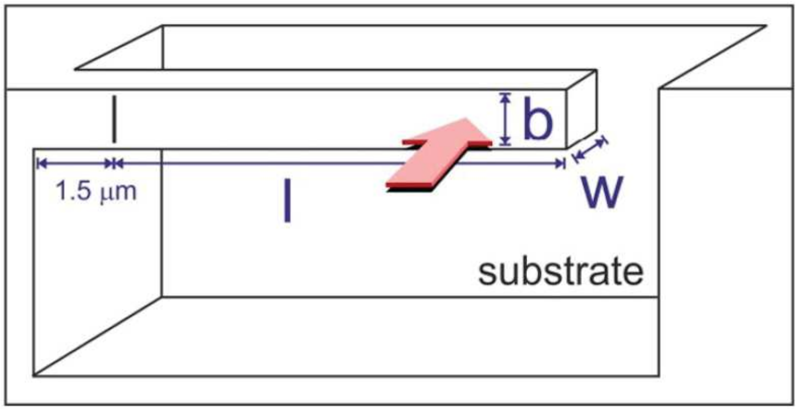

Figure G.1.: Geometry of microcantilevers used for fracture toughness investigations by microbending testing. The specimens were prepared by FIB milling with a length l, width b and height w (corresponding to the film thickness) and with a pre-crack of a depth of 500 ± 50 nm at a distance of 1.5 µm from the beam support.

In this way, the film is separated from the substrate, which allows for determination of the mechanical properties exclusively of the film without the effect of the residual stresses. For the TiN/SiO$_x$ samples, $l = 9.1 \pm 0.1\,\mu$m, $b = 1.7 \pm 0.2\,\mu$m and $w = 1.3 \pm 0.2\,\mu$m, while for CrN/Cr, $l = 9.1 \pm 0.1\,\mu$m, $b = 2.1 \pm 0.2\,\mu$m and $w = 3.0 \pm 0.2\,\mu$m. The microcantilevers were subsequently loaded using a sphero-conical indenter of 700 nm radius in normal direction in displacement controlled mode with a constant displacement rate of 20 nm/s. The elastic modulus of the microcantilever beams, representing the elastic properties of free standing stress-free films, was calculated from the slope of the load-deflection curves taking into account the cantilever geometry according to

$$E = \frac{4F}{\delta b} \times \left(\frac{l}{w}\right)^3 . \tag{G.1}$$

Here, δ is the beam deflection at the applied load F. Furthermore, the fracture stress σ_F, representing the fracture resistance of the specimens was determined from the maximum applied load at fracture by

$$\sigma_F = 6\frac{Fl}{bw^2}. \tag{G.2}$$

In order to probe fracture toughness K_{IC} of the films, the maximum load prior fracture of the microcantilevers (pre-cracked by a notch with a depth a of 500 ± 50 nm milled by FIB at a distance of 1.5 µm from the beam support) was recorded. The fracture toughness was then calculated by applying linear-elastic fracture mechanics as

$$K_{IC} = \sigma_F \sqrt{\pi a} F\left(\frac{a}{w}\right), \tag{G.3}$$

where σ_F is the fracture stress and $F(a/w)$ a dimensionless shape factor given for specific microcantilever beam geometry as [18]

$$F\left(\frac{a}{w}\right) = \sqrt{\frac{2w}{\pi a}} \tan\left(\frac{\pi a}{2w}\right) \frac{0.923 + 0.199\left(\sin\left(\frac{\pi a}{2w}\right)\right)^4}{cos\left(\frac{\pi a}{2w}\right)}. \tag{G.4}$$

G.3. Results

G.3.1. Toughness of TiN/SiO$_x$ system with elastic modulus variation

The morphology of the SiO$_x$ and TiN single-layers and TiN/SiO$_x$ multilayers in cross-section is shown in Fig. G.2. The deposition time was individually adopted for each material so the overall thickness of all films was kept constant at about 1.5 µm. The architecture of the multilayers was chosen so the thickness of the SiO$_x$ constituent was constant with 35 nm and the thickness of TiN varied between 115 and 350 nm (Fig. G.2c,d). While the SiO$_x$ film appears completely amorphous without any structural features (Fig. G.2a, well corresponding to the X-ray diffraction measurements in Fig. G.3), the TiN film exhibits pronounced columnar morphology with grains gradually developing in size with the film thickness (Fig. G.2b). On the contrary, the columnar growth of TiN in the TiN/SiO$_x$ multilayer system is repeatedly interrupted by the amorphous SiO$_x$ layers (Fig. G.2c). Re-nucleation of TiN at each TiN/SiO$_x$ interface and subsequent coarsening of the columnar grains are also evident from the nanodiffraction experiment as a change of the width of the diffraction peaks (Fig. G.3).

Besides the microstructural diversity, the material selection in this particular multilayer system was intended to combine two constituents which significantly differ in both strength and elastic modulus. While TiN exhibits an indentation hardness $H_I = 24.5\,GPa$ and elastic modulus $E_I = 385\,\text{GPa}$, amorphous SiO$_x$ is much softer and more compliant with $H_I = 10.1\,\text{GPa}$ by spatial heterogeneity: A micromechanical proof for CrN/Cr and and $E_I = 110\,\text{GPa}$. This multilayered system with complex microstructure and mechanical property distributions allowed to study theoretically predicted toughening mechanisms that effectively resist crack propagation by its arrest or deflection at the interfaces of individual constituents (see Section 4).

With the increasing volume fraction of the SiO$_x$ phase in the multi-layered TiN/SiO$_x$ system, the contribution of SiO$_x$ to the mechanical properties of the composite increases and the hardness and elastic modulus reduce accordingly. While the TiN/SiO$_x$ multilayer with 9 vol % of SiO$_x$ (Fig. G.2c) exhibits an indentation hardness of 12.5 GPa and elastic modulus of 220 GPa, these are reduced to 12.1 GPa and 162 GPa (Table G.1), respectively, while the volume fraction of the SiO$_x$ phase increases to 18 vol % (Fig. G.2d). It is, however, worth to note that the hardness of the TiN top-layer does not change and this is the composite hardness, which changes instead. The measurements at very low indentation depths (below 20 nm) revealed approximately the same hardness as that of the TiN single-layer.

Additional information to the mechanical behavior of this hierarchical composite system was gained by micromechanical testing of microcantilever beams prepared by FIB milling. The bending tests of unnotched microcantilevers allowed revealing the ability of the material to elastically deform, which is shown for two representative samples in Fig. G.4. While the maximum deflection prior fracture was 0.52 µm for TiN, it was about three times higher (1.55 µm) in the case of the TiN/SiO$_x$ multilayer with 21 alternating layers.

By probing the pre-cracked microcantilever beam specimens, the fracture toughness K_{IC} of the films was determined according to Eq. (G.3). The representative averaged load-deflection curves for the single- as well as multi-layered films are summarized in Fig. G.5 showing a significant enhancement of the fracture resistance with

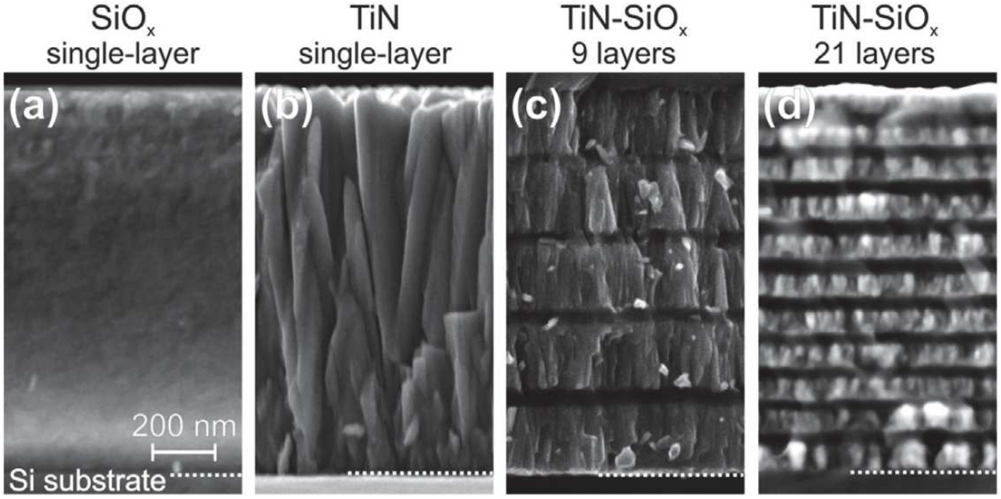

Figure G.2.: SEM cross-sectional micrographs of single-layered (a) SiO$_x$ and (b) TiN films and TiN/SiO$_x$ multilayers consisted of (c) 5 TiN and 4 SiO$_x$ layers and (d) 11 TiN and 10 SiO$_x$ layers. The overall thickness and the thickness of the SiO$_x$ constituent were constant with 1.5 µm and 35 nm, respectively, while the thickness of TiN was varied between 115 and 350 nm.

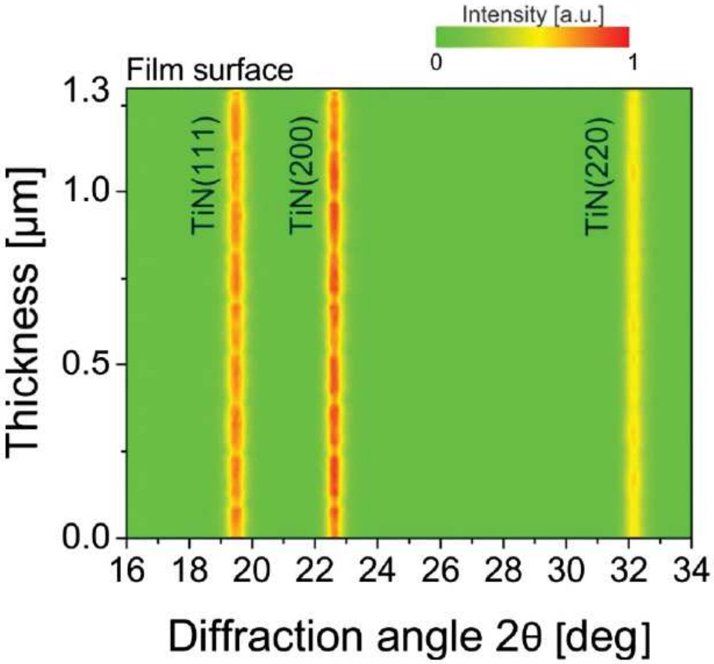

Figure G.3.: Intensity distribution of the TiN(111), (200) and (220) diffraction peaks across the thickness of the TiN/SiO$_x$ multilayer consisted of 21 layers revealing the repetitive fashion of the film microstructure where TiN re-nucleates at each TiN/SiO$_x$ interface (demonstrated by the variation of the peak width) while preserving its crystallographic texture across the entire film thickness.

Table G.1.: Indentation hardness H_I, elastic modulus E_I and fracture toughness K_{IC} of individual constituents and the composite structure of the TiN/SiO$_x$ and CrN/Cr multilayer systems.

TiN/SiO$_x$	H_I [GPa]	E_I [GPa]	K_{IC} [MPa·m$^{1/2}$]	CrN/Cr	H_I [GPa]	E_I [GPa]	K_{IC} [MPa·m$^{1/2}$]
SiO$_x$	10.1	110	0.6	Cr	8	290	2.7
TiN	24.5	385	1.2	CrN	21	320	3.6
TiN/SiO$_x$ (9 layers)	12.5	220	1.4	CrN/Cr (4 layers)	19	330	4.2
TiN/SiO$_x$ (21 layers)	12.1	162	1.9	CrN/Cr (8 layers)	17	345	5.0

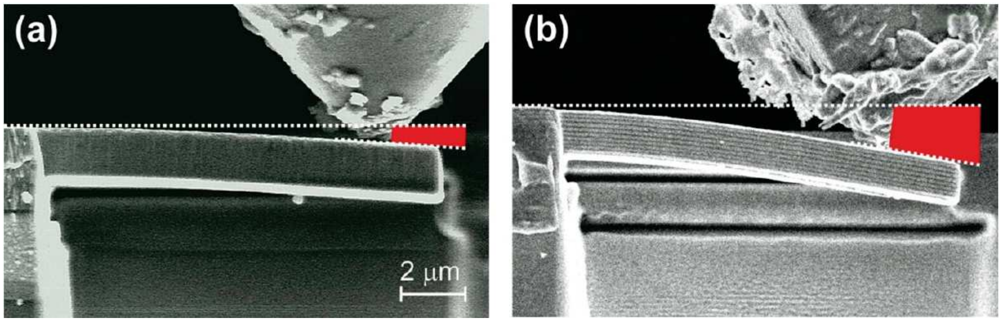

Figure G.4.: Ability of the (a) single-layered TiN and (b) TiN/SiO$_x$ multilayer (21 layers) films to elastically deform as demonstrated by micro-bending tests of unnotchedmicrocantilevers. The maximum specimen deflection prior fracture was three times higher for the TiN/SiO$_x$ multilayer.

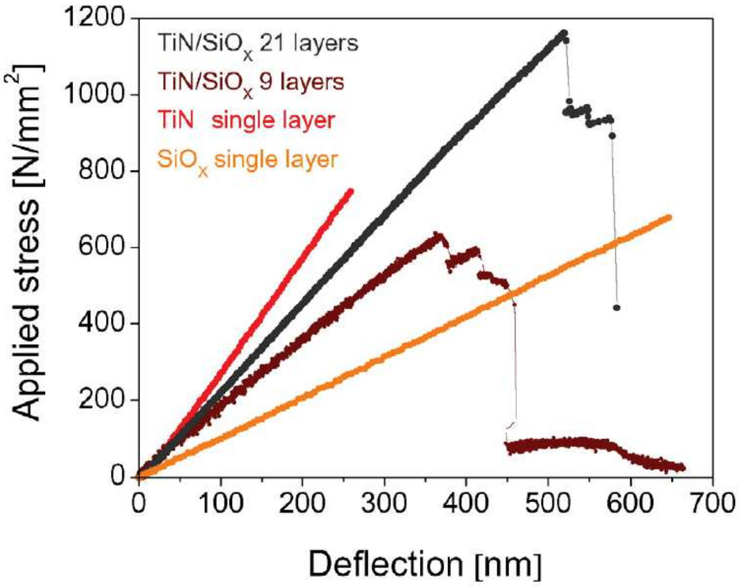

Figure G.5.: Representative load-deflection curves of notched microcantilevers of single-layered TiN and SiO$_x$ films and of TiN/SiO$_x$multilayers (consisted of 9 and 21 layers). The increase of the maximum applied stress prior fracture with increasing number of the SiO$_x$ layers demonstrates the fracture toughness enhancement of the hierarchical composite structure (up to 60 % with respect to the single-layered TiN). Some of the fracture events could not be resolved due to limited acquisition rate of the nanoindentation system. (For interpretation of the references to color in this figure legend, the reader is referred to the web version of this article.)

increasing number of SiO$_x$ layers within the TiN/SiO$_x$ multilayer system (note the increase of the maximum applied stress). The inconsistent variation of the maximum

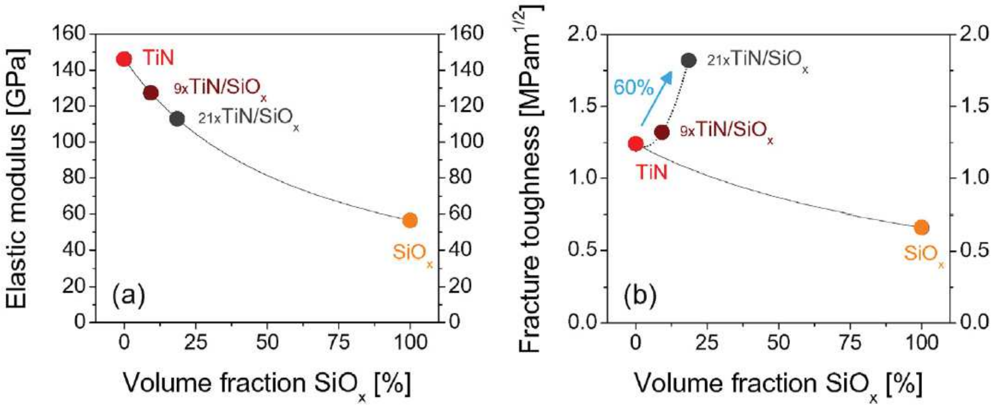

Figure G.6.: The variation of (a) the elastic modulus and (b) fracture toughness of single-layered TiN and SiO_x films and of TiN/SiO_x multilayers as a function of the volume fraction of SiO_x incorporated as layers in the films. While the material elastic modulus E decreases following the rule of mixture expressed as $E = \left(\frac{f_{SiO_x}}{E_{SiO_x}} + \frac{1-f_{SiO_x}}{E_{TiN}}\right)$, where $E_{TiN} = 146\,\mathrm{GPa}$ and $E_{SiO_x} = 56\,\mathrm{GPa}$ are the elastic moduli of TiN and SiO_x single layers determined from the microbending experiments, respectively, and f_{SiO_x} is the volume fraction of SiO_x, the fracture toughness increases significantly as the composite structure is formed.

deflection and the slope of the load-deflection curves are given by a slight variation of the cantilevers dimensions and also by various depths of the notch. Thus, SiO_x appears from Fig. G.5 to be more damage tolerant than TiN and TiN/SiO_x films due to greater width and height of the SiO_x microcantilevers. The calculated fracture toughness, however, accounts for the actual geometry of the probed cantilever and the results are corrected by the shape factor $F(a/w)$ according to Eq. G.4. The values of the fracture toughness summarized in Table G.1 demonstrate the quantitative enhancement of the fracture resistance by the incorporation of the SiO_x layers up to 60 % with respect to the single-layered TiN film (from 1.2 to 1.9 $\mathrm{MPa{\cdot}m}^{-1/2}$). This is surprising as one could expect a decrease of the fracture toughness of the composite structure with increasing volume fraction of the SiO_x phase according to the rule of mixture similarly to the elastic modulus as shown in Fig. G.6a. Instead, the fracture toughness of the TiN/SiO_x system increases while the SiO_x phase is incorporated into TiN forming a composite layered structure (Fig. G.6b). This phenomenon will be discussed in detail in Section 4.

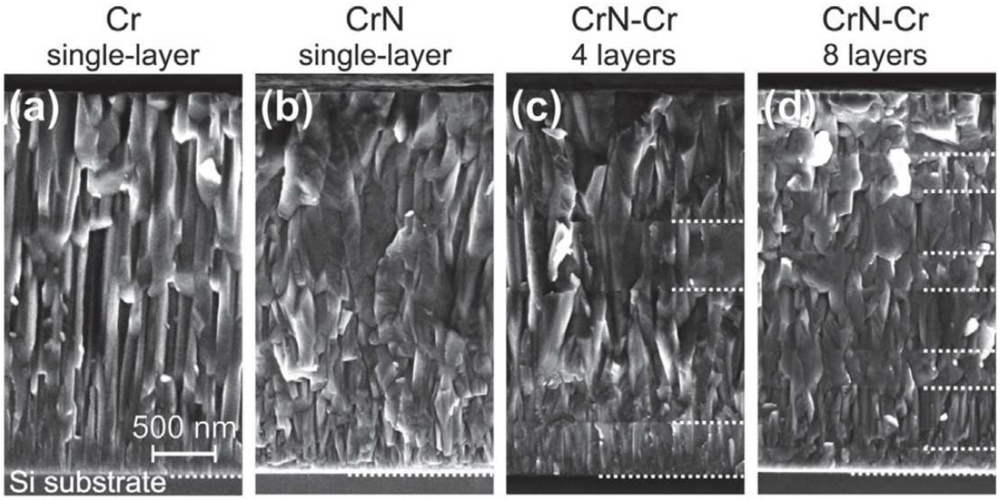

Figure G.7.: SEM cross-sectional micrographs of (a) Cr and (b) CrN single-layers and CrN/Cr multilayers consisted of (c) 4 and (d) 8 layers. While the overall thickness of the films was constant of 3 µm, the thickness of each CrN layer was either 1 µm or 500 nm and the thickness of each Cr layer was either 500 or 250 nm, respectively.

G.3.2. Toughness of CrN/Cr system with strength variation

While in the case of the TiN/SiO$_x$ multilayer system, the constituents have been chosen due to their significant difference especially in the elastic properties, another approach of an enhancement of the fracture toughness of composite structures was studied for CrN/Cr multi-layers [19]. The intention in that case was to prove the theoretical prediction that not only the variation in the elastic properties but also in the material strength should result in an enhancement of the fracture resistance and fracture flow [20]. Cr as a metal exhibits relatively large stiffness (represented by the elastic modulus) especially when synthesized by plasma-assisted vapor deposition. The elastic modulus of 290 GPa is thus well comparable with the elastic modulus of CrN, which was 320 GPa in this particular case. The strength of both materials, however, significantly differs. The indentation hardness of the Cr single-layer was 8 GPa, while the CrN film exhibited a hardness of 21 GPa, which is almost three times greater than that of Cr. The large elastic modulus and strength of both materials with respect to their coarse-grained bulk counterparts have its origin in the nanocrystalline structure shown in Fig. G.7. Both materials exhibit a columnar morphology with the in-plane grain size varying across the thickness between 15 and 30 nm [21] and [22]. Although the Cr film had a more equiaxed columnar structure

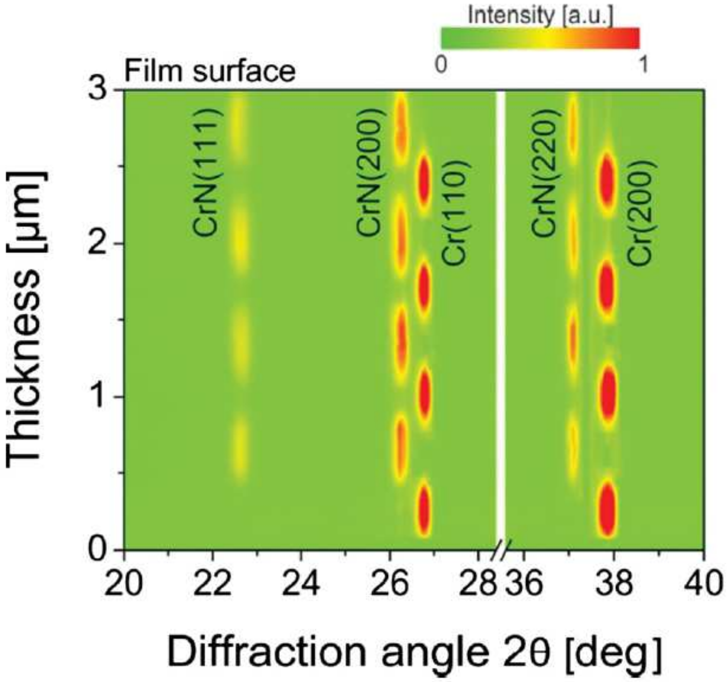

Figure G.8.: Phase analysis of the CrN-Cr multilayer (8 layers) across its thickness performed with 100 nm steps during the nanodiffraction experiment in transmission geometry showing the intensity distribution of reflections emanating from Cr and CrN. High intensity of the Cr(200) and CrN(200) reflections demonstrates the structural alignment of the CrN layers after the highly (100) textured Cr sublayers which is preserved through the entire film thickness. Note that CrN tends to grow as a single-layer with the (111) texture under the same growth conditions.

compared to the V-shaped columnar microstructure of CrN (Fig. G.7a,b), both materials are well aligned within the multi-layered structure. This is demonstrated by uninterrupted growth of the columnar grains across the interfaces through the entire film thickness (Fig. G.7c,d). The column to column alignment observed in the SEM cross-sections is promoted by a crystallographic match of the constituents, both exhibiting cubic crystallographic structure (body-centered for Cr and face-centered for CrN) [23]. The structural alignment is further demonstrated by the phase analysis of the CrN/Cr multilayer performed during the nanodiffraction experiment across its thickness (Fig. G.8). While the CrN single-layer film preferentially grows with (111) texture under the given growth conditions (see [21] for details), it spontaneously changes to (100) while growing on the highly (100) textured Cr interlayer (see Fig. G.8). This local epitaxial alignment, well documented for the dual-layer

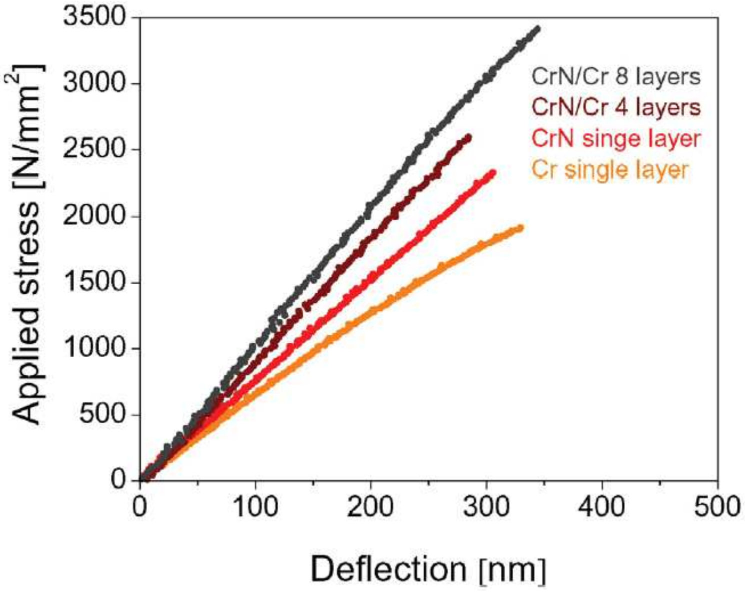

Figure G.9.: Averaged load-deflection curves of notched microcantilevers of the Cr and CrN single-layers and CrN/Cr multilayers (4 and 8 layers) during the microbending experiments. An increase of the maximum applied stress prior fracture with incorporation of Cr sublayers demonstrates the enhancement of the fracture toughness of the composite structure, which is up to 40 % higher than that of the single-layered CrN.

CrN/Cr system [21] and [23], is preserved through the entire film thickness. The dominant difference of this composite structure across its thickness is thus given predominantly by the spatial variation in mechanical properties (strength) rather than in microstructure. The architecture of this multilayer system also differs compared to TiN/SiO$_x$. While the thickness of the SiO$_x$ layer in the previous case was kept constant at 35 nm and only the thickness of the TiN constituent was varied, in the case of the CrN/Cr system, thickness of both constituents was varied, i.e. the thickness of each CrN layer was either 1 µm or 500 nm and the thickness of each Cr layer was either 500 or 250 nm, respectively. The overall thickness was kept constant of 3 µm in this case (Fig. G.7).

The bending experiments of notched microcantilever beam specimens of the Cr and CrN single-layers and the CrN/Cr multilayers (separated from the substrate by FIB milling) are summarized in Fig. G.9 and Table G.1. An increase of the average applied stress at fracture from 2.3 to 2.6 and 3.4 GPa for the CrN single-layer and the CrN/Cr multilayers, respectively, corresponds to a fracture toughness enhancement of 40 % from 3.6 for CrN to 5 MPa·m$^{1/2}$ for the CrN/Cr multilayer composed of 8 layers (see Table G.1). The fracture stress σ_F of the unnotched microcantilever beams (not shown here) also significantly increased from 5.7 to 7.8 GPa for the CrN/Cr multilayer composed of 8 layers with respect to the CrN single layer. Interestingly, the stiffness of the multilayered CrN/Cr system (given by the slope of the stress-deflection curves of unnotched microcantilever beams, not shown here) slightly increased while Cr interlayers were incorporated into the CrN/Cr multilayer system. This is given by a large elastic anisotropy of CrN ($E_{CrN(111)} = 285\,\text{GPa}$, $E_{CrN(100)} = 439\,\text{GPa}$ [24]) which changes its texture from (111) towards the stiffer (100) orientation while growing on the Cr sublayer (Fig. G.8).

G.4. Discussion

A disadvantage of hard yet brittle materials such as ceramics is that they eventually catastrophically fracture once a crack is initiated during loading beyond a critical limit. This is because in ceramics, the local stress and energy level cannot be decreased by plastic deformation via e.g. dislocation movement, typical for metals [25]. A different type of atomic bonding in ceramic materials causes that the supplied energy from external loading is predominantly available to initiate a crack and subsequently consumed to create a new surface through fracture rather than to induce plastic deformation. Brittle fracture in polycrystalline ceramics occurs preferentially along cleavage planes or grain boundaries, which represent areas of weaker atomic bonding and thus paths of lower fracture energy. The presence of grain boundaries is also a reason why polycrystalline ceramics are more resistant to fracture than single crystals of the same material, since a greater energy is needed for a crack to grow if it is repeatedly deflected [26]. The macroscopic toughness enhancement is thus associated with an increase in roughness of the fracture surface and thus with the total fracture surface area [25].

In transition metal nitrides, ceramics with a partially metallic character, the generation of dislocations upon loading effectively increases strength and also fracture toughness due to partial plasticity involved during deformation [27]. Plasticity of such materials is, however, significantly reduced by a decrease of the grain size and the presence of point defects associated with the synthesis of the material (e.g. ion-assisted deposition of thin films). As the dislocation mobility is thus suppressed, intergranular brittle fracture dominates and causes catastrophic failure of the material [28].

Obviously, in order to increase the fracture toughness of these hard yet brittle materials, more energy needs to be dissipated during fracture by more efficient and frequent crack deflection and/or by introduced plasticity. This can be realized by making the materials structure highly heterogeneous, e.g. by incorporation of new phases either as crystallites [29] and [30], embedding matrix [31] or as layers in a multilayered architecture [32] and [33]. The selection of right constituents is, however, crucial in enhancement of the fracture toughness. Generally, materials which exhibit high stiffness and strength and are simultaneously outstandingly damage-resistant and flaw-tolerant are composed of constituents significantly differing in their microstructure and mechanical properties [34]. Most of them are built in a complex hierarchical arrangement with characteristic structural features, which may range from nano- to macroscale and thus subsequently allow to control fracture over multiple length scales [8] and [35]. Toughening mechanisms acting during deformation are, however, closely related not only to the compositional and structural heterogeneity but also to spatial variations of properties [33] and [36]. Theoretical models predict that materials with material property variations should offer greater energy dissipation efficiency than homogeneous materials [1] and [37]. A very effective way of energy dissipation during fracture is the crack deflection by weak interfaces with a subsequent increase of the crack growth resistance [38]. This is, however, implicated by specific architectural criteria allowing combination of such constituents, which significantly differ in stiffness as only these give rise to crack deflection or even crack arrest during deformation [20] and [39]. These principles reflecting extraordinary fracture toughness and damage tolerance of hierarchical materials [40] have been successfully applied for various synthetic materials [41], [42], [43], [42], [44] and [45]. It is, however, worth to further study and validate these principles by experimental methods and establish general concepts for damage-tolerant materials, which is a focus of our recent work.

A composite of two alternating constituents with very different properties (and thicknesses above critical limit for any hardening effects typical for superlattices [46] and [47]) is expected to behave according to the rule of mixture so that the property of one constituent dominates over the other if its volume fraction becomes dominant in the composite structure. This is true in the case of the composite hardness and composite stiffness of the TiN/SiO$_x$ system as demonstrated in Fig. G.6a but this rule may completely fail in the case of the fracture stress or fracture toughness (see Fig. G.6b and Table G.1). This is due to the spatial variation in material structure and properties, which effectively contributes to damage-tolerance of the composite material through local dissipation of high stresses that would otherwise cause the material to fracture. A special case is a composite material consisting of stiff and compliant constituents in a multilayered architecture, in which the fracture resistance/strength can be unexpectedly high due to an effective reduction of the crack driving force while the crack has entered the compliant layer [20]. As a consequence, the crack is deflected at the interface and, because of the corresponding energy dissipation associated with the change of the crack growth direction, also the fracture toughness increases. The crack deflection at the interfaces of individual constituents differing in their elastic properties is experimentally demonstrated in Fig. 10, showing the step-like fracture pattern of a TiN/SiO$_x$ multilayer cantilever (Fig. 10a) and free standing film (Fig. 10b). The crack propagating through the TiN/SiO$_x$ interfaces in a tortuous manner well corresponds to the crack propagation in biological materials [2] and [40] or in advanced ceramics combining stiff and elastic constituents [10] exposed to flexural loading. The interfacial crack deflection mechanism acting in the TiN/SiO$_x$ composite during loading is also evident in the load-displacement curves shown in Fig. 5 (dark red and grey curves). After achieving the critical applied stress, the first fracture event | occurred (manifested by abrupt load drop); the crack, however, did not propagate through the entire film thickness. Instead, the crack was arrested at the SiO$_x$/TiN interface and started to further grow when the critical stress, corresponding to the remaining unbroken portion of the microcantilever beam, was again exceeded. Approaching the next compliant/stiff interface, the same fracture event repeated until the last TiN sublayer of the composite fractured. Every loading segment between the fracture events is characterized by a continuously reduced stress needed for fracture and also a slightly different slope of the load-deflection curve, which is given by the ever decreasing unbroken portion of the microcantilever beam specimen. These results validate the theoretical predictions and are consistent with the abovementioned model of a stepwise fracture in these types of composite materials.

Is, however, the difference in the elastic properties of individual constituents the only prerequisite for effective dissipating processes at the interfaces and thus for tougher materials? In Fig. G.10c, a rough fracture plane of the CrN/Cr multilayer system demonstrates that also in this case the crack was deflected at the interfaces, although the elastic properties of both constituents were rather the same (Table G.1). The topography of the fracture plane investigated by AFM reveals alternating crack propagation during loading of the microcantilever beam in more detail (Fig. G.10d). Since the columnar grains in the case of the CrN/Cr multilayer grow structurally aligned through the entire coating thickness (Fig. G.8), the stressed crack propagating from the tip of the notch cannot be affected by incoherent interfaces. Instead, the continuous columnar growth would have favored intergranular fracture. This, however, did not happen and the crack was evidently deflected at the interface with the

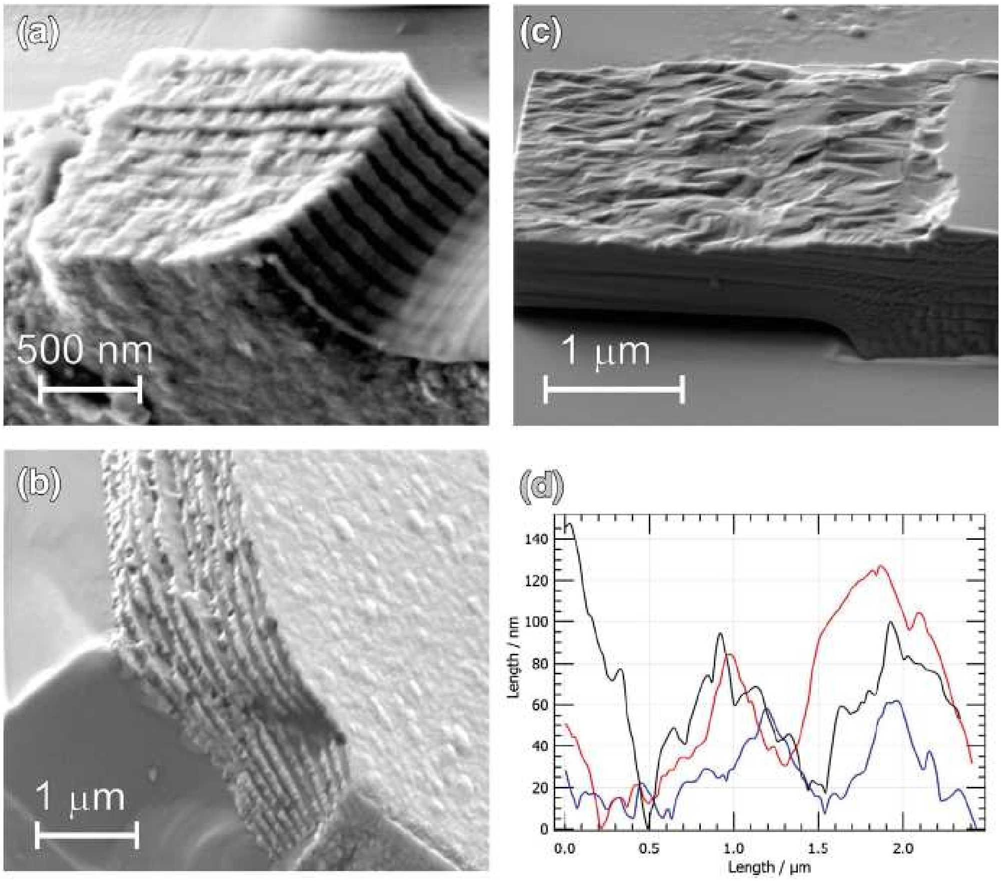

Figure G.10.: SEM micrographs of fracture surfaces of a representative (a) notched microcantilever and (b) unnotched free standing sample of the TiN/SiO$_x$ multilayer consisted of 21 layers. (c) Fracture surface of a notched microcantilever of the CrN/Cr multilayer consisted of 8 layers, cut by FIB and transferred by amicromanipulator inside the SEM onto a Si substrate for AFM line profile measurements performed at three different positions of the fracture surface (d). The step-like fracture patterns demonstrate the effective crack deflection at the interfaces of individual constituents differing either in the elastic properties (TiN/SiO$_x$) and/or strength (CrN/Cr).

softer Cr layer. That means that the difference in strength of individual constituents also ensures local dissipation of stress at the interfaces and gives subsequently rise in the fracture toughness enhancement (although this effect is not as pronounced as in the case of a multilayered material composed of constituents differing in both strength and stiffness, see Table G.1). This experimental evidence allows the model of the fracture resistance enhancement based on the principal difference of the stiffness between individual constituents alternating in a multilayer composite to be extended also for the case of various strengths of individual constituents and thus to establish the variation in (micro)mechanical property distributions as a universal concept for fracture toughness enhancement of brittle nanostructured films.

According to the theoretical predictions, the difference in elastic properties should be as high as possible to effectively decrease the crack driving force and to enhance the fracture toughness [20] and [35]. This may, however, limit the potential of such composites in some applications since the composite hardness and/or stiffness may be significantly reduced by incorporation of compliant/soft constituents. Nevertheless, a crack should be effectively arrested in a compliant/soft layer even if it is very thin. This means that the reduction of the volume fraction of the compliant/soft phase in a composite structure by reducing its thickness should still ensure high fracture toughness while preserving the composite hardness or stiffness. Another obstacle in using such type of composite materials could be its possibly low strength and fracture toughness if exposed to load in the direction parallel to the interfaces. This eventual issue may, however, be avoided if constituents with relatively high stiffness and strength are combined. Some other solution would be to make the structure of the material more hierarchical to account for loading in various directions [20]. This is, however, not only the fracture toughness that can be enhanced by the concept referred to above. As we also showed, the implementation of compliant/soft layers increases the flexibility of the composite (Fig. G.4) even if the brittle phase is the dominant constituent of the material.

One of important aspects, which affect the mechanical properties of thin films, is the residual stress. High compressive stress effectively contributes to enhanced hardness, elastic properties [48] and fracture toughness [49]. The microcantilever beam specimens investigated in this work represent films which were separated from the substrate and subsequently milled by FIB to dimensions, which allow for almost complete stress recovery (the stress state is below the detection limit of the nanodiffraction technique). The mechanical properties of the free standing specimens are thus correspondingly lower with respect to their counterparts adhered to the substrate and exhibiting compressive stress state in GPa range. The discrepancy in the elastic modulus determined by nanoindentation and microbending experiments, as shown above, is also given by the polycrystalline nature of the film material with a high volume fraction of grain boundaries. Grain boundaries are characteristic of disordered structure with a certain amount of nanoporosity, which affects material response upon indentation loading and bending to a different extent [50]. However, remaining residual stresses in the microcantilever beams, which were not relaxed after FIB milling, may still affect the fracture toughness as they play a key role in the crack deflection and arrest. Detailed investigation of the role of the material microstructure and residual stresses on the fracture toughness is a subject of our ongoing research.

The results shown above for multilayered composites together with the knowledge of other natural or synthetic materials [8] and [9] suggest that the key for enhanced fracture resistance of materials is the spatial material heterogeneity in terms of microstructure and properties. A hierarchical arrangement of constituents differing in their properties manifests an involvement of various intrinsic or extrinsic toughening mechanisms contributing to increased flexural strength and fracture resistance of composite materials. The microstructure variations include dimensions and distributions of individual building blocks but also defects at various scales as well as boundaries and interfaces between individual constituents. In principle, the more complex is the hierarchical structure, especially if consisting of constituents with the right combination of properties, the more effectively can the initiation and propagation of cracks be controlled under loading over multiple length scales [34]. Moreover, the property variations are not limited only to the elastic properties or strength at larger (macro- or micro-) scales. Variations of atomic bonding strength, for instance, are also known to effectively contribute to enhanced damage tolerance of hierarchical materials [51]. This fact significantly widens the potential of the microstructural design in the development of novel damage-tolerant materials with hierarchical structures over large scales, similarly as it is known in biological materials [35].

G.5. Conclusions

We have demonstrated that the fracture toughness of brittle materials can be effectively enhanced if a brittle material is combined with compliant and/or soft constituents. The principal origin of a high fracture toughness of such composite materials is given by the microscale structural heterogeneity and spatial variations of the mechanical properties, which give rise to a reduction of the crack driving force at the interfaces with the compliant/soft constituents, deflection of the propagating crack and subsequently increase of fracture resistance. It has been experimentally shown that the variation of the mechanical properties include not only stiffness but also strength of individual constituents of a multilayer structure. This concept is generally valid for any brittle material although the performance of such composite strongly depends on the materials selection and final microstructure. If materials differing in their microstructure and properties are combined in a hierarchical fashion, the fracture resistance (as well as flexibility) of such composite structure can be significantly higher than either of its constituents. The extent of that enhancement, however, strongly depends on the geometric, micro-architectural and material factors, which determine whether toughening mechanisms controlling subcritical crack growth can act across multiple hierarchical levels and thus affect structural performance at larger length scales.

Acknowledgements

The work on film characterization in this study has received research funding from the European Union, within the large collaborative project ISTRESS, Grant Agreement No. 604646. The financial support of the film synthesis by the Austrian Federal Ministry of Science, Research and Economy and the National Foundation for Research, Technology and Development in the frame of the Christian Doppler Laboratory is also gratefully acknowledged. Dr. Livia Chitu is acknowledged for performing the AFM measurements.

Bibliography to paper G

[1] S. Bechtle, S. F. Ang, and G. A. Schneider, *Biomaterials* (2010) **31**, 6378–6385, DOI: `10.1016/j.biomaterials.2010.05.044`.

[2] A. Woesz, J. C. Weaver, M. Kazanci, Y. Dauphin, J. Aizenberg, D. E. Morse et al., *Journal of Materials Research* (2006) **21**, 2068–2078, DOI: `10.1557/jmr.2006.0251`.

[3] M. P. Rao, A. J. Sánchez-Herencia, G. E. Beltz, R. M. McMeeking, and F. F. Lange, *Science* (1999) **286**, 102–105, DOI: `10.1126/science.286.5437.102`.

[4] E. Munch, M. E. Launey, D. H. Alsem, E. Saiz, A. P. Tomsia, and R. O. Ritchie, *Science* (2008) **322**, 1516–1520, DOI: `10.1126/science.1164865`.

[5] C. Wang, J. Han, J. M. Pureza, and Y.-W. Chung, *Surface and Coatings Technology* (2013) **237**, 158–163, DOI: `10.1016/j.surfcoat.2013.08.014`.

[6] C.-H. Seo, K. H. Kwon, K. Choi, K.-H. Kim, J. Kwak, S. Lee et al., *Scripta Materialia* (2012) **66**, 519–522, DOI: `10.1016/j.scriptamat.2011.12.026`.

[7] R. Hannink, *Journal of the American Ceramic Society* (2000) **83**, 461–487.

[8] R. O. Ritchie, *Nature Materials* (2011) **10**, 817–822, DOI: `10.1038/nmat3115`.

[9] M. E. Launey, and R. O. Ritchie, *Advanced Materials* (2009) **21**, 2103–2110, DOI: `10.1002/adma.200803322`.

[10] M. Launey, E. Munch, D. Alsem, H. Barth, E. Saiz, A. Tomsia et al., *Acta Materialia* (2009) **57**, 2919–2932, DOI: `10.1016/j.actamat.2009.03.003`.

[11] W. Yang, H. Araki, C. Tang, S. Thaveethavorn, A. Kohyama, H. Suzuki et al., *Advanced Materials* (2005) **17**, 1519–1523, DOI: `10.1002/adma.200500104`.

[12] Z. Xie, M. Hoffman, P. Munroe, A. Bendavid, and P. Martin, *Acta Mater.* (2008) **56**, 852–861, DOI: `10.1016/j.actamat.2007.10.047`.

[13] L. S. Walker, V. R. Marotto, M. A. Rafiee, N. Koratkar, and E. L. Corral, *ACS Nano* (2011) **5**, 3182–3190, DOI: `10.1021/nn200319d`.

[14] A. N. Ranade, L. R. Krishna, Z. Li, J. Wang, C. S. Korach, and Y.-W. Chung, *Surface and Coatings Technology* (2012) **213**, 26–32, DOI: `10.1016/j.surfcoat.2012.10.007`.

[15] J. Keckes, M. Bartosik, R. Daniel, C. Mitterer, G. Maier, W. Ecker et al., *Scr. Mater.* (2012) **67**, 748–751, DOI: `10.1016/j.scriptamat.2012.07.034`.

[16] A. P. Hammersley, S. O. Svensson, M. Hanfland, A. N. Fitch, and D. Hausermann, *High Pressure Res.* (1996) **14**, 235–248, DOI: 10.1080/08957959608201408.

[17] W. Oliver, and G. Pharr, *J Mater Res* (1992) **7**, 1564–1580, DOI: 10.1557/JMR.1992.1564.

[18] H. Tadae, American Society of mechanical engineers, 3rd edn., (2000) pp. 55–57.

[19] A. Zeilinger, R. Daniel, M. Stefenelli, B. Sartory, L. Chitu, M. Burghammer et al., *J Phys D Appl Phys* (2015) **48**, 295303, DOI: 10.1088/0022-3727/48/29/295303.

[20] O. Kolednik, J. Predan, F. D. Fischer, and P. Fratzl, *Advanced Functional Materials* (2011) **21**, 3634–3641, DOI: 10.1002/adfm.201100443.

[21] R. Daniel, K. J. Martinschitz, J. Keckes, and C. Mitterer, *Journal of Physics D: Applied Physics* (2009) **42**, 075401.

[22] R. Daniel, J. Keckes, I. Matko, M. Burghammer, and C. Mitterer, *Acta Mater.* (2013) **61**, 6255–6266, DOI: 10.1016/j.actamat.2013.07.009.

[23] R. Daniel, K. Martinschitz, J. Keckes, and C. Mitterer, *Acta Mater.* (2010) **58**, 2621–2633, DOI: 10.1016/j.actamat.2009.12.048.

[24] L. Zhou, F. Körmann, D. Holec, M. Bartosik, B. Grabowski, J. Neugebauer et al., *Phys. Rev. B* (2014) **90**, 184102, DOI: 10.1103/PhysRevB.90.184102.

[25] A. G. Evans, *Journal of the American Ceramic Society* (1990) **73**, 187–206, DOI: 10.1111/j.1151-2916.1990.tb06493.x.

[26] S. Freiman, (1990) vol. 1, ch. Fracture of polycrystalline ceramics, pp. 72–83, DOI: 10.1007/978-94-011-6827-4_4.

[27] P. H. Mayrhofer, C. Mitterer, L. Hultman, and H. Clemens, *Prog. Mater Sci.* (2006) **51**, 1032–1114, DOI: 10.1016/j.pmatsci.2006.02.002.

[28] A. Riedl, R. Daniel, M. Stefenelli, T. Schöberl, O. Kolednik, C. Mitterer et al., *Scr. Mater.* (2012) **67**, 708–711, DOI: 10.1016/j.scriptamat.2012.06.034.

[29] J. Musil, *Surface and Coatings Technology* (2000) **125**, 322–330, DOI: 10.1016/S0257-8972(99)00586-1.

[30] C. Wang, K. Shi, C. Gross, J. M. Pureza, M. de Mesquita Lacerda, and Y.-.-.-W. Chung, *Surface and Coatings Technology* (2014) **257**, 206–212, DOI: 10.1016/j.surfcoat.2014.08.018.

[31] S. Zhang, D. Sun, Y. Fu, and H. Du, *Surface and Coatings Technology* (2003) **167**, 113–119, DOI: 10.1016/S0257-8972(02)00903-9.

[32] K. Chan, M. He, and J. Hutchinson, *Materials Science and Engineering: A* (1993) **167**, 57–64, DOI: 10.1016/0921-5093(93)90337-E.

[33] S. Zhang, D. Sun, Y. Fu, and H. Du, *Surf. Coat. Technol.* (2005) **198**, 2–8, DOI: 10.1016/j.surfcoat.2004.10.020.

[34] P. Fratzl, O. Kolednik, F. D. Fischer, and M. N. Dean, *Chem. Soc. Rev.* (2016) **45**, 252–267, DOI: 10.1039/C5CS00598A.

[35] P. Fratzl, and R. Weinkamer, *Progress in Materials Science* (2007) **52**, 1263–1334, DOI: 10.1016/j.pmatsci.2007.06.001.

[36] J. W. Hutchinson, *Theoretical and Applied Mechanics*, Elsevier, (1989) pp. 139–144, DOI: 10.1016/B978-0-444-87302-6.50017-X.

[37] R. Ritchie, *Materials Science and Engineering: A* (1988) **103**, 15–28, DOI: 10.1016/0025-5416(88)90547-2.

[38] J. W. Hutchinson, *J. Appl. Mech* (1987) **54**, 828–832, DOI: 10.1115/1.3173124.

[39] M. He, *Int. J. Solids Struct.* (1989) **25**, 1053–1067.

[40] X. L. Z. Huang, *Scientific Reports* (2013) **3**, DOI: 10.1038/srep01693.

[41] E. Chason, and B. W. Sheldon, *Surf. Eng.* (2003) **19**, 387–391, DOI: 10.1179/026708403225010118.

[42] J. Hutchinson, *Adv. Mater. Sev. Serv. Appl.* (1986)

[43] J. Watts, and G. Hilmas, *International Journal of Refractory Metals and Hard Materials* (2006) **24**, 222–228, DOI: 10.1016/j.ijrmhm.2005.04.005.

[44] W. Clegg, *Acta Metallurgica et Materialia* (1992) **40**, 3085–3093, DOI: 10.1016/0956-7151(92)90471-P.

[45] H. M. Chan, *Annual Review of Materials Science* (1997) **27**, 249–282, DOI: 10.1146/annurev.matsci.27.1.249.

[46] U. Helmersson, S. Todorova, S. A. Barnett, J. E. Sundgren, L. C. Markert, and J. E. Greene, *Journal of Applied Physics* (1987) **62**, 481–484, DOI: 10.1063/1.339770.

[47] P. C. Yashar, and W. D. Sproul, *Vacuum* (1999) **55**, 179–190, DOI: 10.1016/S0042-207X(99)00148-7.

[48] R. Daniel, A. Zeilinger, T. Schöberl, B. Sartory, C. Mitterer, and J. Keckes, *J Appl Phys* (2015) **117**, 235301, DOI: `10.1063/1.4922666`.

[49] M. Sebastiani, E. Bemporad, N. Schwarzer, and F. Carassiti, *Nanomechanical Analysis of High Performance Materials*, Springer Netherlands, (2014) pp. 263–284, DOI: `10.1007/978-94-007-6919-9_14`.

[50] J. Zalesak, M. Bartosik, R. Daniel, C. Mitterer, C. Krywka, D. Kiener et al., *Acta Mater.* (2016) **102**, 212–219, DOI: `10.1016/j.actamat.2015.09.007`.

[51] E. Degtyar, M. J. Harrington, Y. Politi, and P. Fratzl, *Angewandte Chemie International Edition* (2014) **53**, 12026–12044, DOI: `10.1002/anie.201404272`.

H

Grain boundary design of thin films: Using tilted brittle interfaces for multiple crack deflection toughening

Rostislav Daniel[a,*], Michael Meindlhumer[b], Walter Baumegger[c], Jakub Zalesak[c], Bernhard Sartory[d], Manfred Burghammer[e], Christian Mitterer[c], Jozef Keckes[b]

[a]Christian Doppler Laboratory for Advanced Synthesis of Novel Multifunctional Coatings at the Department of Physical Metallurgy and Materials Testing, Montanuniversität Leoben, Leoben, Austria
[b]Department of Materials Physics, Montanuniversität Leoben and Erich Schmid Institute for Materials Science, Austrian Academy of Sciences, Leoben, Austria

[c]Department of Physical Metallurgy and Materials Testing, Montanuniversität Leoben, Leoben, Austria
[d]Materials Center Leoben Forschung GmbH, Leoben, Austria
[e]ESRF, 38043 Grenoble, France

Abstract

Though hard and superhard ceramic nanocrystalline thin films exhibit extraordinary strength, they typically suffer from brittleness. The lack of plasticity and associated toughness in these materials is due to brittle fracture along grain boundaries of a low cohesive energy, which is favored over dislocation emission. The catastrophic intergranular fracture of ceramic films is undesirable in many applications and limits their exploitation potential despite of other exceptional physical properties. We demonstrate here that it is possible to increase fracture toughness of ceramic nanostructured materials of more than 150 % by a dedicated grain boundary orientation design with respect to the direction of the expected crack path without loss of hardness. The concept was applied to nanocrystalline monolithic TiN thin films which were mechanically tested as notched and unnotched microcantilever specimens inside a scanning electron microscope. The films with a columnar chevron-like grain morphology exhibit multiple crack deflections at the kink planes of the repeatedly tilted grains resulting in energy dissipation at the crack tip and in an increase of fracture surface area. The results document that the number of predefined crosssectional crack turns as well as the film density play decisive roles in the measured overall material fracture resistance. We suggest that by a dedicated design of grain boundary orientations, it is possible to synthetize novel types of hard and tough nanomaterials.

H.1. Introduction

The ability of most hard materials to deform inelastically isusually rather limited. The main deformation mechanism in ma-terials such as ceramics is brittle fracture, since the activation ofdislocation glide on most slip systems in ceramic materials requiresmuch higher stress than that for fracture [1]. On the contrary,materials with enhanced plasticity are usually not very strong. Anenhancement of the material fracture toughness without compromising the strength is thus of vital importance for many applica-tions. As the fracture toughness represents the ability of a material to resist crack propagation upon loading, its enhancement relies essentially on an increase of energy needed to cause fracture. Thisrequires the control of deformation mechanisms associated withthe initiation and propagation of cracks. In brittle ceramics lacking plasticity due to limited mobility of dislocations, an enhancementof the intrinsic toughening mechanisms (suppressing crack initiation) is rather challenging. Extrinsic toughening (inhibiting crack propagation) is, on the other hand, easier to be realized. It is in mostcases the only source of toughening in brittle materials allowing forfracture toughness enhancement even without an increase ofductility [2]. Some established strategies for extrinsic tougheningrely on the formation of structures with a large structural andmechanical heterogeneity [3, 4], e.g. by incorporation of ductilephases [2, 5, 6], formation of composite [7], lamellar [8–10] or layered structures [11–13]. By the implementation of extrinsic toughening mechanisms, such as grain bridging [2], crack deflection [14], reduction of the crack driving force by grain boundarydesign [15] or phase transformation [16], even brittle materials such as ceramics can be made tough and thus more damage tolerant.

The objective of the present work is to study the possibility toextensively enhance damage tolerance of brittle materials bydedicated grain boundary orientation design resulting in multiple deflections of cracks propagating in the material. The concept wasapplied to nanocrystalline TiN films, representing a typical brittlethinfilm material, which were for this purpose synthesized by glancing angle deposition (GLAD) technique allowing to control thegrowth direction of the columnar grains. The resulting chevron-likestructure demonstrates a promising way for an enhancement of theresistance of brittle nanostructured materials to fracture, whichmay achieve up to 150 % higher values than that of correspondingfilms with a common columnar microstructure.

H.2. Experimental details

The TiN films with tilted chevron microstructure were prepared by magnetically unbalanced reactive pulsed direct current magnetron sputtering alternately from two Ti targets arranged in confocal configuration at a tilting angle of 50 ° with respect to the substrate normal on a static silicon substrate located at the center of the substrate holder. The synthesis of the films was carried out in an Ar + N_2 plasma discharge under deposition conditions, which allowed to grow two sets of samples very much differing in their density and microstructure. In the first set of samples A, the total pressure ptot was 0.75 Pa with partial pressures of argon p_{Ar}= 0.5 Pa and nitrogen p_{N_2}= 0.25 Pa, target current density I_d = 17 mA/cm^2, bias voltage U_s= 80 V, substrate temperature T_s= 550 °C and target-to-substrate distance d_{ts}= 50 mm. In the second set of samples B, higher plasma density and energy of the sputter flux associated with higher target current density I_d of 28 mA/cm^2, bias voltage U$_s$ = 140 V and lower total pressure $p_{tot} = p_{Ar} + p_{N_2} = 0.13 + 0.03$ Pa (effectively reducing thermalization of sputtered flux) resulted in much denser films exhibiting enhanced mechanical properties (see section 3.2). The substrate temperature was 550 °C and d_{ts} = 100 mm in this case. The deposition time from each sputtering source was varied so that the resulting multilayer architecture consisted either of 6 or 12 sublayers with individual thicknesses of 500 and 250 nm, respectively. For comparison, reference single-layer TiN films with columnar grains grown perpendicular to the substrate surface were synthesized from a Ti target on a rotating Si substrate under otherwise same deposition conditions as in the case of the corresponding multilayer films with chevron microstructure. The total thickness of all samples was constant with 3 mm. The Si(100) substrates with dimensions of 20×20×0.3 mm^3 were polished, pre-cleaned in acetone and ethanol (5 min in each) and plasma-etched in an Ar discharge for 10 min at 500 V bias voltage prior deposition. The base pressure was 1×10^{-4} Pa or lower.

Nanoindentation experiments (UMIS, Fischer-Cripps Laboratories Ltd.) and in-

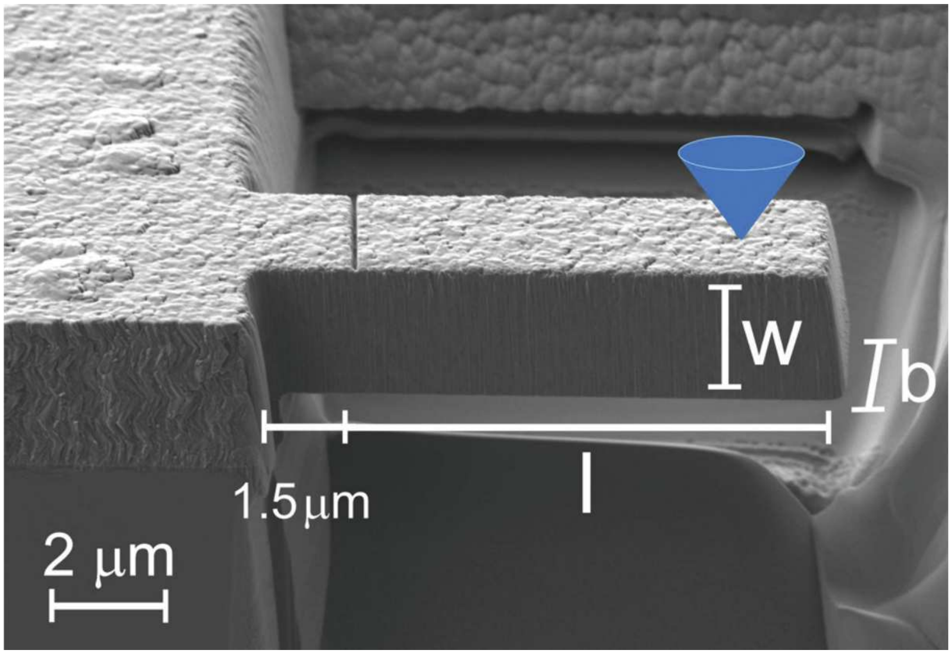

Figure H.1.: SEM micrograph of a representative microcantilever beam specimen used for micro-bending testing. All specimens were prepared by FIB milling with a length $l = 8.8 \pm 0.5$ mm, width $b = 3.1 \pm 0.1$ mm and height $w = 3.2 \pm 0.1$ mm (corresponding to the film thickness) with and without a pre-crack of a depth of 500± 50 nm at a distance of 1.5 mm from the beam support.

situ micromechanical tests of microcantilever beam specimens inside a scanning electron microscope (SEM, LEO 982, Crossbeam 1540XB, Zeiss) equipped with a nanoindenter (PicoIndenter 85, Hysitron) were carried out to study mechanical properties of the films. Indentation hardness and modulus of the films were determined from the load-displacement curves by using a Berkovich tip according to the Oliver&Pharr method [17]. In addition, the elastic modulus of the microcantilever beams was calculated from the slope of the load-deflection curves according to

$$E = \frac{4F}{\delta b} \times \left(\frac{l}{w}\right)^3, \tag{H.1}$$

which represents the elastic properties of free-standing films without the effect of residual stress. In the calculation, the geometry of the microcantilevers fabricated by focused ion beam (FIB) in a dual beam FIB/SEM (Zeiss NVision 40) workstation was taken into account. $l = 8.8 \pm 0.5$ mm and $b = 3.1 \pm 0.1$ mm are the length and width of the cantilever beams, respectively, $w = 3.2 \pm 0.1$ mm corresponds to the film thickness (H.1). δ is the beam deflection at the applied load F. The microcantilevers were loaded using a sphero-conical indenter of 700 nm radius in normal direction in displacement controlled mode with a constant displacement rate of 20 nm/s. The data was corrected for the instrument compliance.

From the bending of the microcantilever beams, the fracture stress σ_F was calculated from the maximum applied load at fracture according to

$$\sigma_F = 6\frac{Fl}{bw^2}. \tag{H.2}$$

While σ_F of an unnotched microcantilever beam represents the fracture strength of the specimen, fracture toughness K_{IC} was determined from the maximum load prior fracture of the microcantilever pre-cracked by a notch with a depth a of 500 ± 50 nm, which is milled by FIB at a distance of 1.5 mm from the beam support (H.1). By applying linear-elastic fracture mechanics, K_{IC} was calculated as

$$K_{IC} = \sigma_F \sqrt{\pi a} F\left(\frac{a}{w}\right), \tag{H.3}$$

where $F(a/w)$ is a dimensionless shape factor given for specific microcantilever beam geometry as [18].

$$F\left(\frac{a}{w}\right) = \sqrt{\frac{2w}{\pi a}} \tan\left(\frac{\pi a}{2w}\right) \frac{0.923 + 0.199\left(\sin\left(\frac{\pi a}{2w}\right)\right)^4}{cos\left(\frac{\pi a}{2w}\right)}. \tag{H.4}$$

SEM was also used to study the cross-sectional microstructure of the films in their as-deposited state as well as of the fracture planes of the microcantilever beams after the bending experiments. Detailed analysis of the film morphology was carried out by transmission electron microscopy (TEM, JEM-2100F, JEOL) equipped with spherical aberration correction. TEM lamellae of selected films were cut from the samples by FIB and polished to electron transparency with currents from 13 nA down to 10 pA at 30 kV.

Advanced local structure analysis of selected films was performed by a cross-sectional X-ray nanodiffraction experiment in transmission geometry at the nanofocus extension of ID13 beamline of the European Synchrotron Radiation Facility (ESRF) in Grenoble, France. The samples prepared as slices with a typical width of about 100 mm [19] were exposed to a high brilliance X-ray beam with energy of 14.7 keV, focused by dedicated X-ray optics to 100 nm in diameter. A precise sample positioning allowed collecting the diffracted Debye-Scherrer rings at a 2D detector in 100 nm steps and thus performing a precise spatially resolved microstructure characterization across the film thickness. The data were processed by Fit2D software package [20].

H.3. Results

H.3.1. Straight and chevron-like grain morphology of TiN films

In a typical face-to-face sputter configuration with a substrate surface facing the sputter source, the particles of the sputter flux impinge onto the substrate surface at a normal direction. This gives rise to the formation of a typical columnar microstructure of nanocrystalline films consisting of straight elongated grains grown perpendicular to the film/substrate interface [21]. In contrast, if incident particles impinge onto the substrate surface in off-normal direction, the deposited films subsequently develop with tilted columnar grain morphology [22]. By alternating incidence angle during deposition from two sputter sources arranged in a confocal configuration and tilted at the same angle with respect to the substrate normal, films with symmetric chevron microstructure may develop, as demonstrated for TiN films in H.2a and b. The tilting angle of the columnar grains and the resulting film microstructure strongly depend on the incident angle of the sputter flux and the growth conditions. By their variation, synthesis of films with columns tilted in a wide range with respect to the substrate normal, having either dense or porous microstructure, is possible [23, 24]. If the sputter flux arrives at a very oblique angle of incidence, the formed nuclei at the substrate surface shadow the area behind them, thus preventing the entire substrate surface to be coated. This phenomenon represents the main contribution to the formation of intergranular voids and pores during film growth and the development of highly defective and porous films by GLAD process [25]. For this reason, a relatively small inclination angle of 50 ° during the deposition of the chevron-like TiN films was chosen in this study to achieve a microstructure with high density and possible absence of micro- or nanoscale pores at the grain boundaries. Further important contributors to sufficient film density are also an adequately high substrate temperature and energy of the sputter flux promoting surface adatom diffusion during film growth. This may, to a certain extent, compensate the shadowing effects and contribute to the formation of a dense microstructure of the films, free of macroscopic defects at the grain boundaries as shown in the SEM cross-sectional micrographs of the representative films of series A (H.2a and b). A typical columnar microstructure oriented perpendicular to the substrate surface of a TiN film deposited from one Ti target on a rotating Si substrate is depicted in H.2c for comparison.

More detailed investigation of the film microstructure by TEM revealed the presence of nanoscale pores along some grain boundaries in the 12-layer chevron film of

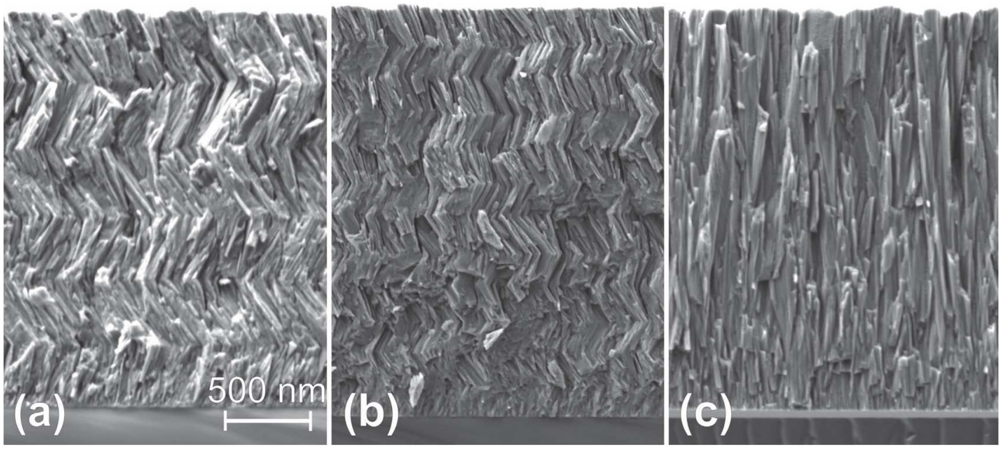

Figure H.2.: SEM cross-sectional micrographs of representative TiN films with chevron-like microstructure consisting of (a) 6 and (b) 12 layers and (c) a reference TiN film grown on a rotating Si substrate with columnar microstructure oriented perpendicular to the substrate surface.

series A (H.3). Their origin is associated, on the one hand, with the specific film growth conditions of the GLAD process as discussed above but also with the preparation of the TEM lamella by FIB due to preferential removal of weakly bonded atoms during milling. This, however, also indicates an underdense structure of the grain boundaries. On the contrary, no pores were observed at the grain boundaries of the films of series B indicating the importance of the growth conditions on the development of a dense film microstructure. The advantages and disadvantages of the porous microstructure of the grain boundaries on the mechanical properties will be discussed in detail in section 4. The TEM investigations further showed that the columnar structure is preserved across the entire film thickness without significant variation in the width of the columns. Moreover, the change in the growth direction did not result in any discontinuity of the columnar grains across the kink planes and the columns developed continuously throughout the film. This is more evident in the high-resolution TEM micrograph in H.4a showing the continuous kinks without any evidence of renucleation at the kink planes upon changing the direction of the incident sputter flux or a significant change in the crystallographic orientation. One of the reasons for the uninterrupted growth is that the growing surface was always exposed to an incident sputter flux from the plasma discharge from one of the two sputter sources, which alternated during deposition. The second reason is sufficiently high surface diffusion resulting in a well aligned columnar structure without any grain boundary at the kink planes.

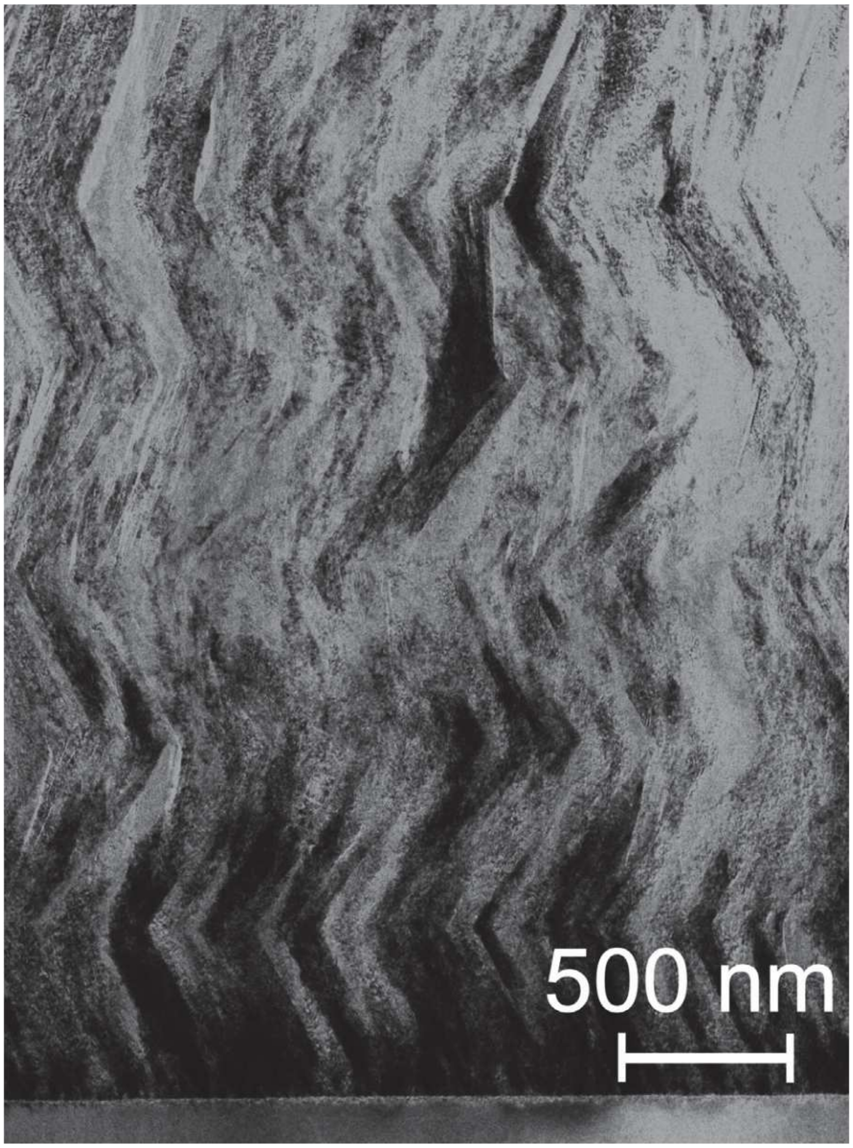

Figure H.3.: TEM cross-sectional micrograph of a representative 6-layer TiN film revealing the continuous chevron-like microstructure.

A detailed analysis of the crystallographic structure of the chevron-like TiN films by X-ray nanodiffraction revealed a crystallographic continuity across the film thickness irrespective of the direction of the incident sputter flux. Details on the experimental setup and data evaluation can be found in Refs. [19, 26]. The phase plot of the TiN film of series A with 12 sublayers depicted in H.5a shows that the film develops initially with the (100) texture in the near film/substrate interface region

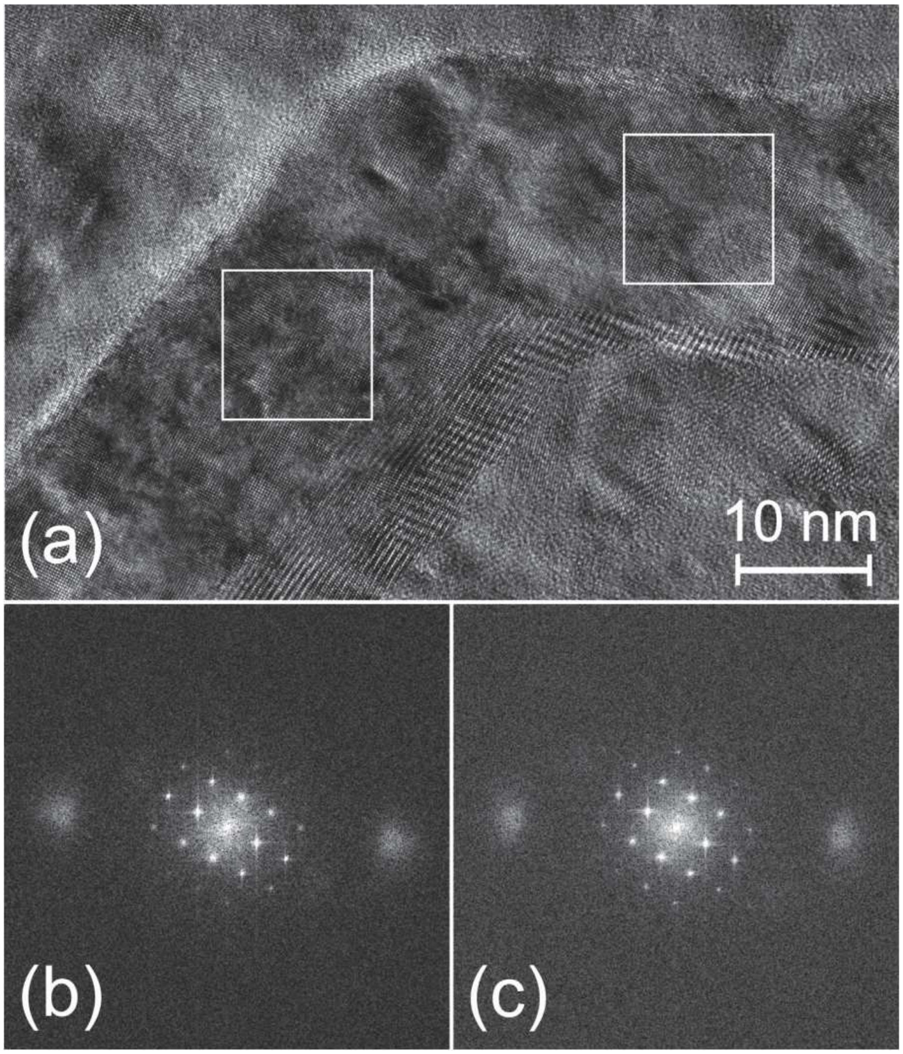

Figure H.4.: High-resolution TEM micrograph of the 6-layer chevron-like TiN film (a) reveals microstructure continuity across the kink planes without an evidence of renucleation upon changing the direction of the incident sputter flux. Fast Fourier transform images (b) and (c) obtained from two positions of the columnar grain further show continuity also in the crystallographic structure and orientation.

which continuously changes towards the (110) texture in further growth stages. This structure development with increasing film thickness is also evident from the contrast variation in the DF TEM micrograph in H.3 revealing differently oriented columnar grains within the initial stage of the film growth and at greater thicknesses. These results are consistent with the results obtained for the 12-layer chevron-like TiN films

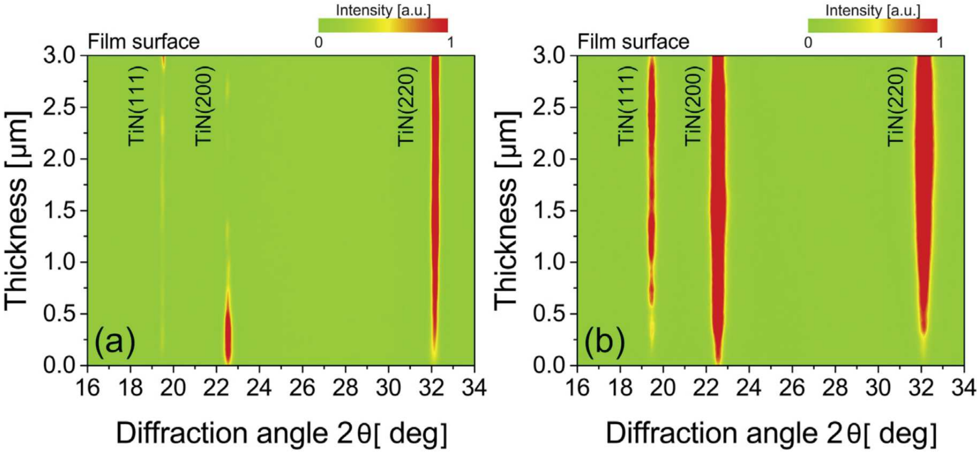

Figure H.5.: (a) Intensity distribution of TiN (111), (200) and (110) diffraction peaks across the thickness of the 12-layer chevron-like TiN film of series A showing a texture cross-over from (100) towards (110) at about 350 nm, given by the anisotropy in the surface adatom diffusivity. The texture cross-over does not affect the continuity of the grain orientation upon changing the direction of the incident sputter flux, which remains unaltered below and above the critical film thickness of 350 nm. (b) In contrast, the grain orientation of the reference TiN film with columnar microstructure oriented in the substrate normal is independent of the film thickness.

of series B. The initial development of the (100) texture is typical for transition metal nitride films prepared by physical vapor deposition and is commonly explained as due to the thermodynamically driven minimization of the surface energy of nuclei formed on the substrate surface prior and during coalescence [27]. However, under highly non-equilibrium conditions typical for sputtering processes, the kinetic restrictions easily overrule the thermodynamic effects and the microstructural evolution is thus predominantly controlled by the anisotropy in the surface adatom diffusivity [28, 29]. This may subsequently result in a texture crossover as observed for the chevron-like TiN film at the thickness of 350 nm (H.5a). The crystallographic continuity is, however, independent of the actual grain orientation. The preserved crystallographic structure across the kinks can be found in both (100)- and (110)-oriented columnar grains, i.e. below and above the film thickness of 350 nm (H.5a). This is further demonstrated by fast Fourier transform images obtained from two positions of the columnar grain shown in H.4a, before and after a kink. For both cases, the crystallographic structure and orientation of the tilted columnar grain are identical (H.4b,c). The effect of the incident direction of the sputter flux on the development of the film structure is evident from the phase plots shown in H.5. While the texture of the chevron-like TiN film changed during growth from (100) to (110) (H.5a), the grain orientation of the reference TiN film with columnar microstructure oriented in the substrate normal remained unaltered (H.5b). This indicates that under given process conditions with the normal incidence of the sputtered flux, no preferential surface diffusion adatom flux exists between differently oriented TiN grains.

H.3.2. Cross-sectional grain morphology-dependent mechanical properties

Nanoindentation experiments of the as-deposited TiN films revealed a strong effect of the film microstructure on the mechanical properties. While the hardness of the reference TiN sample of a series A was 21.5 GPa, it slightly reduced with tilting the columnar grains to 19.5 GPa for the film with 6 sublayers. The hardness reduction was, however, reversed with an increase of the number of tilted sublayers so that the hardness of the 12-layer chevron-like TiN films of series A reached basically the same value of 21.3 GPa as that of the corresponding reference sample. The importance of a dense, porous-free microstructure of thin films on their hardness is demonstrated for the films of series B. The reference sample of series B exhibited significantly higher hardness of 25 GPa than that of the corresponding film of series A. Similarly, the hardness of the chevron-like film of series B with 12 sublayers of 24.5 GPa was higher than that of the 12-layer chevron-like film of series A. Moreover, no hardness reduction was observed with respect to the reference sample, which indicates that the loss of strength by tilting the columnar grains can be significantly reduced by increasing the number of sublayers in the film. The results of the nanoindentation testing of films of both series summarized in H.1 further demonstrate the importance of the film density on the mechanical properties of the films. Not only hardness and elastic modulus but also resistance of films to fracture are higher in the case of dense films of series B. This is more pronounced for chevron-like films where the possible presence of voids and pores significantly deteriorates film strength.

Although the tilted columnar microstructure does not seem to be beneficial for hardness enhancement, it significantly contributes to the enhancement of fracture toughness. The fracture toughness was determined by in-situ bending of pre-cracked microcantilever beam specimens and the values are given in H.1. The elastic modulus and fracture stress were obtained by probing unnotched microcantilevers. Representative stress-deflection curves of both experiments are depicted in H.6 showing that the values of the maximum applied stress prior fracture vary depending on the

Table H.1.: Indentation hardness H_I and elastic modulus E_I, determined by nanoindentation, and elastic modulus E, fracture stress σ_F and fracture toughness K_{IC} of TiN films with columnar grains oriented perpendicular to the film/substrate interface and of TiN films with tilted microstructure. Films of series A exhibits lower density than corresponding films of series B.

Film system		Nanoindentation testing	
		Indentation hardness H_i GPa]	Indentation modulus E_i GPa]
Series A	TiN (columnar structure)	21.5±1	390±20
	TiN 6-layer (chevron structure)	19.5±1	450±25
	TiN 12-layer (chevron structure)	21.3±1	380±15
Series B (dense)	TiN (columnar structure)	25±1	450±15
	TiN 12-layer (chevron structure)	24.5±1	440±20

Film system		Micromechanical testing in SEM		
		Elastic modulus E [GPa]	Fracture stress σ_F [GPa]	Fracture toughness K_{IC} [MPa $\mathrm{m}^{\frac{1}{2}}$]
Series A	TiN (columnar structure)	114±2	1.6±0.1	1.2±0.1
	TiN 6-layer (chevron structure)	113±3	1.8±0.1	1.4±0.1
	TiN 12-layer (chevron structure)	140±5	2.3±0.1	1.9±0.1
Series B (dense)	TiN (columnar structure)	–	–	–
	TiN 12-layer (chevron structure)	134±34	2.9±0.1	3.0±0.1

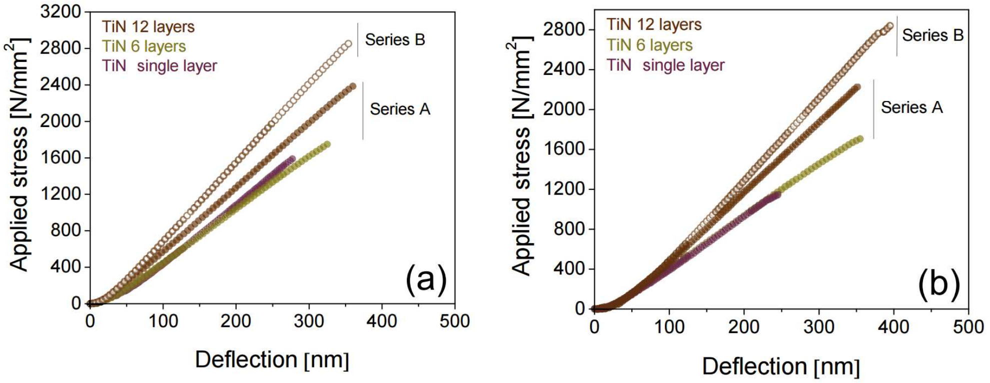

Figure H.6.: Stress-deflection curves of (a) unnotched and (b) notched microcantilever beam specimens of the TiN films with straight and chevron-like columnar morphology used for the evaluation of the fracture stress and fracture toughness, respectively. The films of series A and B differ particularly in their density.

film density and architecture. The fracture resistance of the films obviously increases when the columnar grains are tilted and the enhancement becomes more pronounced with the higher number of tilted grain boundaries (see the maximum applied stress in H.6 and corresponding values in H.1). Besides the enhancement of the fracture stress and toughness of the chevron-like films with respect to the columnar reference samples up to 80 and 150 %, respectively (see H.1), also the ability of the films to elastically deform under bending significantly increased. This is documented by an increase of the maximum deflection at fracture of the unnotched chevron-like films with 12 sublayers with respect to corresponding reference sample from 280 to 363 nm (series A) and further to 357 nm (series B) (H.6). Moreover, a comparison of the results for the chevron-like films of the series A and B indicates the importance of a dense, porous-free microstructure of materials in achieving high fracture stress and toughness. Obviously, a reduction of defect concentration, e.g. micro- and nano-scale defects in the grains and at the grain boundaries, results in an enhancement of damage tolerance as more energy is required to initiate and propagate cracks of various sizes in such materials.

H.4. Discussion

Brittle fracture in polycrystalline ceramics typically occurs along grain boundaries due to the weaker atomic bonding within the interfacial area. A crack initiated during loading thus preferentially propagates along these paths of lower fracture

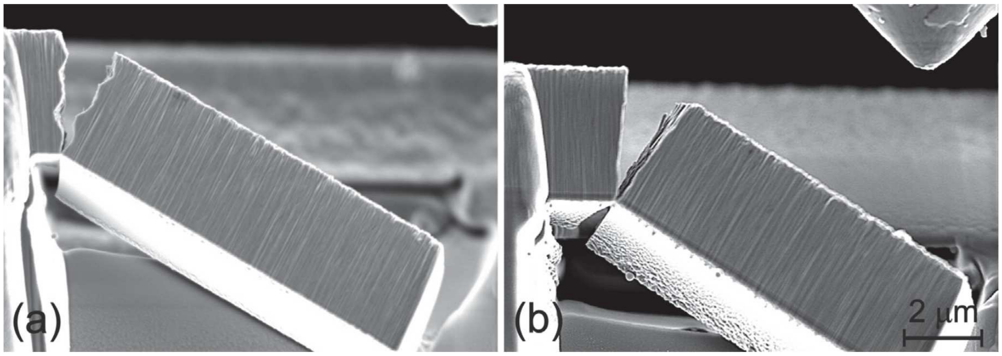

Figure H.7.: (a) Multiple crack deflection demonstrated for a microcantilever beam specimen of the 6-layer TiN film with chevron-like microstructure. (b) Typical brittle fracture of a reference TiN film with a columnar oriented perpendicular to the film/substrate interface.

energy, being deflected at each grain boundary. With a reduction of the grain size to the sub-micrometer scale, the number of such events significantly increases, which requires more energy for a crack to propagate than for a smooth cleavage plane. This makes polycrystalline ceramics more fracture resistant than their single crystal counterparts [30]. The increase in roughness of the fracture surface is, however, not dramatic in the case of nanocrystalline ceramics, which are still very brittle. An increase of the total fracture surface area has thus to be very pronounced to observe a significant effect.

A repeatedly tilted columnar microstructure is demonstrated here as a perspective concept of a fracture toughness enhancement of otherwise brittle nanocrystalline materials. Although the enhancement shown for nanocrystalline brittle TiN films is partially compromised by a loss of strength associated with easier dislocation motion at tilted grain boundaries, the reduction of hardness is not excessively pronounced (can even be reversed by an increase of the number of sublayers) and is compensated by other positive effects. In contrast to the reference films with columnar microstructure developed perpendicular to the film/substrate interface, the films with tilted microstructure exhibit a more than 30 % higher ability to elastically deform under bending (H.6a) and up to 150 % higher fracture toughness (H.1). This is given by the specific arrangement of the tilted columnar grains, which involves different deformation mechanisms. In conventional monolithic nanocrystalline strong yet brittle ceramic films, once initiated, a propagating crack grows to a critical dimension and subsequently propagates in an unstable fashion through the entire film. The spontaneous crack propagation without a significant variation in the crack driving force

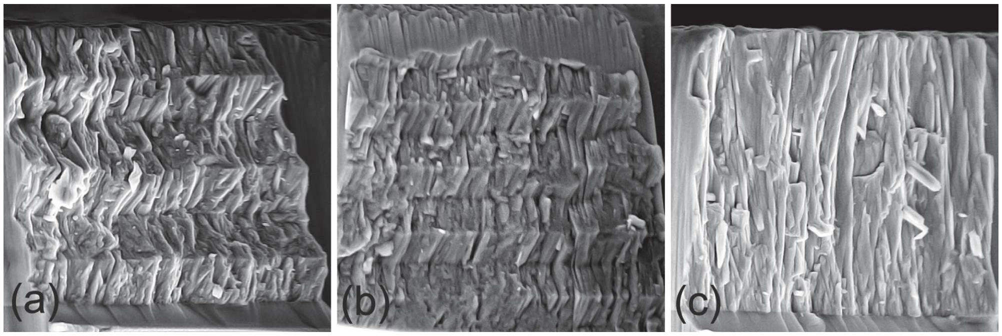

Figure H.8.: SEM micrographs of fracture surfaces of microcantilever beam specimens of TiN films with tilted microstructure consisted of (a) 6 layers and (b) 12 layers. The rough fracture surface originated from multiple crack deflection associated with a significant fracture toughness enhancement. In contrast, (c) the fracture surface of a reference TiN film with columnar grains oriented perpendicular to the film/substrate interface originated from spontaneous unstable crack growth along the boundaries of columnar grains.

is associated with the presence of disordered weakly bonded grain boundaries gradually developed throughout the film, which serve as preferential paths for propagating cracks. On the other hand, in a film with tilted columnar grains, a weak interfacial bonding advances a crack to deflect along the curved grain boundaries at the kink planes rather than passing through a strongly bonded grain interior laying in its original path. The multiple deflections macroscopically visible on the fracture surface generated during the bending experiment on the 6-layer chevronlike TiN film are shown in H.7a, which is in contrast to the spontaneous unstable crack growth, characteristic for common ceramic films (H.7b). Since the crack deflection at the kink planes of the tilted grains is associated with a reduction of the crack driving force and local dissipation of stresses at the crack tip, these effects, together with the subsequent increase of the fracture surface area (H.8a and b), effectively contribute to the fracture toughness enhancement of the films (H.1).

The importance of the material microstructure in the fracture resistance can be further demonstrated by a comparison of the fracture stress and toughness of films differing predominantly in their density (H.6). The obviously lower fracture resistance of the films of series A compared to their counterparts of the series B is associated with the underdense grain boundaries. The presence of voids, nano- or micro-sized pores between individual columnar grains significantly reduces the energy needed for a continuous crack tip opening along these underdense regions and thus promotes rapid brittle fracture. On the other hand, densification of the grain boundaries resulting in a stronger atomic bonding between neighboring grains effectively suppresses crack propagation. This effect on the fracture toughness enhancement is, however, only minor compared to the effect of the tilted microstructure, which allows for a better control of a crack propagation, more effective dissipation of stresses during deformation of the material and thus enhanced fracture toughness (H.1).

The concept of the fracture toughness enhancement by grain boundary design is different to the strategy to enhance fracture toughness by a combination of constituents well differing in microstructure and mechanical properties, which relies on the material heterogeneity and plasticity at the crack tip [8, 13, 14, 31]. In the films with chevron-like microstructure, an enhancement of the fracture toughness may be achieved even without plasticity if the multiple crack deflection along tilted columnar grains is involved during fracture. The grain boundaries with the chevron-like morphology operates like potential sacrificial channels or predefined crack propagation paths, a concept which was recently reported for branch-stem interfaces of conical tress [32]. The implementation of this concept demonstrates that a control of crack propagation by grain boundary engineering is a promising way to achieve high toughness even in brittle man-made materials.

H.5. Conclusions

We have shown that sophisticated grain boundary design allows for an effective control of crack propagation during fracture of hard yet brittle films with sculptured microstructure. A controlled multiple crack deflection at the kink planes of tilted columnar grains with sub-micrometer size and chevron-like shape ensures an effective reduction of the crack driving force with subsequent increase of crack extension energy. These effects, together with an increase of the fracture surface by microscopic fracture surface patterning result in an effective suppression of crack propagation and fracture toughness enhancement up to 150 % compared to films with common columnar microstructure developed perpendicular to the substrate surface without loss of hardness. We have demonstrated that grain boundaries with weak cohesive energy may be used as a toughening element of brittle nanostructured materials if they are specifically structured and oriented with respect to the expected crack path. A dedicated design of grain boundaries thus offers great potential in the synthesis of novel hard fracture resistant materials.

Acknowledments

The film characterization in this work has received research funding from the European Union, within the large collaborative project ISTRESS, Grant Agreement No. 604646. The financial support of the film synthesis by the Austrian Federal Ministry of Science, Research and Economy and the National Foundation for Research, Technology and Development in the frame of the Christian Doppler Laboratory is also gratefully acknowledged.

Bibliography to paper H

[1] A. G. Evans, *Journal of the American Ceramic Society* (1990) **73**, 187–206, DOI: `10.1111/j.1151-2916.1990.tb06493.x`.

[2] R. O. Ritchie, *Nature Materials* (2011) **10**, 817–822, DOI: `10.1038/nmat3115`.

[3] S. M. Z. Tang, N. A. Kotov, and B. Ozturk, *Nature Materials* (2003) **2**, 413–418, DOI: `10.1038/nmat906`.

[4] U. G. K. Wegst, H. Bai, E. Saiz, A. P. Tomsia, and R. O. Ritchie, *Nature Materials* (2014) **14**, 23–36, DOI: `10.1038/nmat4089`.

[5] M. Launey, E. Munch, D. Alsem, H. Barth, E. Saiz, A. Tomsia et al., *Acta Materialia* (2009) **57**, 2919–2932, DOI: `10.1016/j.actamat.2009.03.003`.

[6] Z. Xia, L. Riester, W. Curtin, H. Li, B. Sheldon, J. Liang et al., *Acta Materialia* (2004) **52**, 931–944, DOI: `dx.doi.org/10.1016/j.actamat.2003.10.050`.

[7] C. Wang, K. Shi, C. Gross, J. M. Pureza, M. de Mesquita Lacerda, and Y.-.-.-W. Chung, *Surface and Coatings Technology* (2014) **257**, 206–212, DOI: `10.1016/j.surfcoat.2014.08.018`.

[8] E. Munch, M. E. Launey, D. H. Alsem, E. Saiz, A. P. Tomsia, and R. O. Ritchie, *Science* (2008) **322**, 1516–1520, DOI: `10.1126/science.1164865`.

[9] F. Bouville, E. Maire, S. Meille, B. V. de Moortèle, A. J. Stevenson, and S. Deville, *Nature Materials* (2014) **13**, 508–514, DOI: `10.1038/nmat3915`.

[10] M. P. Rao, A. J. Sánchez-Herencia, G. E. Beltz, R. M. McMeeking, and F. F. Lange, *Science* (1999) **286**, 102–105, DOI: `10.1126/science.286.5437.102`.

[11] K. Chan, M. He, and J. Hutchinson, *Materials Science and Engineering: A* (1993) **167**, 57–64, DOI: `10.1016/0921-5093(93)90337-E`.

[12] S. Zhang, D. Sun, Y. Fu, and H. Du, *Surf. Coat. Technol.* (2005) **198**, 2–8, DOI: `10.1016/j.surfcoat.2004.10.020`.

[13] R. Daniel, M. Meindlhumer, J. Zalesak, B. Sartory, A. Zeilinger, C. Mitterer et al., *Materials & Design* (2016) **104**, 227–234, DOI: `dx.doi.org/10.1016/j.matdes.2016.05.029`.

[14] M. He, *Int. J. Solids Struct.* (1989) **25**, 1053–1067.

[15] T. Watanabe, (1991) **46**, 25–48, DOI: `10.4028/www.scientific.net/MSF.46.25`.

[16] R. Hannink, *Journal of the American Ceramic Society* (2000) **83**, 461–487.

[17] W. Oliver, and G. Pharr, *J Mater Res* (1992) **7**, 1564–1580, DOI: `10.1557/JMR.1992.1564`.

[18] H. Tadae, American Society of mechanical engineers, 3rd edn., (2000) pp. 55–57.

[19] J. Keckes, M. Bartosik, R. Daniel, C. Mitterer, G. Maier, W. Ecker et al., *Scr. Mater.* (2012) **67**, 748–751, DOI: `10.1016/j.scriptamat.2012.07.034`.

[20] A. P. Hammersley, *FIT2D: An Introduction and Overview*, ESRF, (1997) `http://www.esrf.eu/computing/scientific/FIT2D/FIT2D_INTRO/fit2d.html`.

[21] P. Barna, and M. Adamik, *Thin Solid Films* (1998) **317**, 27–33, DOI: `10.1016/S0040-6090(97)00503-8`.

[22] K. Robbie, and M. J. Brett, *Journal of Vacuum Science & Technology A* (1997) **15**, 1460–1465, DOI: `10.1116/1.580562`.

[23] K. Robbie, L. J. Friedrich, S. K. Dew, T. Smy, and M. J. Brett, *Journal of Vacuum Science & Technology A* (1995) **13**, 1032–1035, DOI: `dx.doi.org/10.1116/1.579579`.

[24] D. Henderson, M. H. Brodsky, and P. Chaudhari, *Applied Physics Letters* (1974) **25**, 641–643, DOI: `dx.doi.org/10.1063/1.1655341`.

[25] K. D. Harris, D. Vick, T. Smy, and M. J. Brett, *Journal of Vacuum Science & Technology A* (2002) **20**, 2062–2067, DOI: `dx.doi.org/10.1116/1.1517258`.

[26] R. Daniel, J. Keckes, I. Matko, M. Burghammer, and C. Mitterer, *Acta Mater.* (2013) **61**, 6255–6266, DOI: `10.1016/j.actamat.2013.07.009`.

[27] J. Pelleg, L. Zevin, S. Lungo, and N. Croitoru, *Thin Solid Films* (1991) **197**, 117–128, DOI: `dx.doi.org/10.1016/0040-6090(91)90225-M`.

[28] J.-S. Chun, I. Petrov, and J. E. Greene, *Journal of Applied Physics* (1999) **86**, 3633–3641, DOI: `dx.doi.org/10.1063/1.371271`.

[29] R. Daniel, K. J. Martinschitz, J. Keckes, and C. Mitterer, *Journal of Physics D: Applied Physics* (2009) **42**, 075401.

[30] S. Freiman, (1990) vol. 1, ch. Fracture of polycrystalline ceramics, pp. 72–83, DOI: `10.1007/978-94-011-6827-4_4`.

[31] J. Gunnars, P. Ståhle, and T. C. Wang, *Computational Mechanics* (1997) **19**, 545–552, DOI: `10.1007/s004660050207`.

[32] U. Müller, W. Gindl-Altmutter, J. Konnerth, G. A. Maier, and J. Keckes, *Sci. Rep.* (2015) **5**, DOI: `10.1038/srep14522`.